

X-RAY DETECTION AND STRAIN SENSING APPLICATIONS OF COLLOIDAL QUANTUM DOTS

THESIS

Michael D. Sherburne, 2d Lt., USAF

AFIT-ENG-M20-M-060

DEPARTMENT OF THE AIR FORCE
AIR UNIVERSITY

AIR FORCE INSTITUTE OF TECHNOLOGY

Wright-Patterson Air Force Base, Ohio

DISTRIBUTION STATEMENT A
APPROVED FOR PUBLIC RELEASE; DISTRIBUTION UNLIMITED.

The views expressed in this document are those of the author and do not reflect the official policy or position of the United States Air Force, the United States Department of Defense or the United States Government. This material is declared a work of the U.S. Government and is not subject to copyright protection in the United States. This research was supported in part by the U.S., Dept. of Energy, National Nuclear Security Administration under grant NA000103. This work was supported by the National Nuclear Security Administration of the U.S. Department of Energy under contract 89233218CNA000001. Approved for unlimited release, LA-UR-20-XXXXX. Part of this work was performed at the Center for High Technology Materials, University of New Mexico, under the support of the Office of Naval Research Grants N00014-17-1-2975 and N00014-19-1-2117, and of the Navy HBCU/MI Program Grant N00014-18-1-2739. The views expressed are those of the authors and do not reflect the official policy or position of the U.S. Air Force, Department of Defense, Department of Energy, University of New Mexico, or the U.S. government. Additionally, this work was performed, in part, at the Center for Integrated Nanotechnologies, an Office of Science User Facility operated for the U.S. Department of Energy (DOE) Office of Science. Los Alamos National Laboratory, an affirmative action equal opportunity employer, is managed by Triad National Security, LLC for the U.S. Department of Energy's NNSA, under contract 89233218CNA000001. This work made use of the Advanced Photon Source, an Office of Science User Facility operated for the U.S. Department of Energy (DOE) Office of Science by Argonne National Laboratory, was supported by the U.S. DOE under Contract No. DE-AC02-06CH11357.

AFIT-ENG-M20-M-060

X-RAY DETECTION AND STRAIN SENSING APPLICATIONS OF COLLOIDAL QUANTUM DOTS

THESIS

Presented to the Faculty

Department of Electrical and Computer Engineering

Graduate School of Engineering and Management

Air Force Institute of Technology

Air University

Air Education and Training Command

in Partial Fulfillment of the Requirements for the

Degree of Master of Science in Electrical Engineering

Michael D. Sherburne, B.S.E.E.,

2d Lt., USAF

20 March 2020

DISTRIBUTION STATEMENT A
APPROVED FOR PUBLIC RELEASE; DISTRIBUTION UNLIMITED.

AFIT-ENG-M20-M-060

X-RAY DETECTION AND STRAIN SENSING APPLICATIONS OF COLLOIDAL QUANTUM DOTS

Michael D. Sherburne, B.S.E.E.,

2d Lt., USAF

Committee Membership:

Maj T. V. Laurvick, Ph.D.
Chairman

Dr. T. E. Weber
Member

Dr. L. W. Burggraf
Member

Dr. H. Chandrahalim
Member

Mr. E. R. Burke
Member

AFIT-ENG-M20-M-060

Abstract

Colloidal Quantum Dots (CQD)s are a growing field in research and show promise for impacting both x-ray and Non-Destructive Technique (NDT) applications. Due to the nature of how CQDs can be applied to both Los Alamos National Laboratory (LANL) and National Air and Space Administration (NASA) Langley Research Center partnered with Air Force Institute of Technology (AFIT) to further investigate their use in such applications. This research brought in a diverse team of some of the country's best scientist and engineers from the following institutions: Center for High Technology Materials (CHTM) at the University of New Mexico (UNM) for the collection of both Photoluminescence (PL) and Photoluminescence Excitation (PLE) data, Center for Integrated Nanotechnologies (CINT) at the Sandia National Laboratory (SNL) branch for the collection of PL decay data, Virginia Polytechnic Institute and State University (VT) as a redundant measure for the collection of PL decay data, NASA Langley for their sharing of Photonic Crystal Fiber (PCF) resources, Argonne National Laboratory (ANL)'s x-ray beamline to initially test pulsed x-rays, AFIT as the main hub for the fabrication of the CQD scintillators and the central control for the direction of all research activities, and LANL for its sponsorship of the project. The results from the five experiments conducted within this thesis showed tantalizing data that motivates further work into CQD technologies for use in the following applications: fast radiation detection, more flexible detection of defects within any structure, up-conversion of photon emission which could improve the responsiveness of Night-Vision Goggles (NVG), and state-of-the-art integration of CQDs within PCF which allows for a plethora of sensing capabilities (e.g. magnetic, temperature, strain, radiation) all within a single strand of fiber.

There was a lack of centralized information regarding the characterizing of various Commercially Available Off-the-Shelf (COTS) CQDs for the focus in fast temporal diagnostics, and therefore this thesis characterized eight of these nanomaterials within three tested structures: thin-film, 3D printed, and CQD-loaded polymer. This data can be used for various institutions and federal agencies for improving their imaging diagnostics. Four experiments were conducted to evaluate the capability of each nanomaterial, these being:

1. An approximate modeling study to compare the required thickness of material needed for interacting with a given incident x-ray energy.

2. Another approximate modeling study to compare the Quantum Efficiency (QE) of each nanomaterial while under a specified energy of x-ray irradiation.

3. The PL spectra of each nanomaterial was studied for characterizing their stability (how well does the measured PL spectra emulate the PL spectra from the manufacturer when within various structures?).

4. A study of the PL decay for each nanomaterial to characterize their potential for use in high temporal resolution imaging systems.

In addition, another design project was conducted to investigate the optical strain properties of CQDs which has shown excellent potential to revolutionize the NDT industry. Initially designs were completed to create a lab-on-a-chip using Micro-Electro-Mechanical Systems (MEMS) to strain the CQDs under various environmental conditions. Then, a macro-scale test was performed using a coating of CQD-loaded polymer on a dog-bone structure to study the optical trends emitted by the CQDs under strain. They have demonstrated the ability to detect the yield strength point and a measurable trend to determine amount of strain and convert internal stress into an easily detectable change of photon emission energy.

Out of all the nanomaterials investigated during this thesis, it was determined that InP/ZnS would be the best to carry-forth as a next-gen radiation diagnostic for both LANL and AFIT due to their fast temporal decay and excellent spectral stability within various structures. In addition, InP/ZnS would also be an excellent candidate nanomaterial for use in next-gen NDT utilizing their optical strain properties which in turn can help NASA Langley Research Center in not their use in x-ray imaging, but also by more versatile mechanical means as it is also suited for real-time monitoring of defects within space and airframes.

This technology demonstrated within this thesis will prove useful for a number of Department of Defense (DoD) applications including: cost savings in the development of fast radiation detection while using more adaptable structures, ability to up-convert wavelengths of CQDs which has implications for NVG and other Near-Infrared (NIR) devices, and versatile optical NDT utilizing CQDs which can better the safety of various aircraft and other structural systems.

Acknowledgements

Unless someone like you cares a whole awful lot, nothing is going to get better. It's not - The Lorax

What has sparked interest in pursuing colloidal quantum dots for streak camera imaging came from the work of Dr. Joel Grim's from the Naval Research Laboratory and his colleagues from European Organization for Nuclear Research (CERN). Dr. Grim was gracious enough to answer a few of my questions regarding their experiment. NASA Langley Research Center has been invaluable in helping me with my experiments. Dr. Jason Moore's contribution in telling us what optical fiber was used during their CQD scintillation experiments saved me countless hours. Colson Brasch from MITRE provided invaluable connections at the beginning stages of my thesis.

I would like to extend my warmest gratitude for all of my additional collaborators who have contributed invaluable support for this project...

From the Center for High Technology Materials (CHTM) team at UNM in their gracious availability to gather both PL and PLE spectra of the nanomaterials. In addition, hand off the nanomaterials and coordinate the PL decay measurements with CINT:

- Dr. Marek Osinski, Professor
- Dr. Nathaniel Withers, Post-Doc
- Arjun Senthil, Graduate Student
- Shruti Gharde, Graduate Student
- Dominic Bosomtwi, Graduate Student

- Gema Alas, Undergraduate Student

From the Space@VT team at VT in providing project support:

- Dr. Colin Adams, Associate Professor
- Ian Bean, Graduate Student
- Minzhen Du Graduate Student
- Patrick Crandall, Undergraduate Student

From the Los Alamos National Laboratory team in providing useful theoretical knowledge of the topic, borrowing nanomaterials, and access to Argonne National Laboratory's beamline:

- Dr. Victor Klimov, Scientist
- Dr. Igor Fedin, Post-Doc
- Dr. Zhehui Wang, Scientist

From the CINT team located at both SNL and LANL for getting PL decay measurements of the nanomaterials and useful theoretical knowledge of the topic:

- Dr. Jennifer Hollingsworth, Scientist
- Dr. Sergei Ivanov, Scientist
- Dr. Hahn Htoon, Scientist

From the Air Force Institute of Technology team, technicians, and machinists in their critical support on various aspects of this thesis:

- Dr. Yun Xing, Post-Doc

- Major James Bevins, PhD., Assistant Professor
- Major John Brewer, Graduate Student
- Major Ronald Aung, Graduate Student
- Lt Col Edward Hurd, Graduate Student
- 2d Lt Candice Roberts, Graduate Student
- 2d Lt Jeremiah Williams, Graduate Student
- 2d Lt Dylan Martin-Abood, Graduate Student
- Adam Fritzche, AFIT Cleanroom Technician
- Rich Johnson, AFIT Cleanroom Technician
- AFIT 3D Print Shop Technicians
- AFIT Model Shop Technicians

In addition, one of my good friends Ensign Joe Cottone for his invaluable assistance during my literature review. I would also like to thank my group of friends and colleagues who were kind enough to read through my thesis for issues. These friends and colleagues include:

- David Gwizdala
- Benjamin Rothberg
- Ensign Bradley Polidoro
- 1st Lt Jacob DuHadway
- Dr. John Morrison

I would also like to thank the support of both Bob Vince and Rex Curry for their invaluable connections to scientists during this thesis. Of great importance, are the hard working commercial companies that allowed me to carry out the experiments and make informed decisions for the LANL team to continue on the experiments. The following companies below have my thanks:

- NN-Labs (excellent customer service from Mike Cate)
- Sydor Technologies
- Spectral Instruments
- Raptor Technologies
- Leica Microsystems

Finally, and most importantly, I would like to thank my wife, mother, father, brother, sister, mother-in-law, father-in-law, and sister-in-law for all of their support during this process.

Michael D. Sherburne

Table of Contents

Page

Abstract . . . iv

Acknowledgements . . . vii

List of Figures . . . xvii

List of Tables . . . xxxvi

List of Acronyms . . . xl

I. Introductions . . . 1

1.1 Purpose and Goals . . . 2
1.2 Structure of Thesis . . . 3

II. Background and Related Research . . . 5

2.1 Scintillator Fundamentals . . . 6
2.2 Beer-Lambert Law . . . 7
2.3 Electron Mean Free Path (MFP) . . . 10
2.4 Inorganic and Organic Scintillators . . . 14
2.4.1 Theory . . . 14
2.4.2 Capabilities . . . 16
2.4.3 Shortcomings . . . 16
2.5 Cherenkov Radiation . . . 18
2.5.1 Theory . . . 18
2.5.2 Capabilities . . . 21
2.5.3 Shortcomings . . . 21
2.6 Time-of-Flight (TOF) Method . . . 22
2.6.1 Theory . . . 22
2.6.2 Capabilities . . . 23
2.6.3 Shortcomings . . . 23
2.7 Photocathode X-Ray Detection . . . 24
2.7.1 Theory . . . 24
2.7.2 Capabilities . . . 25
2.7.3 Shortcomings . . . 25
2.8 Changing Photocathode Geometry to Detect X-Rays . . . 26
2.8.1 Theory . . . 26
2.8.2 Capabilities . . . 27
2.8.3 Shortcomings . . . 28
2.9 2D Monolayer Scintillators . . . 29
2.9.1 Theory . . . 29
2.9.2 Capabilities . . . 29

Page

2.9.3 Shortcomings . . . 30
2.10 Nanowires . . . 31
2.10.1 Theory . . . 31
2.10.2 Capabilities . . . 32
2.10.3 Shortcomings . . . 32
2.11 Colloidal Quantum Dot Scintillators . . . 33
2.11.1 Theory . . . 33
2.11.2 Advantages . . . 34
2.11.3 Shortcomings . . . 34
2.12 Streak Camera Fundamentals . . . 36
2.12.1 Scintillator . . . 40
2.12.2 Slit . . . 40
2.12.3 Lens . . . 41
2.12.4 Photocathode . . . 41
2.12.5 Accelerating Mesh . . . 43
2.12.6 Focusing Electrode . . . 43
2.12.7 Sweep Electrode . . . 43
2.12.8 Micro-Channel Plate . . . 44
2.12.9 Phosphor Screen . . . 44
2.12.10 Scientific Camera . . . 45
2.12.11 Camera processing board . . . 46
2.12.12 Computer software . . . 46
2.13 Colloidal Quantum Dot Theory . . . 47
2.13.1 Semiconductor Principles . . . 47
2.13.2 Physical Makeup of Colloidal Quantum Dots . . . 50
2.13.3 Discrete Energy State Explanation of CQDs . . . 51
2.13.4 CQD Bandgap Model . . . 54
2.13.5 Alloying CQDs . . . 65
2.13.6 Förster Resonance Energy Transfer . . . 66
2.13.7 Surface Applications of Ligands . . . 70
2.13.8 Quantum Dot Blinking . . . 73
2.13.9 Charge-Transfer Complex . . . 74
2.13.10 Crystal Structures . . . 74
2.13.11 Strain Effects on CQDs . . . 76
2.14 Gamma Exposure Degradation . . . 77
2.15 CQD Scintillator Fabrication . . . 79
2.15.1 Monolayer Application . . . 81
2.15.2 CQDs Loaded Into Polymer . . . 82
2.15.3 Inkjet Printing . . . 83
2.15.4 3D Printing . . . 84
2.15.5 Sol-Gel Technique . . . 85
2.15.6 Loading CQDs into PCF . . . 86

Page

III. Methodology . . . 88

3.1 X-ray Feasibility Study . . . 90
3.1.1 Educated Estimation About Sapphire CQD Geometry . . . 92
3.1.2 Incident X-ray Attenuation Experiment Written in MATLAB . . . 93
3.1.3 Monolayer QE Experiment Written in MATLAB . . . 99
3.2 Fabrication of CQD Loading Structures . . . 100
3.2.1 Polymer Scintillator . . . 100
3.2.2 Photonic Crystal Fiber Scintillator . . . 110
3.2.3 3D Printed Scintillator . . . 115
3.2.4 Thin-Film Scintillator . . . 119
3.3 PL and PLE Measurements with Pulsed Ultra-Violet (UV) Lifetime Decay . . . 120
3.3.1 PL and PLE Wavelength Spectra Experiment . . . 120
3.3.2 UV-Vis Temporal Response Experiment . . . 122
3.4 Pulsed X-ray PL Decay at ANL . . . 123
3.4.1 Experimental Materials and Equipment . . . 123
3.4.2 Experimental Setup . . . 124
3.4.3 Experimental Issues . . . 125
3.5 Pulsed X-ray PL Decay . . . 126
3.5.1 Setting Up Monte Carlo eXtreme (MCX) Studio . . . 127
3.5.2 Verification of MCX Studio Results . . . 128
3.5.3 Simulating MCX Studio Results for a Topical Case . . . 129
3.5.4 Characterizing X-ray Emission . . . 130
3.5.5 Pulsed X-ray Experimental Setup . . . 131
3.6 X-ray Lifetime Decay . . . 132
3.7 3^2 Two Factor Experimental Setup from PL Spectra and PL Decay Measurements . . . 134
3.8 Strain NDT Test . . . 136
3.8.1 MEMS Lab-On-A-Chip . . . 136
3.8.2 Macro Scale Dog-Bone Test . . . 140

IV. Results and Analysis . . . 146

4.1 X-ray Attenuation Thickness and QE Modeling Using MATLAB . . . 146
4.1.1 Incident X-ray Attenuation Experiment Written in MATLAB Results . . . 146

Page

4.1.2 Monolayer QE Experiment Written in MATLAB Results . . . 152
4.2 PL Spectra Experiment . . . 156
4.3 PL Decay Time Experiment . . . 170
4.4 3D Print Charge-Transfer (CT) Relative Intensity and CT PL Decay Experiments . . . 175
4.5 CQD Strain Experiment . . . 187
4.6 Decision Matrix for CQDs . . . 192

V. Conclusion and Future Work . . . 195

5.1 Overview . . . 195
5.2 Research Conclusions . . . 195
5.3 Research Significance . . . 198
5.4 Future Work . . . 199
5.4.1 3D Printed Structure Future Ideas . . . 201
5.4.2 Stress-Strain Future Ideas . . . 206
Appendix A. Leica DVM6 Colored Surface Maps of Polymer Scintillators . . . 212
Appendix B. 3D Printed Structure Version Two . . . 216
Appendix C. Design and Initial Testing of MEMS Cantilever Chip . . . 219
C.1 MATLAB Calculations . . . 219
C.2 Fundamental Frequency . . . 219
C.3 Applied Alternating Current (AC) voltage needed for resonance excitation . . . 220
C.4 RLC Equivalent Circuit . . . 220
C.5 Pull-In Voltage . . . 220
C.6 Max Strain . . . 220
C.7 LTSpice Simulations . . . 221
C.8 COMSOL Finite-Element Analysis (FEA) Simulations . . . 222
C.8.1 Empirical Calculations and FEA Results . . . 222
C.9 Prepping the Cantilever for CQDs Layer . . . 225
C.10 CQDs Layer . . . 225
C.10.1 Photoresist Layer Before Au Sputtering . . . 225
C.11 Au Sputtering Layer . . . 226
C.12 Removal of Excess Au . . . 226
C.13 Releasing the MEMS Cantilever . . . 227
C.13.1 Zygo Profilometer Measurements . . . 228
C.14 Experimental Results . . . 229
C.14.1 Calculating Residual Stress . . . 229
C.14.2 Resistance Measurements of PolyMUMPs Layers . . . 230
C.14.3 Pull-In Voltage of Working Cantilevers . . . 231
C.15 Comparing Experimental Results to Theory . . . 232

Page

Appendix D. Cherenkov Radiation Calculations . . . 234
Appendix E. Loading CQDs as a Sol-Gel Procedure . . . 241
Appendix F. Explanation of the Nuclear Shell Model . . . 242
Appendix G. Visualization for Electron and Structural Analysis (VESTA) Crystal Structures of Quantum Dots . . . 244
G.1 ZnS . . . 244
G.2 InP . . . 244
G.3 PbS . . . 245
G.4 CdS . . . 246
G.5 CuInS . . . 247
G.6 PbSe . . . 248
Appendix H. Leica DVM6 Quantum Dot Loaded Polymer Scintillator Images . . . 250
H.1 CdS . . . 250
H.2 CdSe NPL . . . 251
H.3 CuInS/ZnS . . . 252
H.4 CdSe . . . 253
H.5 InP/ZnS . . . 254
H.6 PbS . . . 255
H.7 PbSe . . . 256
H.8 CdSe/ZnS . . . 257
H.9 Control (Blank Polymer) . . . 258
H.10 No Polymer . . . 259
Appendix I. Gluing Aluminum Ring to Quartz Disc . . . 260
Appendix J. Polymer Scintillator Fabrication Procedure . . . 262
Appendix K. Leica Digital Microscope Taking Thickness Measurement Procedure . . . 264
Appendix L. Removal of 3D Printed Wax Structural Support Procedure . . . 266
Appendix M. Application of CQDs into 3D Printed Structure Procedure . . . 267
Appendix N. Dispersing Thin-Film of CQDs onto Quartz Procedure . . . 268
Appendix O. Loading CQDs within PCF Procedure . . . 269
Appendix P. PCF Tip Shock Wave Scanning Electron Microscope (SEM) Image . . . 274
Appendix Q. Structural Support for Polymer Scintillator Orthographic Drawing . . . 275
Appendix R. 3D Printed Honeycomb Scintillator Orthographic Drawing . . . 276
Appendix S. Structural Support for 3D Printed Scintillator Orthographic Drawing . . . 277
Appendix T. CQD Ligand 3D Models . . . 278

Page

Appendix U. PL Decay Bi-Exponential Components for Main Experiment . . . 279
Appendix V. PL Decay Bi-Exponential Components for 3^2 Factorial Experiment . . . 280
Appendix W. PL Relative Intensity Values at $\approx 460\ nm$ for 3^2 Factorial Experiment Raw Data . . . 281
Appendix X. PL Decay Bi-Exponential Component 3^2 Factorial Experiment Raw Data . . . 282
Appendix Y. Lamp Spectra . . . 283
Appendix Z. MATLAB Codes . . . 284
Z.1 Cherenkov Feasibility Code . . . 284
Z.2 Frank-Tamm Photon Count Code . . . 285
Z.3 Gathering X-ray Data Code . . . 287
Z.4 X-ray Absorption and Attenuation Calculation Code . . . 288
Z.5 User Input and Presentation Code . . . 296
Z.6 PL and PLE Peak and Full Width at Half Maximum (FWHM) Finder Code . . . 301
Z.7 Absorption Thickness Code . . . 304
Z.8 Import Stress-Strain and Optical Information and Present Information Code . . . 312
Z.9 Monolayer X-ray Quantum Efficiency Code . . . 316
Z.10 Create 3D Quantum Dot Geometry . . . 324
Z.11 Monte Carlo Function for Monolayer X-ray Code . . . 330
Z.12 Geometry Function for X-ray Voxel Codes . . . 331
Z.13 PL Decay Plotter Code . . . 332
Z.14 Stress-Strain Yield Point Plotter Code . . . 334
Z.15 Smoothing Function for Stress-Strain Yield Point Plotter Code . . . 339
Bibliography . . . 340

List of Figures

Figure Page

1 An example of testing in the nuclear stockpile stewardship program. The Nova laser pictured here led to the creation of the National Ignition Facility (NIF). High-energy lasers are one example of the numerous testing facilities that the National Nuclear Security Administration (NNSA) runs within the science-based stockpile stewardship program to ensure the stockpile safety, reliability, and effectiveness. This program has been able to bring an end to hazardous underground testing and uses cutting-edge science to achieve the same levels of confidence [72]. 2

2 A F-117 aircraft undergoing x-ray NDT [136]. 2

3 Mass attenuation and absorption coefficient plot data for cadmium from 1 keV to 100 MeV. Data from National Institute for Standards and Technologies (NIST) [96]. 10

4 Inorganic scintillators can be modeled with the bandgap model. They usually contain an activator such as Thallium for NaI(Tl) inorganic scintillators. This activator helps to increase overall QE in the inorganic scintillator but guiding phonons into a lower conductive band to make fluorescence easier [123]. 14

5 The interatomic distance between the organic molecules determines the bandgap between excited and ground states. The organic scintillator becomes excited by an incident charged particle and an exciton would occur from A_0 to A_1 energy levels. At this point, phonon vibrational energy (wasted energy due to heat loss) would bring the excited energy from A_1 to B_1. Then, a fluorescent photon would occur as the energy de-excites from B_1 to B_0[123]. 16

6 Huygen's principle when applied to a boundary between two media. Diagram from Lumen website [80]. 18

Figure Page

7 An incident charged particle traveling through a medium creates a shock wave effect, resulting in constructive interference of the emitting photons at an angle [90]. . . . 19

8 Sketch of Cerenkov radiation geometry (Diagram created by Arpad Horvath) [114]. . . . 20

9 Infographic displaying how Time-Of-Flight (TOF) works. Image from LANL [124]. . . . 22

10 The lower the angle of incidence, the higher the electron yield in the photocathode. Figure from Opachich *et al.* [99]. . . . 26

11 Recessed cavity design to take advantage of the grazing incidence. In this case, the base material is a microstructured Silicon on Insulator (SOI) wafer followed by electron beam sputtering layers of 20Å of titanium and 700Å of gold [100]. Figure from Opachich *et al.* [99]. . . . 27

12 Four monolayer materials excited with a 400 nm laser with a 30 s exposure time. Image from Xu *et al.* [158]. . . . 30

13 SEM images of ZnO nanowires within a polycarbonate matrix and with the polycarbonate matrix removed. Image from Taheri *et al.* [137]. . . . 31

14 Example scenario of a rotating mirror represented as a cylinder and a light collecting screen represented as a rectangle. . . . 37

15 Streak tube model rendering that highlights the main components usually found within a streak camera. . . . 39

16 Image of the Photochron 5 streak tube sold by Photek Limited through Sydor Technologies. Image from Photek Limited [10]. . . . 40

17 Selection of photocathodes provided by Sydor Technologies and their respective output versus incident wavelength. [105] . . . 42

Figure Page

18 Graphic showing the three categories of materials: conductors, semiconductors, and insulators in relation to their resistivity. This graphic also shows some examples of materials in each category. Image from Electronics Tutorial website [149]. 47

19 Graphic showing the three types of band diagrams: metal, semiconductor, and insulator. The difference between each material is their bandgap separation which changes how easily electrons can flow through the material. Image from Hanania *et al.* [56]. 48

20 Graphic showing how temperature changes the carrier concentration, with cooler temperatures shifting the carriers towards the valence band. 50

21 Visual graphic of the structures that make up a CQD. The pink-blue area represents the core, the yellow encompassing the pink-blue area represents the shell, and the black lines represent the ligands. 50

22 Graphic showing the Density of States (DOS) versus energy for the following dimensional structures: 3D bulk material, 2D quantum well, 1D quantum wire, and 0D quantum dot. Graphic from Rabouw *et al.* [115]. 53

23 CQD bandgap model with discrete energy levels near the band edges. Highest Occupied Molecular Orbital (HOMO) band edge is the highest discrete energy state over the valence band edge and Lowest Unoccupied Molecular Orbital (LUMO) is the lowest discrete energy state under the conduction band edge. CQD emission color for each of the bandgaps in part A) can be seen in part B). Graphic from Rabouw *et al.* [115]. 55

24 Type-I CQD bands, where the shell bandgap surrounds the core band. 56

25 Type-II CQD bands, where the core bandgap is either under or over the shell bandgap. 57

26 A descriptive figure detailing the different mechanisms shown in a Jablonski diagram. Image modified from Chasteen [35]. 58

Figure Page

27 An example of the Kane and Pidgeon-Brown eight-band model plot. This figure shows both the band-gap energy and the wave vectors which can be used to determine to the emission and absorption spectra of a Nanoplatelets (NPL). Image from Richard *et al.* [119]. 64

28 Visual graphic for seeing the effects alloying has on CQD bandgaps. From figures A) to C), additional alloying is applied. As more alloying is applied, the difference in energy levels for an exciton to go down from becomes smaller and smaller, which in turn reduces trap states and Auger recombination. For additional information regarding these specific alloyed CQDs, read Selopal *et al.'s* paper. Graphic from Selopal *et al.* [129]. 65

29 This graphic explains Förster Resonance Energy Transfer (FRET) concepts. Both A1 and A2 represent the donor and acceptor fluorophores respectively with different wavelengths. B1 is when the concentration of both fluorophores is small, thus a low FRET efficiency due to a large distance between fluorophores. B2 is when the the concentration of both fluorophores is high, thus a high FRET efficiency. C1 shows the emission of the donor able to escape the medium without being absorbed by an acceptor due to a low FRET efficiency. C2 shows the donor pass off a phonon to a nearby acceptor due to being in close proximity to the donor and the acceptor emits a photon out of the media. Figure from Neveu [95]. 68

30 Summary that highlights the different chemical structures of four types of ligand capping layers. Image from Zhou *et al.* [63]. 70

31 Organic polymer chain. Image information from PubChem [109] and rendered in MolView v2.4 [24]. 71

32 Organic polymer chain. Image from PubChem [110] and rendered in MolView v2.4 [24]. 72

33 Organic polymer chain. Image from PubChem [111] and rendered in MolView v2.4 [24]. 72

Figure Page

34 This is a time resolved fluorescence emission spectra plot showing three cases: DOPO-Br on the left most side, ZnS-capped in the middle, and Oligo-(Phenylene Vinylene) (OPV) covered CdSe quantum dots on the right most side. The left most image shows photodegradation which blue shifts, the middle image shows quantum dot blinking, and the right most image shows the suppression of quantum dot blinking. Image from Hammer *et al.* [55]. 73

35 3D crystal structure model of CdSe. Figure created in VESTA [91]. 76

36 Direct band-edges changing under tensile or compressive strain. Image modified from NNSE 618 lecture slide at University of Albany [12]. 77

37 PL lifetime degradation of gamma irradiation. The research group used CdSe/ZnS CQDs for these tests. Image from Withers *et al.* [155]. 78

38 "A) Schematic of the nucleation and growth stage for the preparation of monodisperse nanocrystals in the framework of the LaMer model. B) Representation of the simple synthetic apparatus employed to prepare monodisperse nanocrystals." Referenced from Sinatra *et al.* [133]. 80

39 Chemical representation of how the UV curable Polyurethane Acrylate (PUA) process works [103]. 82

40 SEM image of 20% water content in polymer [75]. 83

41 SEM image of 5% water content in polymer [75]. 83

42 3D printed colloidal crystals when viewed under a light microscope [38]. 84

43 Example of the PCF used in the NASA experiment [27]. 86

44 UV excitation of CQDs in fiber from the side; notice the light emission output towards the bottom left of the fiber [27]. 87

Figure Page

45 Chart of where each of the effects: photoelectric, Compton, and pair production are dominate. Effect dominance is related to the Z of the material and the incident energy of the photon. Image from Almahwasi [13] 94

46 An example of a Sapphire CQD suspended in a Polymethyl Methacrylate (PMMA) polymer matrix at 10% loading volume. Each layer of the CQD was represented by a unique value. This unique value acted as an identifier to load the correct calculated mass attenuation coefficient into that voxel. 97

47 An example of a Sapphire CQD with its spherical matrix of calculated mass attenuation coefficients flattened into a 2D matrix. The more red the voxel, the less incident x-rays that were absorbed/scattered. 98

48 Top side rendering of supporting structure before loading in polymer. 101

49 Leica DVM6 digital microscope used to characterize the thickness of each CQD-loaded polymer scintillator. 104

50 Overview scan image of a top down view of CdS loaded polymer scintillator. 105

51 The left side of the surface plot represented the aluminum ring. Going towards the blue end on the right side represented the CQD-loaded polymer surface. The random peaks throughout the region between the aluminum ring and towards the middle of the CQD-loaded polymer surface would be the locations where the light reflected off the surface. The CQD-loaded polymer formed a bowl shape within the interior of hole in the aluminum ring, thus any peaks that go back up to the height of the aluminum ring were noise. While not perfect, this non-destructive optical method showed the difficulty in imaging a mostly clear CQD-loaded polymer without other modifications made to the CQD-loaded polymer. 106

52 LED blacklight sold by Viribus. Image from Viribus [153]. 109

Figure Page

53 Fluorescence for the visible emitting CQDs can be quickly checked by using a standard Light Emitting Diode (LED) blacklight to ensure they still worked before sending them out to another laboratory for testing. . . . 109

54 Badly cleaved fiber tip when viewed from the side under a microscope. . . . 111

55 Badly cleaved fiber tip when viewed with a SEM. . . . 112

56 Well cleaved fiber tip when viewed from the side under a microscope. . . . 112

57 Well cleaved fiber tip when viewed from top down under a microscope. . . . 113

58 Well cleaved fiber tip when viewed in a SEM 113

59 Light emission coming out from one end of the PCF after loading of CQDs and before cleaning the outside surface of the PCF. . . . 114

60 Light emission coming out from one end of the PCF after loading of CQDs and after cleaning the outside surface of the PCF. . . . 115

61 Rendering of the 3D printed honeycomb. Rendering created in SolidWorks. . . . 117

62 ProJet MJP 3600 Series printer used in the creation of the 3D printed honeycomb structures. Image from 3D Systems [135]. . . . 118

63 3D printed stand to keep the 3D printed honeycomb structure suspended while CQDs were applied. Rendered using SolidWorks. . . . 119

64 Experimental setup using a Horiba-Jovin Fluorolog-3 system. . . . 121

65 Setup of CQD experiment in ANL's beam line 125

66 Isotropic point source photon distribution. Simulated using MCX Studio [47]. . . . 128

Figure Page

67 Cone source photon distribution similar to the emission of a bremsstrahlung x-ray tube source. Simulated using MCX Studio [47]. . . . 130

68 Pulsed x-ray detection setup to test CQD samples. . . . 131

69 Lifetime x-ray exposure setup to test CQD samples at 100 keV. . . . 133

70 A 150 μm long and 60 μm wide MEMS cantilever designed in L-edit. . . . 137

71 SEM image of one of the multiple cantilevers fabricated to characterize the strain effects of CQDs. SEM settings used in the capturing of this photo were: x300 magnification and 4 kV emission energy. . . . 138

72 SEM image showing all the layers used in the PolyMUMPs processed and taken at the connection point between the poly2 layer and the anchor. SEM settings used in the capturing of this photo were: x2000 magnification and 4 kV emission energy. . . . 139

73 This SEM image showed a release failure mode of the sacrificial poly1 layer. The poly1 layer was unable to get fully out from under the cantilever poly2 layer. SEM settings used in the capturing of this photo were: x180 magnification and 15 kV emission energy. . . . 140

74 3D surface model of the coated 301 stainless steel dog-bone with CQD polymer matrix applied. Taken with the Leica DVM6 microscope. Left half of the image contained the CQD-loaded polymer matrix coating while the right half was only the pre-coating (Solvay BR 6747-1) on top of the 301 stainless steel. Microscope settings: 0° tilt, Z-step size of 0.25 μm, and a FOV3.6 lens. . . . 142

75 A flame fiber optic spectrometer (model: FLAME-S-VIS-NIR) sold by Ocean Optics was secured to the load frame and fiber optically connected to a Thorlabs zoom fiber collimator ZC618APC-A. A standard blacklight was clamped to the load frame. A dog-bone cured with a sample of InP/ZnS CQDs loaded in a proprietary polymer was placed between the load frame's clamps. A piece of cardboard was used to help lessen the intensity of the overhead lights (background noise) in the laboratory. (a) illustration of the experimental setup. (b) labeled photo of the experimental setup. 144

76 PL spectra of CdS CQDs applied to: thin-film, 3D printed structure, and CQD-loaded polymer structure. Data collected using a Horiba-Jobin Fluorolog-3. Data taken with the following attributes: 320 nm excitation, 1 nm excitation slit width, 1 nm emission slit width, 1 nm wavelength steps, right angle configuration at 30°, 1200/500 emission grating, 1200/330 excitation grating. Data in this plot was averaged over five trials. 157

77 PL spectra of CdSe CQDs applied to: thin-film, 3D printed structure, and CQD-loaded polymer structure. Data collected using a Horiba-Jobin Fluorolog-3. Data taken with the following attributes: 335 nm excitation, 1 nm excitation slit width, 1 nm emission slit width, 1 nm wavelength steps, right angle configuration at 30°, 1200/500 emission grating, 1200/330 excitation grating. Data in this plot was averaged over five trials. 158

78 PL spectra of CdSe NPL CQDs applied to: thin-film, 3D printed structure, and NPL-loaded polymer structure. Data collected using a Horiba-Jobin Fluorolog-3. Data taken with the following attributes: 275 nm excitation, 1 nm excitation slit width, 1 nm emission slit width, 1 nm wavelength steps, right angle configuration at 30°, 1200/500 emission grating, 1200/330 excitation grating. Data in this plot was averaged over five trials. 160

79 PL spectra of CdSe/ZnS CQDs applied to: thin-film, 3D printed structure, and CQD-loaded polymer structure. Data collected using a Horiba-Jobin Fluorolog-3. Data taken with the following attributes: 395 nm excitation, 1 nm excitation slit width, 1 nm emission slit width, 1 nm wavelength steps, right angle configuration at 30°, 1200/500 emission grating, 1200/330 excitation grating. Data in this plot was averaged over five trials. 161

80 PL spectra of CuInS/ZnS CQDs applied to: thin-film, 3D printed structure, and CQD-loaded polymer structure. Data collected using a Horiba-Jobin Fluorolog-3. Data taken with the following attributes: 405 nm excitation, 1 nm excitation slit width, 1 nm emission slit width, 1 nm wavelength steps, right angle configuration at 30°, 1200/500 emission grating, 1200/330 excitation grating. Data in this plot was averaged over five trials. 163

81 PL spectra of InP/ZnS CQDs applied to: thin-film, 3D printed structure, and CQD-loaded polymer structure. Data collected using a Horiba-Jobin Fluorolog-3. Data taken with the following attributes: 405 nm excitation, 1 nm excitation slit width, 1 nm emission slit width, 1 nm wavelength steps, right angle configuration at 30°, 1200/500 emission grating, 1200/330 excitation grating. Data in this plot was averaged over five trials. 164

82 PL spectra of PbS CQDs applied to: thin-film, 3D printed structure, and CQD-loaded polymer structure. Data collected using a Horiba-Jobin Fluorolog-3. Data taken with the following attributes: 823 nm excitation, 1 nm excitation slit width, 1 nm emission slit width, 1 nm wavelength steps, right angle configuration at 30°, 1200/500 emission grating, 1200/330 excitation grating. Data in this plot was averaged over five trials. 166

83 PL spectra of PbSe CQDs applied to: thin-film, 3D printed structure, and CQD-loaded polymer structure. Data collected using a Horiba-Jobin Fluorolog-3. Data taken with the following attributes: 823 nm excitation, 1 nm excitation slit width, 1 nm emission slit width, 1 nm wavelength steps, right angle configuration at 30°, 1200/500 emission grating, 1200/330 excitation grating. Data in this plot was averaged over five trials. 167

84 PL spectra of the control case applied to: thin-film, 3D printed structure, and polymer structure. Data collected using a Horiba-Jobin Fluorolog-3. Data taken with the following attributes: 275 nm excitation, 1 nm excitation slit width, 1 nm emission slit width, 1 nm wavelength steps, right angle configuration at 30°, 1200/500 emission grating, 1200/330 excitation grating. Data in this plot was averaged over five trials. 169

85 Bi-exponential model curve fitting of PL decay of CQDs applied as a thin-film structure. Data averaged over three trials and a 0.5 s integration time for each data point before curve fitting. Plot begins at 0.5 ns (temporal resolution limit of equipment used). Data collected using a PTI Felix 32 Spectrofluorimeter. 170

86 Bi-exponential model curve fitting of PL decay of CQDs applied as a 3D printed structure. Data averaged over three trials and a 0.5 s integration time for each data point before curve fitting. Plot begins at 0.5 ns (temporal resolution limit of equipment used). Data collected using a PTI Felix 32 Spectrofluorimeter. 171

87 Bi-exponential model curve fitting of PL decay of CQDs applied as a CQD-loaded polymer structure. CdSe NPL had a modified pre-exponential for A_1 to 0.00 since the component was a negative value, thus this line may not be fully representative of the collected data. Data averaged over three trials and a 0.5 s integration time for each data point before curve fitting. Plot begins at 0.5 ns (temporal resolution limit of equipment used). Data collected using a PTI Felix 32 Spectrofluorimeter. 173

88 Bi-exponential model curve fitting of PL decay of InP/ZnS CQDs applied as a CQD-loaded polymer structure. One PL decay line represented the 572 nm FRET acceptor peak and the other PL decay line represented the 530 nm donor peak. Data averaged over three trials and a 0.5 s integration time for each data point before curve fitting. Plot begins at 0.5 ns (temporal resolution limit of equipment used). Data collected using a PTI Felix 32 Spectrofluorimeter. 174

89 Bar graph comparing the Time-to-Half-Amplitude (THA) values in nanoseconds for each structure experimented in this thesis. The left most bar (blue) for each nanomaterial category represented the thin-film structure. The middle bar (orange) for each nanomaterial category represented the CQD-loaded polymer structure. Finally, the right most bar (yellow) for each nanomaterial category represented the 3D printed structure. 175

90 Two factor test showing PL spectra between all of the different levels used. It was observed that the intensity of the CT peak at 460 nm can be controlled. 176

91 Pareto chart which showed that both the thickness of the 3D printed structure and the amount of loaded CQDs had a significant effect on the CT peak intensity measured at 460 nm. 178

92 Residual plots showed that this 3^2 experimental data was not taken in randomized manner. This was due to time constraints, however a future study could incorporate a random ordering of runs. 179

93 Contour plot showing how both the amount of CQDs loaded and the thickness of the 3D printed structure factors can be tuned to create a desired relative intensity of the secondary peak at approximately 460 nm. 181

94 Graphic showing increasing concentrations of CQDs from Figure 93 when going along the x-axis at under 300 μm 3D printed structure thickness. a) low concentration of CQDs mitigate reabsorption of the 460 nm wavelength, thus increasing its intensity. b) a higher concentration of CQDs would start allowing reabsorption of the 460 nm while not adding enough CT to the polymer matrix, thus lowering its intensity. c) a critical concentration of CQDs would cause reabsorption of the 460 nm, but this effect would be less pronounced than the additional energy being transferred into the overall polymer matrix system, thus an increase in the 460 nm wavelength intensity could occur. 182

95 Graphic which shows increasing the thickness of the CQD structure would increase the probability of absorbing the 460 nm wavelength emission as the photon travels through the structure. This was represented by the dashed green arrows. When the 460 nm photon was reabsorbed, it would emit in this case a 520 nm-530 nm characteristic photon from the light absorbing CQD. This graphic also correlated with Figure 93 at 160 μL on the x-axis and going up the y-axis. The inverse could also occur at lower concentrations of CQDs such as while looking at 40 μL along the y-axis. With such a low concentration of CQDs, the thicker the structure, the less likely the 460 nm photon would get reabsorbed by another CQD along the way. However, across all of the CQD concentrations, the intensity of the 460 nm peak begun to greatly decrease at the thickest structure of 960 μm. This was most likely due to photons being lost within the 3D printed structure since it was not designed to be waveguiding and the thicker the amount of SU-8-5 a visible photon travels through, the more it will attenuate. Thus, the lower intensity of the 460 nm wavelength occurred from structural geometry, rather than from the CQDs themselves. 183

96 Bi-exponential model curve fitting of PL decay of CQDs applied as a 3D printed structure for the 3^2 factorial experiment. Data averaged over three trials and a 0.5 s integration time for each data point before curve fitting. Plot begins at 0.5 ns (temporal resolution limit of equipment used). Data collected using a PTI Felix 32 Spectrofluorimeter. 185

97 Contour plot showing how both the amount of CQDs loaded and the thickness of the 3D printed structure factors can be tuned to create a desired PL decay THA of the CQDs peak emission wavelength of 520 nm-530 nm. 186

98 Figure showing both the optical spectra being emitted from the CQDs and the stress-strain curve. The optical spectra was located in the top sub-figure and the stress-strain curve was located on the bottom sub-figure. For the optical spectra, the intensity is normalized. An orange curve signified the first data point which could then be compared against the blue line which represented the data at the present time. The optical spectra plot showed the experimental time in seconds, when the ultimate strength had been reached by being added to the plot, and percent change of the present optical spectra in relation to the plateau rising from the peak of the spectra. 188

99 A magnified version of Figure 98. The percent change in intensity in order to get stress-strain measurements for this sample was taking as the percent difference between the rising plateau (yellow dot) and the side of the plateau (purple dot). It was observed that the side of the plateau remained relatively consistent with the rest of the present optical spectra as more strain was applied, but the rising plateau continued to climb higher. 189

100 A magnified version of Figure 98 with PL spectra changing over time due to applied strain to the dog-bone sample. 190

101 Two trendlines were noticed as the sample was strained. 190

102 Stress-strain curve highlighting the following: yield stress point, yield strain point, and the elastic modulus. Plot created by Major John Brewer and Major Ronald Aung. . . . 191

103 The invention can be modified by using a two-photon polymerization 3D printer to create about 100 nm sized holes in the 3D printed structure. The exact diameter of this hole can be designed to waveguide emitted light from the CQD down to the bottom of the structure. . . . 202

104 An engineering 3D printed scintillating polymer can charge transfer energy deposited into it over to nearby CQDs to emit additional photons and increase quantum efficiency. . . . 203

105 Instead of one single thick 3D printed structure, this alternative slices up the structure into thinner slices. In between each 3D printed slice would be a transparent medium to guide light emitted by the CQDs out to a detector located to the side of the entire structure. This medium could be quartz or even a polymer. . . . 204

106 Metal surrounding the 3D printed honeycomb will prevent warping during fabrication. . . . 205

107 Two metal pieces are pushed into each other to surround the 3D printed honeycomb. . . . 206

108 Graphic showing alternative which applies the stress-strain wavelength changes from the main invention within an aircraft frame. . . . 207

109 Evanescent waves from the fiber optic can be used to excite nearby CQDs. . . . 207

110 Excited CQDs emitting their photons can be sensed by collecting photons that enter a nearby fiber optic cable and meeting the Total Internal Reflection (TIR) angle criteria. . . . 208

Figure Page

111 Graphic showing alternative design which is an improved modification. Here, the composite material must be designed to allow both the excitation wavelength of light to the layer of CQDs within a polymer and the excited emission of the CQDs. 210

112 Overall system setup to use for CQD emission transmission through material alternative. 210

113 CdSe NPL polymer colored surface map taken with a 10° tilt. 212

114 CuInS/ZnS polymer colored surface map taken with a 10° tilt. 212

115 Control polymer colored surface map taken with a 9° tilt. 213

116 CdSe polymer colored surface map taken with a 9° tilt. 213

117 CdSe/ZnS polymer colored surface map taken with a 5° tilt. 214

118 InP/ZnS polymer colored surface map taken with a 5° tilt. 214

119 PbS polymer colored surface map taken with a 10° tilt. 215

120 PbSe polymer colored surface map taken with a 10° tilt. 215

121 Orthographic drawing of version two of the 3D printed honeycomb structure. Drawn within SolidWorks. 216

122 Orthographic drawing of the right metal support that slides onto the 3D printed honeycomb structure. Drawn within SolidWorks. 217

123 Orthographic drawing of the left metal support that slides onto the 3D printed honeycomb structure. Drawn within SolidWorks. 218

124 LTSpice model drawn with RLC equivalent cantilever and all associated transmission line effects to drive and sense the cantilever. 221

Figure Page

125 3D model made in COMSOL to simulate a MEMS cantilever with a PMMA layer used to simulate the CQDs layer. . . . 222

126 LTSpice simulation as seen from oscilloscope probe. . . . 223

127 f_0 over cantilever beam lengths. . . . 224

128 V_{pi} over cantilever beam lengths. . . . 224

129 3D profile of a 500 μm length and 60 μm width cantilever with gold on top . . . 228

130 Height data of the MEMS cantilever using a Zygo profilometer. . . . 228

131 MATLAB modeling for electron threshold energy versus refractive index. . . . 236

132 Cherenkov photon emission versus incident x-ray energy in a diamond medium. . . . 240

133 An example of multiple shell models, where going all the way to spin-orbit coupling gives the best approximation of the different energy states available within a nucleus. Image from Combley *et al.* [41] . . . 242

134 3D crystal structure model of ZnS. Figure created in VESTA [91]. . . . 244

135 3D crystal structure model of InP. Figure created in VESTA [91]. . . . 245

136 3D crystal structure model of PbS. Figure created in VESTA [91]. . . . 246

137 3D crystal structure model of CdS. Figure created in VESTA [91]. . . . 247

138 3D crystal structure model of $CuInS_2$. Figure created in VESTA [91]. . . . 248

139 3D crystal structure model of PbSe. Figure created in VESTA [91]. . . . 249

Figure Page

140 CdS top down overview image with local tone mapping enhancement. . . . 250

141 CdSe NPL top down overview image. . . . 251

142 CdSe NPL top down overview image with local tone mapping enhancement. . . . 251

143 CuInS/ZnS top down overview image. . . . 252

144 CuInS/ZnS top down overview image with local tone mapping enhancement. . . . 252

145 CdSe top down overview image. . . . 253

146 CdSe top down overview image with local tone mapping enhancement. . . . 253

147 InP/ZnS top down overview image. . . . 254

148 InP/ZnS top down overview image with local tone mapping enhancement. . . . 254

149 PbS top down overview image. . . . 255

150 PbS top down overview image with local tone mapping enhancement. . . . 255

151 PbSe top down overview image. . . . 256

152 PbSe top down overview image with local tone mapping enhancement. . . . 256

153 CdSe/ZnS top down overview image. . . . 257

154 CdSe/ZnS top down overview image with local tone mapping enhancement. . . . 257

155 Blank polymer top down overview image. . . . 258

156 Blank polymer top down overview image with local tone mapping enhancement. . . . 258

157 No polymer top down overview image. . . . 259

Figure Page

158 No polymer top down overview image with local tone mapping enhancement. . . . 259

159 A Fujikura CT-20 fiber cleaver. . . . 269

160 PCF taped at an angle and point straight up on a block. . . . 270

161 PCF wrapped in a U-shape within a SEM holder. . . . 271

162 ImageJ used to automatically count the number of good holes on the tip of a PCF . . . 271

163 Vacuum system using a syringe, putty, and electrical tape to hold the vacuum. . . . 272

164 Rippling on top of a fiber tip that occurred during the shock wave that occurred during the cleaving process when viewed in a SEM . . . 274

165 Orthographic drawing of supporting structure for polymer. Drawn within SolidWorks. . . . 275

166 Orthographic drawing of 3D printed honeycomb. Drawn within SolidWorks. . . . 276

167 Orthographic drawing of 3D printed stand. Drawn within SolidWorks. . . . 277

168 Organic polymer chain 3D model. Image information from PubChem [109] and 3D rendered in MolView v2.4 [24]. . . . 278

169 Organic polymer chain 3D model. Image from PubChem [110] and 3D rendered in MolView v2.4 [24]. . . . 278

170 Organic polymer chain 3D model. Image from PubChem [111] and 3D rendered in MolView v2.4 [24]. . . . 278

171 Lamp spectra of the Horiba-Jobin Fluorolog-3 used. Peaks in the NIR wavelengths were used to excite the lead-based CQDs. . . . 283

List of Tables

Table | Page

1 Table of commonly used inorganic x-ray scintillators from Luo *et al.'s* search [81]. . . . 15

2 Commercially available phosphor screens from Sydor Technologies [105]. . . . 44

3 A table of time scale values for each process shown in the Jablonski diagram. The faster the process, the more likely it is to occur. It is of note that these time scales are not indicative of all PL systems since phosphorescence is defined by the Inter-System Crossing (ISC) transfer of phonon energy to a triplet state and then emitting a photon. Usually this process is slower because of the additional transfers that must occur, but it does not have to be. Data for the table is from McEwen [87]. . . . 59

4 Overview of crystal structure parameters used to generate VESTA models. . . . 75

5 Overview of nanomaterials being studied for their x-ray emission PL decay properties. ***Company did not deliver material and unresponsive. Only theoretical experiments were done to evaluate the their CQD technology. Temporal response was unknown due to not having the material to test. . . . 89

6 Weighted evaluation rubric used to select top performing nanomaterial scintillator to be fielded at Magnetic Shock Experiment (MSX). . . . 90

7 Table with recommendations in viscosity changes when buying the CQD-loaded polymer materials used in this experiment from NN-Labs. . . . 103

8 Average thickness values of the CQD-loaded polymer scintillators after fabrication. Note, the high error values were due to the difficulty in being able to reliably get a proper focus off of the surface of the CQD-loaded polymer with the microscope. . . . 108

Table Page

9 List of equipment used to cleave and conduct quality control on the PCFs. . . . 111

10 Equipment used at Argonne National Laboratory experiment. . . . 124

11 Table that shows what each device in the experimental handles. . . . 125

12 Degrees-of-Freedom (DOF) of each source in a 3^2 factorial experiment where n is the number of replicates. . . . 135

13 3^2 factorial experiment setup. In addition, the CQD material used for each level was annotated since a lack of resources required using two similar CQDs for this experimental study. . . . 136

14 Modeled thickness of CQDs within a PMMA polymer at 10% loading by volume. 100 keV incident x-rays were sent through and thickness set to have 99% of the incident x-rays absorbed/scattered. Scores range from 1-8, with 8 being the best material for this experiment. . . . 147

15 Modeled thickness of CQDs within a PMMA polymer at 10% loading by volume. 100 keV incident x-rays were sent through and thickness set to have 10% of the incident x-rays absorbed/scattered. Scores range from 1-8, with 8 being the best material for this experiment. . . . 148

16 Modeled thickness of CQDs within a PMMA polymer at 10% loading by volume. 10 keV incident x-rays were sent through and thickness set to have 99% of the incident x-rays absorbed/scattered. Scores range from 1-8, with 8 being the best material for this experiment. . . . 149

17 Modeled thickness of CQDs within a PMMA polymer at 10% loading by volume. 10 keV incident x-rays were sent through and thickness set to have 10% of the incident x-rays absorbed/scattered. Scores range from 1-8, with 8 being the best material for this experiment. . . . 150

18 Standard deviation of each test and the weight importance as a percentage for each test resulting from the standard deviation. . . . 151

Table Page

19 Weighted scores of each CQD material for the x-ray absorption/scattering thickness experiment. Final scores range from 1-8, with 8 being the best material for this experiment. 151

20 Repeatability test of the Monte Carlo (MC) simulation with 10 keV incident x-rays. Percent difference between the two tests were $< 2\%$ which was good enough to confidently rank the different CQD materials. 152

21 MC simulation using 10% loading by volume of CQDs in a PMMA polymer matrix as a monolayer. The monolayer was set to be a 8×10^3 nm diameter disk. Incident x-ray energy was set to 10 keV. QE values in % were collected. Scores range from 1-8, with 8 being the best material for this experiment. 153

22 Repeatability test of the MC simulation with 100 keV incident x-rays. Percent difference between most of the two tests were $< 10\%$ which was not ideal, but still useful to rank the different CQD materials. A lower percent error would mean running each CQD over a period of days in simulation time. 153

23 MC simulation using 10% loading by volume of CQDs in a PMMA polymer matrix as a monolayer. The monolayer was set to be a 22×10^3 nm diameter disk. Incident x-ray energy was set to 100 keV. QE values in % were collected. Scores range from 1-8, with 8 being the best material for this experiment. 154

24 Standard deviation of each test and the weight importance as a percentage for each test resulting from the standard deviation. 154

25 Weighted scores of each CQD material for the monolayer MC simulation x-ray QE experiment. Final scores range from 1-8, with 8 being the best material for this experiment. 155

Table Page

26 Analysis of Variance (ANOVA) table from the 3^2 PL spectra factorial experiment. The amount of CQDs applied to the 3D structure had slightly more importance than changing the thickness of the 3D printed structure. Both factors were significant. The p-value for all sources in this table was more than 16 zeros, which was less than the significance value of 0.05. 177

27 Scoring rubric used to evaluate the most promising CQD for future work. The reasoning for no scores for the of the CQDs were the following: PL spectra data was not possible to collect for the PbS in the 3D printed structure due to equipment limitations, sapphire CQDs did not arrive from the manufacturer, thus could not be experimentally tested, and PL decay from UV excitation was not possible for the NIR CQDs. 193

28 Calculated values using a Q = 1,000 and a 150 μm Length and 30 μm cantilever. 223

29 Table of various release processes used on MEMS chip. 227

30 Table of residual stress values for varying gold thin-film coated cantilever lengths with 30 μ m width. 230

31 Table of pull-in voltages of four gold thin-film coated MEMS cantilevers of varying lengths and widths. 231

32 Temporal resolution of PL decay is 0.5 ns, thus any values less than 0.5 ns may not be the response of the CQD under test. CQD loaded into the three following structures: 3D, thin-film, and polymer are all shown in this table. 279

33 Temporal resolution of PL decay is 0.5 ns, thus any values less than 0.5 ns may not be the response of the CQD under test. 280

34 PL relative intensity measurements at 460 nm for each level in the 3^2 factorial experiment. 281

35 PL decay times for each level in the 3^2 factorial experiment. The THA for each level was measured. 282

List of Acronyms

AC Alternating Current. xiv, 220

AFIT Air Force Institute of Technology. iv, vi

ANL Argonne National Laboratory. iv, xiii, xxiii, 88, 123–125

ANOVA Analysis of Variance. xxxix, 177

API Application Programming Interface. 46

BOE Buffered Oxide Etch. 227

CCD Charged-Coupled Device. 44, 46

CERN European Organization for Nuclear Research. vii

CHTM Center for High Technology Materials. iv

CINT Center for Integrated Nanotechnologies. iv, vii, 122, 123, 170

COTS Commercially Available Off-the-Shelf. v, 23, 38

CQD Colloidal Quantum Dots. iv–vii, xii–xv, xix–xxxiii, xxxv–xxxix, 1–3, 33–36, 47, 49–57, 59, 61–63, 65, 66, 70, 71, 73–94, 96–110, 114–116, 118–120, 122, 123, 125, 126, 130–138, 140–142, 144–188, 193–211, 219, 222, 225–227, 231, 241, 244, 262, 267–269, 272, 278–280, 283

CT Charge-Transfer. xiv, xxviii, xxix, 1, 88, 134, 158–160, 162, 163, 165, 168, 169, 171–173, 175, 176, 178, 180–183, 196, 198, 201

CUDA Compute Unified Device Architecture. 127, 128

DC Direct Current. 220

DoD Department of Defense. vi, 199, 200

DoE Department of Energy. 199

DOF Degrees-of-Freedom. xxxvii, 135

DOS Density of States. xix, 51–54, 64

DRIE Deep Reactive-Ion Etching. 27

EMA Effective Mass Approximation. 53, 61, 62

FEA Finite-Element Analysis. xiv, 222

FGR Fermi's Golden Rule. 51

FIR Far-Infrared. 42

FRET Förster Resonance Energy Transfer. xx, xxviii, 47, 66–69, 72, 74, 100, 157, 161–165, 168, 172–174, 196

FWHM Full Width at Half Maximum. xvi, 79, 85, 157, 163, 193, 200, 301

GOST Giant Oscillator Strength Transition. 62–65

GPU Graphical Processing Unit. 126–128

GUI Graphical User Interface. 127

HF Hydrofluoric Acid. 140, 226, 227

HMDS Hexamethyldisalazane. 225

HOMO Highest Occupied Molecular Orbital. xix, 55

IC Internal Conversion. 58

ICSD Inorganic Crystal Structure Database. 74

IPA Isopropyl Alcohol. 111, 204, 267, 269, 273

IR Infrared. 42

ISC Inter-System Crossing. xxxvi, 58, 59

LANL Los Alamos National Laboratory. iv, vi, viii, x, xviii, 1, 22, 123, 195, 199

LBNL Lawrence Berkeley National Laboratory. 15

LED Light Emitting Diode. xxiii, 48, 49, 108, 109, 264

LLNL Lawrence Livermore National Laboratory. 26, 34, 45, 46

LMCT Ligand-to-Metal Charge-Transfer. 74

LUMO Lowest Unoccupied Molecular Orbital. xix, 55

MBE Molecular Beam Epitaxy. 79

MC Monte Carlo. xxxviii, 91, 99, 100, 126, 152–155, 194

MCP Micro-Channel Plate. 38, 44

MCX Monte Carlo eXtreme. xiii, 126–129

MEMS Micro-Electro-Mechanical Systems. v, xiii, xiv, xxiv, xxxiii, xxxix, 136–138, 140, 200, 219–222, 226, 227, 231, 232

MFP Mean Free Path. xi, 10, 11

MIT Massachusetts Institute of Technology. 84

MLCT Metal-to-Ligand Charge-Transfer. 74

MOSFET Metal-Oxide-Semiconductor Field-Effect Transistor. 43

MSX Magnetic Shock Experiment. xxxvi, 1, 3, 5, 23, 36, 39, 88–90, 195, 199

NASA National Air and Space Administration. iv, vi, xxi, 2, 34, 36, 81, 86, 87, 110, 195, 199, 200

NDT Non-Destructive Technique. iv–vi, xiii, xvii, 1, 2, 36, 136, 193, 199, 201, 206

NIF National Ignition Facility. xvii, 1

NIH National Institute of Health. 127

NIR Near-Infrared. vi, xxxv, xxxix, 110, 166, 167, 193, 194, 201, 283

NIST National Institute for Standards and Technologies. xvii, 9, 10

NNSA National Nuclear Security Administration. xvii, 1, 199

NNSS Nevada National Security Site. 26

NPL Nanoplatelets. xx, xxv, xxvii, 1, 34, 47, 51, 62–65, 119, 120, 123, 159–161, 171, 173, 175, 197, 201

NVG Night-Vision Goggles. iv, vi, 42, 198

ODA Octadecylamine. 85, 241

OPV Oligo-(Phenylene Vinylene). xxi, 73, 198

PCF Photonic Crystal Fiber. iv, xii, xv, xxi, xxiii, xxxv, xxxvii, 1, 81, 86, 88, 89, 100, 108, 110, 111, 113–115, 195, 200, 269–271, 274

PCI Peripheral Component Interconnect. 46

PL Photoluminescence. iv, v, vii, viii, xiii, xiv, xvi, xxi, xxv–xxviii, xxx, xxxvi, xxxix, 1, 16, 31–33, 50, 57–59, 65, 66, 73, 78, 79, 81, 88, 89, 120–123, 126, 134, 136, 145, 156–177, 184–186, 189, 190, 193, 194, 196–198, 201, 279–282, 301, 332

PLE Photoluminescence Excitation. iv, vii, xiii, xvi, 89, 120, 121, 156, 301

PMMA Polymethyl Methacrylate. xxii, xxxvii, xxxviii, 90, 93, 96–100, 147–150, 153, 154

PMT Photomultiplier Tube. 22, 130, 132–134

PUA Polyurethane Acrylate. xxi, 82, 83

PVT Polyvinyl Toluene. 172, 200

QD Quantum Dots. 33

QE Quantum Efficiency. v, xiii, xiv, xvii, xxxviii, 1, 14, 16, 31–34, 45, 51, 63, 65, 71, 77, 78, 89, 91, 93, 99, 100, 104, 110, 120, 122, 123, 135, 136, 146, 152–156, 172, 175, 194, 196–198, 200, 239, 240

QIS Quantum Information Science. 198

QLED Quantum Dot Light Emitting Diode. 86

SEM Scanning Electron Microscope. xv, xviii, xxi, xxiii, xxiv, xxxv, 31, 83, 112, 113, 137–140, 229, 270, 271, 274

SNL Sandia National Laboratory. iv, viii, 122

SNR Signal-to-Noise Ratio. 167, 168

SOI Silicon on Insulator. xviii, 27

TEM Transmission Electron Microscope. 92, 165, 168

TEOS Tetraethyl Orthosilicate. 241

THA Time-to-Half-Amplitude. xxviii, xxx, xxxix, 1, 170, 175, 185, 186, 197, 282

TIR Total Internal Reflection. xxxi, 87, 207, 208

TISE Time-Independent Schrödinger Equation. 61

TMD Transition Metal Dichalcogenides. 29, 30

TOF Time-Of-Flight. xviii, 5, 22, 23

TOP Trioctyl Phosphine. 80

TOPO Trioctylphosphine. 80

UNM University of New Mexico. iv, vii

UV Ultra-Violet. xiii, xxi, xxxix, 42, 81–85, 87, 89, 120, 122, 193, 196, 197, 225, 260, 267

VESTA Visualization for Electron and Structural Analysis. xv, xxxiii, xxxvi, 74–76, 244–249

VT Virginia Polytechnic Institute and State University. iv, viii

XRD X-Ray Diffraction. 10

X-RAY DETECTION AND STRAIN SENSING APPLICATIONS OF COLLOIDAL QUANTUM DOTS

I. Introductions

A team at Los Alamos National Laboratory (LANL) running an experiment called the Magnetic Shock Experiment (MSX) is addressing the need of the National Nuclear Security Administration (NNSA)'s science-based stockpile stewardship program to detect broadband x-rays (10 keV-100 keV) with $\approx$ 100s of picosecond temporal resolution. X-rays have other uses for the military as well, such as Non-Destructive Technique (NDT) for checking cracks in aircraft frames, an example of which can be seen in Figure 2. A group at National Air and Space Administration (NASA) Langley Research Center has been looking into lowering the needed x-ray dose to do radiation based NDT of aircraft [27].

These applications share a common need for better x-ray diagnostics for both the stockpile stewardship program and aircraft NDT. Toward those ends, nanomaterials in the form of artificial atoms (Colloidal Quantum Dots (CQD)s) provide a promising solution. Recently, CQDs have been used as optical stress-strain gauges, which could allow the same CQDs used for imaging x-rays to be useful for sensing stress-strain using non-ionizing radiation [160] [131]. From the multiple ways in which CQDs could be utilized to solve defense oriented problems, this thesis investigated their use for both x-ray diagnostic for nuclear survivability and NDT applications.

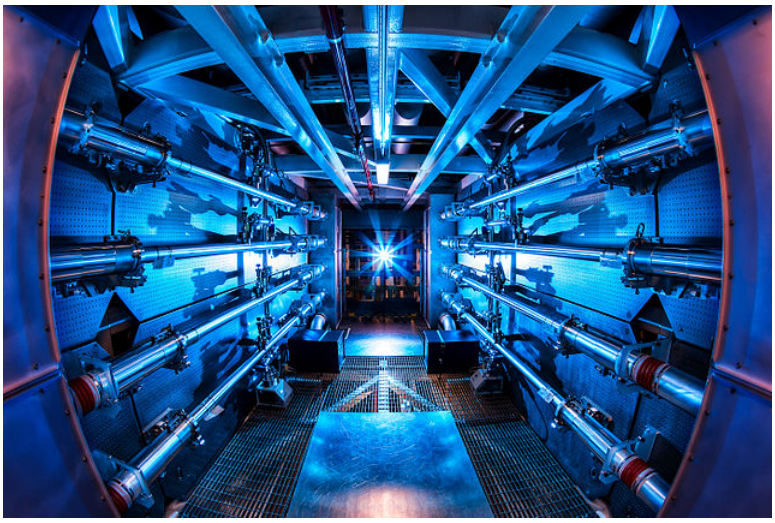


Figure 1. An example of testing in the nuclear stockpile stewardship program. The Nova laser pictured here led to the creation of the National Ignition Facility (NIF). High-energy lasers are one example of the numerous testing facilities that the NNSA runs within the science-based stockpile stewardship program to ensure the stockpile safety, reliability, and effectiveness. This program has been able to bring an end to hazardous underground testing and uses cutting-edge science to achieve the same levels of confidence [72].



Figure 2. A F-117 aircraft undergoing x-ray NDT [136].

1.1 Purpose and Goals

This thesis focused on characterizing commercially available CQDs for both x-ray detection and stress-strain measurements. The primary focus of this thesis was on the x-ray scintillation capability of the CQDs. The stress-strain experiments are provided

as a proof-of-concept which used a single material type of CQD that was also used in the x-ray scintillation experiments.

Another goal for this thesis was to do an exhaustive literature review of the available x-ray detecting methods that could work with a streak camera and to help motivate the reasoning to look into CQDs.

When it came to x-ray scintillation, the sponsor needed a scintillator with fast temporal characteristics within the 10 keV-100 keV range for MSX. An ideal goal would be to achieve 100 ps temporal resolution using CQDs, however due to time and resource constraints, only the steps that helped to characterize the CQDs before going into x-ray experiments were done. Suggestions were made for future laboratory x-ray experiments in the pursuit of testing the temporal response.

The research methods used to make a recommendation on the CQD technology to carry-forward in future research were conducted in an engineering-oriented manner. Everything from the experimental performance of the CQDs, their fabrication into a useful scintillating structure, and approximated physics models were used in their evaluation. More rigorous physics models were not simulated due to being outside the scope of this thesis.

1.2 Structure of Thesis

This thesis was organized by first examining the various x-ray detection mechanisms and determining why CQD scintillators were being studied (located in Chapter 2). All additional background and concepts required to understand CQDs were discussed in the last half of Chapter 2. CQD modeling setups and experimental setups

were discussed in Chapter 3. The results from the modeling and experimental tests were explained in Chapter 4. Finally, conclusions and suggestions for future work were reviewed Chapter 5.

II. Background and Related Research

New x-ray diagnostics are needed in order to evaluate MSX's broadband x-rays over time. One of the standard fast diagnostics with a proven track record in sub-ps temporal imaging is the streak camera. By itself, a streak camera is not be able to directly image x-rays. In some designs, streak camera photocathodes are sensitive up to 10 keV x-rays. Higher energy x-rays require the use of other radiation detection methods to interact with the incident x-rays into a usable wavelength of light that the streak camera photocathode can use. The streak camera for the MSX application needs to be able to detect x-rays between the range of 10 keV-100 keV. The minimal project requirement can work with sub-nanosecond timescales, but faster temporal resolution is preferred. The reach goal is to achieve a temporal resolution of under 100 ps throughout the entire 10 keV-100 keV x-ray spectrum. Another specification is detecting 10 keV-100 keV x-rays without needing to switch out components to capture the entire spectral range. Fortunately, there is a wealth of literature describing various fast x-ray detection methods. The eight different methods of x-ray detection with plausible use in front of or within a streak camera are further discussed in this section. These eight methods are listed below (hyperlinks for each detection method will bring reader to the desired section):

- Inorganic and Organic Scintillators
- Cherenkov scintillation
- Time-Of-Flight (TOF) method
- Photocathode x-ray detection
- Changing photocathode geometry to detect x-rays

- 2D monolayer scintillators
- Nanowire scintillators
- Colloidal quantum dot scintillators

To prevent any confusion, this thesis looks at both x-rays and gammas interchangeably in terms of their interaction with atoms. The standard definition of an x-ray is that the x-ray energies are between 100 eV-100 keV originated by the emission of an energetic photon from the dexcitation of an electron in either the K, L, or M shell of an atom that is excited by an incident electron. In comparison, a gamma is emitted by the nuclear decay of a nucleus. Both x-rays and gammas have the same type of interactions with an atom [17]. Thus, papers showing either the use of x-rays or gammas irradiating a detector are referenced in this thesis.

Numerous scintillators are commercially available and they are able to take incoming radiation and emit wavelengths sensitive to photocathodes. These scintillators are available in: solid, liquid, and gas. The fundamentals in scintillation are explained next.

2.1 Scintillator Fundamentals

Consider a material medium that interacts with charged particles (α,β, or an e^-), where the charged particles release some of their kinetic energy into the material, and thereby exciting the material's electrons. The excited electrons then relax back to their ground state [143]. Provided the energy imparted is larger than the bandgap, the material would emit a photon during its de-excitation. This mechanism of excitation, de-excitation, and then the emission of a photon within a material from an incident charged particle is called scintillation. Non-charged particles such as x-rays, gammas, and neutrons, would indirectly scatter an electron from an atom or could

be absorbed by an atom and knock out one of its electrons which could then be used for scintillation [120]. The important takeaway here would be to take advantage of the radiative scintillating properties of a material in order to detect radiation [143].

2.2 Beer-Lambert Law

When considering the non-charged particle cases of both x-rays and gammas, atoms must be ionized which in turn causes electrons to become unbounded. These unbounded electrons can then be used to excite a scintillating medium. In addition, the unbounded electron may deflect during scattering events with other electrons to cause bremsstrahlung x-rays which can ionize more atoms. Depending on which electron within an atom is unbounded, it could also cause a characteristic x-ray from the rapid relaxation of higher energy bound electrons.

The material being irradiated by x-rays or gammas has an inherent efficiency when it comes to how much of the kinetic energy of a non-charged particle can be used to ionize atoms or scatter electrons for a given thickness of material. Too low of an absorption of incident radiation while competing with the non-radiative processes of a scintillator may not generate enough scintillated photons to be detectable by a sensor. How well a material can absorb ionizing radiation such as x-rays and gammas can be characterized by the Beer-Lambert law, and can be seen in Equation 1 [144].

$$I = I_0 \, e^{\frac{\mu}{\rho} \, \rho \, x} \tag{1}$$

Each term in Equation 1 was summarized below:

- I: Transmitted photon flux (photons per second)

- I_0: Incident photon flux (photons per second)
- μ: Linear attenuation coefficient ($\frac{1}{cm}$)
- $\frac{\mu}{p}$: Mass attenuation coefficient ($\frac{cm^2}{g}$)
- p: Element density ($\frac{g}{cm^3}$)
- x: Thickness of media through which the radiation travels (cm)

The Beer-Lambert law is used to estimate the number of incident photons of a given energy that passes unaltered through a medium, with the mass attenuation coefficient dependent of the incident photon energy. This coefficient can be estimated or experimentally determined to consider consider all radiation effects. Equation 2 highlights the different radiation effects that go into the mass attenuation coefficient [130].

$$\frac{\mu}{p} = \frac{\mu_T}{p} + \frac{\mu_c}{p} + \frac{\mu_k}{p} \tag{2}$$

The variables in Equation 2 were explained in the list below:

- $\frac{\mu_T}{p}$: mass attenuation coefficient contributed to the photoelectric effect
- $\frac{\mu_c}{p}$: mass attenuation coefficient contributed to Compton scattering
- $\frac{\mu_k}{p}$: mass attenuation coefficient contributed to pair production

The photoelectric effect, Compton scattering, and pair production all deviate by their microscopic cross-section. The mass attenuation coefficient for each case is seen in Equation 3 [130].

$$\frac{\mu}{p} = \frac{N_0}{A}\,\sigma \tag{3}$$

σ is the microscopic cross-section for each case: σ_T, σ_c, and σ_k respectively. To approximate the microscopic cross-section, three equations can be used: Equation 4, Equation 5, and Equation 6 [130].

$$\sigma_T \approx \frac{Z^{4to5}}{(\hbar\ \omega)^{3.5}} \tag{4}$$

$$\sigma_c \approx \frac{Z}{\hbar\ \omega} \tag{5}$$

$$\sigma_k \approx Z^2\ ln\frac{2\ \hbar\ \omega}{m_e\ c^2} \tag{6}$$

A summary of the coefficients and variables for Equation 4, Equation 5, and Equation 6 were shown in the list below.

- Z: atomic number
- $\hbar$: reduced Plank's constant $(6.5821 \times 10^{-16} eV\ \cdot\ s)$
- ω: angular frequency of incident photons $(2\ \pi\ v)$
- v: incident photon frequency (Hz)
- m_e: rest mass of an electron $(5.489 \times 10^{-4} amu)$
- c: speed of light $(2.999 \times 10^8 \frac{m}{s})$

The most important mass attenuation coefficient components here would be the photoelectric effect and Compton scattering due to having prevalence from 10 keV-100 keV. Pair-production only occurs at energies $\geq$ 1.022 MeV, thus does not need to be considered. Mass attenuation coefficient data is available on the National Institute for Standards and Technologies (NIST) website for all elements. An example of a NIST plot for cadmium is shown in Figure 3.

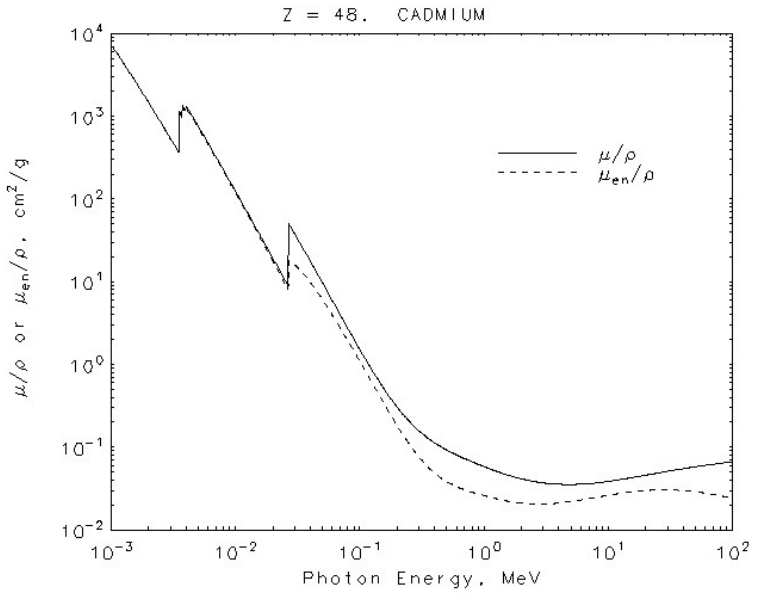


Figure 3. Mass attenuation and absorption coefficient plot data for cadmium from 1 keV to 100 MeV. Data from NIST [96].

Of interest in Figure 3 are the peaks along the plot. These peaks represent an inner shell electron being ejected from the atom. While only two peaks were shown for cadmium in this figure because the energy range is from 1 keV to 100 MeV, it is expected to see additional outer shell electrons if the plot goes down to 0 eV. These peaks can be used to characterize impurities and elements within a material when applying a range of incident photon energies using tools such as X-Ray Diffraction (XRD).

2.3 Electron Mean Free Path (MFP)

The Beer-Lambert Law is only the first step in x-ray scintillation. For the photoelectric effect, Compton scattering, and pair production, electrons are emitted or recoiled. The electrons then travel in a random trajectory until they lose enough energy to be fully absorbed by another atom. There are three possible paths the

electrons could take:

1. Electrons could escape the scintillating medium and not be used for scintillation
2. They could interact and deposit their energy within the scintillating medium
3. The electrons get deflected by an electrical field of an atom with little to no energy loss

In the majority of cases for a scintillator, an electron would likely experience only the second and third options from the list above due to a small MFP. However, there is a chance an electron could experience all three options if the photon interaction occurs near the surface of the scintillator or the scintillator is smaller than the MFP.

The average distance an electron within a material travels before having an elastic scattering event is known as the MFP $\lambda_{elastic}$. In nanometers, $\lambda_{elastic}$ is given by Equation 7 [53].

$$\lambda_{elastic} = 10^7 \frac{A}{N_0 \ \rho \ Q_{elastic(>\phi_0)}} \tag{7}$$

Where the variables in Equation 7 are given as:

- A: atomic weight ($\frac{g}{mol}$)
- N_0: Avogadro's number ($6.022 \times 10^{23} \ \frac{atoms}{mol}$)
- ρ: density ($\frac{g}{cm^3}$)
- $Q_{elastic(>\phi_0)}$: inelastic cross-section

The only variable not discussed yet is $Q_{elastic(>\phi_0)}$ which is given by Equation 8 [53].

$$Q_{elastic(>\phi_0)} = 1.62 \ \times \ 10^{-20} \ (\frac{Z^2}{E^2} \ cot^2(\frac{\phi_0}{2})) \tag{8}$$

Where the variables in Equation 8 are given as:

- ϕ_0: elastic scattering angle (e.g. 2°)
- Z: atomic number
- E: incident electron energy (keV)

In addition, an electron could also deposit some or most of its energy into an atom, or also known as inelastic scattering of an electron. As an electron travels through a medium, it loses energy per unit distance. This loss of energy must be integrated as a change in energy would also change the energy loss rate. A well known Bethe formula that used a continuous energy loss approximation can be seen in Equation 9 [53].

$$\frac{dE}{ds}(eV/nm) = -\frac{7}{85} \ (\frac{Z \ \rho}{A \ E}) \ ln(\frac{1.166 \ E}{J}) \tag{9}$$

Where the variables in Equation 9 are given as:

- ϕ_0: elastic scattering angle (e.g. 2°)
- Z: atomic number
- ρ: density ($\frac{g}{cm^3}$)
- E: incident electron energy (keV)
- J: mean ionization potential (keV)

Where the mean ionization potential is given by Equation 10.

$$J(keV) = (9.76\ Z + 58.5\ Z^{-0.19})\ \times\ 10^{-3} \tag{10}$$

Where Z in Equation 10 is the atomic number.

Since Equation 9 is an approximation, it is important to note that it has degraded accuracy with electron energies below $\approx 5\ keV$ [64]. There are additional models that could be used such as Rao-Sahib and Wittry and Tung *et al.* [117] [18]. Tying this back to how electron transport can become more troubling for modeling for the following reasons:

- The deposition of energy from an electron could be high enough to eject additional loosely bound outer shell electrons.
- A high enough electron energy deposition could cause characteristic x-rays from an atom itself.
- A primary incident x-ray can cause secondary effects of both additional x-rays and electrons, which in turn could cause tertiary x-rays and electrons.

This process continues repeating itself until the energy of each particle becomes low enough to be fully absorbed by a material. For scintillation purposes, inelastic scattering would result in absorbed energy that can cause scintillation, and thus emit photons. However, elastic scattering is useful to know and understand as an elastically scattered electron would eventually interact with an atom inelastically at a further distance.

2.4 Inorganic and Organic Scintillators

2.4.1 Theory

Conventional scintillators can be made from both inorganic and organic materials.

Inorganic Scintillators

An inorganic scintillator's physical mechanism can be visualized using a bandgap model as seen in Figure 4. The bandgap model can be used to represent inorganic scintillators since the crystal structure of this class of scintillators determines the bandgap.

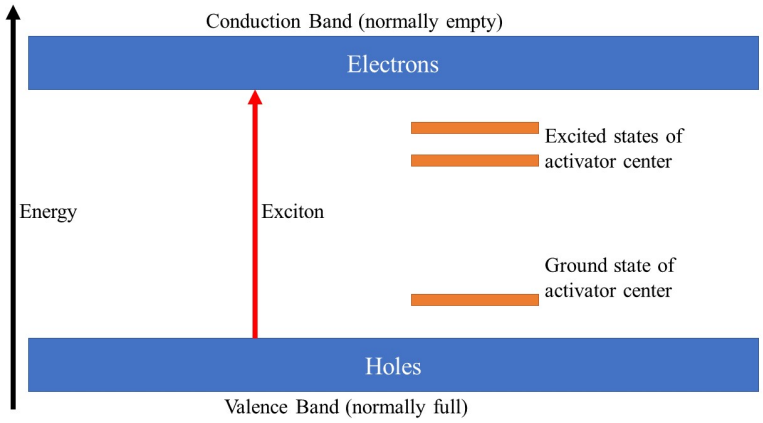


Figure 4. Inorganic scintillators can be modeled with the bandgap model. They usually contain an activator such as Thallium for NaI(Tl) inorganic scintillators. This activator helps to increase overall Quantum Efficiency (QE) in the inorganic scintillator but guiding phonons into a lower conductive band to make fluorescence easier [123].

As can be seen in Figure 4, the Thallium activator can help guide additional excitons (non-radiative emission) in order to increase the inorganic scintillator's QE [58]. NaI(Tl) is not the only inorganic scintillator available. A useful overview of commonly used inorganic scintillators can be seen in Table 1.

Phosphor	Density (g/cm^3)	Light Yield (photon-MeV)	Decay Time (ns)	Emission Maximum (nm)
BaF_2	4.88	1,500	0.6–0.8	180–220
$Bi_4Ge_3O_{12}$	7.1	8,600	300	480
$CdWO_4$	7.9	20,000	5,000	495
CsI	4.51	2,000	16	315
CsI : Na	4.51	40,000	630	420
CsI : Tl	4.51	66,000	800	550
Gd_2SiO_5 : Ce	6.7	8,000	60	420
K_2LaI_5 : Ce	4.4	55,000	24	420
$LaBr_3$: Ce	5.3	61,000	35	358
$LaCl_3$: Ce	3.86	46,000	25	330
$LuAlO_3$: Ce	8.34	12,000	18	365
$Lu_3Al_5O_{12}$: Ce	6.67	12,500	55	530
Lu_2SiO_5 : Ce	7.4	26,000	30	390
NaI : Tl	3.67	41,000	230	410
$PbWO_4$	8.28	300	2–3	410
$YAlO_3$: Ce	5.6	21,000	20–30	360
$Y_3Al_5O_{12}$: Ce	4.56	24,000	90–120	550
Y_2SiO_5 : Ce	4.45	9,200	42	420
ZnO	5.61	3,200	10	520

Table 1. Table of commonly used inorganic x-ray scintillators from Luo *et al.'s* search [81].

From Luo *et al.'s* search, BaF_2 is the fastest decaying inorganic crystal scintillator and this search concurs with the more extensive list of available inorganic scintillators from Lawrence Berkeley National Laboratory (LBNL) [44]. Of note, there are short decay times in BaF_2 as low as 100 ps, however this comes at a cost of efficiency. Note in Table 1 that despite BaF_2 being a fast scintillator, it inherently has a lower photon-MeV than the other scintillators available.

Organic Scintillators

Organic scintillators have a different bandgap spectra than their inorganic counterparts. Instead of the structure of the crystal lattice that determines the fluorescence,

organic scintillators occur from the excitation of single molecules [107]. An example of an organic scintillator molecular bandgap model can be seen in Figure 5.

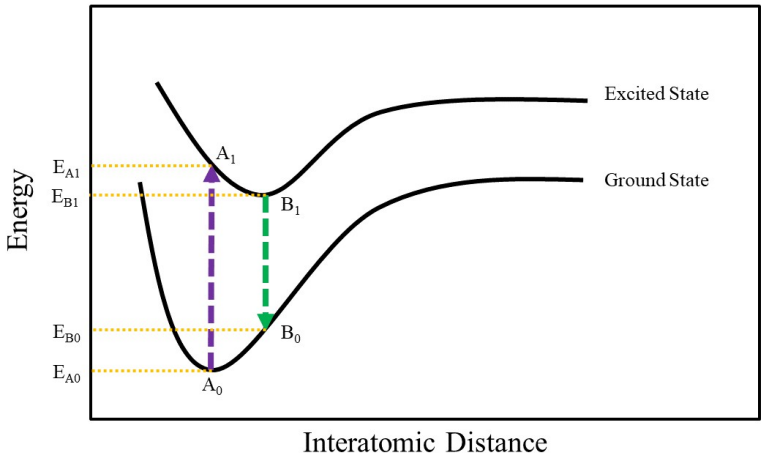


Figure 5. The interatomic distance between the organic molecules determines the bandgap between excited and ground states. The organic scintillator becomes excited by an incident charged particle and an exciton would occur from A_0 to A_1 energy levels. At this point, phonon vibrational energy (wasted energy due to heat loss) would bring the excited energy from A_1 to B_1. Then, a fluorescent photon would occur as the energy de-excites from B_1 to B_0[123].

Due to the unique structure of organic scintillators, they can decay faster than inorganic scintillators. However, this comes at a large cost to their QE.

2.4.2 Capabilities

Both inorganic scintillators and organic scintillators were common and affordable depending on the material. In addition, there were numerous varieties readily available in the commercial market. The Photoluminescence (PL) decay time for certain inorganic scintillators such as BaF_2 and for organic scintillators were within the picosecond time scale.

2.4.3 Shortcomings

The temporal resolution for both inorganic and organic scintillators have slow 1/e decay times (hundreds of picoseconds to nanosecond range) at room temperature.

This means all of the scintillating materials available in the market would take well over a few nanoseconds to hundreds of nanoseconds in order to fully decay. Better temporal resolution could be made by gating the fluorescence response.

2.5 Cherenkov Radiation

2.5.1 Theory

Cherenkov radiation can be harnessed to make one of the fastest particle detectors. To put it in the simplest terms, think of a dielectric medium almost perpendicular to a sensitive photodetector. As a charged particle passes through the medium, it would travel faster than the speed of light can travel through the given medium. This creates optical shock waves which emit visible photons (Cherenkov radiation) [101]. Huygen's principle can be applied to quantize the effect [114]. The principle states that incident light on a medium can be thought of as many little points that propagate a spherical wavefront. A graphic of this concept can be seen in Figure 6 [80].

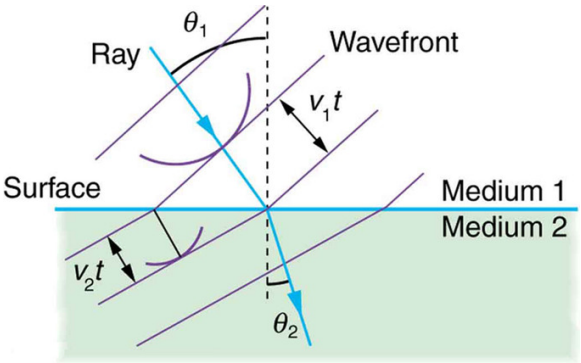


Figure 6. Huygen's principle when applied to a boundary between two media. Diagram from Lumen website [80].

As the incident light touches the boundary between medium one and medium two, it will continue to emit that light at an angle through medium two. Not only is the light at a different angle as it propagates through medium two, it also travels at a slower speed. When applying the Cherenkov concept, instead of an incident light going in between medium one and medium two, there is a charged particle or charged particles created by the interaction of non-charged particles with the atoms in the dielectric medium. If there is enough velocity in the charged particle, it will

emit shock waves of photons through medium two, as long as the emitted photons travel slower than the incident charged particle. This shock wave can be thought of as applying Huygen's principle throughout all of medium two, creating new wave fronts as the charged particle passes through. Since the emitted photons are slower than the charged particle's velocity, they mimic normal light interaction as seen before in Figure 6. The graphic in Figure 7 helps to demonstrate the shock wave effect [90].

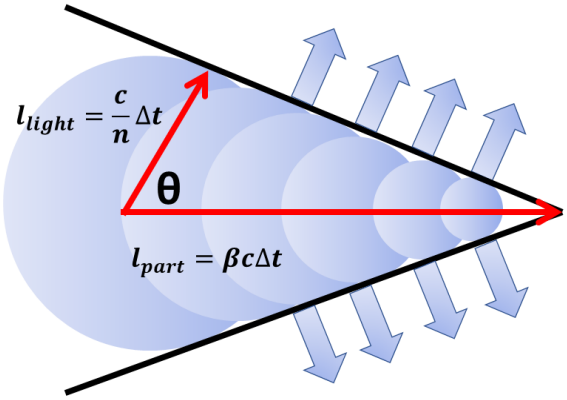


Figure 7. An incident charged particle traveling through a medium creates a shock wave effect, resulting in constructive interference of the emitting photons at an angle [90].

Thinking about Cherenkov radiation in terms of Huygen's Principle, a right triangle can be used to calculate the trajectories of the emitted photon. It is easiest to explain this with a graphic first which can be seen in Figure 8 [114].

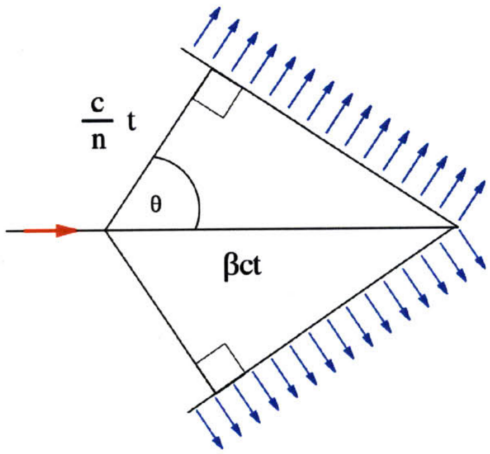


Figure 8. Sketch of Cerenkov radiation geometry (Diagram created by Arpad Horvath) [114].

The red arrow is the incident charged particle, creating a spherical wavefront. Its velocity is $\beta\ c\ t$, while the emitted photon's velocity from Cherenkov radiation is $\frac{c}{n}\ t$ At a single point, the right triangle method can be used. Equation 11 shows how θ_c is solved [101].

$$cos(\theta_c) = \frac{1}{n\ \beta} \tag{11}$$

The variables in Equation 11 are listed below:

- β: $\frac{v}{c}$
- v: the velocity of the charged particle in the material $\frac{m}{s}$
- c: speed of light $(2.999 \times 10^8 \frac{m}{s})$
- n: the refractive index of the material

Letting $\theta_c = 0$ then allows the following assertion. If β is greater than $\frac{1}{n}$, then Cherenkov radiation will be emitted [101]. Since the speed of an electron approaches the speed of light, relativistic kinematics must be used. Additional work to provide

the correct formulas and an analysis of how well Cherenkov radiation could work in the 10 keV to 100 keV x-ray band can be read in Appendix D.

2.5.2 Capabilities

Since Cherenkov radiation produces light emissions, the temporal resolution is the speed of light. This makes it an excellent method to achieve picosecond resolution. In addition, the method is relatively simple, since a single crystal can be used for light transmission. Cherenkov detection is friendly to couple with an optical system.

2.5.3 Shortcomings

From the feasibility study in Appendix D Cherenkov radiation is useful, but only for values at about 50 keV and over with a n value of 2.5 or less. In addition, to reduce energy to 50 keV assumes one must create a perfect diamond. The threshold can be lowered by using higher refractive index material (AlGaAs with n of 2.5-3.5) which is also not easy to make. This leaves a whole range of photons from 10 keV to 50 keV that cannot be reliably measured. If no method can reliably measure between the entire 10 keV to 100 keV x-ray band, then Cherenkov could be a useful substitute to measure the 50 keV-100 keV spectrum. There is new research occurring in the field of meta-materials that could one day allow for Cherenkov radiation to not have an energy threshold, but the research is not yet developed enough [156].

2.6 Time-of-Flight (TOF) Method

2.6.1 Theory

A commonly used technique to measure photons and particles would be the TOF method, which measures the energy of a particle by the elapsed time it takes to travel over a defined distance. One of the difficult aspects is differentiating the gammas from the neutrons, which TOF is excellent at differentiating. Since gammas have no mass, they travel at the speed of light and will hit the detector (e.g. scintillator in front of a Photomultiplier Tube (PMT)) before any neutrons can. Then, the neutrons will spread out between the higher energy neutrons and the lower energy neutrons. Higher energy correlates to a faster traveling neutron. Thus, higher energy neutrons make it to the detector first. This is great for pulsed neutrons since the time between the source going off and the first detection determines the velocity and, thus the energy of the neutron [124]. Figure 9 shows how to practice TOF.

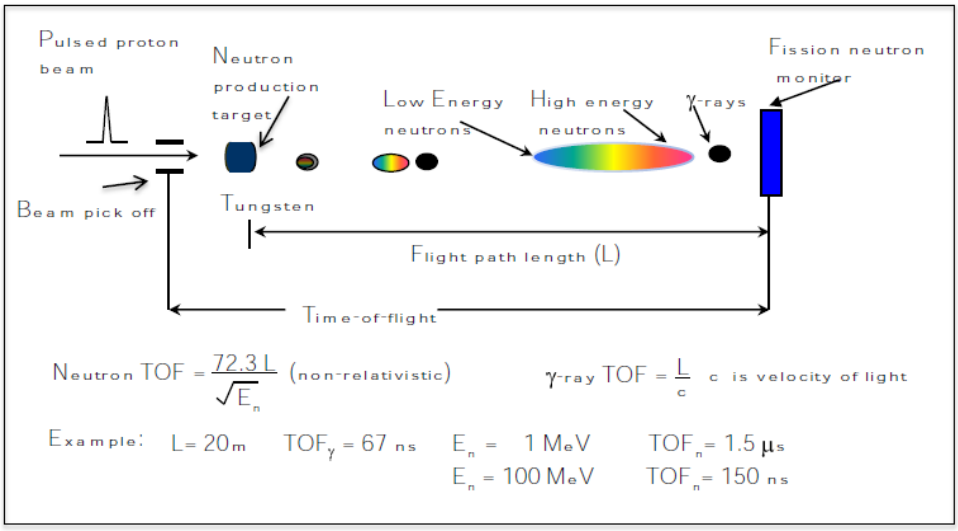


Figure 9. Infographic displaying how TOF works. Image from LANL [124].

There is a possibility that the gamma rays and higher energy neutrons could end up hitting the detector at the same time as the lower energy neutrons. This is known

as “wrap around” and sets the detectable lower energy limit [125].

2.6.2 Capabilities

Since x-ray detection is the goal of this thesis, only capabilities relating to x-ray detection for TOF will be mentioned here. Since x-rays travel at the speed of light in a vacuum, TOF is not able to separate out the different x-ray energies. This means TOF would not have any useful capabilities for fast x-ray detection. TOF is designed for particles with mass such as neutrons.

2.6.3 Shortcomings

TOF can become problematic for x-rays since they travel at the speed of light in a vacuum. This means different energies within the x-ray flux cannot be differentiated. In addition, the detector used for TOF measurements must have the same temporal resolution or better of the entire TOF setup. This already causes issues when wanting to achieve 100 ps temporal resolution since COTS x-ray detectors do not exist with 100 ps temporal resolution for 10 keV-100 keV x-rays. Unfortunately, this means TOF would not be feasible for the MSX’s temporal resolution needs.

2.7 Photocathode X-Ray Detection

2.7.1 Theory

Streak cameras employ the use of a photocathode as their front-side detection mechanism, with a photocathode being an applied use of Einstein's photoelectric effect. The photoelectric effect can be represented by Equation 12 [151].

$$E_k = hf - W \tag{12}$$

Where E_k is the kinetic energy an incident photon must have in order to cause electrons to be emitted from a metal, h is Plank's constant, ν is the frequency of the incident photon, and W is the work function of the metal being irradiated. While in a vacuum, the frequency of a photon can be calculated by using Equation 13.

$$\nu = \frac{c}{\lambda} \tag{13}$$

Where ν is the frequency of the photon, λ is the wavelength of the photon, and c is the speed of light. λ can be determined by the de Broglie wavelength which is given in Equation 14 [151].

$$\lambda = \frac{h}{p} \tag{14}$$

The only new variable introduced is p, the p is the momentum of the photon. After knowing the incident photon's momentum, Equation 14 and Equation 13 can be applied to Equation 12 to determine if an electron would be emitted. To determine the angle that the emitted electron would travel, the Compton effect can be used applying both principles of conservation of energy and momentum.

In photocathodes, there exists a high potential electric field which could be in the thousands of volts. This provides a direction for the emitted electrons to travel in order to be captured by either a phosphor screen or a semiconducting material.

2.7.2 Capabilities

The inherent advantage of using a photocathode with no other scintillation media in front of it is the sub-picosecond resolution already available. A soft X-ray streak camera sensitive to 10 keV was developed by Belolipetski *et al.*, and their results were published in 2009. The streak camera used in this research had a temporal resolution of 10 ps. The photocathode used a double-layer of cesium-antiominite (S11) deposited onto a $100-300$ Å gold layer on top of a mica substrate, with the gold layer providing soft x-ray detection [23]. The materials used within the photocathode are applied in the photoelectric effect and the work function. As stated in Busse's thesis, the theoretical work function of gold is different from the actual work function due to impurities when applying a gold layer [28].

2.7.3 Shortcomings

As discussed in capabilities, gold-coated photocathodes are only good up to 10 keV. This leaves the entire 10 keV-100 keV spectrum undetectable by using only a coated photocathode.

2.8 Changing Photocathode Geometry to Detect X-Rays

2.8.1 Theory

An upcoming solution in raising the x-ray detection limit for photocathodes is being done by Nevada National Security Site (NNSS) for Lawrence Livermore National Laboratory (LLNL). Their goal is to create a photocathode capable of measuring 10 keV-50 keV x-rays. Their solution is by fabricating microstructures within the surface of a photocathode to take advantage of the grazing incidence. They theorize this can be accomplished by matching the x-ray path length to the electron escape depth of a material. The shallower the angle of incidence, the more distance the x-ray travels through the escape depth thickness in the photocathode material, which in turn emits more electrons. A better picture of this effect can be seen in Figure 10 [99].

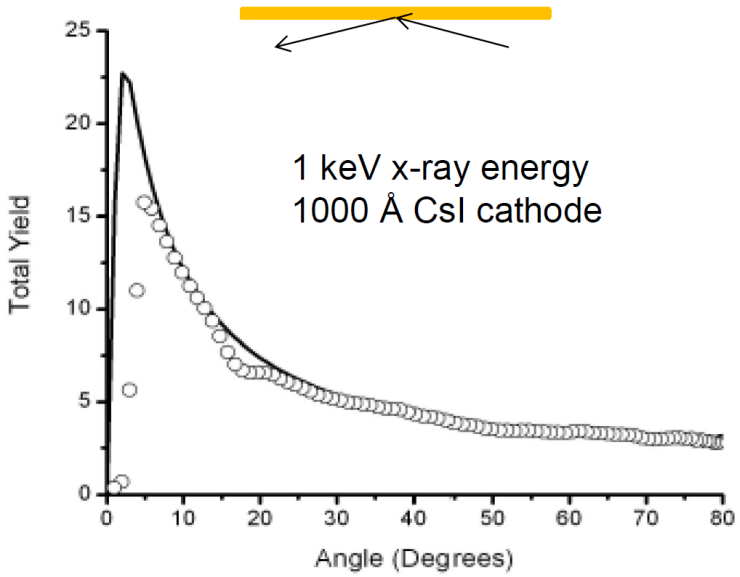


Figure 10. The lower the angle of incidence, the higher the electron yield in the photocathode. Figure from Opachich *et al.* [99].

A physical example of what this microstructured photocathode looks like can be

seen in Figure 11.

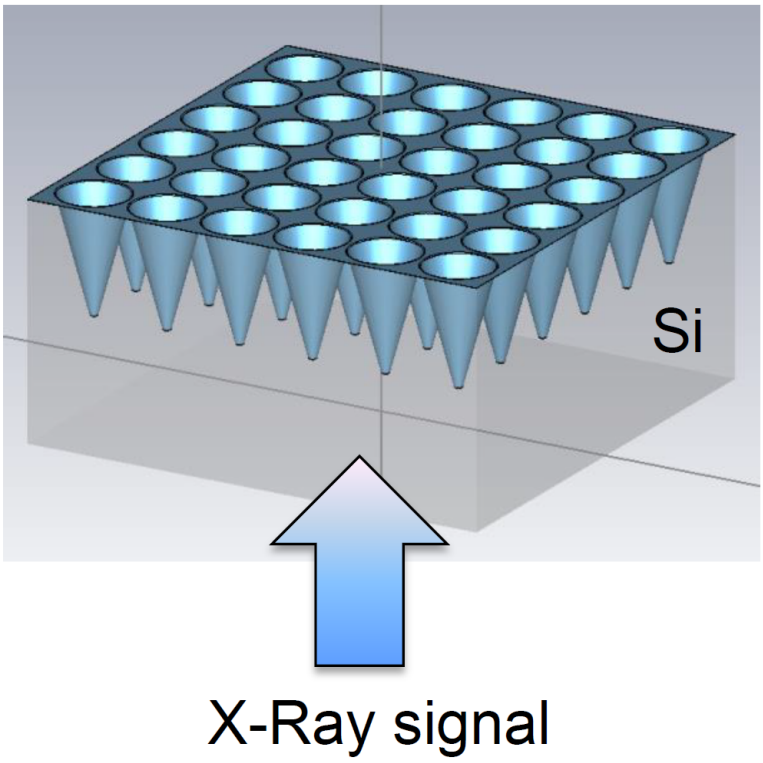


Figure 11. Recessed cavity design to take advantage of the grazing incidence. In this case, the base material is a microstructured Silicon on Insulator (SOI) wafer followed by electron beam sputtering layers of 20Å of titanium and 700Å of gold [100]. Figure from Opachich *et al.* [99].

The coned structures help to match the x-ray path length to the escape depth. If an x-ray signal is going to be radiating perpendicular to a photocathode, the cones artificially create the shallower angle to the direction the x-ray is headed. The cones are fabricated by using six iterations of Deep Reactive-Ion Etching (DRIE) [100].

2.8.2 Capabilities

Opachich *et al.* expected total yield enhancement to be 1.63-3.6 times greater at 7.5 keV. The authors did mention that in previous measurements, a four times increase in yield was possible at grazing incidence [99] [100]. A 3.5 times increase in yield compared to a flat photocathode at 7.5 keV was demonstrated which would

allow the photocathode to operate up to $\approx$ 26 keV. Since this uses photocathodes, the temporal resolution would still be in the sub-ps range as this would go directly into a streak camera system.

2.8.3 Shortcomings

While creating microstructures within a photocathode shows promise in yielding more electrons per keV, this method is still at least 70 keV away from being able to detect up to 100 keV x-rays from published literature. More complex geometries and better materials may be able to improve this technique in detecting x-rays, however there is no certainty that this method could be improved to detect up to 100 keV x-rays without a great deal of effort.

2.9 2D Monolayer Scintillators

2.9.1 Theory

Transition Metal Dichalcogenides (TMD) are a type of semiconducting material made to be the thickness of a single crystal structure. Hence, these TMD are known as monolayers. They are of type M X_2 materials, with the M standing for a transition metal atom which could be either Mo or W, and the X standing for a chalcogen atom which could be a S, Se, or a Te [45].

TMD monolayers exhibit direct band gap properties [161]. This in turn allows them to emit photons quickly, since there are less inter-system crossings. Due to their unique properties, TMD monolayers can emit both excitons and biexcitons at 50 K with fast decay times (tens of picoseconds). It is noted that at temperatures above 40 K, the biexcition emission intensity matches the exciton emission and losses intensity as temperature is increased. Between 40 K and 20 K, the biexciton emission intensity is more than the exciton intensity. Finally, below 20 K, the biexciton emission quickly suppresses and is non existent at $\approx 5\ K$ [161].

2.9.2 Capabilities

The photoresponse time of TMD monolayers are promising. In multiple publications, the fastest response time emitted by WSe_2 monolayers are $\approx$ 10 ps to a few tens of picoseconds [161] [85]. In addition, the wavelength emission of TMD monolayers can go from 600 nm into the near-infrared region. Figure 12 shows four of the TMD materials and their wavelength emission spectra [142] [158].

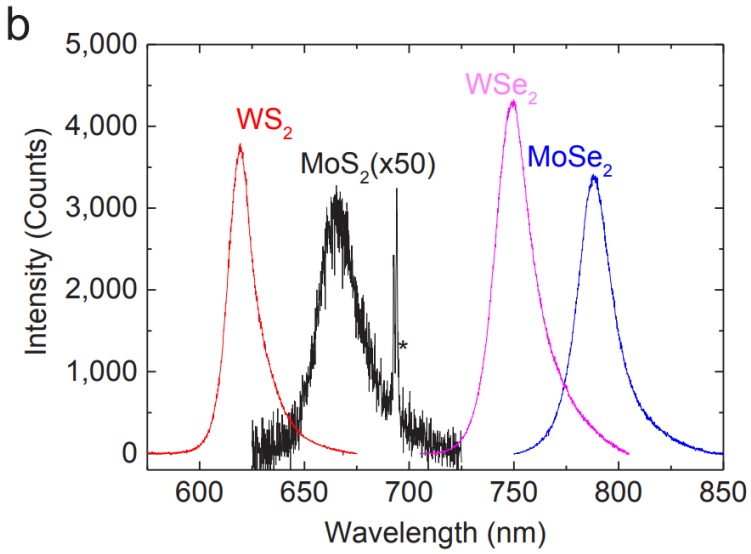


Figure 12. Four monolayer materials excited with a 400 nm laser with a 30 s exposure time. Image from Xu *et al.* [158].

2.9.3 Shortcomings

First and foremost, TMD monolayers are difficult to make into bulk scintillators. In order get enough x-ray absorption at higher energy x-rays, additional layers need to be created. This could be done by fabricating monolayers onto optically transparent glass or polymer and create a number of these stacks to get the desired amount of x-ray absorption. The emitted light could escape through the side of the scintillator. Fabricating potentially thousands to millions of these stacks would not be time feasible. Along with the difficulty in the fabrication of a bulk scintillator, TMD monolayers emit in the orange-infrared regime, which limits the available photocathodes that can utilize them. Thus, TMD monolayers are not a viable scintillator that works within the time constraints and flexibility needed for the given x-ray scintillation application. This does not rule out their potential for other applications, such as low energy x-rays which can be done with a small material thickness.

2.10 Nanowires

2.10.1 Theory

Nanowires are defined as materials that are nanometers in diameter while being long in length (microns). These exhibit unique properties in waveguiding emitted photons, which prevents photons from spreading away, thus are excellent in their spatial resolution. An example of what nanowires look like can be seen in Figure 13 [137].

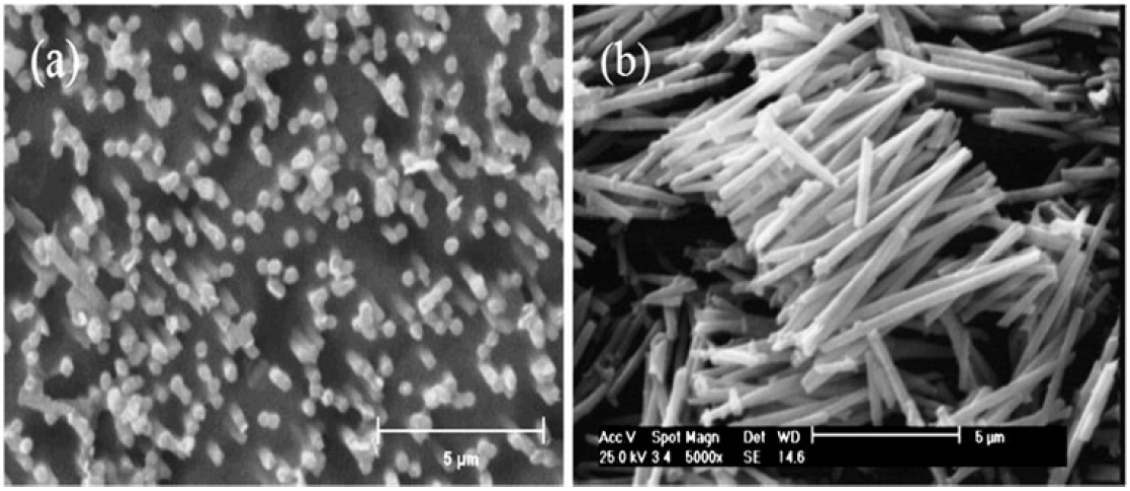


Figure 13. Scanning Electron Microscope (SEM) images of ZnO nanowires within a polycarbonate matrix and with the polycarbonate matrix removed. Image from Taheri *et al.* [137].

Due to the nanoscale diameter, the nanowires exhibit quantum confinement properties, like quantum dots. However, unlike quantum dots, nanowires can be anisotropic in their light emission. If the nanowire is suspended in a polymer matrix then a critical angle phenomena can occur, and allow for the waveguiding of the photon, instead of the photon escaping in any other direction [138].

It is demonstrated that by adding a shell layer of MgO around a ZnO nanowire, that the PL intensity increases. This means the QE of these nanowires can be im-

proved from their core version that suffers from surface defects [86].

2.10.2 Capabilities

ZnO nanowires have a fast response time constant of 10 ps and a slow response time constant of 70 ps [86]. It is of note that the time constant does not mean PL decay time of the material. However, if willing to take a reduction in efficiency, high temporal resolution in the tens of picoseconds would be attainable. In terms of full PL decay time, George *et al.* showed that $BaSiF_6$ nanowires have a PL decay time close to 50 ns at room temperature [52].

2.10.3 Shortcomings

QE of ZnO and GaN nanowires as scintillators is shown to be low (a little under 20%) in between 2013 and 2015 [137] [138]. The recent demonstrations of nanowires as scintillators did not improve the QE upon earlier designs. In 2000, Kleimann *et al.* demonstrated scintillating guide screens to both better the spatial resolution of CsI:Tl scintillators and increase QE through waveguiding. However, they reported about about a 20% QE [69]. Another factor is the wavelength spread of the photon emission of the nanowire. PL emission spectra are anywhere from under 400 nm to over 700 nm; if coupling the nanowire scintillator to a photocathode, efficiency will degrade due to Gen-II photocathodes having the highest QE for wavelengths $\leq$ 400 nm [138]. This means the 20% QEs reported could be lower when coupled to a streak camera.

2.11 Colloidal Quantum Dot Scintillators

2.11.1 Theory

Since the theory of CQDs is discussed in great detail in the rest of Chapter 2, only the history of CQDs is discussed in this sub-section.

CQDs are not new materials; in fact the original Quantum Dots (QD)s were discovered in 1981 by Russian solid-state physicist Alexey I. Ekimov. However, the QDs discovered in Ekimov's research was not not like the present liquid mixtures that we know of today. At the foundational level, Ekimov discovered the core of QDs which were the semiconductor nanocrystals. In 1985, Louis E. Brus took the semiconductor nanocrystals and placed them in a colloidal mixture, which created the first known instance of modern QDs. However, Brus did not coin the term QDs, it was Mark Reed who made the term in his paper in 1988 [7]. The majority of QD research did not begin until the successful synthesis of colloidal cadmium based CQDs. This breakthrough created the ability to tune the absorption and emission of CQDs depending on their size. The breakthrough was due to the work of Murray, Norris, and Bawendi in 1993 [65]. Research continued and the first commercialization of CQDs was in 2013 with the Sony XBR X900A flat panel televisions [7].

While CQDs are being commercialized, their full potential is still a growing area of research. All of the potential applications will not be listed in this paper, however one application of interest is using CQDs in imaging x-rays from 10 keV to 100 keV energies. CQDs have a unique ability in absorbing higher energy wavelengths and emitting discrete visible wavelengths. They have also been demonstrated to achieve about 80 ps PL decay constant [148]. Provided there is a high enough QE to be detectable, CQDs are an excellent candidate in replacing conventional crystal scin-

tillator materials such as BaF_2, which is the fastest decaying scintillator of its class with $\approx$ 400 ps decay time [126]. CQDs have the possibility of lowering the cost of fast x-ray streak cameras and other x-ray imaging applications. For example, NASA is investigating CQDs for imaging cracks in aircraft [27].

2.11.2 Advantages

When considering Nanoplatelets (NPL) structure, CQDs have been shown to achieve 77 ps effective decay time [148]. Additionally, perovskite NPL have been shown to attain a 90 ps decay time at 10 K using $CsPbBr_3$ and a 30 ps decay time at 10 K using $CsPbCl_3$ [141].

2.11.3 Shortcomings

While CQDs have been shown to achieve a fast decay time, their QE is questionable. In a phone call with Dr. Nerine Cherepy from LLNL, Dr. Cherepy mentioned the following shortcomings related to exciton annihilation:

- Due to their small size, CQDs become much less efficient at higher gamma energies as excitons annihilate each other, whereas bulk crystal material have more room for excitons to move independently.
- The annihilation of excitons can quench the fluorescence.

In addition, going down to cryogenic temperatures decreases the decay times, however quenching may occur as the number of available states for the excitons to travel through decreases as discussed in a conversation with Dr. Larry Burggraf. It is important to note that even though CQDs may not have the QE of crystal scintillators, they can be made into a polymer or channel that essentially allows them to behave more similary to a bulk crystal material. The drawback to a thicker

amount of CQDs would be if the absorption and emission wavelengths are the same, the material could experience reabsorption of photons. Having a proper Stokes shift to move the absorption band to smaller wavelengths is a solution to this problem. The catch is that a good Stokes shift is usually done through the application of a shell, which in literature has been seen to have hundreds of picosecond decay time with an ideal emission wavelength for certain photocathodes.

Out of all the above methods, it was decided that CQD scintillators would satisfy the needed requirements at MSX. Coincidentally, CQDs have already been studied by NASA for NDT of aircraft. Figuring out an economically friendly method in implementing CQDs at MSX would also help NASA in turn. In addition, the same CQDs being used for x-ray scintillation could be used in a different way to optically detect strain on aircraft. The theory behind this is discussed later in this chapter.

To understand the utility of a CQD scintillator for a fast temporal resolution, the concepts surrounding its application were researched and discussed.

2.12 Streak Camera Fundamentals

This section goes over the basic operations of a streak camera. Streak cameras in essence capture both the timing of a particle and its wavelength in one image. The easiest way to visualize its operation is to think of a slit in front of a rotating mirror. When light is beamed through the slit, it will spatially localize the light's wavelengths. A rotating mirror is then rotated quickly, streaking the diffracted light across a collection screen. One could then collect the varying wavelengths of incident light, the rate of rotation of the mirror will collect its wavelength information over time, and the amount of flux of light (represented as the intensity of a pixel of the resulting streaked image). Historically, some of the first streak cameras such as the Mack Streak Camera developed for the Trinity test used a rotating mirror [9] [8].

While mechanical rotation of a mirror can make a streak camera, it would not be fast enough to achieve picosecond resolution. As an example, a rotating mirror of a diameter of 2 cm would achieve a temporal resolution of 1 ns. Thinking about the mirror as a cylinder, the circumference would be 6.28 cm. The collector screen would

be such that the diffracted light reflected from the mirror would be collected from a -45° to a $+45^\circ$ angle. The image collector would be 1 cm away, creating a collector length of 4 nm. This makes a total rotation of 90° to be useful for data collection. To help visualize the scenario, a model can be seen in Figure 14.

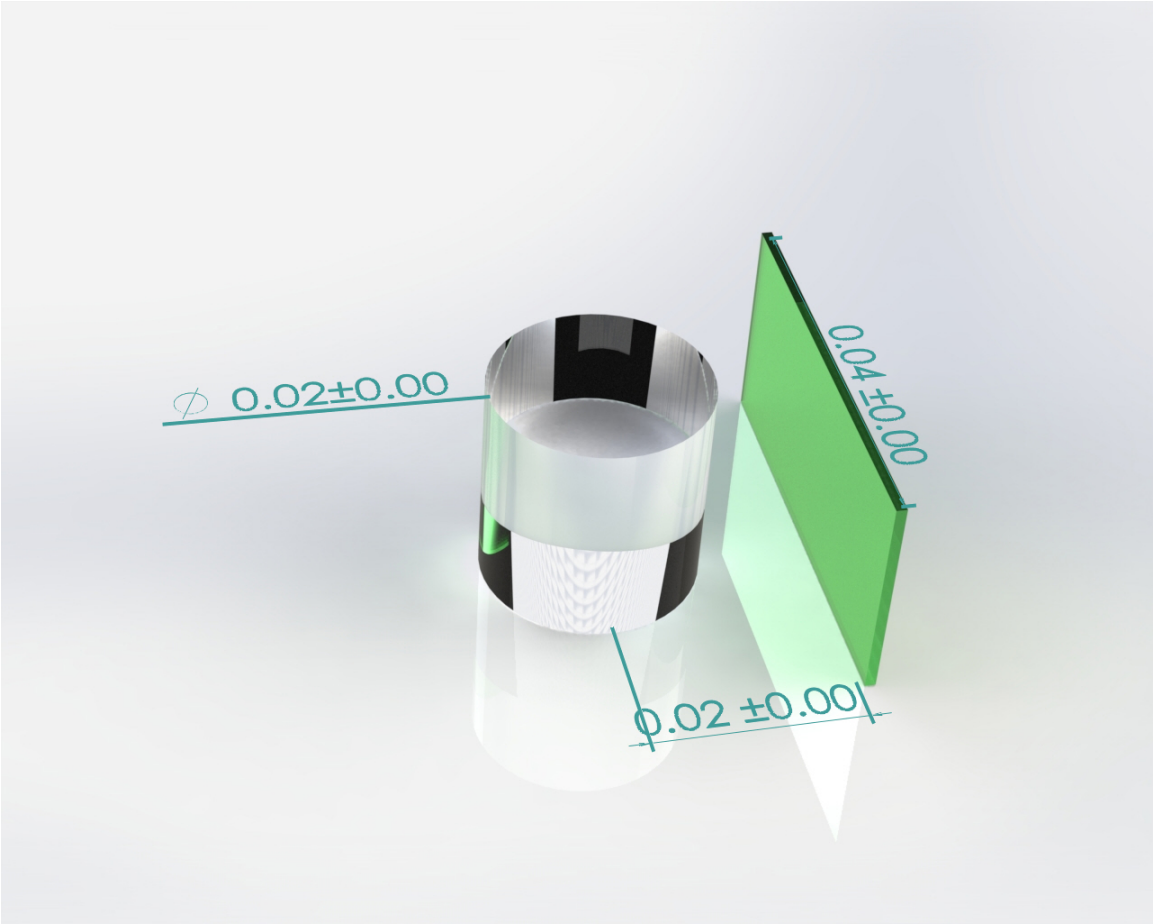


Figure 14. Example scenario of a rotating mirror represented as a cylinder and a light collecting screen represented as a rectangle.

Keep in mind the pixel resolution of the collector matters, and for this example, a 13 μmx13 μm sized pixel is selected. This means along one dimension there are 3,076 pixels. Each pixel represents a single point in time, in this case 1 ns. With a 90° rotation to cover a 3,076 pixel screen, that means the mirror must rotate 90° in 3,076 ns. This would result in an angular velocity of 510,662 radians per second, which would be equivalent to 487,643 rpm. At the moment, assume the mirror has

no weight and does not affect the performance of a spinning motor. High speed motors from Celeroton are rated at 500,000 rpm with cooling applied [30]. Getting towards 1 ns temporal resolution with a mechanical streak camera would be theoretically achievable, but what about 1 ps temporal resolution? Instead of 3,076 ns, this device would need to rotate 90° in 3,076 ps. That requires an angular velocity of 510,662,005 radians per second or 4,876,462,941 rpm. This angular speed is not presently mechanically feasible using only COTS components.

The slit and rotating mirror example motivates the need to go towards a changing electric field, which solid-state devices can achieve sub-nanosecond to picosecond sweep rates. However, unlike the mechanical streak camera case, a solid-state streak camera has to convert an incident photon to an electron before it can be streaked. The main components within a streak camera system in the order of photon interaction are: the scintillator (if needed for imaging $\geq$ 10 keV energy photons), slit, lens, photocathode, accelerating mesh, focusing electrode, sweep electrode, Micro-Channel Plate (MCP) (if amplifying electron signal), phosphor screen, scientific camera, camera processing board, and finally the computer software.

There are many working parts that are needed to make a streak camera work. All items beginning from the slit to the phosphor screen are contained into one package called a streak tube. The streak tube is kept under vacuum in order to prevent scattering and or absorption of the traveling electrons throughout the tube. A model of a streak tube can be seen in Figure 15.

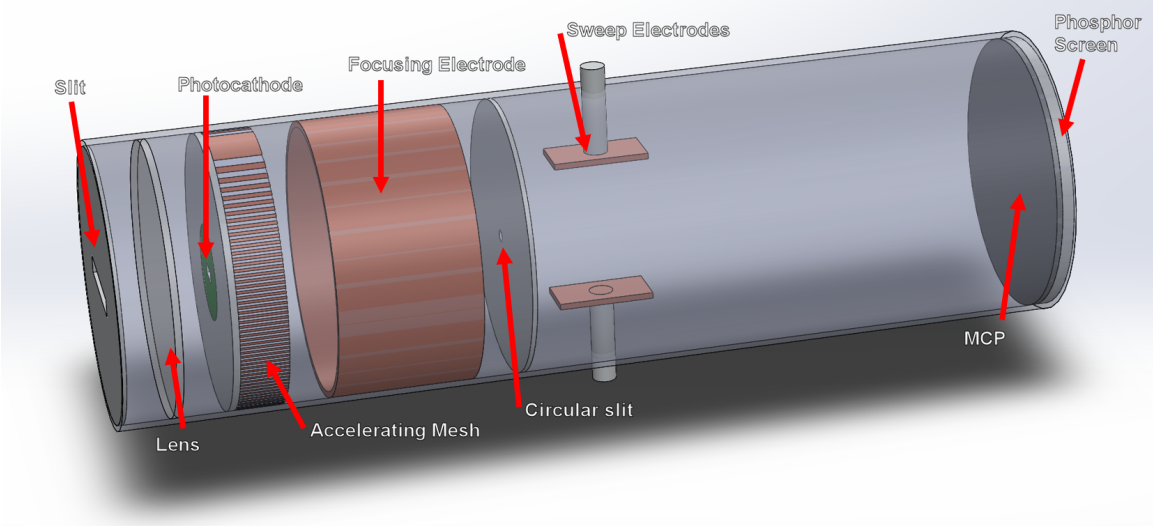


Figure 15. Streak tube model rendering that highlights the main components usually found within a streak camera.

There are presently two preeminent streak tube distributors within the United States, Sydor Technologies and Hamamatsu. There is an additional streak tube supplier called Photek Limited, however has an exclusive partnership with Sydor Technologies for North American sales [139].

After discussion with Sydor Technologies' representatives, it was decided that the Photochron 5 streak tube would be the fastest temporal resolution and most affordable streak tube for the MSX application for its future streak camera. A graphic of the Photochron 5 streak tube can be seen in Figure 16.

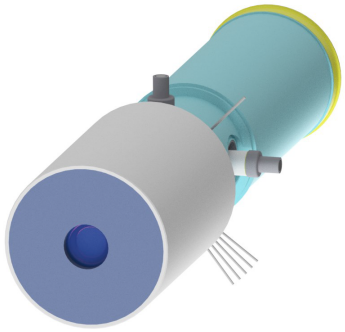


Figure 16. Image of the Photochron 5 streak tube sold by Photek Limited through Sydor Technologies. Image from Photek Limited [10].

The streak tube would cost $\approx$ \$33,600 for a typical time resolution of 2 ps with up to 400 fs resolution [10].

2.12.1 Scintillator

A scintillator is needed to image $\geq$ 10 keV x-rays. As explained earlier in Chapter 2 about the different x-ray imaging technologies, a scintillator is not the only method that can emit the needed wavelength of light for streak camera photocathodes. An optically transparent crystal using Cherenkov radiation can also be used, but as explained before, this method cannot do the entire 10 keV-100 keV range needed for the application of this thesis.

2.12.2 Slit

The slit diffracts the incident photons in order to spatially localize the photon's wavelengths within the streak tube [5].

2.12.3 Lens

The lens focuses the incident photons that are in a rectangular shape to fit within the photocathode [5].

2.12.4 Photocathode

The theory behind photocathodes was already discussed in the photocathode x-ray detection section. This section focused on what happened after the electron was emitted from the photocathode within a streak camera.

The efficiency of the photocathode is dictated by the voltage gradient applied between the photocathode and the anode. In between the photocathode and anode are an accelerating mesh and a focusing electrode. Since the photoelectric effect is isotropic, a stronger electric field focuses the emitted electrons to become more anisotropic and be directed down the tube of the camera. Thus, it is imperative to use the highest voltage possible between the photocathode and the anode.

The photocathode stage of a streak camera can be used as a shutter. If voltage is not applied between the photocathode and the anode, a useful amount of electrons would not be able to make it to the phosphor screen at the back end. However, this presents challenges as creating a field between the photocathode and the anode creates capacitance that must be drained quickly in order to effectively cut off electrons being emitted by the photocathode. Going back to using the highest voltage possible the higher the voltage, the more challenging it will become to use the photocathode as a fast shutter.

The commercial market presently has what are called Gen-II photocathodes. This

line of photocathodes can be seen in Figure 17 provided by Sydor Technologies.

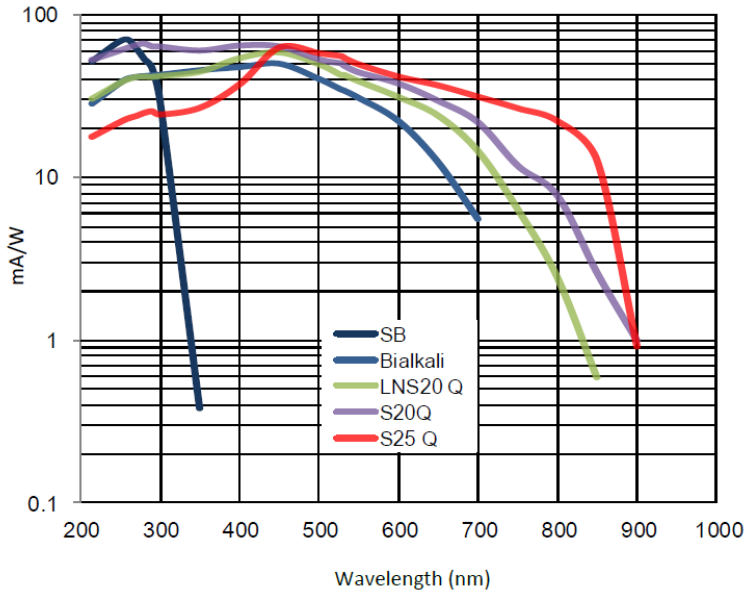


Figure 17. Selection of photocathodes provided by Sydor Technologies and their respective output versus incident wavelength. [105]

For the thesis application, the S20Q photocathode would be selected as it has the highest efficiency in the Ultra-Violet (UV) to blue wavelengths. These Gen-II photocathodes are not efficient in the Infrared (IR) and Far-Infrared (FIR) regions. There exists Gen-III photocathodes, however the commercially available ones are used for NVG. The industry has seen the importance in providing scientific grade photocathodes that work in both the IR and FIR regions. Photocathodes that can operate in this range will be called Gen-IV photocathodes. For x-ray imaging applications, higher Z materials will have better energy absorption, and lead is one of those useful semiconductor elements. Unfortunately, lead-based quantum dots emit in the IR region. Fortunately, there is an older Hamamatsu IR streak camera available for this thesis.

2.12.5 Accelerating Mesh

The accelerating mesh is the application of a high-voltage potential between the photocathode and a mesh. As discussed, an electric field can help capture electrons and direct them down the streak tube [5].

2.12.6 Focusing Electrode

The focusing electrodes take the incoming electrons from the accelerating mesh and focus them into a tiny circular slit at the anode. The circular slit acts as an aperture [6].

2.12.7 Sweep Electrode

After the electrons pass through the circular slit in the anode, they enter the sweep electrode. As discussed before with the rotating mirror in a mechanical streak camera, the sweep electrodes quickly change in voltage potential, thereby steering the beam of electrons along the streak tube [6]. The circuit that controls the sweep electrode, known as the sweep circuit, can output up to a few thousand volts. In general, avalanche circuits are used to create picosecond and sub-nanosecond rise times. However, avalanche circuits by themselves are not able to control their rise times. Some methods involve multiplexing filters on the output of the avalanche circuit to select a desired sweep rate [1]. As newer SiC Metal-Oxide-Semiconductor Field-Effect Transistor (MOSFET) and GaN MOSFET technologies enter the market, there is the possibility in obtaining more control by changing the amount of current that enters the gate of the MOSFET. This will in turn change the rise time of the voltage, and could be programmed in real time with a digital potentiometer or an inductive coil.

2.12.8 Micro-Channel Plate

If required, a MCP is able to amplify the number of electrons coming out of the sweep electrodes. However, the greater the amplification the greater the distortion to the image. Additionally, the MCP is another way to act as a shutter in the streak camera. If no voltage is applied to the MCP, no electrons can pass through [5].

2.12.9 Phosphor Screen

The phosphor screen can be thought of as an image integrator. It collects electrons and causes phosphorescence over a characteristic length of time until its phosphorescence emission fully decays. The longer the decay, the better the phosphor screen's spatial resolution due to smaller grain size. However, if an experiment requires multiple images in a fast time period, lower resolution phosphors are available that have output emission decays within 80 ns. A table of phosphor screens provided by Sydor Technologies can be seen in Table 2.

Type (wavelength nm)	Anode Efficiency (%)	Photons per Electron at 5 kV	Decay Characteristic
P20 (540)	12	320	Fast initial decay with long decay at low level. 1 ms to 1%
P43 (548)	8.7	240	1.2 ms/decade, true exponential
P46 (530)	1.8	55	300 ns
P47 (410)	3	64	80 ns
FS (513, 668, 768)	4.2	96	12 μs to 10%

Table 2. Commercially available phosphor screens from Sydor Technologies [105].

The emission wavelength spectra from these commercially available phosphors are anywhere from 410 nm-768 nm. Their emission wavelength selection is based upon the scientific camera available in a given laboratory. However, green has been a standard for some time and a green phosphor screen can work with a wider range of Charged-Coupled Device (CCD)s.

2.12.10 Scientific Camera

The scientific camera is the weakest link of a streak camera system, and therefore great expense is made to ensure the best technology is used. Their detectable lower limits ultimately set the QE requirement for any x-ray detection mechanism used in front of the streak camera's photocathode in order to ensure enough electrons make it to the scientific camera to be detectable. For example, if the electron noise level of a scientific camera is ten electrons, then more than ten electrons must be sent through the streak camera to the camera. This can be back-calculated using the QE of the streak camera's photocathode and then engineering the right QE of the scintillator placed in front of the photocathode in order to get the required number of electrons to image over the noise.

In terms of choices of a scientific camera that have optimal performance and while keeping the overall streak camera under $100,000, there are two dedicated scientific camera companies: Spectral Instruments and Raptor Photonics. Spectral Instruments sells a radiation-hardened camera for $9,800 called the RVT100, which the price includes a CMV-4000 CMOS sensor with a dark noise of 13 electrons. If radiation hardness is not a concern, then the higher resolution scientific camera from Spectral Instruments would be the 800 series camera with a dark current at $-35\ ^{\circ}C$ of less than 0.1 electrons per pixel/s using the 47-10 CCD. The direct competitor to this camera is Raptor Photonics' Eagle camera with the E2V CCD. It has a dark current of less than 0.001 electrons per pixel/s at $-90\ ^{\circ}C$. The Eagle camera is priced around $40,000. The Spectral Instrument's equivalent is also around the same price after communicating with the vendor. The main difference between the two companies is in the coupling of the camera to the streak camera tube. Usually scientific cameras are either fiber-coupled or optically lens-coupled. After correspondence with two LLNL

scientists, Dr. Andrew MacPhee and Dr. Joe Holder, the fiber-coupled route would be too challenging due to the susceptibility of the fiber-coupling breaking and ensuring proper aligning for maximum light transmittance. This leaves using an optical lens-based system between the phosphor screen and the scientific camera, which requires some thought into efficiently directing light from the phosphor screen into the scientific camera. However, a Raptor Photonics' Eagle camera has been custom ordered by a LLNL group to have its CCD directly in front of the phosphor screen of a streak tube. This requires taking the f-mount of the camera off and attaching a custom flange, which can be designed and purchased from Raptor Photonics for an additional fee of $\approx \$2,000$.

2.12.11 Camera processing board

Usually not the case for slower frame rate scientific cameras, the faster scientific cameras usually require a proprietary control board attached to a desktop computer. This control board sits in on one of the desktop's Peripheral Component Interconnect (PCI) slots.

2.12.12 Computer software

The computer software used to operate a streak camera can be a proprietary commercial software for a fully made streak camera. For a user-made streak camera, multiple pieces of software may be used. For instance, one may use LabVIEW or Python in order to control the timing circuits to operate the streak camera power supply and streak circuit while running the imaging software used for the scientific camera all in the same program. However, this usually requires buying an Application Programming Interface (API) developer kit provided by the camera company.

2.13 Colloidal Quantum Dot Theory

Both spherical and 2D NPL CQDs are used in this thesis. At the fundamental level, all CQD properties can be explained through quantum mechanics. This section will highlight: semiconductor principles, the physical makeup of CQDs, quantum mechanical models, surface application of ligands, crystal structures within the tested CQDs, the physics behind Förster Resonance Energy Transfer (FRET), and strain effect properties of CQDs.

2.13.1 Semiconductor Principles

CQDs are made up of elements in the periodic table's groups III through V. A few of these elements are also semiconducting materials. There are three categories of electrical materials: metals, semiconductors, and insulators. Figure 18 helps to visualize each category's relative resistivity level.

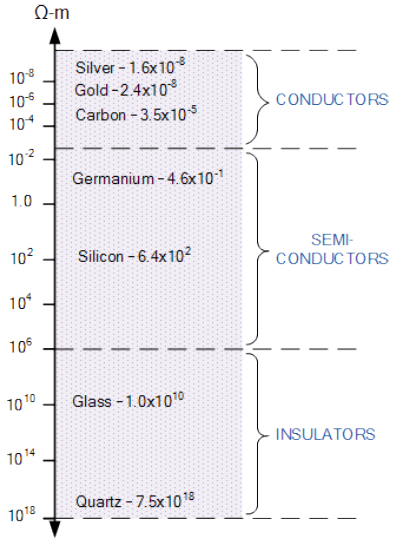


Figure 18. Graphic showing the three categories of materials: conductors, semiconductors, and insulators in relation to their resistivity. This graphic also shows some examples of materials in each category. Image from Electronics Tutorial website [149].

Metals are highly conductive because both their valence and conduction bands are overlaying on each other. Insulators are not conductive due to having a high bandgap.

This does not mean they cannot transfer electrons as a high enough electric field can still break down the material. For semiconductors, their bandgap is large enough to prevent an easy flow of electrons, but small enough to allow electrons with the help of an applied electric field.

Semiconductors fit in between metals and insulators with a resistivity ranging from $10^{-2}\ \Omega m - 10^{6}\ \Omega m$. They are called semiconductors due to demonstrating both properties of both metals and insulators. By applying or removing an electric field, a semiconductor could become conductive or insulative. This is due to the bandgap or the energy required to move an electron from the ground state (valence band) to a state outside the material (conduction band). Figure 19 shows an example of how the bandgap appears in each type of material.

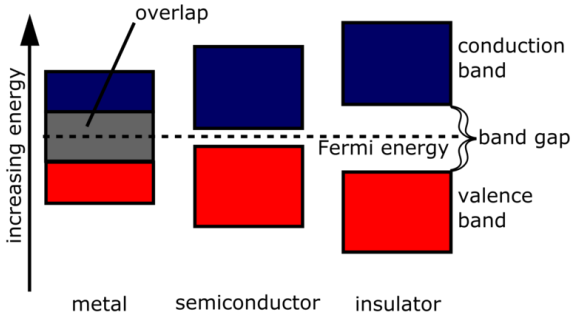


Figure 19. Graphic showing the three types of band diagrams: metal, semiconductor, and insulator. The difference between each material is their bandgap separation which changes how easily electrons can flow through the material. Image from Hanania *et al.* [56].

Semiconductors are classified by the kind of charge carrier used when they are able to conduct. They are referred to as n-type when electron donors are used, and p-type when hole accpetors are used. Semiconductor devices use multiple types of semiconducting materials in their fabrication. The most common application is a diode, which can act as a check valve for electron flow. One example of a diode is an Light Emitting Diode (LED). LEDs are made of certain materials, that which

excited by a charge, will relax and emit a photon. This works by exciting an electron away from its hole in the valence band, which in turn creates photons as the electron returns to its original hole. The emission of photons takes energy away from the relaxing electron, with additional thermal phonon losses. This is where CQDs can be introduced to improve performance: CQDs are analogous to the mechanics of LEDs, but their physics are different in terms of the number of available energy levels and their absorption properties.

The carriers within a semiconductor can be influenced by the temperature of the material. This is due to additional internal energy that the carriers can experience, and their distribution across a semiconducting material is a probabilistic distribution. This comes from quantum mechanics where the Pauli Exclusion principle states that only one half-integer spin particle can exist in any given single quantum state. This probabilistic distribution of carriers is explained by a function called the Fermi-Dirac distribution and is neatly described by Equation 15 [164].

$$f(E) = \frac{1}{1 + \exp \frac{E - E_F}{kT}} \tag{15}$$

Where the variables in Equation 15 are listed below [164]:

- k: Boltzmann constant ($8.617333262145 \times 10^{-5}\ eV \cdot K^{-1}$)
- T: temperature (K)
- E: thermal equilibrium (eV)
- E_F is the Fermi energy (eV)

Equation 15 can be plotted across three temperatures: 150 K, 300 K, and 600 K to demonstrate how temperature affects the carrier distribution, which can be seen

in Figure 20.

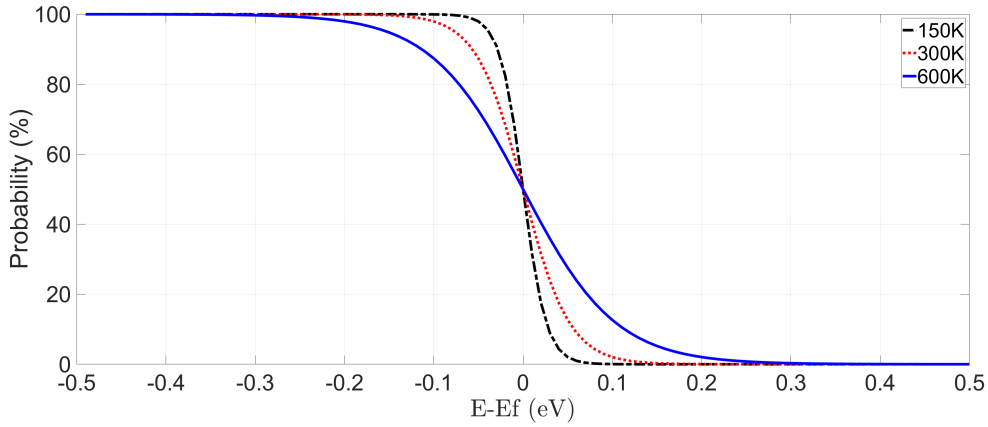


Figure 20. Graphic showing how temperature changes the carrier concentration, with cooler temperatures shifting the carriers towards the valence band.

Connecting back to Figure 20 and the research into CQDs: temperature has an effect on the available energy states that an excited electron can go travel in a CQD. This can change two characteristics of a CQD: its emission wavelength due to a change in bandgap and its temporal PL decay response.

2.13.2 Physical Makeup of Colloidal Quantum Dots

CQDs are usually structured in the manner that is graphically represented in Figure 21.

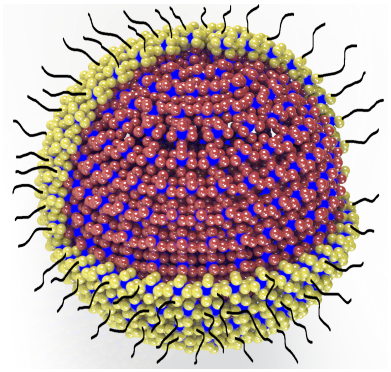


Figure 21. Visual graphic of the structures that make up a CQD. The pink-blue area represents the core, the yellow encompassing the pink-blue area represents the shell, and the black lines represent the ligands.

Every CQD and NPL contains a core, the primary compound, which can function as-is. However, to avoid clumping of the nanocrystals and to help with loading into different media, another structure called ligands are applied across the surface. These are organic polymer chains that help to functionalize the dots. The last structure that Figure 21 shows is called the shell. Due to the inherent defects across the surface of the core of a CQD, a shell compound material (usually ZnS) is applied around the core. This helps to fill in defects, along with reducing trap states, thus greatly increasing QE. An additional observation is that shells usually promote a Stokes shift between the absorption and emission spectra. This also helps increase QE as reabsorption of emitted photons may be greatly mitigated or non-existent. Both CQDs and NPLs can have shells, but in the NPL case they are known as crowns [147].

2.13.3 Discrete Energy State Explanation of CQDs

Energy state transitions are the first step to estimate a CQD's bandgap energy along with the CQD's emission wavelength. First, consider Fermi's Golden Rule (FGR). The decay rate from FGR is as follows [146]:

$$R_{fi}(\omega) = \frac{2\,\pi}{\hbar}\ |F(\omega)|^2|\ |< E_f|\mathcal{V}|E_i >|^2\ \delta(E_f - E_i - \hbar\,\omega) \tag{16}$$

From Equation 16, one can determine the transition rate between eigenstates in terms of its probability per unit time. The matrix element $|< E_f|\mathcal{V}|E_i >|^2$ considers the electric and/or magnetic interaction from a set between the final and initial states. The density of states ($\delta(E_f - E_i - \hbar\,\omega)$) considers how many states are possible for an eigenstate to transition [146]. The most important parameter to get out from FGR is that increasing the Density of States (DOS) will increase the probability of an eigenstate transition. In the next paragraph about DOS, it will be shown that CQDs

have limited energy states available and have limited available eigenstate transitions.

Density of States CQDs make use of quantum confinement. This goes back to Schrödinger's equation and to the derivation of a 3D particle-in-a-box model. If the size of the material is smaller than the de Broglie wavelength of their electron wave function, the material sees an increase in its bandgap. This causes a spatial confinement which can be visualized by using the concept of DOS, which is the number of available electronic states per unit area of energy from Lee's PhD thesis [73]. DOS can be used since CQDs are semiconducting materials. From Pugh-Thomas's PhD thesis, typically a particle size of 100 nm or less would start to exhibit quantum confinement effects [112]. The following dimensions can exhibit quantum confinement:

- 0D quantum dots (confined in three spatial dimensions)
- 1D nanowires(confined in two spatial dimensions)
- 2D quantum wells (confined in one spatial dimension)

In Figure 22, all quantum confinement dimensions are compared against a 3D conventional bulk material's density of states.

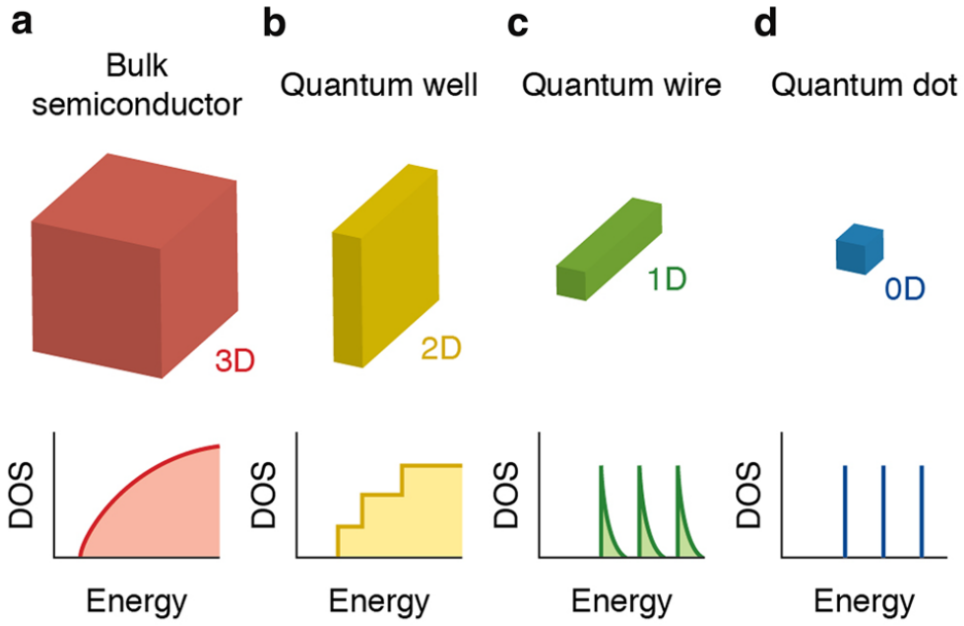


Figure 22. Graphic showing the DOS versus energy for the following dimensional structures: 3D bulk material, 2D quantum well, 1D quantum wire, and 0D quantum dot. Graphic from Rabouw *et al.* [115].

Figure 22 helps to show that in different dimensional states the DOS begins to show discrete energy levels that contain available electron states. This enters the concept of quantum confinement, as lower dimensional states like quantum dots experience discrete energy states. Only certain energy levels will have a transition, which is the reason why CQDs emit at a specific wavelength instead of a broadband spectrum [73] [112]. To explain quantum confinement in mathematical terms, the DOS equations used to develop the plot in Figure 22 can be seen in the list below. The equations use the Effective Mass Approximation (EMA). Effective mass is denoted as m^* and Lee's PhD thesis is used as the reference material for all the equations in the list [73].

- 0D quantum dots DOS

$$DOS_{0D}(E) = \delta(E - E_i) \tag{17}$$

- 1D nanowires DOS

$$DOS_{1D}(E) = \frac{\sqrt{2}\ m^{*\ \frac{1}{2}}(E - E_0)^{-\frac{1}{2}}}{\pi\ \hbar} \tag{18}$$

$E > E_i$ for each sub-band

- 2D quantum wells DOS

$$DOS_{2D}(E) = \frac{m^*}{\pi\ \hbar^2} \tag{19}$$

$E > E_i$ for each sub-band

- 3D bulk material DOS

$$DOS_{3D}(E) = \frac{\sqrt{2}\ m^{*\ \frac{3}{2}}(E - E_0)^{\frac{1}{2}}}{\pi^2\ \hbar^3} \tag{20}$$

Notice from the above equations how the zero dimensional case for CQDs can be thought of mathematically as a series of delta functions. Scholars and researchers tend to call CQDs as artificial atoms due to having discrete energies like the energy shell bands around an atom. However, this is a generalization to help others understand how CQDs work since defects can occur in the formation of the CQDs, thus it is unlikely any two CQDs will exhibit the exact same properties [73].

2.13.4 CQD Bandgap Model

Now that CQD theory has been discussed, bandgap diagrams which help to visualize energy transitions within CQDs will be explained. Unlike the standard bulk semiconductor bandgap as seen previously in Figure 19, CQDs have discrete energy levels near the band edges. They are also confined in three dimensions and the width of confinement (CQD diameter) will determine how large the bandgap between the

Highest Occupied Molecular Orbital (HOMO) and Lowest Unoccupied Molecular Orbital (LUMO) levels. The HOMO is the highest discrete energy state above the valence band edge and the LUMO is the lowest discrete energy state below the conduction band edge. In addition, an excited electron promoted from the valence band to the conduction band will leave a hole and form an exciton which is an electron-hole pair that is kept together by Coulomb interaction [115] [66]. This is graphically represented in Figure 23.

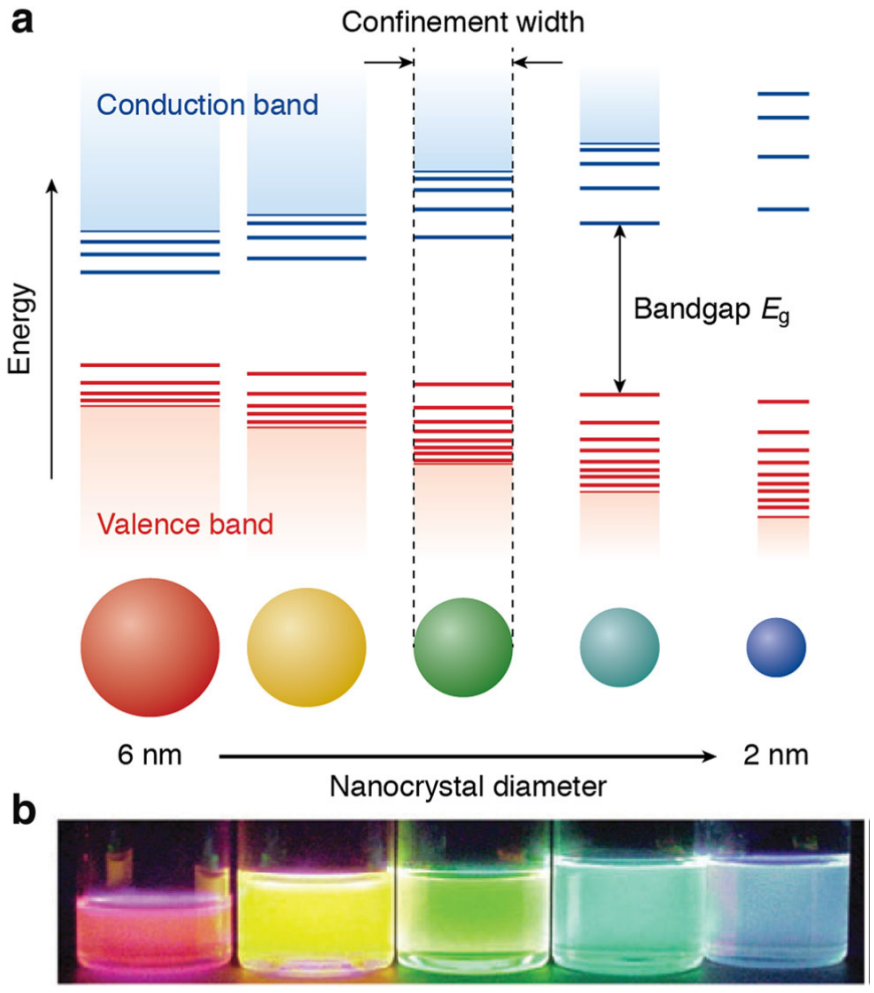


Figure 23. CQD bandgap model with discrete energy levels near the band edges. HOMO band edge is the highest discrete energy state over the valence band edge and LUMO is the lowest discrete energy state under the conduction band edge. CQD emission color for each of the bandgaps in part A) can be seen in part B). Graphic from Rabouw *et al.* [115].

Photon emission of a CQD occurs when an exciton relaxes back to its ground state in the valence band. How fast the emission decays from a CQD is dependent on the path length of the exciton back to its ground state. There could be additional trap states (additional energy states between the valence band and conduction band levels) from defects in the CQD that makes the exciton take a longer path.

When looking at the overall CQD system with both a core and a shell, the bandgap diagram changes. The detailed core bandgap would appear as seen previously in Figure 23. There are two types of shells commonly seen in literature: Type-I and Type-II. Type-I bandgap engineered CQDs can be represented by Figure 24 [59] [106].

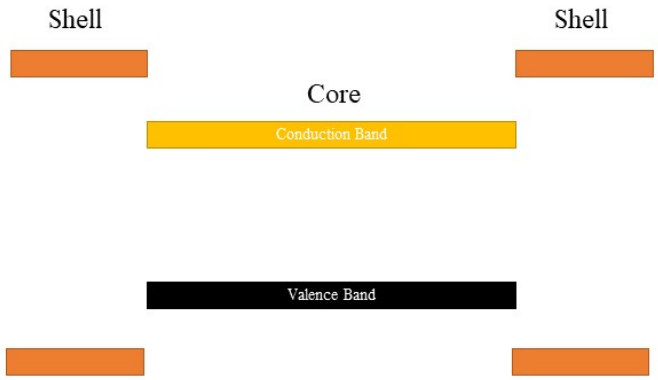


Figure 24. Type-I CQD bands, where the shell bandgap surrounds the core band.

Type-II bandgap engineered CQDs can be represented by Figure 25 [59] [106].

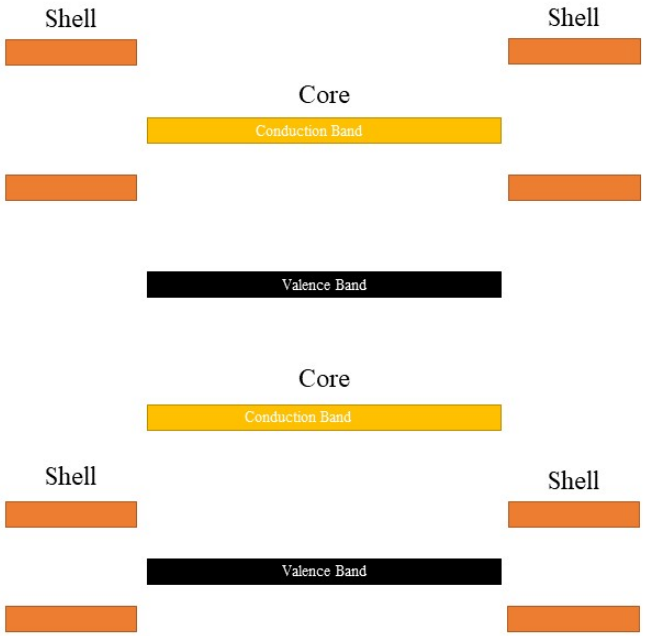


Figure 25. Type-II CQD bands, where the core bandgap is either under or over the shell bandgap.

One can engineer a CQD using band offset physics to either help speed up or slow down exciton recombination. A paper written by Thuy *et al.* showed a few differences between Type-I and Type-II CQDs. Type-I CQDs decayed an order of magnitude faster than Type-II CQDs [140].

Since the CQDs in this thesis are not used in isolation, an additional diagram known as Jablonski is required to explain their behavior. CQDs that are near polymer materials could transfer their energy to an adjacent polymer molecule or the polymer molecule itself could absorb an incident wavelength of light and fluoresce. In addition, the ligands passivating the CQD could be fluorescent as well. Unlike bulk semiconductors and CQDs, polymer materials emit photons through molecular interaction. This leads to the use of the Jablonski diagram to describe an organic PL system. An analogous diagram to Jablonski would be the nuclear shell model and its explanation is referenced in Appendix F. The Jablonski diagram as seen in Figure 26

visualizes how an organic PL system transfers absorbed energy.

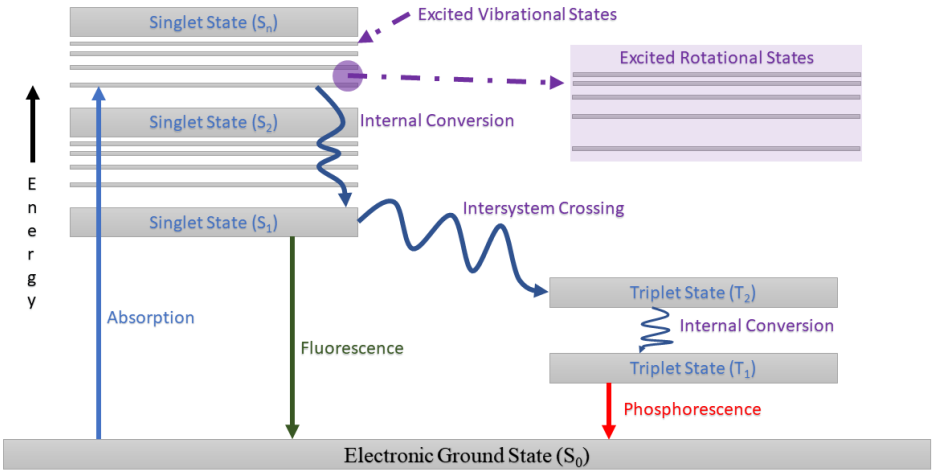


Figure 26. A descriptive figure detailing the different mechanisms shown in a Jablonski diagram. Image modified from Chasteen [35].

There are two radiative emission properties shown from a Jablonski diagram: fluorescence and phosphorescence. From Figure 26 it can be seen that fluorescence is at a higher energy level than phosphorescence, which is on purpose. Fluorescence is a faster radiative process, which occurs at lower wavelengths, requiring more energy. Phosphorescence is a slower radiative process, which occurs at higher wavelengths, thus requiring less energy. In addition, there are three non-radiative processes: Internal Conversion (IC), Inter-System Crossing (ISC), and vibrational relaxation. Through IC, energy transitions occur between energy levels with the same spin state. It is possible for a vibrational energy to have its wave function overlap a lower energy level, and thus transition to the lower energy level. In ISC, energy transitions between different spin states. With vibrational relaxation, energy is transferred into kinetic energy either within the same molecule or to a neighboring molecule [35] [87].

In Figure 26 the energy states are not as detailed as in Figure 133. This is because as the energy level increases, the energy bands become closer and closer which can

eventually be approximated with classical mechanics. Thus, usually only the most important energy levels/vibrational states are used. Each column represents a different spin state, with the first column representing singlet states and the second column representing triplet states.

A useful table of time scale values from energy transitions in the Jablonski diagram can be seen in Table 3 using data from McEwen [87].

Transition	Time Scale	Radiative Process?
Internal Conversion	$10^{-14}s$ to $10^{-11}s$	No
Vibrational Relaxation	$10^{-14}s$ to $10^{-11}s$	No
Absorption	$10^{-15}s$	Yes
Phosphorescence	$10^{-4}s$ to $10^{-1}s$	Yes
Intersystem Crossing	$10^{-8}s$ to $10^{-3}s$	No
Fluorescence	$10^{-9}s$ to $10^{-7}s$	Yes

Table 3. A table of time scale values for each process shown in the Jablonski diagram. The faster the process, the more likely it is to occur. It is of note that these time scales are not indicative of all PL systems since phosphorescence is defined by the ISC transfer of phonon energy to a triplet state and then emitting a photon. Usually this process is slower because of the additional transfers that must occur, but it does not have to be. Data for the table is from McEwen [87].

When designing fast CQD scintillators that make use of organic molecules, the phosphorescent mechanism needs to be suppressed as much as possible to lower the overall PL decay time.

Wannier-Mott and Frenkel Excitons CQDs work by using excitons, which are electron-hole pairs with a Coulomb potential. There are additional energy states that occur right under the conduction band, and the spacing between these levels to the ground state is termed the binding energy of the exciton. Having energy states under the conduction band is important as the energy threshold for

photon absorption is lowered.

In literature, there are two well established approximations to describe the binding energy of excitons [84]. The first description, the Frenkel exciton, relates to tightly bound excitons within the atom (materials with a small dielectric constant), thus their binding energies are in the range of 0.1 eV-1 eV. Frenkel excitons are usually found in alkali halide crystals [50]. These crystals are compounds that are the most ionic of all compounds and are made up of groups I and VII elements. An example of one of the alkali halides is LiCl [21]. However, since Frenkel excitons are not entirely useful to describe the excitons found in semiconductors, the focus here is on the Wannier-Mott exciton. This exciton can model weakly bound quasi-particles that can have a greater separation than the semiconductor lattice and closely approximates semiconducting materials [84].

The derivation of the Wannier-Mott exciton is first started by approximating the exciton as a single isometric electron-hole pair. Due to being particles in a semiconductor, they have a reduced effective mass. The reduced effective mass equation can be seen in Equation 21.

$$\mu = \frac{m_e \; m_h}{m_e + m_h} \tag{21}$$

Where m_e in units of $\frac{m_e}{m_0}$ and m_h in units of $\frac{m_h}{m_0}$ are the effective electron and hole masses respectively [154]. The rest mass of an electron m_0 is $9.11 \times 10^{-31}\ kg$. Next, the Coulomb potential is generated by the exciton electron-hole pair. This potential is described in Equation 22.

$$V(a) = -\frac{e^2}{\kappa \; a} \tag{22}$$

Where e is the charge of an electron ($1.602 \times 10^{-19}\ C$), a is the distance of charge separation (m), and κ is the dielectric constant of the semiconductor. Now that both Equations 21 and 22 are made, it is possible to make use of the hydrogen atom's model to derive the Wannier-Mott exciton, using the Time-Independent Schrödinger Equation (TISE), $\hat{H}\ \phi = E\ \phi$ can be used [128]. Expanding out the TISE in its general form, Equation 23 is made.

$$-\frac{\hbar^2}{2\ m}\ ^2\ \phi(r) + V(r)\ \phi(r) = E\ \phi(r) \tag{23}$$

From here, the Hamiltonian can be derived by simplifying out the $\phi(r)$ term. This simplification of Equation 23 can be seen in Equation 24.

$$\hat{H} = -\frac{\hbar^2}{2\ m}\ ^2 + V(r) \tag{24}$$

From Equation 24, this is where the Wannier-Mott exciton deviates away from the hydrogen model. The reduced effective mass μ can be put in terms of m and substituted into Equation 22 for the potential $V(r)$. These substitutions lead to Equation 25.

$$H = -\frac{\hbar^2}{2\ \mu}\ ^2_{e,h} - V(a) \tag{25}$$

From the Hamiltonian seen in Equation 25, multiple expansions can be made for varying dimensionality cases to solve for the system's binding energy [84]. Literature calls the energy and radius associated with the Wannier-Mott exciton as the exciton Rydberg energy and the exciton Bohr radius respectively [49].

Effective Mass Approximation Model By far one of the most influential models in the development of CQDs is the EMA model. Initially formulated by Brus

in 1986, the model comes from the Hamiltonian seen in Equation 26 [22].

$$\hat{H} = \frac{-\hbar^2}{2\ m_h}\nabla_e^2 - \frac{\hbar^2}{2\ m_h^*}\nabla_h^2 - \frac{e^2}{\epsilon_0\ |r_e - r_h\ |} \tag{26}$$

From Equation 26, the EMA was made. However, there were varying models in literature. One of the newer formulations of the Brus Equation was created by Vatankhah *et al.* Their version of the model also included polarization terms that bring in the effects of Coulombic interaction produced between both the nano particle surfaces and the internal materials. The model can be seen in Equation 27 [152].

$$E = E_{g(bulk)} + \frac{\hbar^2\ \pi^2}{2\ \mu\ R} - 1.786\ \frac{e^2}{\epsilon\ R} - 0.248\ E_{gr}^* \tag{27}$$

Where μ is $(\frac{1}{m_e^*} + \frac{1}{m_h^*})$, m_e^* is the effective mass of the electron, m_h^* is the effective mass of the hole, R is the radius of the quantum dot, μ is the reduced mass, ϵ is the permittivity of the vacuum, and E_{gr}^* is the effective Rydberg energy [152].

In Vatankhah *et al.'s* experiments, they found that the EMA falls short when the diameter of their quantum dot becomes smaller than 2.5 nm. To account for this, they then made use of the Density Functional Theory for nano particles which works well for the region of quantum dots under 2.5 nm. To unite the two cases together, the authors created the Variation of Effective Mass theory. This method makes use of Equation 28 [152].

$$\frac{\mu}{m_e} = 0.21 + 2.39\ \exp -\frac{R}{5.59} \tag{28}$$

NPLs and Giant Oscillator Strength Transition Throughout this section, the quantum mechanical models have been for spherical CQDs. However, there is another concept that is pertinent for NPLs: Giant Oscillator Strength Transition

(GOST). Unlike spherical CQDs, NPLs have a reduction in the number of accessible states for Auger transitions. Auger is an unwanted effect when wanting to achieve a higher QE for CQDs. As an exciton relaxes, it may excite another exciton on its way back down to its ground state instead of the electron-hole pair recombining. This is known as Auger recombination and the effect can be a chain of returning excitations, which causes non-radiative energy losses, thus lowering the overall QE of the system.

The properties of NPLs are reminiscent of quantum wells. They also have a collective phasing of dipoles over many unit cells [148]. More specifically, GOST is when the radius of the bound exciton is far greater than the excitation radius. Excitons in GOST are weakly bound to defects in crystals and their wave function spans across a large area around the defects. The excitons' oscillations of the electronic polarization are coherent across this entire region of influence [118]. It is known that NPLs are thickness-dependent for both their absorption and emission spectra and can be described by the eight-band Pidgeon-Brown model [61]. An example of the eight-band model, which is formally known as the Kane and Pidgeon-Brown eight-band model can be seen in Figure 27.

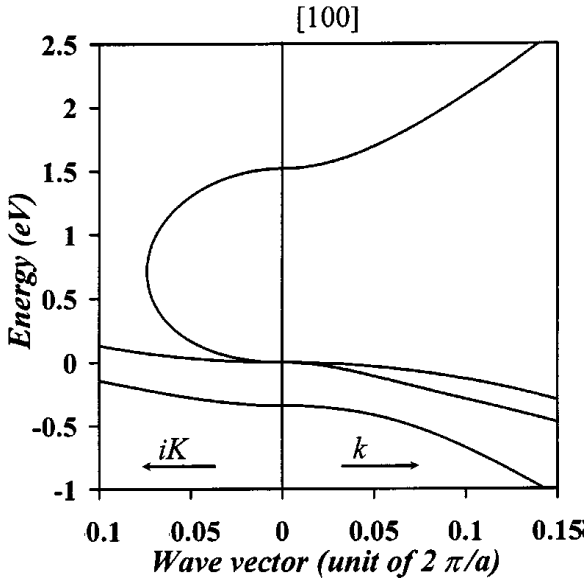


Figure 27. An example of the Kane and Pidgeon-Brown eight-band model plot. This figure shows both the band-gap energy and the wave vectors which can be used to determine to the emission and absorption spectra of a NPL. Image from Richard *et al.* [119].

The DOS for NPLs resembles the 2D quantum wells previously discussed, where the DOS resembles a step function. Since the dielectric constant of the media surrounding the NPLs is small, it modifies the strength of the electron-hole Coulomb coupling. This means the exciton binding energy is increasing in these 2D structures. The reason NPLs can fluoresce quickly (fast decay) is because the tangential component of the photon electric field shows no changes when it goes through the 2D structure [61].

Returning to why NPLs have GOST, the concept comes from the exciton center of mass coherent motion. A PhD thesis by Siarkos goes over the derivation of an analytical formula for the ground state center-of-mass and the important takeaway is that the ground state exciton is nearly identical in shape to the ground state of a 2D exciton [132]. Relating this back to GOST, the ground state exciton is what enhances the absorption cross-section of a NPL which in turn significantly reduces the exciton's

radiative decay time. A research group demonstrated a signature of GOST in a NPL by showing that decreasing the temperature resulted in both a faster PL decay and an increase in emission intensity [61]. An additional research group found GOST signatures in their NPLs which demonstrated 1 ps exciton lifetime and theoretically, since the exciton lifetime is a function of the surface area of the NPL, a longer NPL could achieve 100 fs exciton lifetime [94].

2.13.5 Alloying CQDs

For those new to the field, hearing the word alloy for CQDs brings upon imagery of varying metals. In this case, alloying refers to smoothing out the energy states between the core and the shell materials. The alloying method has been well studied for its ability to increase QE of CQDs [20] [129]. One of the main sources of low QE in CQDs has been with Auger recombination. Alloying reduces the energy level step size between the core and shell which better transports excitons. This in turn lowers the rate of Auger recombination [20]. The alloying concept can be visualized in Figure 28.

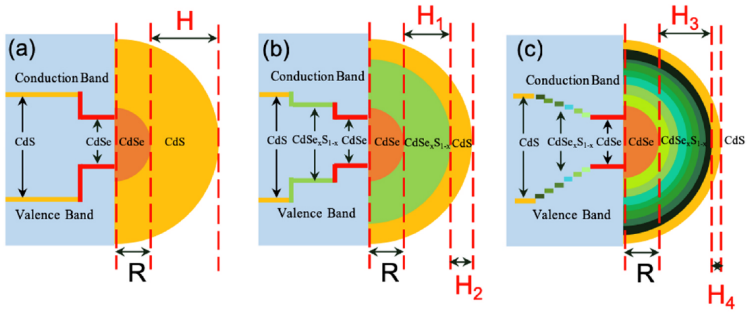


Figure 28. Visual graphic for seeing the effects alloying has on CQD bandgaps. From figures A) to C), additional alloying is applied. As more alloying is applied, the difference in energy levels for an exciton to go down from becomes smaller and smaller, which in turn reduces trap states and Auger recombination. For additional information regarding these specific alloyed CQDs, read Selopal *et al.'s* paper. Graphic from Selopal *et al.* [129].

Selopal *et al.* wrote that in alloyed CQDs, both electron and holes can leak into

the CQD's shell. This in turn lowers the decay lifetime of these CQDs since the distance between both electrons and holes are shortened. The greater the electron and hole overlap, the lower the decay lifetime. In addition, the relative absorption of an incident photon greatly increases with alloying. Also, the CQD's PL emission can be tuned to be a different wavelength by changing the alloying ratio [129]. With alloying's ability to control Auger recombination rates and emission wavelength, it has also been termed interface engineering [20].

2.13.6 Förster Resonance Energy Transfer

A possible CQD to CQD interaction within an overall CQD scintillating system is FRET. Possible signs that FRET is occurring would be observing a secondary red shifted peak in the PL spectra and that this red shifted peak fluoresces later in time than the primary PL emission peak. FRET is a process where two compounds/ molecules (with one being the donor and the other the acceptor transfer energy in a non-radiative way). The donor material is excited by incident energy, but instead of the excited energy within the donor radiatively relaxing within itself, it could transfer over as a phonon to an acceptor material. This phonon between the donor and the acceptor is also known as a virtual photon. The virtual photon is non-observable and the term is used to help visualize the instantaneous transfer of energy from one fluorophore to another [16]. FRET is a highly distance dependent process and a point dipole-dipole approximation can be seen in Equation 29 [127].

$$E = \frac{1}{1 + \frac{r}{R_0}^6} \tag{29}$$

The variables within Equation 29 are explained in the list below:

- r: separation distance between acceptor and donor (m)

- R_0: The value at which energy transfer efficiency is 50% and is known as the Förster distance of the donor and acceptor pair (m)

However, a more accurate model can be seen in Equation 30 [127].

$$E = \frac{k_{ET}}{k_f + k_{ET} + \sum k_i} \tag{30}$$

Where the variables in Equation 30 are defined in the list below as:

- k_{ET}: rate constant of FRET energy transfer
- k_f: radioactive decay rate constant (for example fluorescence)
- k_i: any additional non-radiative relaxation rate constants (for example inter-system crossing, etc.)

Where rate constant for all three terms in Equation 30 is defined as the probability per unit time [104]. From Equation 29 and Equation 30, it is easier to visualize how FRET operates. If an acceptor is close enough to a donor, a phonon transfer from donor to acceptor creates what is known as resonance. As the donor de-excites from a higher energy state to the lowest singlet state S_1, it spontaneously transfers energy to the acceptor, all while the remaining energy in the donor de-excites further to the ground state (S_0). While the donor de-excites, the acceptor becomes excited, hence why the term resonance is used here. It is an important note that the donor's fluorescence spectra needs to overlap with the absorption spectra of the acceptor [60]. A visual graphic in Figure 29 helps to illustrate using a fluorescence spectra how FRET works.

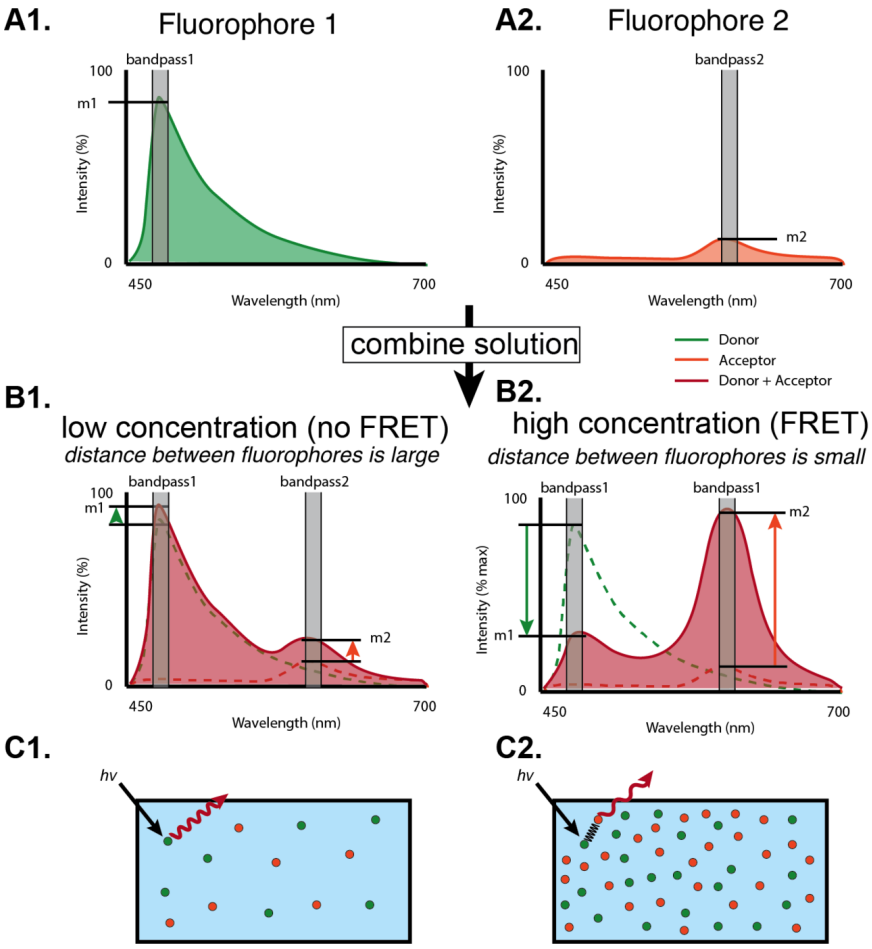


Figure 29. This graphic explains FRET concepts. Both A1 and A2 represent the donor and acceptor fluorophores respectively with different wavelengths. B1 is when the concentration of both fluorophores is small, thus a low FRET efficiency due to a large distance between fluorophores. B2 is when the the concentration of both fluorophores is high, thus a high FRET efficiency. C1 shows the emission of the donor able to escape the medium without being absorbed by an acceptor due to a low FRET efficiency. C2 shows the donor pass off a phonon to a nearby acceptor due to being in close proximity to the donor and the acceptor emits a photon out of the media. Figure from Neveu [95].

To go into more detail, the Förster distance R_0 is determined by a few parameters as seen in Equation 31 [40].

$$R_0^6 = \frac{9\ log(10)\ \kappa^2\ Q_D\ J}{128\ \pi^5\ N_A\ n^4} \tag{31}$$

Where the variables in Equation 31 are defined in the list below as:

- Q_D: Fluorescence quantum yield of the donor in absence of the acceptor
- κ: dipole orientation factor
- n: refractive index of the medium
- N_A: Avogadro's number ($6.022 \times 10^{23} \frac{atoms}{mol}$)
- J: spectral overlap integral

The spectral overlap J is defined in Equation 32.

$$J = \int \overline{f_D}\ (\lambda)\ \epsilon_A\ (\lambda)\ \lambda^4\ d\ \lambda \tag{32}$$

Where the variables in Equation 32 are defined in the list below as:

- f_D: donor emission spectrum
- $\overline{f_D}\ (\lambda)$: donor emission spectrum normalized to an area of one
- ϵ_A: acceptor molar extinction coefficient (obtained from an absorption spectrum [43])

Finally, the orientation factor κ which can be seen in Equation 33 [43].

$$\kappa = \hat{\mu_A}\ \cdot\ \hat{\mu_D} - 3\ (\hat{\mu_D}\ \cdot\ \hat{R})\ (\hat{\mu_A}\ \cdot\ \hat{R}) \tag{33}$$

Where the variables in Equation 33 are defined in the list below as:

- $\hat{\mu_i}$: normalized transition dipole moment of the respective fluorophore
- $\hat{R}$: normalized inter-fluorophore displacement

κ is often assumed as $\frac{2}{3}$ for FRET calculations [43].

2.13.7 Surface Applications of Ligands

Ligands are organic polymer chains that passivate CQDs, in effect functionalizing them to be useful in a variety of media. A useful graphic can be seen in Figure 30 that shows a wide variety (not all) of different ligand capping layers for quantum dots in different applications [63] [14].

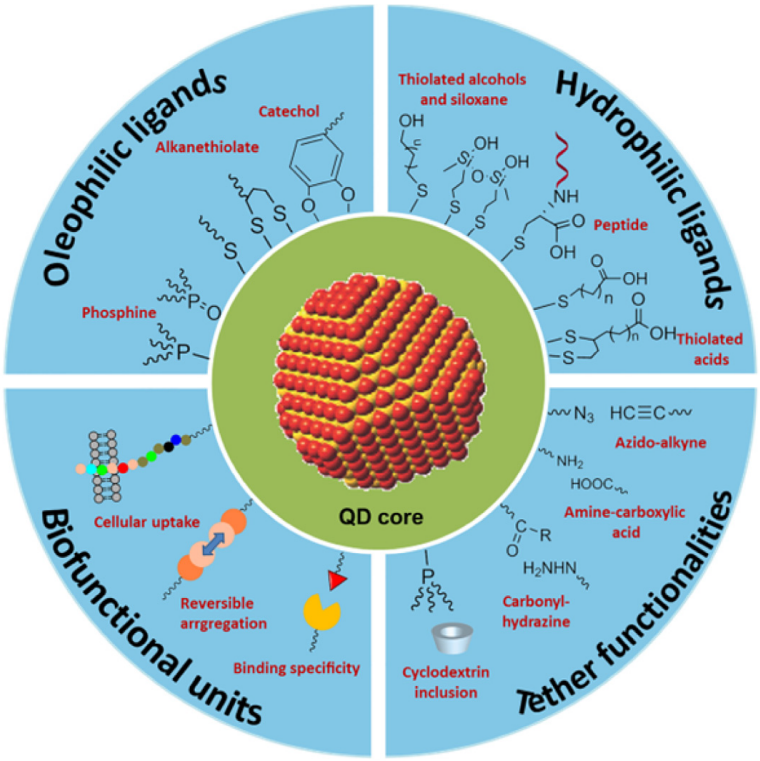


Figure 30. Summary that highlights the different chemical structures of four types of ligand capping layers. Image from Zhou *et al.* [63].

The ligands from Figure 30 are only a subset of other ligands available since these are more for medical applications; however, it goes over a few terms that will be important to understand. In terms of definitions, hydrophilic ligands are useful when looking to absorb a CQD in water-based applications, while Oleophilic ligands are useful when looking to absorb a CQD in an oil-based application. The last two groups from Figure 30 go over ligands that can be useful for targeting cancer cells: for example for the biofunctional units group and tether functionality by using selective

reactions or interactions [63]. The types of ligands within this thesis are in the hydrophilic ligand group.

It is important to note that optical properties are affected when using different chain lengths of ligands. One research group showed how the QE of CQDs increased in relation to the length of the polymer chain. They tested four carbon length chains to 18 carbon length chains capping around InPZnS/ZnS CQDs. They additionally found that shorter chain length ligands such as Hexanoic acid have an increased Stokes shift compared to longer length ligands such as Oleic acid. Even more important for this thesis is that longer length ligands have a faster decay response compared to shorter length ligands. The authors extrapolated from the data that the longer length ligands help suppress non-radiative channels. This in turn increases the QE, where shorter length ligands were giving a QE of $\approx$ 49% while longer length ligands were giving $\approx$ 70% [14].

For the CQDs being used in this thesis, there are three types of ligands being used that are provided by the supplier, NN-Labs.

- Octadecylamine (structural model in Figure 31)

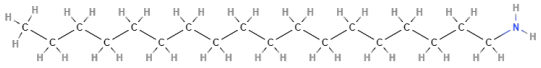


Figure 31. Organic polymer chain. Image information from PubChem [109] and rendered in MolView v2.4 [24].

- Oleic Acid (structural model in Figure 32)

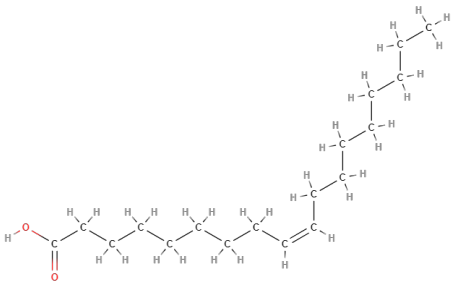


Figure 32. Organic polymer chain. Image from PubChem [110] and rendered in MolView v2.4 [24].

- Oleylamine (structural model in Figure 33)

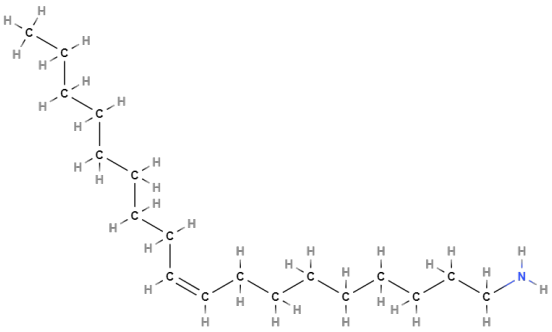


Figure 33. Organic polymer chain. Image from PubChem [111] and rendered in MolView v2.4 [24].

All three ligands above are 18 carbons long. Long carbon chains will greatly mitigate FRET as mentioned through an email correspondence with Dr. Andrew Smith from University of Illinois at Urbana-Champaign. This is because of the $\frac{1}{R^6}$ efficiency relationship for FRET to occur and it has been seen by Smith that about six carbons is the threshold to greatly reduce its effect. 3D models of each ligand chain used can be seen in Appendix T.

2.13.8 Quantum Dot Blinking

An important CQD defect affecting the PL stability of CQD systems is blinking. This defect can especially be seen in continuously excited applications. Over time the CQDs can fluoresce on and off due to surface trap defects. A visual example can be seen in Figure 34 [55].

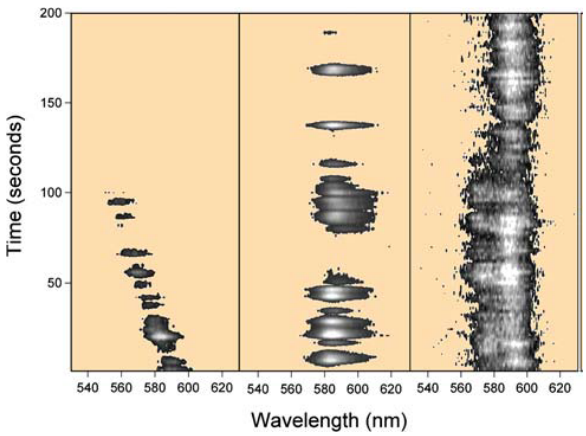


Figure 34. This is a time resolved fluorescence emission spectra plot showing three cases: DOPO-Br on the left most side, ZnS-capped in the middle, and Oligo-(Phenylene Vinylene) (OPV) covered CdSe quantum dots on the right most side. The left most image shows photodegradation which blue shifts, the middle image shows quantum dot blinking, and the right most image shows the suppression of quantum dot blinking. Image from Hammer *et al.* [55].

Three case are demonstrated in Figure 34, where the first set on the left most side shows photodegradation over time. This blue shifting makes sense as the degradation of a quantum dot causes their diameter to become smaller, thus becoming more blue. This left most set also shows signs of blinking. The middle set shows no degradation, but also experiences blinking. The right most set shows the mitigation of blinking due to a coating of OPV ligands that are good electron donors which can contribute charge whenever an exciton becomes trapped [55].

2.13.9 Charge-Transfer Complex

In certain circumstances, it is possible for an exciton to transfer charge to a nearby polymer chain [55]. This is different compared to FRET which requires a spectral overlap between two fluorophores. However, concepts of FRET are shared such as the proximity of molecules to enhance energy transfer. If a ligand is electron rich, it could transfer its charge from the molecular orbitals to empty or partially filled metal d-orbitals. This is known as Ligand-to-Metal Charge-Transfer (LMCT). On the other hand, it is possible to have an electron rich metal with ligands that have low empty orbitals such as CO and CN^-. Charge from the metal to the ligand can then occur, which is known as Metal-to-Ligand Charge-Transfer (MLCT) [121].

2.13.10 Crystal Structures

There are eight different CQDs under investigation in this thesis. An open-sourced crystal structure software called Visualization for Electron and Structural Analysis (VESTA) is used to create 3D models of each type of crystal structure [91]. This section will show a single unit cell for each crystal structure.

Crystal structure data is found by using Inorganic Crystal Structure Database (ICSD) created by FIZ Karlsruhe which compiles journal article data of each crystal structure. These journal articles are also cited for each structure presented in this section. Table 4 is a high level overview of the crystal structure parameters used for each material. Additional crystal structure details can be read in the references listed for each material.

Compound	**Space Group**	**a**	**b**	c	α	β	γ	Reference
CdSe	P 63 m c	4.3	4.3	7.033	90	90	120	[54]
PbS	F m -3 m	5.94	5.94	5.94	90	90	90	[116]
InP	F m -3 m	5.94	5.94	5.94	90	90	90	[79]
ZnS	P 63 m c	3.82	3.82	6.261	90	90	120	[68]
CdS	P 63 m c	4.15	4.15	6.737	90	90	120	[150]
CuInS	I -4 2 d	5.52167	5.52167	11.1411	90	90	90	[159]
PbSe	F m -3 m	6.128	6.128	6.128	90	90	90	[97]

Table 4. Overview of crystal structure parameters used to generate VESTA models.

CdSe The synthesis process used in the creation of the CdSe cores in the CQDs used in this thesis is not known, thus the crystal structure of the core is unknown. A research group observed CdSe CQDs displaying both wurzite and zinc blende structures. Fernandez-Delgado *et al.* stated that it is common to have polymorphism in CdSe nanocrystals exhibiting both structures. It is beneficial to have the core be as zinc blende as possible since it exhibits higher quantum yield [48]. The CdSe crystal structure shown in Figure 35 has its crystal data referenced from Golovei *et al.* [54].

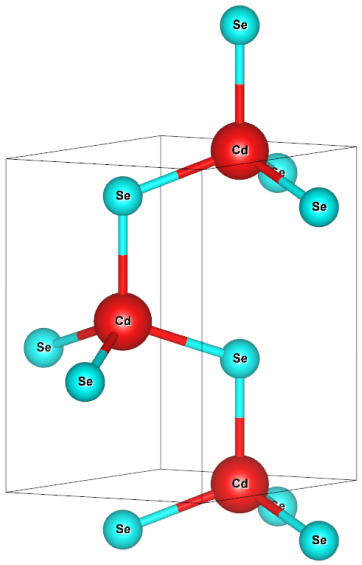


Figure 35. 3D crystal structure model of CdSe. Figure created in VESTA [91].

Figure 35 shows an example of what the crystal structures look like in VESTA. The VESTA crystal models and explanations behind them for the remaining materials in Table 4 are in Appendix G.

2.13.11 Strain Effects on CQDs

CQDs change their wavelength when subjected to both tensile and compressive strain The change of wavelength due to strain is because the interatomic spacing between the atoms in a CQD determines the relative energy of the electrons [26]. When electron energy changes, the effective bandgap in the CQD changes. This effect is illustrated in Figure 36 [12].

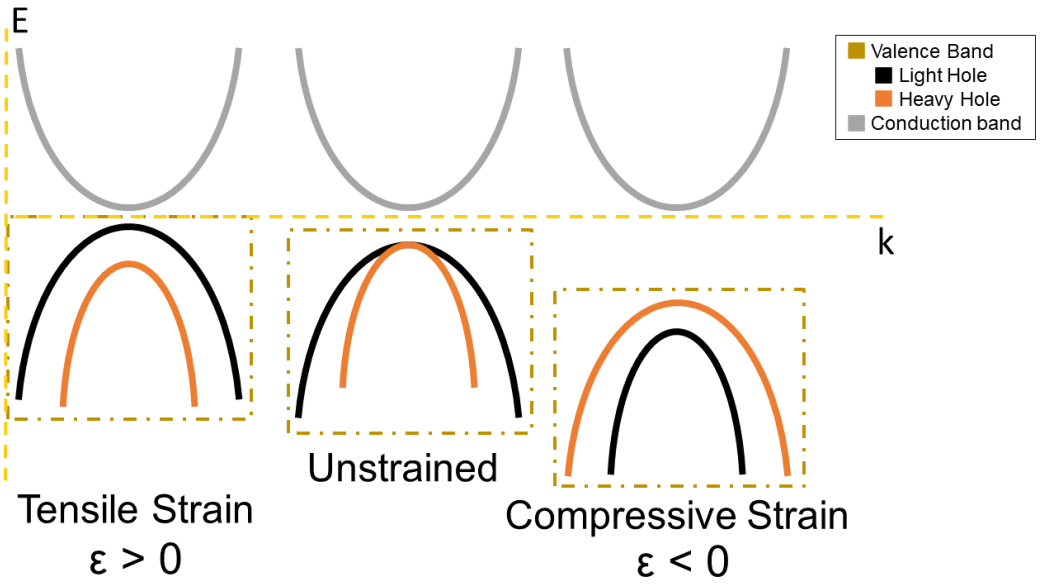


Figure 36. Direct band-edges changing under tensile or compressive strain. Image modified from NNSE 618 lecture slide at University of Albany [12].

From Figure 36, the heavy holes and light holes are changing in the semiconducting material from strain. The full details concerning the mathematical theory can be read in Yu's *Fundamentals of Semiconductors* textbook [162].

2.14 Gamma Exposure Degradation

A concern when using CQDs as an x-ray scintillator is the possibility of damage from gamma irradiation. A useful primer about this effect can be seen in Withers *et al.* which states that a scintillator must have a radiation hardness of at least 250 Mrad absorbed gamma dose to be useful in aerospace and terrestrial applications. In their study, they found that CdSe/ZnS CQDs lose 50% of their light output intensity after $\approx$ 11.5 krad exposure [155]. However, there is a redeeming quality for at least CdSe/ZnS CQDs. In another study by Normand *et al.*, NaI:Tl scintillating crystals quickly lose their luminescent emission output after 500 rad dose from a ^{60}Co source [98]. In the CQDs used by Withers *et al.*, they observed a drop in

QE from 23.4% before 120 krad gamma irradiation to 0.2% after 120 krad gamma irradiation. However, according to their collected data, shown in Figure 37, a fast temporal response could still be detected by the CQDs even after the 120 krad gamma irradiation. Recall that NaI:Tl starts to have scintillating issues after a 500 rad dose. From Wither's *et al.'s* team, about half of the original PL emission intensity from the CQDs occurs at 10 krad [155]. While not ideal for space applications due to eventually needing replacement due to gamma irradiation, CdSe/ZnS CQDs are certainly viable for ground-based laboratory work.

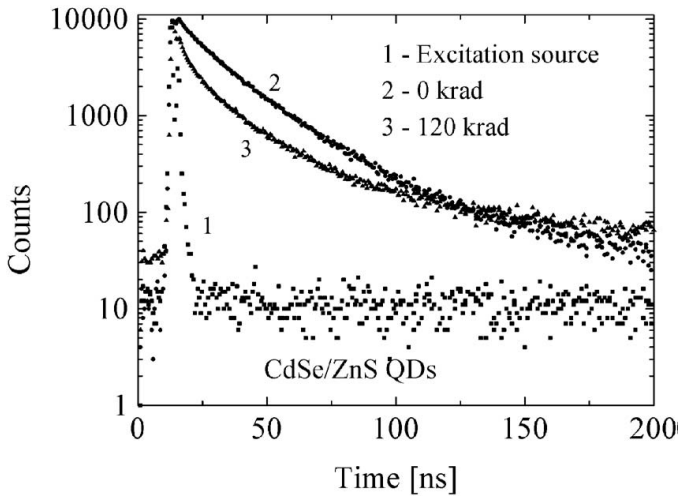


Figure 37. PL lifetime degradation of gamma irradiation. The research group used CdSe/ZnS CQDs for these tests. Image from Withers *et al.* [155].

A recent paper from Gaur *et al.* explained the mechanism behind gamma irradiation damage of CQDs. They showed that photoxidation of the thiol ligands caused surface trap states along with permanent damage in the crystal lattice structure led to quenching the PL. They demonstrated that a thiol-rich surface treatment nearly recovered all of the lost PL after x-ray irradiation. Although, under higher gamma irradiation, only a partial PL recovery occurred. In addition, they have shown that irradiated CQDs exhibit a slight blue shift in their output emission wavelength [51]. Their research is promising for CQD scintillators under x-ray irradiation since it is

possible to repair their PL emission intensity. The blue shifting when using the S20 photocathode is an advantage as it will increase QE due to the emission wavelength better matching the optimal wavelength of the S20 photocathode. The main concern would be the calibration of these CQDs. If x-ray irradiation damage is observed with all the other CQD compounds, then energy resolution measurements would be difficult. The objective of this thesis is to focus on temporal resolution, thus this is not a concern at the moment.

2.15 CQD Scintillator Fabrication

Since this thesis uses commercially supplied CQDs, synthesis details will not be discussed. It is beneficial to understand the formation of CQDs to understand what occurs in the PL spectra when fabrication defects happen. While observing the CQDs' PL emission, seeing unexpected Full Width at Half Maximum (FWHM) and blue/red shifting could be a sign of defects in the fabrication process.

There are two different synthetization techniques: epitaxial and colloidal. Epitaxial uses Molecular Beam Epitaxy (MBE) to directly grow quantum dots onto a substrate [39]. Colloidal typically uses hot-injection to grow the CQDs in a three-neck flask. This is the most likely method used to create the CQDs being used in this thesis as it is a well characterized process [133]. A visual example of how the hot-injection method worked to create CQDs can be seen in Figure 38.

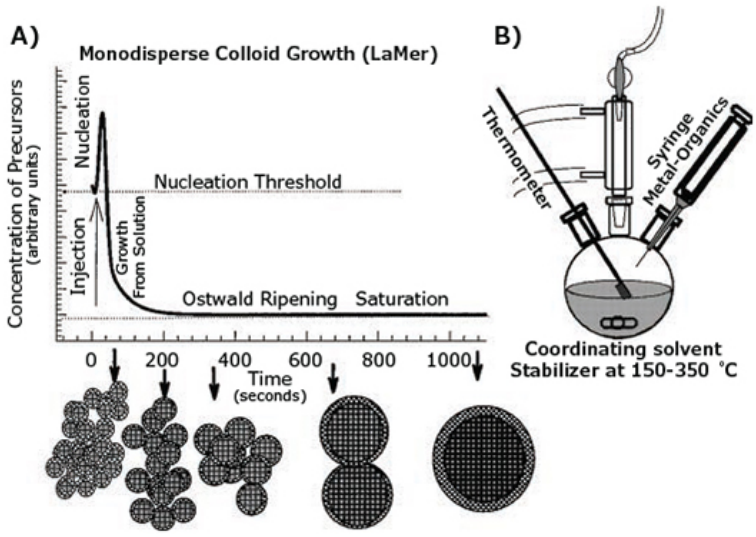


Figure 38. "A) Schematic of the nucleation and growth stage for the preparation of monodisperse nanocrystals in the framework of the LaMer model. B) Representation of the simple synthetic apparatus employed to prepare monodisperse nanocrystals." Referenced from Sinatra *et al.* [133].

From Mahajan *et al.*, the summarized process for synthesizing CdSe CQDs is [82]:

1. Disperse in a liquid Trioctylphosphine (TOPO) organic solution (the ligands to attach to the CQDs)
2. The three-neck flask is placed on top of a stirrer hot plate
3. A temperature controller is placed in one of the necks of the flask
4. Heat up the TOPO solution to 300 $^{\circ}C$
5. Inject a precursor through another neck in the flask consisting of $CdMe_2$ and Se within Trioctyl Phosphine (TOP)
   (a) Formation of CdSe nuclei is instantaneous
6. Drop temperature to about 170 $^{\circ}C$ to prevent new nuclei formation
7. Slowly increase temperature towards and below 300 $^{\circ}C$ to grow present nuclei

8. Separate out the CQDs by using a non-solvent and then dissolve into an organic solvent to keep the CQDs suspended

With the fast PL response time of CQDs comes the challenges in applying them to a camera application. A group at NASA tried to grow CQD crystals inside a formed cavity, however this technique did not make single crystal sheets. Another technique impregnated a polymer with quantum dots before curing it with UV. This resulted in an observed cloudy sheet, though it is not fully characterized. The NASA group also tried an additional technique by absorbing CQDs into a Photonic Crystal Fiber (PCF). A matrix of these fibers could be used to make a screen [27].

There are additional fabrication techniques to load CQDs into a structure as well. The methods listed here are not an exhaustive list of everything available, but viable methods for a small laboratory. Techniques such as spin-coating, inkjet printing, 3D printing, and Sol-Gel are discussed in this section.

2.15.1 Monolayer Application

The least complicated method, dispersing or spin coating a thin film of CQDs is a useful solution. One could disperse or spin coat each layer and let the liquid evaporate, however this means all of the quantum dots are held together by weak van der Waals forces. If the film becomes too thick, it will flake away. As the solution evaporates, there is a risk of the CQDs forming empty domes as the liquid escapes. Another method is to use salt bridges to form CQDs monolayer by monolayer. The acid-based ligands on the CQDs could be used to make the first layer on a piece of quartz. Then dipped into a base solution to form a salt bridge and dipped back into the CQD solution. This process can be repeated until the desired thickness has

been reached. Another method already used in the industry is to load CQDs into a polymer.

2.15.2 CQDs Loaded Into Polymer

Polyurethane Acrylate (PUA) is a common material used for UV curing a polymer film. An example of a UV curable PUA process can be seen in Figure 39.

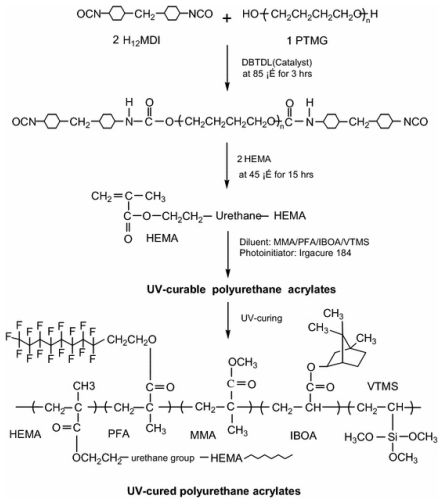


Figure 39. Chemical representation of how the UV curable PUA process works [103].

The UV curable polymers are surrounding the CQD, and when UV light interacts, it causes a chemical reaction to bind them together. When forming thicker structures, it may take more time to hard bake the photoresist. After this process, it is important to note whether the CQDs on the surface are protected against oxygen and moisture in the air [29]. If they are hydrophobic, then an additional layer of blank UV curable polymer should be applied as a thin-film over the structure would protect the CQDs from the environment.

To ensure equal placement of CQDs within a polymer matrix, mixing the matrix is the safest option. It is not recommended to use an ultrasonic machine due to

its ability to atomize the CQDs releasing their atoms into the air, creating a safety concern.

2.15.3 Inkjet Printing

Research from Du *et al.* demonstrated that it was possible to use an inkjet printer to print out UV curable PUA as a thin-film with CQD. They used a SEM to view the changes in structure of the thin-film depending on the water content of the thin-film [75]. The SEM images illustrating structural defects associated with water content are shown in Figure 40 and Figure 41.

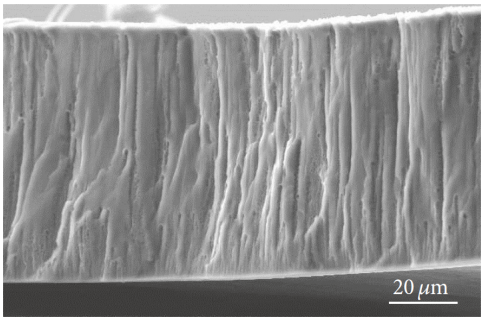


Figure 40. SEM image of 20% water content in polymer [75].

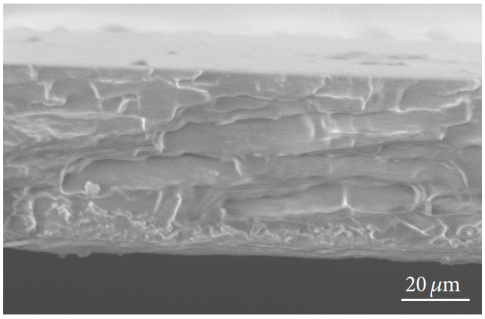


Figure 41. SEM image of 5% water content in polymer [75].

From the SEM images above, less severe water concentration in the polymer structure meant that defects became visibly lower and more uniform. In the paper, the authors noted that lower water content improved the fluorescence stability of the CQDs [75].

2.15.4 3D Printing

A Massachusetts Institute of Technology (MIT) team recently demonstrated that it was possible to 3D print colloidal nanocrystals as the structural material and possibly CQDs as a printing material. It was important to note that this 3D printing technique differed slightly from a standard 3D printer. Below was a summary of their 3D printing steps [38]:

1. A thin needle and a glass syringe were above two heated aluminum plates
2. When nanoparticles were applied, the syringe went through a hole in the top aluminum plate and then dispensed the solution onto a material laying on the bottom aluminum plate
3. They have the bottom aluminum plate rotate and move up and down to create a 3D structure
4. The colloidal solution dropped onto the bottom aluminum plate had its liquid evaporated and with only the nanocrystals remaining

Figure 42 shows the physical appearance of 3D printed colloidal crystals.

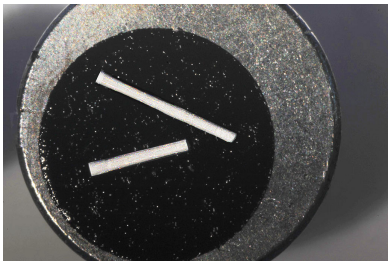


Figure 42. 3D printed colloidal crystals when viewed under a light microscope [38].

The 3D printing article did not mention whether the MIT team utilized UV curing as they built up the 3D printed structure. If no chemical curing process occurred, then

the nanoparticles were only being held together by van der Waals forces. If the process included UV curable polymers, then complex nano-structures for x-ray scintillation would be feasible. For instance, one could use different sized nanoparticles to emit different wavelengths when exposed to light, or having light sensitive nanoparticles paired with conductive elements [38].

2.15.5 Sol-Gel Technique

Similar to using polymers to create solid structures, another technique called sol-gel can be used to create a thin-film of CQDs. The sol term means a colloidal liquid (think of CdSe CQDs suspended within toluene) while the gel term means a wet solid-like material that takes all the nanoparticles in the volume of a liquid medium. A good example of the consistency would be Jell-O ®. To transition from the sol consistency to a sol-gel, the nanoparticles need to stick to each other. Sometimes this is automatic with nanoparticles that have reactive surfaces. Other times, an additive must be used to help bond the nanoparticles together. This process can also be known as gelation [2].

A group of researchers from the University of Alabama used commercially available CdSe and CdS CQDs in a non-acid Sol-Gel. When CQDs are mixed in SiO_2 sol, they are damaged by the acid catalyst (in this case, HCl) used to form the sol-gel. The authors developed a solution by using Octadecylamine (ODA) ligands to help the SiO_2 thin film synthesis. The sol-gel recipe from the research group's paper can be seen in Appendix E. The authors observed that the sol-gel technique created clear emission peaks and the FWHM also appears to be smaller than the CQDs without sol-gel. A noticeable blue shift effect occurred, most likely due to surface oxidization that formulated during the sol-gel process [57].

An additional use of sol-gels that is worth mentioning would be to create a better electron-injection layer before a CQD layer using s-ZnO sol-gel. They have been found to be a cheap and effective method for Quantum Dot Light Emitting Diode (QLED)s [163]. Potentially this could be useful in having CQDs directly convert wavelengths of light to voltages.

2.15.6 Loading CQDs into PCF

In 2014, Burke *et al.* investigated CQDs for x-ray imaging. They looked at a few methods to integrate CQDs for the application, and one of their most unique ideas was absorbing CQDs into a PCF [27]. The PCF (Model F-SM8) was supplied by Newport Corporation. An example of the PCF used can be seen in Figure 43.

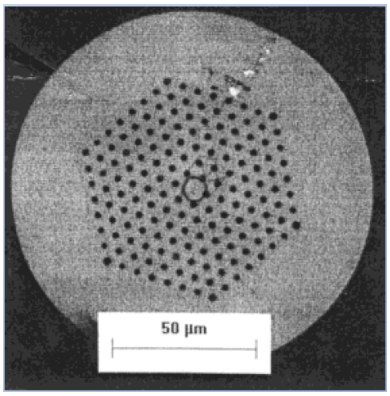


Figure 43. Example of the PCF used in the NASA experiment [27].

The CQDs were small enough to be drawn through the PCF via capillary action. The NASA team also used a small pressure gradient to help ease the drawing process [27]. An image showing the light emission of the CQDs within the PCF from the NASA team can be seen in Figure 44.

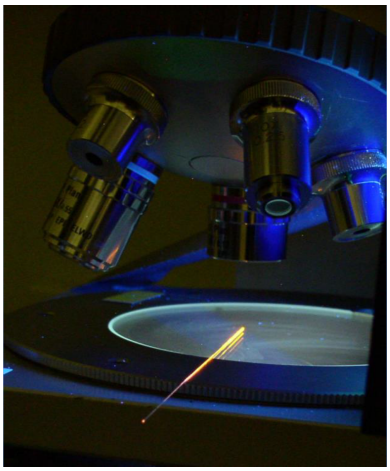


Figure 44. UV excitation of CQDs in fiber from the side; notice the light emission output towards the bottom left of the fiber [27].

From this image, it can be seen that UV stimulation of the CQDs can occur isotropically due to some of the light emitting out of the sides of the fiber by not meeting the angle needed for Total Internal Reflection (TIR). However, the photons that meet the TIR angle become anisotropic coming out of the fiber through wave guiding. As mentioned in the NASA presentation, the CQD infused fibers can be spliced into a main fiber to guide the light to a sensor [27].

III. Methodology

This research was focused on a comparison characterization study of the various flavors of CQDs available in the commercial market. In order to identify the best alternative for the the MSX, multiple experiments were carried out. First, an approximation model was used to help stratify the different nanomaterials under x-ray irradiation. The research then focused on creating recipes for the development of the CQD-loaded polymer, 3D printed, thin-film, and PCF structures. After the fabrication of the nanomaterial samples, additional experiments were conducted to look at both their PL spectra and PL decay. These PL experiments helped determine the compatibility of a CQD's PL emission spectra with a streak camera's photocathode. In addition, they will give a good representation of the overall PL decay time when under pulsed x-ray irradiation. A 3^2 full factorial experiment was conducted after noticing Charge-Transfer (CT) occurring in the PL spectra of a couple of the nanomaterials dispersed within the 3D printed structure. This experiment looked at how changing both the thickness of the 3D printed structure and the amount of CQDs dispersed within the 3D printed structure affected the amount of CT. All of the data gathered in these experiments were used for the stratification of what nanomaterial technology to pursue in the future.

The research methodology continued with experiments planned to gather both the pulsed x-ray PL decay and the overall x-ray irradiation lifetime till photobleaching of the nanomaterials. An attempt to measure the pulsed x-ray response of CQDs at Argonne National Laboratory (ANL)'s beamline was done with the reasons for its difficulties described.

From Table 5, four experiments out of six were carried out in order to find the

best CQD scintillator for the MSX application.

Nanomaterial	Dot or Nanoplatelet	Emission Wavelength (nm)	Manufacturer
CdSe	Dot	460	NN-Labs
CdSe/ZnS	Dot	520	NN-Labs
CdS	Dot	400	NN-Labs
CdSe	NPL	400	NN-Labs
CuInS/ZnS	Dot	530	NN-Labs
InP/ZnS	Dot	530	NN-Labs
PbS	Dot	1200	NN-Labs
PbSe	Dot	1200	NN-Labs
Sapphire	Dot	490	Crystalplex***

Table 5. Overview of nanomaterials being studied for their x-ray emission PL decay properties. ***Company did not deliver material and unresponsive. Only theoretical experiments were done to evaluate the their CQD technology. Temporal response was unknown due to not having the material to test.

The experiments were conducted in the following order:

1. MATLAB x-ray attenuation/absorption study
2. MATLAB x-ray QE study
3. PL and Photoluminescence Excitation (PLE) spectra measurements
4. Pulsed UV excitation PL decay
5. Pulsed x-ray excitation PL decay (future work)
6. X-ray lifetime tests (future work)

Experiments three and four utilized three CQD loading structures: thin-film, dispersion within a 3D printed structure, and polymer matrix. CQDs drawn through PCF fibers were also fabricated, however due to time and material constraints this structure could not be properly evaluated. To evaluate the potential use of each CQD as a fast scintillator, an evaluation rubric was used that considered the four completed experiments, with a score measured out of eight; eight being the best CQD

in the experiment. This rubric was weighted in order to ensure priority functions were met for the sponsor. The CQD with the most points at the end would be recommended for further evaluation in future experiments and fielded for fast x-ray diagnostic applications. The evaluation rubric and the weights for each experiment is shown in Table 6.

Nanomaterial — Experiment	**M1**	**M2**	**M3**	**M4**	**M5**	**M6**	**M7**	**M8**	**M9**
Experiment 1 Total Points									
Experiment 2 Total Points									
Experiment 3 Total Points									
Experiment 4 Total Points									
EXP 1 Weight Applied: 20%									
EXP 2 Weight Applied: 20%									
EXP 3 Weight Applied: 10%									
EXP 4 Weight Applied: 50%									
Total									

Table 6. Weighted evaluation rubric used to select top performing nanomaterial scintillator to be fielded at MSX.

For all experiments that handled CQDs, standard safety precautions were taken. While CQDs were being loaded into their structures, work was performed within a Class 1000 cleanroom under a fume hood. Double nitrile gloves were worn. The following subsections go over the setup for each experiment and how the nanomaterials were evaluated.

3.1 X-ray Feasibility Study

Two modeling experiments were conducted to compare CQD technology performance under x-ray irradiation. The tested structure for both experiments was a homogenous suspension of CQDs within Polymethyl Methacrylate (PMMA) which has similar properties to photoresist polymers. The first experiment compared how thick each CQD structure had to be in order to interact with a desired percentage

of incident x-rays. A thinner application of CQDs to attenuate an incident x-ray by a desired percentage would be more favorable due to emitted photons having shorter distance to travel to a camera. The longer the distance, the more attenuation the photons could experience when in a polymer matrix material and the greater the probability of experiencing absorption/reabsorption effects from the CQDs while traveling. Thicker CQD applications could increase the time for the scintillator to decay and lower its QE.

The second experiment determined the QE of CQDs in a monolayer of a certain diameter. Use of a monolayer reduced computing power necessary due to a reduction in x-ray scattering effects. A Monte Carlo (MC) method was used in order to estimate QE for each CQD material in both the 10 keV and 100 keV energies. The two energies bounding the energy range for the problem were used to help compare different CQD materials. Since the goal of this thesis was to find a material that could be used across the entire 10 keV-100 keV range, there was no need to calculate additional data points which could show k-edges. K-edge optimization would be more important for CQD materials if wanting to prioritize certain ranges of energies within the 10 kev-100 keV energy range. The CQD materials that require the least amount of structural thickness and have the highest QE overall at the energy bounds would be most useful for temporal measurements.

This section mainly discusses the attenuation experiment since the monolayer experiment used the attenuation simulation code as a framework, with slight code modifications.

3.1.1 Educated Estimation About Sapphire CQD Geometry

The Sapphire CQD material geometry was unknown for its various layers. This sub-section describes the thought process that was used to predict the diameter of each layer within the Sapphire CQD. This was important to know for the models that were used in MATLAB when comparing the Sapphire CQD to other CQD materials.

Due to the unavailability of the material, it was not possible to get Transmission Electron Microscope (TEM) images of the Sapphire dots to measure core and shell dimensions. However, the alloying technology behind the Sapphire dots was well established. Additional details about the benefits of alloying were discussed in Chapter 2. The manufacturer stated that all of their dots were between 8 nm-10 nm in diameter. A safe value for doing x-ray simulations would be to use an average, or 9 nm, diameter. The manufacturer also stated that the Sapphire layer on the outermost surface of the dot was five aluminum atoms thick before oxidation. That would mean there was a thickness of 12 atoms containing Al_2O_3 coating the dot. It was assumed that this Al_2O_3 layer was 1 nm thick. The layer under the Sapphire layer was ZnS. Since this CQD used CdSe as the core material, it was assumed that the ZnS shell would not vary by much compared to another manufacturer's dots. On average, the ZnS shell was about 2 nm. It was also assumed that the CdSe core was about the same diameter as another manufacturer's dots, approximately 2 nm. In terms of the alloying gradient, all alloyed dots that used both CdSe and CdS used a $CdSe_xS_{1-x}$ material mixture as the alloying layer. At this point, x could be any value between zero and one. To work as a conservative guess, it was assumed that x was 0.5. Alloying layer thickness was assumed to be 1 nm. This leaves only the CdS layer to be determined, and the remaining thickness left was 3 nm. The thought process displayed here was based upon reasonable assumptions of the thickness for each layer

to model the x-ray properties of Sapphire CQDs.

3.1.2 Incident X-ray Attenuation Experiment Written in MATLAB

The first challenge addressed was how to simulate varying CQD materials and geometries. This was possible by creating an Excel spreadsheet where each row represented a different material. Each column represented a different parameter. The spreadsheet CQD attributes were organized in the following way:

- Core: up to four materials
- Shell #1: two materials
- Shell #2: two materials
- Shell #3: two materials

Each aspect of the CQD can be loaded with any desired material and the ratio of material can also be programmed. In addition, the total diameter contribution for each layer can be specified. Additional attributes such as the % volume loading within a PMMA matrix, the desired amount of x-rays to be scattered/absorbed by the CQD, and the QE can be inputted into the document. The reason why % volume loading was used instead of % loading density was because there are other factors that determine how densely populated a CQD-loaded polymer matrix could be. These other factors would be the shrinkage factor of the polymer when it is cured/hard-baked which is dependent on the CQD material used according to technical support from NN-Labs. This would have to be experimentally determined in the future, but for now % volume loading makes the calculations easier. For the purpose of this thesis the modeling was used to compare CQD materials rather than being a fully encapsulating physics model to motivate what material should be investigated further in the

future.

The next challenge is calculating the mass attenuation coefficient. As discussed in Chapter 2, the mass attenuation coefficient is determined by a contribution of elastic, inelastic scattering effects, and absorption. Going back to fundamentals, Figure 45 shows where the photoelectric effect, Compton scattering, and pair production become dominate depending on the Z of the material and the incident photon energy.

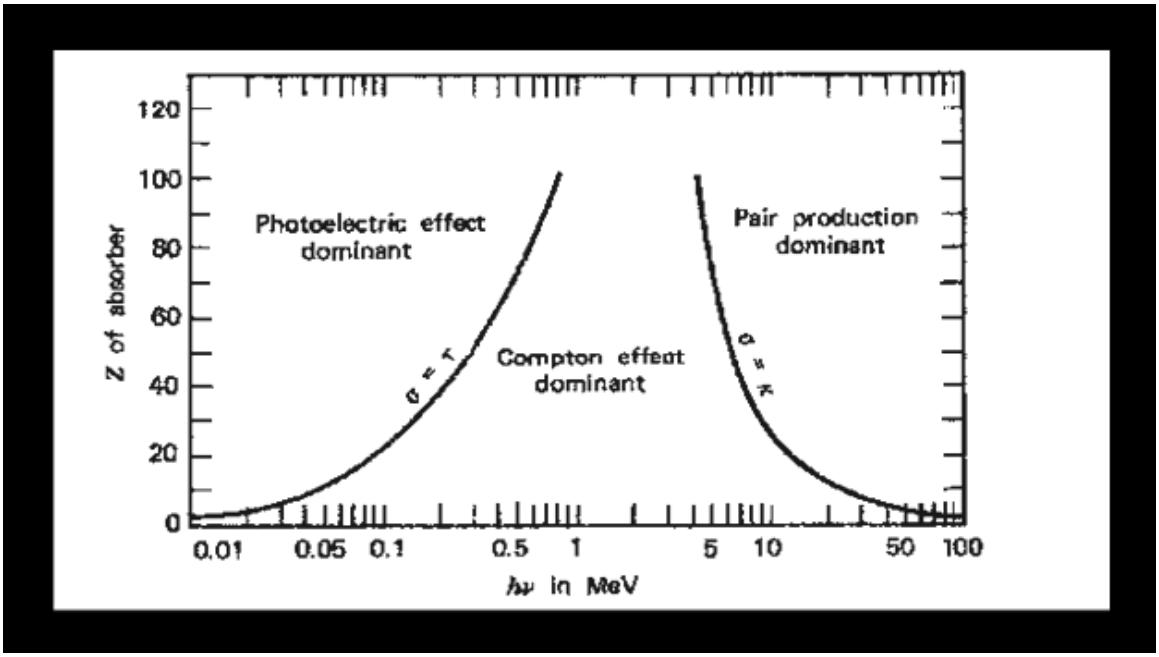


Figure 45. Chart of where each of the effects: photoelectric, Compton, and pair production are dominate. Effect dominance is related to the Z of the material and the incident energy of the photon. Image from Almahwasi [13]

From Figure 45, only the photoelectric effect and Compton scattering would occur for the given application. Pair production would not be possible due to the 1.022 MeV required minimum energy. Thus, for each material within a CQD, both the Compton scattering (inelastic) and photoelectric absorption mass attenuation coefficients were used. The values came from the NIST XCOM database and placed in an Excel spreadsheet. The sheets within the Excel file were labeled by their respective elements.

The values from XCOM were only for a discrete set of incident energies. Linear interpolation was used to determine the mass attenuation coefficient if a modeled incident x-ray energy was not in the mass attenuation coefficient table. The linear interpolation method used can be seen in Equation 34.

$$y = y_0 + (x - x_0) \times \frac{y_1 - y_0}{x_1 - x_0} \tag{34}$$

Where the values in Equation 34 in the context of this experiment are defined in the list below:

- y: linearly interpolated mass attenuation coefficient value
- y_0: next table value under the mass attenuation coefficient to be found on the y-axis
- y_1: next table value over the mass attenuation coefficient to be found on the y-axis
- x_0: next table value under the incident photon energy on the x-axis
- x_1: next table value over the incident photon energy on the x-axis
- x: incident photon energy

The program added both the inelastic scattering and photoelectric absorption mass attenuation coefficients when the Beer-Lambert law was used. Next, in order to use the mass attenuation coefficients of each material using the Beer-Lambert law, the ratio of materials present in each core and shell was calculated. If doing a bulk material case where all the materials present in both the core and shell would be used, then a volume ratio would also have to be calculated. However, for this experiment, only material ratios within each area (core and shell) would need to be calculated

since a 3D model was made. The material ratios led into $\frac{\mu}{\rho} \times \rho$ portion of the Beer-Lambert law which can be calculated by using the calculated mass attenuation coefficient and the elemental density. The elemental density data for each element came from Wolfram Research, Inc [11]. The code used to make the mass attenuation coefficient calculations from the data typed into the Excel spreadsheet can be seen in Appendix Z.7.

Once the mass attenuation coefficient was calculated for each CQD layer, it was then fed to a voxel (using cubes to create a 3D model) code sub-function. This code can be seen in Appendix Z.10. The voxel code used a spherical matrix which built upon the framework provided by Muppirala [93]. It then created the CQD by first calculating the cubic volume of polymer in which the CQD was suspended. The CQD was loaded within the PMMA as a percent volume, which means the overall diameter of a CQD would determine the overall cubic volume of the CQD/PMMA system. This calculation was done by using another sub-function which can be seen in Appendix Z.12. It then gave a unique value to each CQD layer within the spherical matrix. An example of what the spherical matrix looked like using Sapphire CQD as an example can be seen in Figure 46.

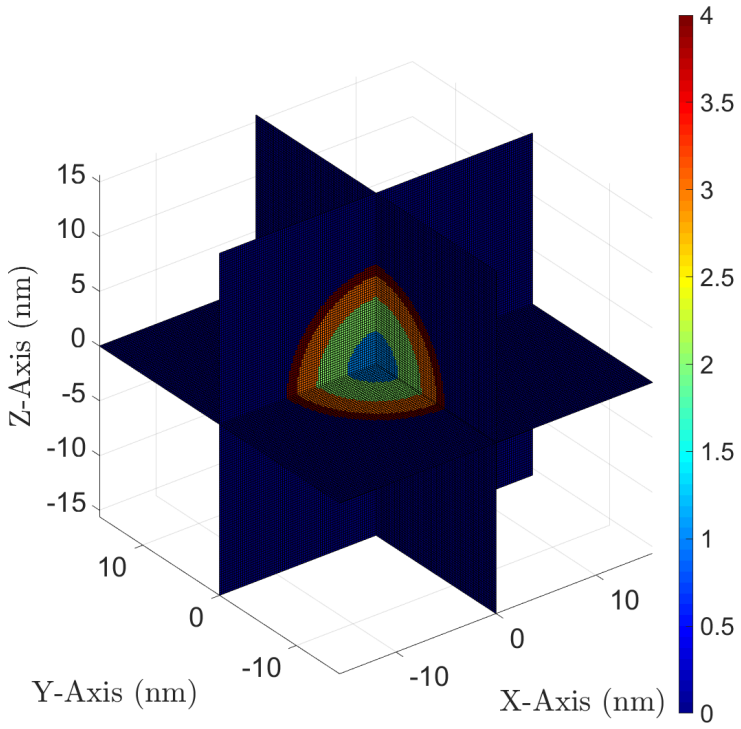


Figure 46. An example of a Sapphire CQD suspended in a PMMA polymer matrix at 10% loading volume. Each layer of the CQD was represented by a unique value. This unique value acted as an identifier to load the correct calculated mass attenuation coefficient into that voxel.

The program then made use of parallel CPU processing to speed up the loading of the calculated mass attenuation coefficients for each of their respective CQD layers and the polymer. Afterward, the spherical matrix was flattened into a 2D matrix by multiplying the voxels to each other in one direction. An example of this spherical matrix flattening can be seen with the Sapphire CQD in Figure 47.

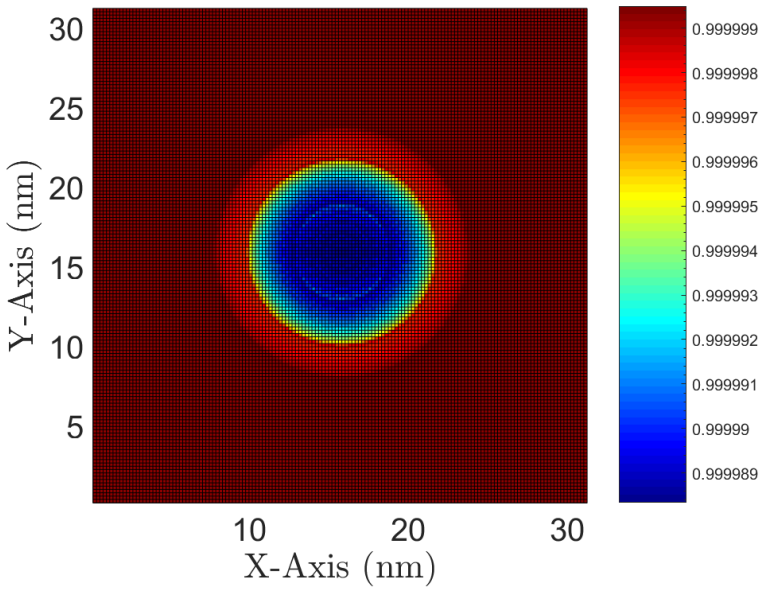


Figure 47. An example of a Sapphire CQD with its spherical matrix of calculated mass attenuation coefficients flattened into a 2D matrix. The more red the voxel, the less incident x-rays that were absorbed/scattered.

The 2D matrix was then summed and divided by the number of elements to get the effective percent transmission of the incident x-ray energy after going through one CQD. This value was then applied to Equation 35 in order to find the total thickness required to interact with a given percentage of an incident x-ray of a specific energy,

$$T(\mu m) = \frac{\log(1-\beta)}{\alpha_{trans}} \, Voxel_{length} \, 0.001 \tag{35}$$

a conversion factor of 0.001 was used to convert the length unit from nm to μm. The variables in Equation 35 were listed below:

- T: total thickness (μm)
- β: percent total absorption and scattering of incident x-ray
- α_{trans}: total mass attenuation coefficient over the length of one CQD suspended within PMMA polymer voxel

- $Voxel_{length}$: total length (nm) of one CQD within PMMA polymer within a voxel

3.1.3 Monolayer QE Experiment Written in MATLAB

For this experiment the nm-scale voxel model as described in the previous modeling experiment was integrated with a MC code to approximate the QE of a monolayer of CQDs. A MC code uses a high number of iterations to have a probabilistic phenomena reach an average steady state. The following are the assumptions used during this simulation:

- Electrons scattered or emitted within CQD material transferred their energy within the CQD
- No scattering of electrons in the PMMA matrix material
- Secondary and tertiary scattering effects were omitted
- Did not use ray tracing
- Assumed incident x-ray flux was homogenous over the entire surface area of the monolayer

These assumptions were made for the purpose of simplifying the problem in order to make an approximation when comparing CQD materials. QE output from this simulation would be by no means completely accurate to actual experimental results.

The program operated in a similar manner to the code used to approximate the CQD scintillator thickness. The main code that calculated the mass attenuation coefficient can be seen in Appendix Z.9. The main difference from the previous code experiment was the post-processing of the data. A monolayer of a certain diameter

was hard-coded. The surface area of this monolayer was then divided by the squared length of the CQD that was 10% of the volume within a PMMA polymer matrix to determine the number of particles to simulate. The code then ran the MC simulation for which the sub-function can be found in Appendix Z.11. The program worked through every voxel in the spherical matrix of the CQD in polymer and used the mass attenuation coefficient in each voxel as a probability if an x-ray interaction occurred. It was assumed that when an x-ray interaction occurred, the CQD would have been excited. The program saved the total number of interactions and then multiplied the number by the QE of the CQD. Then, the algorithm ran a six-sided die probability to determine if the photon went in the desired direction since a CQD was an isotropic emission. This meant one face of the cube would lead to an emitted photon, or a $\frac{1}{6}$ chance. After the MC simulation finished, the program divided the number of emitted photons from the monolayer by the total number of particles simulated to get the QE of the overall system.

3.2 Fabrication of CQD Loading Structures

There were five types of CQD loading structures investigated: polymer, PCF, 3D printed, thin-film, and salt-bridge scintillators. The salt-bridge scintillator was the only one not fabricated due to both resource and time constraints, however it would be a promising structure as CQDs could be more tightly packed together and engineered without showing FRET compared to other methods.

3.2.1 Polymer Scintillator

Design of CQD-Loaded Polymer Scintillator

Multiple iterations were designed to disperse CQD-loaded polymer into a structure. An initial idea had the polymer sandwiched between two quartz slides, however,

this would not allow low energy x-rays through. Thus, the next iteration of the design focused on applying the polymer on one side of a quartz slide. The final design used an aluminum washer that was 0.05″ thick with the washer cured onto a quartz disc. The polymer was then deposited into a 0.5″ diameter hole. An orthographic drawing of this design can be seen in Appendix Q. A 3D SolidWorks rendering of the design can be seen in Figure 61.

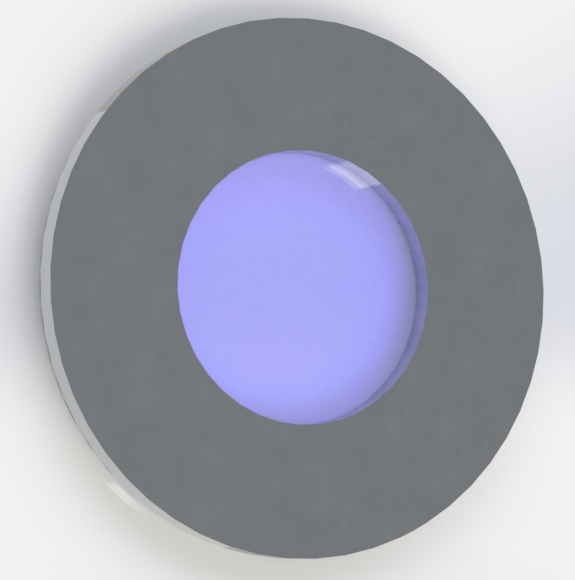


Figure 48. Top side rendering of supporting structure before loading in polymer.

Fabrication Recipe of Polymer Scintillator

Various attempts were made to figure out a productive way to glue the aluminum ring to the quartz slide and hard baking the polymer within the hole. Since there were chemical restrictions in the laboratory, SU-8-5 was the best available material to act as a clear glue between the aluminum ring and quartz disc. The procedures for gluing the ring to the quartz disc can be seen in Appendix I. Nine of these aluminum and quartz disc structures were made. Next, the procedure in Appendix J was followed to cure all of the CQD-loaded polymer samples into the hole of the structure.

While the procedure in Appendix J was sufficient to cure most of the CQD-loaded polymer samples, there was an issue with one CQD-loaded polymer sample that was less viscous compared to the others. If a sample's viscosity was too low, it oozed out from underneath the aluminum ring during the hard baking process on the hot plate. In the future, it would be best to eliminate the hot plate step and hard bake the entire structure at 180 $^{\circ}C$ within a convection oven until cured. This process would equally heat both sides of the CQD-loaded polymer which could help prevent oozing from under the aluminum ring. A lower temperature, 135 $^{\circ}C$, could still work for the entire process, but it would take longer. This CQD-loaded polymer viscosity issue presented the importance of having good quality control of purchased CQD-loaded polymer from a supplier. The CQD-loaded polymer viscosity should be high enough for it to be a little harder to pipette the polymer, but still possible to disperse the material from the pipette. This had the best success in being properly hard baked within the aluminum ring on top of quartz structure. If the material came through the pipette like a liquid, it had issues with oozing under the aluminum ring.

Since the CQD order from the supplier is experimental, below are recommendations for ordering the same CQD-loaded polymer material from NN-Labs in the future with 10% CQD loading by weight:

Material	Viscosity Change?
PbSe	More
InP/ZnS	Less
PbS	Less
CdSe/ZnS	None
CdSe	None
CuInS/ZnS	None
CdSe NPLs	None
Blank Polymer	None

Table 7. Table with recommendations in viscosity changes when buying the CQD-loaded polymer materials used in this experiment from NN-Labs.

Checking Thickness of CQD-Loaded Polymer Scintillator

The thickness of each CQD-loaded polymer sample is measured, taking into consideration the varying thicknesses resulting from different viscosities and a CQD-loaded polymer shrinkage factor which is a function of different CQDs loaded within the polymer. The CQD-loaded polymer thickness will be useful for future x-ray analysis.

Characterizing the thickness of the CQD-loaded polymer scintillator without damaging the sample required an optical method. A Zygo interferometer could be used, however it would have trouble with the clear CQD-loaded polymer. Another optical method used the focusing distance as a way to measure the thickness of an object. One such piece of equipment was the Leica DVM6. It had the capability of recreating objects in a 3D image. The setup of this digital microscope can be seen in Figure 49.

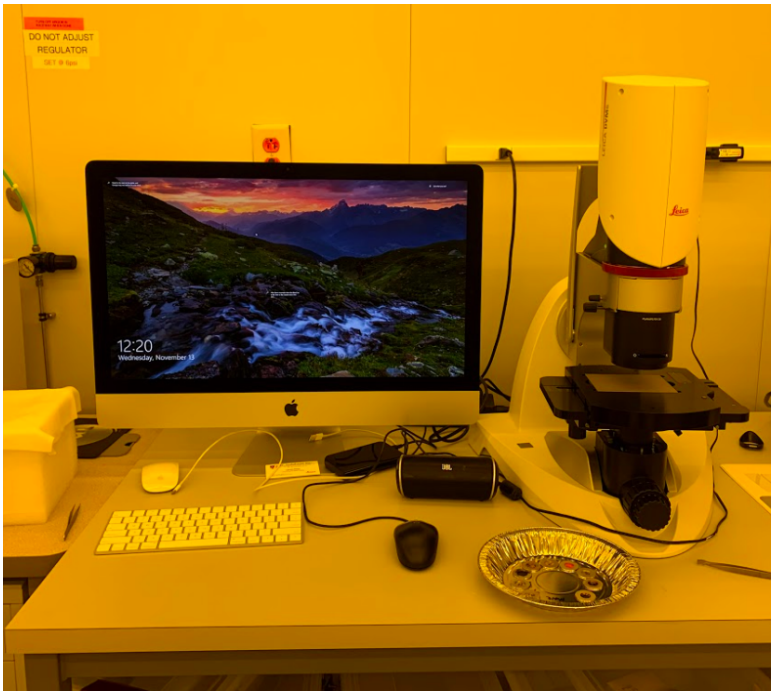


Figure 49. Leica DVM6 digital microscope used to characterize the thickness of each CQD-loaded polymer scintillator.

The documentation for the Leica DVM6 was not a straightforward tutorial on its use. Therefore, the procedure to operate the microscope for this thickness study was provided and can be seen in Appendix K. Top-down overview images were taken for higher-fidelity visuals of the CQD-loaded polymer scintillator (e.g. whether it showed uniform deposition or capillary channels). Capillary channels would introduce pockets of air within the CQD-loaded polymer matrix, thus the scintillator would be expected to have a lower QE due to changes in the index of refraction for the emitted photons. Capillary channels could form from the liquid molecules quickly escaping out from within a CQD-loaded polymer. An example of one of these images can be seen for CdS in Figure 50 with minor brightness, contrast, and shadow adjustments using Corel Paintshop Pro X8 software to better make out the capillary channels.

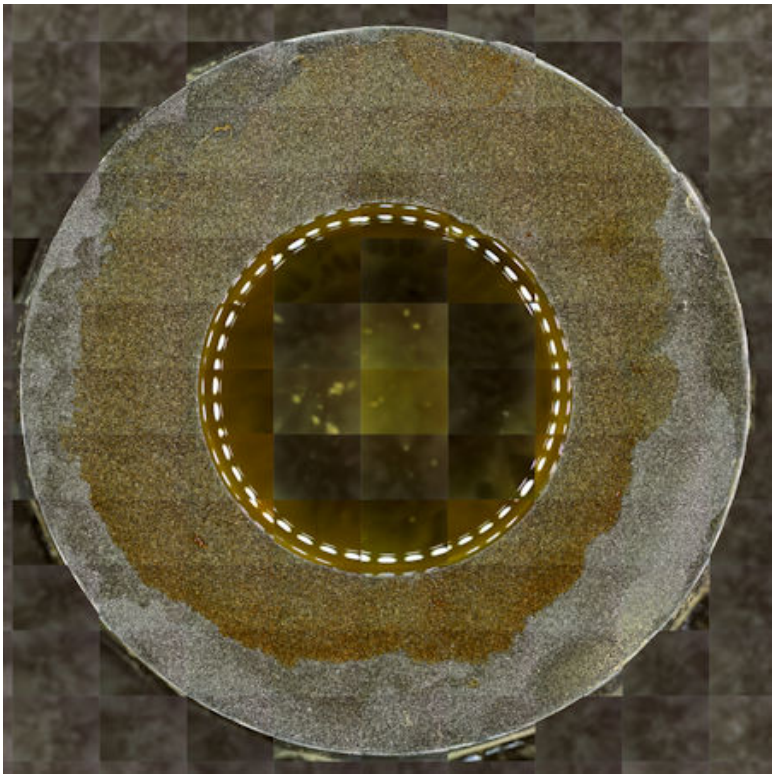


Figure 50. Overview scan image of a top down view of CdS loaded polymer scintillator.

It would be useful to see if only using a convection oven in the future would help mitigate the formation of capillary channels. In addition, lowering the hard baking temperature would help to slow down these formations. To see the original CQD-loaded polymer scintillator overview images for each, go to Appendix H.

It was determined that up to a 10° tilt of the microscope would allow the light to reflect off the surface of the CQD-loaded polymer, which caused a focusing point. Unfortunately, a tilt also caused an offset which required a software upgrade to calculate the tilt compensation. The thickness value toward the center of the depth of field, which in this case was along the circumference of the aluminum ring, would be the most accurate, while moving away from the circumference would begin to show error. Thus, thickness measurements were made from the top of the aluminum ring

to just beyond the edge of aluminum ring on the CQD-loaded polymer. A 3D image taken by the Leica microscope can be seen in Figure 51.

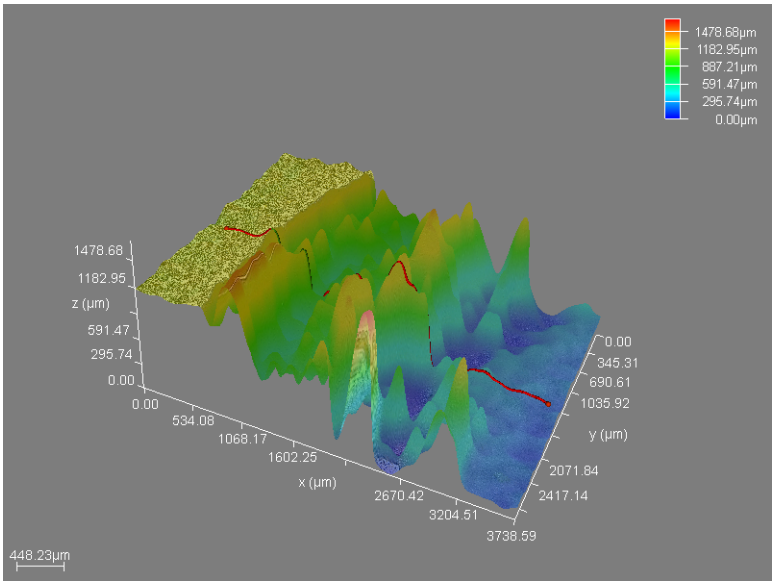


Figure 51. The left side of the surface plot represented the aluminum ring. Going towards the blue end on the right side represented the CQD-loaded polymer surface. The random peaks throughout the region between the aluminum ring and towards the middle of the CQD-loaded polymer surface would be the locations where the light reflected off the surface. The CQD-loaded polymer formed a bowl shape within the interior of hole in the aluminum ring, thus any peaks that go back up to the height of the aluminum ring were noise. While not perfect, this non-destructive optical method showed the difficulty in imaging a mostly clear CQD-loaded polymer without other modifications made to the CQD-loaded polymer.

Figure 51 had a color map overlayed on its surface, where red represented higher points and blue represented lower points. The remaining 3D color surface maps can be seen in Appendix A. Consistently across all of the CQD-loaded polymer samples, the Leica microscope produced poor distance data at the interface between the CQD-loaded polymer and the circumference of the aluminum ring. This was seen as a steep valley and would not be a valid height measurement. In addition, the random tall peaks that appeared as high as the aluminum ring itself were focal noises since measurement of the CQD-loaded polymer's thickness was done by reflecting light off its surface. Through the noise, there were good patches of surfaces to get approximated

thickness readings. Since a bowl shape was noticed for most of the CQD-loaded polymer samples that did not have a high viscosity, this thickness measurement would only work as an average thickness value. The thickness of the CQD-loaded polymer was not the thickness of the CQD-loaded polymer itself since there was a clear quartz disc underneath it. Thus, it was decided that using the top of the aluminum ring as a reference point would be a better measurement. The equation used to calculate the average thickness of the CQD-loaded polymer sample can be seen in Equation 36.

$$T(\mu m) = 1,270 - (Hm_{ring} - Hm_{polymer})(\mu m) \tag{36}$$

Where Hm_{ring} would be the measured height of the aluminum ring and $Hm_{polymer}$ would be the measured average height of the CQD-loaded polymer sample. All height measurements were in μm as the unit value. The 1,270 μm constant was the thickness of the aluminum ring. Due to the noise that occurred in each measurement for every sample, a sanity check was applied to values that were not physically possible from observation. The error for each measurement was half of the step size for the color bar on the colored surface maps and an additional 170 μm which was the thickness of the quartz disc. It was difficult to determine if the microscope was focusing through the quartz disc or not, which made the values less accurate. Equation 36 was applied to all of the CQD-loaded polymer samples and the results can be seen in Table 8.

Material	Height Difference (μm)	Average CQD-Loaded Polymer Thickness (μm)	Error $\pm$ (μm)
Control	379.24	890.76	252
PbS	428.71	841.29	331
InP/ZnS	448.38	821.62	295
CuInS/ZnS	448.66	821.34	239
CdS	450.00	820.00	318
CdSe NPL	506.53	763.47	284
CdSe/ZnS	519.64	750.36	270
CdSe	613.11	656.89	239
PbSe	1,473.60	-203.60	295

Table 8. Average thickness values of the CQD-loaded polymer scintillators after fabrication. Note, the high error values were due to the difficulty in being able to reliably get a proper focus off of the surface of the CQD-loaded polymer with the microscope.

The average thickness value would would be best for approximating the thickness towards the circumference of the aluminum ring. The CQD-loaded polymer thickness was observed to be quite thin for several of the fabricated scintillators at the center. Direct measurements of the center were not possible due to no reliable reference object to focus on since the CQD-loaded polymer was clear. Ideally, an add-on to the Leica DVM6 software called MAPS should be added which would account for the microscope tilt and allow for measuring of the entire CQD-loaded polymer scintillator.

Checking Fluorescence Before Shipping to Experiments

An affordable LED blacklight sold by Viribus such as the one seen in Figure 52 was used to quickly and reliably check the emission of the CQDs that emit in the visible spectrum. This method of checking was also used for checking the PCF and thin-film of CQDs as well.



Figure 52. LED blacklight sold by Viribus. Image from Viribus [153].

The LED blacklight was clamped onto a table and the CQDs were placed under it. This led to Figure 53 which can already be a good indicator about which dots have a higher efficiency (brighter emission), if the CQDs survived the fabrication process, and a quick look into uniformity of deposition.

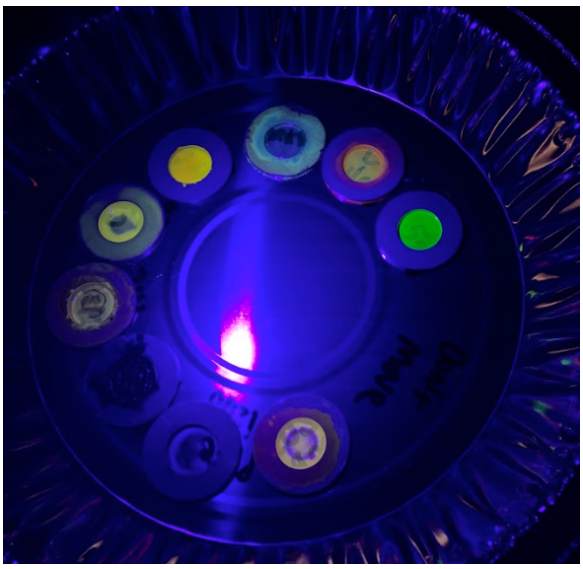


Figure 53. Fluorescence for the visible emitting CQDs can be quickly checked by using a standard LED blacklight to ensure they still worked before sending them out to another laboratory for testing.

The two dark samples in Figure 53 were the lead-based CQDs that emitted in the Near-Infrared (NIR). The brightest emitting CQDs was the CdSe/ZnS sample, due to technological maturity and higher QE than the other CQD flavors tested in this thesis.

3.2.2 Photonic Crystal Fiber Scintillator

Additional communication with the NASA team about how they loaded CQDs within their PCFs unfortunately came back with the recipe being lost. Research was done to figure out this recipe, which was successful. The PCF used by NASA was made by Newport Corporation, model number was F-SM8, and it used a 8.5 μm core. According to the datasheet, the PCF diameter was 2.5 mm, the coating diameter was 245 μm, and the cladding diameter was 125 μm with an uncertainty of ± 5 μm. The Ripley fiber optic stripper used in this experiment were capable of stripping fiber down to 125 μm, which meant there was a possibility of having a residual 5 μm of cladding that could interfere with the cleaving process. Fiber optic cables must use a cleaver in order to keep their waveguiding properties intact at the end of the cable. Using wire cutters or scissors would cause defects on the fiber ends, thus greatly preventing light from getting in or out of the fiber. The cleaving process was perfected over multiple iterations and the best iteration along with the loading of CQDs can be seen in Appendix O. The equipment used can be seen in Table 9.

Equipment	Manufacturer	Model Number
Fiber Optic Cleaver	Fujikura	CT-20
Tweezers	Vomm	SA-T
Fiber Optic Strippers	Ripley	CFS-3
Pliers	Generic	Generic
Scanning Electron Microscope	Hitachi	S-4700
Microscope	Zeiss	Axioplan 2

Table 9. List of equipment used to cleave and conduct quality control on the PCFs.

It was determined that no additional post-processing of the fiber after cleaving should be done as any hole defects always came from the cleaving process. No additional post-processing attempts such as an ultrasonic bath in Isopropyl Alcohol (IPA) and plasma ashing removed defects from the PCF tips. The type of fiber cleaver used made a difference in improving the success rate of a well cleaved fiber tip. The Fujikura CT-30, a spring-loaded fiber cleaver, did not make well cleaved fiber tips of the PCF. The defects of a badly cleaved fiber tip can be seen in Figure 54.

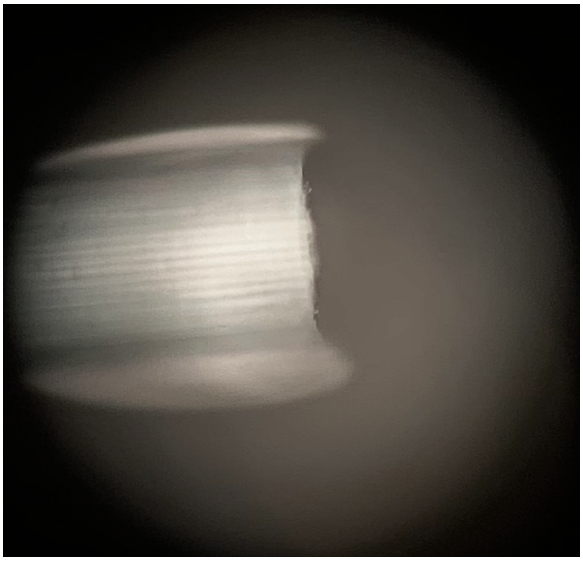


Figure 54. Badly cleaved fiber tip when viewed from the side under a microscope.

When viewed under a SEM, the defects become apparent as seen in Figure 55.

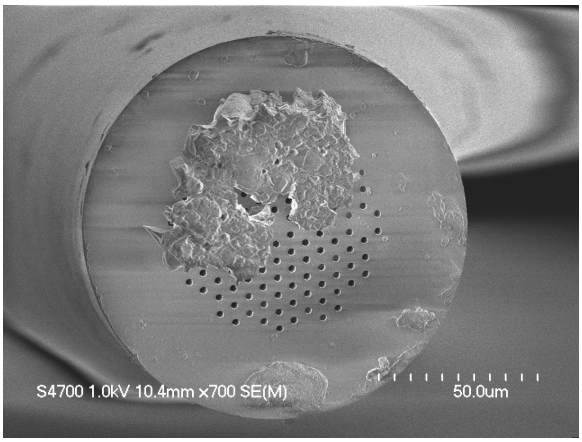


Figure 55. Badly cleaved fiber tip when viewed with a SEM.

The reason post-processing cannot remove the defect from the fiber was because the defect was part of the fiber tip itself, which is glass in this case. What worked well was switching to a Fujikura CT-20 manual fiber cleaver. This allowed the application of additional force to more cleanly cleave the fiber. When viewed under a microscope, a well cleaved fiber tip would like Figure 56 when viewed from the side.

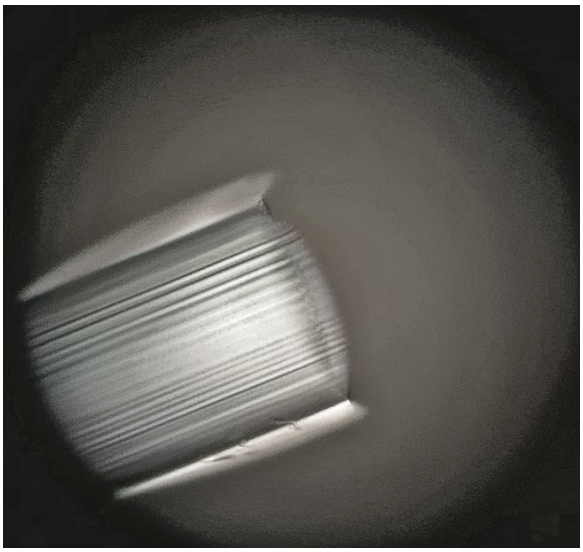


Figure 56. Well cleaved fiber tip when viewed from the side under a microscope.

From a top down view of a well cleaved fiber, it should look like Figure 57.

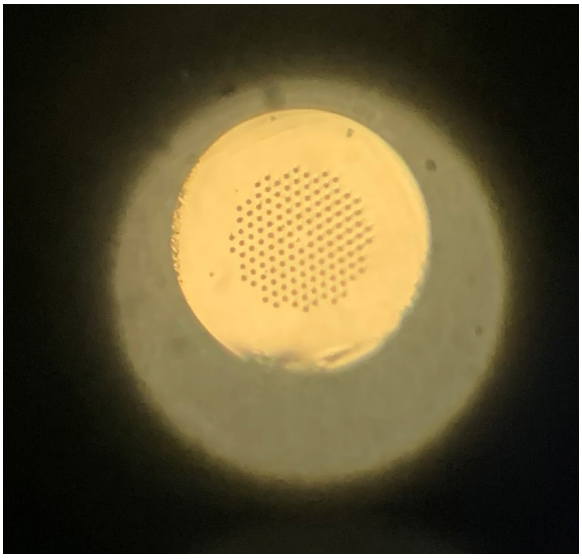


Figure 57. Well cleaved fiber tip when viewed from top down under a microscope.

Then, when viewed under a SEM, the well cleaved fiber tip would look like Figure 58.

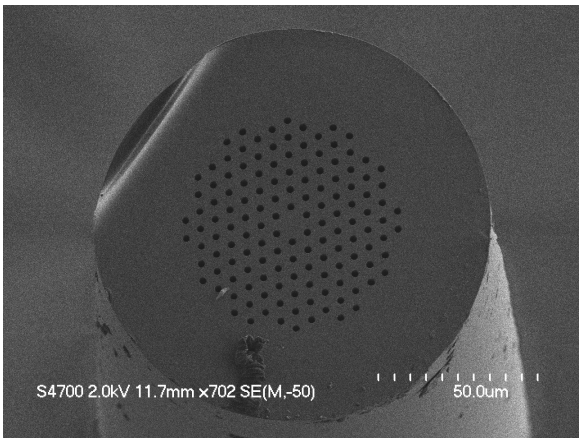


Figure 58. Well cleaved fiber tip when viewed in a SEM

Notice how small defects when viewed under a microscope turn out to be cleaving defects when seen under a SEM. These defects were not an issue as long as they did not interfere with the holes in the PCF. While the surface in Figure 58 appeared smooth, it was full of ripples. This was due to the shock wave that was created while cleaving, but was of no issue since the ripples were small. A SEM image of the ripples

that occured from the shock wave can be seen in Appendix P.

After following the CQD loading procedure and before cleaning the PCF as discussed in Appendix O, a black light was used to verify if the CQDs were drawn in as seen in Figure 59.

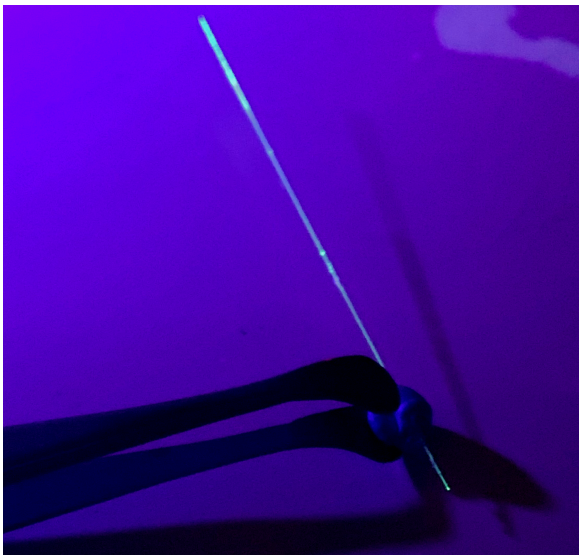


Figure 59. Light emission coming out from one end of the PCF after loading of CQDs and before cleaning the outside surface of the PCF.

After cleaning the outside of the fiber using the last step in Appendix O, the CQDs were drawn through a few millimeters from the tip of the PCF. This can be seen in Figure 60.

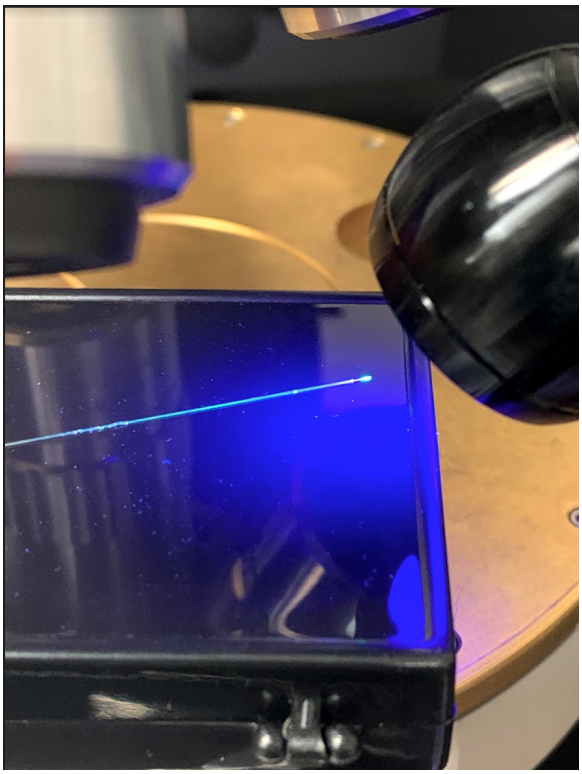


Figure 60. Light emission coming out from one end of the PCF after loading of CQDs and after cleaning the outside surface of the PCF.

Due to time constraints and lack of availability of fiber splicing equipment, only the demonstration of successful loading of CQDs within the PCF fiber was performed.

3.2.3 3D Printed Scintillator

Inspired by looking into PCFs as a structure in which to load CQDs, it was devised to use 3D printing to achieve a similar effect. Using available equipment, the best XY resolution was 500 μm sized holes without defects. A honeycomb support matrix was designed that was utilized to helped with computer processing. The sheer number of holes in the honeycomb matrix made using circular geometries in the workstation prone to crashing. The hexagonal geometries achieve the same effect and conveniently become circular as the 3D printer's XY resolution was pushed.

Every CQD was fabricated into a 960 μm thick 3D printed structure with 160 μL of the nanomaterial's solution dispensed into the structure. During experimentation, it was noticed that a clear secondary peak occurred for both the InP/ZnS and CdSe/ZnS CQDs within the 3D printed scintillator. To investigate how the thickness of the 3D printed structure and the amount of CQDs loaded into the structure had an effect on this secondary peak, a 3^2 factorial design was used as discussed in Section 3.7.

It was worth noting that due to time constraints and amount of available material, both CdSe/ZnS and InP/ZnS were used for the single 3^2 full factorial test. No replicates of the fabrication process were possible.

Design of 3D Printed Honeycomb Structure

SolidWorks was used in the design of the 3D printed honeycomb. It was noticed that using circular geometries made creating the structure impractical as it would crash the workstation due to the hundreds of geometric parts within the honeycomb. Hence, using hexagonal shapes significantly reduced the number of geometric entities with which the computer had to contend. This design could also work with octagons and other geometries, however using a hexagonal geometry was the most geometrically simple shape that still resembled a circle. An orthogonal drawing of the 3D printed scintillator can be seen in Appendix R. Rendering of the 3D printed part can be seen in Figure 61.

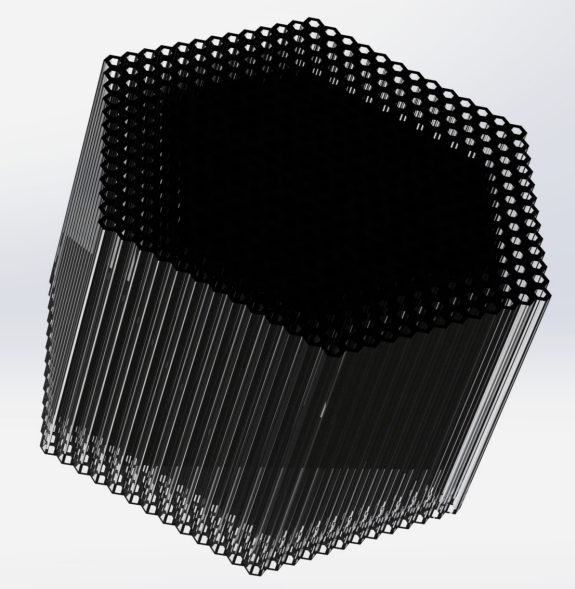


Figure 61. Rendering of the 3D printed honeycomb. Rendering created in SolidWorks.

Printing 3D Printed Honeycomb Structure

The 3D printed honeycomb was produced using the VisiJet M3 Navy ProJect MJP 3600 Series printer. It was imperative to select the UHD option to achieve the machine's highest XY print resolution. Samples had to be done twice over due to an error in selecting a lower resolution. Using a worse quality other than UHD or XHD resulted in a few holes in the 3D print being clogged with plastic. The printer can be seen in Figure 62.



Figure 62. ProJet MJP 3600 Series printer used in the creation of the 3D printed honeycomb structures. Image from 3D Systems [135].

The procedure in Appendix L was used to remove the wax structural supports after 3D printing. Then, each different thickness of 3D printed material was stored in their own respective jar filled with water. In order to properly load CQDs into the 3D printed material, a small stand was fabricated to keep the 3D printed honeycomb structure suspended as much as possible in the air to discourage the CQD solution from binding to a surface other than the 3D printed honeycomb structure. The orthographic drawing of the 3D printed stand can be seen in Appendix S. A 3D rendering of the stand with the 3D printed honeycomb sitting on top of it can be seen in Figure 63.

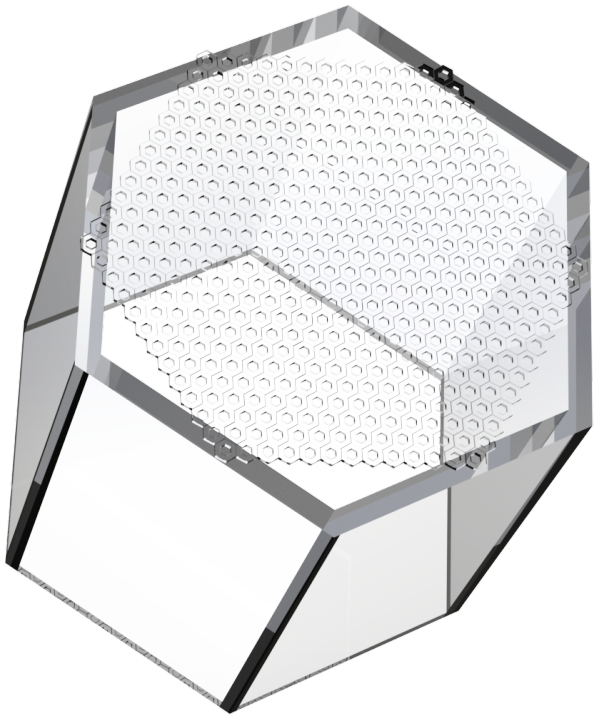


Figure 63. 3D printed stand to keep the 3D printed honeycomb structure suspended while CQDs were applied. Rendered using SolidWorks.

Once ready to load with CQDs, the procedure in Appendix M was followed.

3.2.4 Thin-Film Scintillator

The thin-film scintillators were made in a similar fashion to the CQD-loaded polymer scintillator. The procedure in Appendix J was used to make nine aluminum ring on quartz disc structures. Next, the procedure in Appendix N was used to disperse a thin-film of CQDs using a micro pipette onto the quartz disc portion. All materials except for CdSe NPLs were dispersed as a 10 μL solution. The CdSe NPL's were dispersed as a 20 μL solution due to a difference in their physical geometry. The CdSe NPLs did not disperse as easily as the spherical nanomaterials across the quartz

slide. This was most likely due to the rectangular shape of the NPLs which gave it more surface area to make contact with the quartz disc.

3.3 PL and PLE Measurements with Pulsed UV Lifetime Decay

A baseline of how the CQDs performed under UV excitation would help determine the effects x-rays have on their temporal response. In addition, the experimental PL emission spectra would help determine the QE of an overall streak camera detection setup.

3.3.1 PL and PLE Wavelength Spectra Experiment

PL and PLE spectra were collected for every CQD and for each of the dot's structures. The experiments were conducted at approximately room temperature (23 $^{\circ}C$). The following objectives were answered from this experiment:

- Do any of the materials in the fabricated structures deviate from supplier specifications?
- Do emitted and absorbed PL emission spectra change across different structures?

The experimental setup used a PL spectrometer system called the Horiba-Jovin Fluorolog-3 and can be seen in Figure 64.

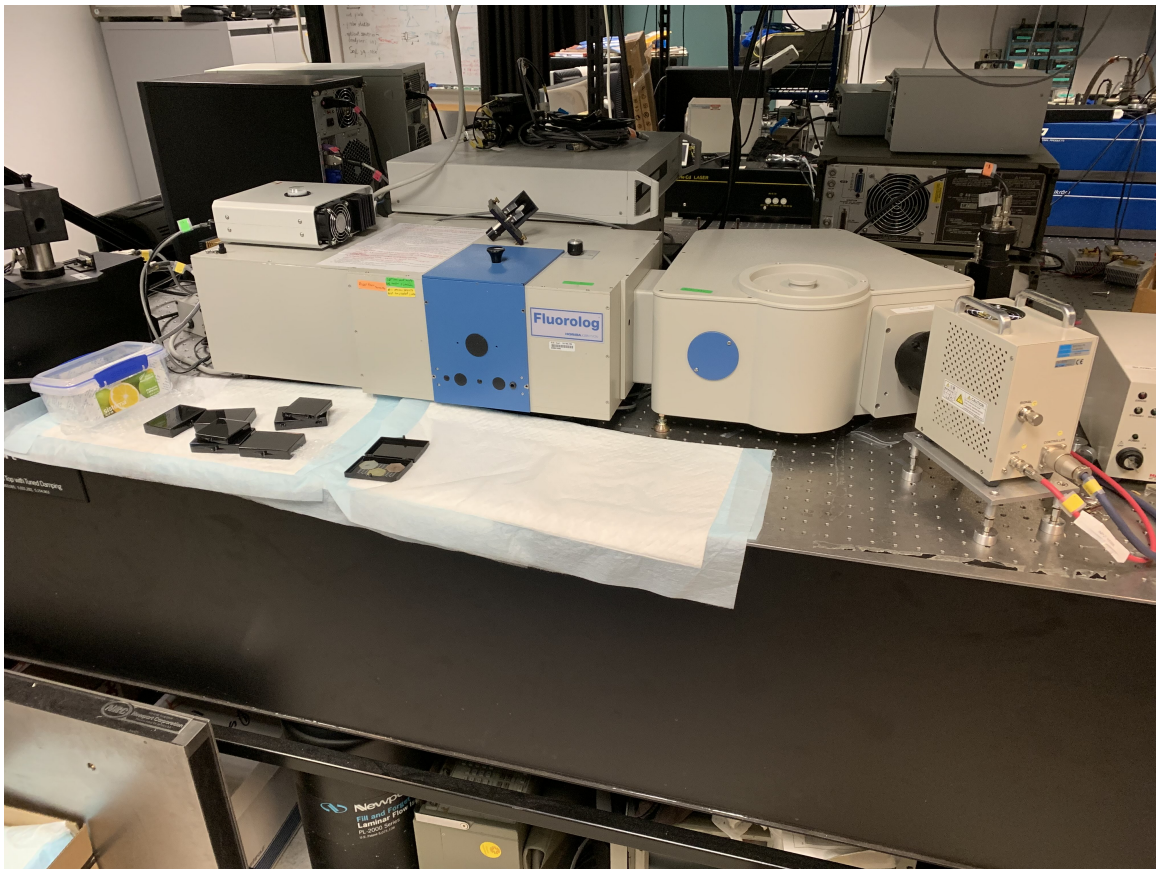


Figure 64. Experimental setup using a Horiba-Jovin Fluorolog-3 system.

The following settings on the Horiba-Jovin Fluorolog-3 were used to collect both the PL and PLE spectras:

- Rotation of sample holder: right-angle
- Sample holder angle: 30 °
- Integration time: 0.1 s
- Wavelength increment: 1.00 nm
- Side entrance slit: 1.00 nm
- Front exit slit: 1.00 nm

- Grating: Density 1200 (Blaze: 500)
- Averaged Scans: 5

All PL intensity data collected for the PL spectra experiment were normalized due to the differences in photon counts between different CQDs and the intensity of the excitation lamp was not constant throughout the entire excitation range of the Horiba-Jobin Fluorolog-3 as can be seen in Appendix Y. This experiment was designed to compare how peaks shifted, widened, or narrowed depending on the material and structure being used. QE data was not possible to collect due to issues with the hardware preventing the acquisition of the QE data.

3.3.2 UV-Vis Temporal Response Experiment

For each CQD sample, the baseline temporal response under UV excitation would be useful. The experiment was conducted at CINT within Sandia National Laboratory (SNL). The PL decay temporal resolution was 500 ps. The machine used was the PTI Felix 32 Spectrofluorimeter. The following machine settings were used for each PL decay spectra:

- Averaged Decays: 3
- Integration time: 0.5 s
- Number of points: 100

There were two reliable methods that can fit an empirical model to the decay curves: Xu and bi-exponential fitting. Due to project scope considerations, bi-exponential fitting was the only model used. It was represented by Equation 37.

$$F(t) = F_0 + A_1 \ \exp -\frac{t - t_0}{\tau_1} + A_2 \ \exp -\frac{t - t_0}{\tau_2} + ... \tag{37}$$

- F_0: Initial intensity
- A: Pre-exponential components
- τ: Decay constant
- t: Time (ns)
- t_0: Initial time (ns)

The bi-exponential model would suffice to make a good approximated fit of a CQD's decay [15]. However, the Xu model was quantum mechanically derived which means the constant values would have physical meaning [157]. Since the data coming from CINT was already a fitted-model of the PL decay data, a MATLAB script was written to process all of the data. The code can be seen in Appendix Z.13. All PL intensity data was normalized due to the inherent QE between the different flavors of CQDs and structures being used. In addition, normalizing the data made it easier to see the differences between each CQD material and structure being evaluated.

3.4 Pulsed X-ray PL Decay at ANL

An opportunity was taken to test CQDs readily available at LANL at a synchrotron beam line at ANL. It was of note that optimal fabrication processes and experimental preparations could not be done due to the spontaneous nature of this experiment.

3.4.1 Experimental Materials and Equipment

The CQDs used for this experiment were CdSe NPLs and CdSe/CdS CQDs created by both Dr. Igor Fedin and Dr. Victor Klimov at LANL. Equipment utilized for this experiment can be seen in Table 10.

Equipment	Manufacturer	Model
2.5GHz Oscilloscope	Keysight Technologies	InfiniiVision DSOX6004A
Digital Delay Generator	Stanford Research Systems	DG645
Fiber Coupled Collimator	Thorlabs	N/A
Optical Equipment	Thorlabs	N/A
Si Avalanche Photodiode	Menlo Systems	APD-210
High Sensitivity Fast Photodetector	Menlo Systems	FPD610-FC-VIS
High Speed Fiber Coupled Detector	Thorlabs	DET08CFC

Table 10. Equipment used at Argonne National Laboratory experiment.

The capabilities of the beam line facility in Sector 32 at ANL were the following: white beam up to 100 keV, monochromatic beam up to 38 keV, max shutter speed of up to 10 μs, and shortest pulse delays of 200 ps. The white beam at Sector 32 was created through the use of an undulator. The majority of the emitted x-rays were at the average energy emission, where additional harmonics of the x-rays become more and more attenuated. The monochromatic beam has an energy resolution of 5 eV and can go up to 38 keV. However, changing from the white beam line to the monochromatic beam line required a three hour setup. It was decided that the best use of limited beam time was to continue using the white.

3.4.2 Experimental Setup

The experimental setup in the beam line facility at ANL can be seen in Figure 65.

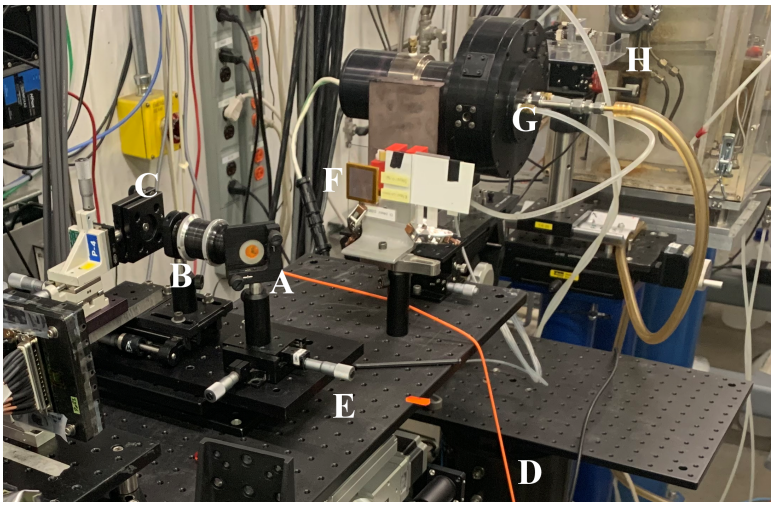


Figure 65. Setup of CQD experiment in ANL's beam line

The labels were defined in Table 11.

Label	Device	Function
A	CQD Sample	Hold CQD sample in front of x-ray beam
B	Collimator	Capture isotropic light emission from CQD sample and focus it into a sharp point
C	Fiber Coupling	Couple focused light from collimator into a fiber cable linked to a photodiode
D	Photodiodes Below	Detect light emission from fiber
E	Vibration Table	Prevent vibrations in building from affecting test results
F	X-ray Attenuator	Lower x-ray dosage to prevent ionizing away sample
G	Shutter	Shutter used to pulse x-rays into experimental setup
H	Beamline Port	X-rays from beamline enter experimental setup from here

Table 11. Table that shows what each device in the experimental handles.

Cabling was routed through the cabling system of the sector to the control room. The oscilloscope was set such that the first channel was the trigger and the other three channels attached to the three types of photodiodes. The fiber from the emission of the CQD was attached to one of the photodiodes at a time. All channel impedances were set to 50 Ω.

3.4.3 Experimental Issues

Unfortunately, no useful data was collected during the experiment, thus no results are shown in Chapter IV for this experiment. A couple of problems contributed to

this:

- Two other experimental teams were running experiments at the same time causing cross-talk to one of the acquisition cables being used
- Allocated time for the experiment was significantly shortened to adjust optical setup
- No operator of this sector was available, thus time was spent trying to figure out the sector's controls
- Poor labeling of sector controls caused time spent trying to understand what each piece of equipment controlled
- Low PL emission from CQDs under test may have required the use of a streak camera to act as a single photon counting mode or integrate the signal coming from the photodiodes over multiple pulses

3.5 Pulsed X-ray PL Decay

With a lack of available dedicated pulsed x-ray sources, an alternate approach was used which employed a continuous x-ray source and utilize geometrical distance to avoid pile-up. The continuous x-ray source would use bremsstrahlung and be fitted with filters to get a desired x-ray energy. A bremsstrahlung source could act as a pulsed x-ray source with the detector placed far enough away to allow the scintillating medium to fully decay before the next photon interacts with it. It was assumed that air would be the only medium between the scintillator and the continuous x-ray source. Since the x-ray source equipment to be used was not known, it was decided to use MCX Studio. This MC algorithm took advantage of Graphical Processing Unit (GPU) processing power. Using Monte Carlo eXtreme (MCX) Studio would be able

to simulate any x-ray emission geometry and was quick to use rather than showing all possible hand-calculations.

One of the first steps in determining how many photons make it to the detector would be to calculate the solid angle, which is defined as the geometric efficiency between the radiation source and the detector. The solid angle can be seen in Equation 38.

$$\Omega = \frac{\text{Photons that Hit Detector's Surface}}{\text{Emitted Photons From Source}} \tag{38}$$

Every geometry between the detector's surface and the type of radiation source can be worked into Equation 38. When working with single photon counts, the solid-angle should be low to avoid pile-up.

3.5.1 Setting Up MCX Studio

MCX Studio was an open source software maintained by both Dr. Qianqian Fang and Dr. David Boas who both worked at Martinos Center for Biomedical Imaging during their first publication of the software in 2009. The software was funded by the National Institute of Health (NIH) and primarily used for simulating photon interaction within brain matter. However, the program could easily be used to calculate geometric efficiencies for use in radiation detection. The well designed Graphical User Interface (GUI) makes running simulations easy, without the need to always use code. If coding was needed for more complicated instructions, MCX Studio was designed to work with MATLAB. Downloadable instructions can be found on their website. The installation of MCX Studio for Compute Unified Device Architecture (CUDA) does not lead to any results unless the workstation being used had a CUDA enabled GPU [47].

3.5.2 Verification of MCX Studio Results

The methodology to verify MCX Studio was to take the radius of the scintillator (in this case 6.35 mm) and assume it was 2 m away from the source. The source was simulated as an isotropic point source. One billion photons were used in the simulation, which only took 2.27 minutes to complete. The GPU used in this test was a EVGA NVIDIA 1080TI FTW3. This GPU had 3,584 CUDA cores. A 3D fluence volume model of the isotropic point source can be seen in Figure 66.

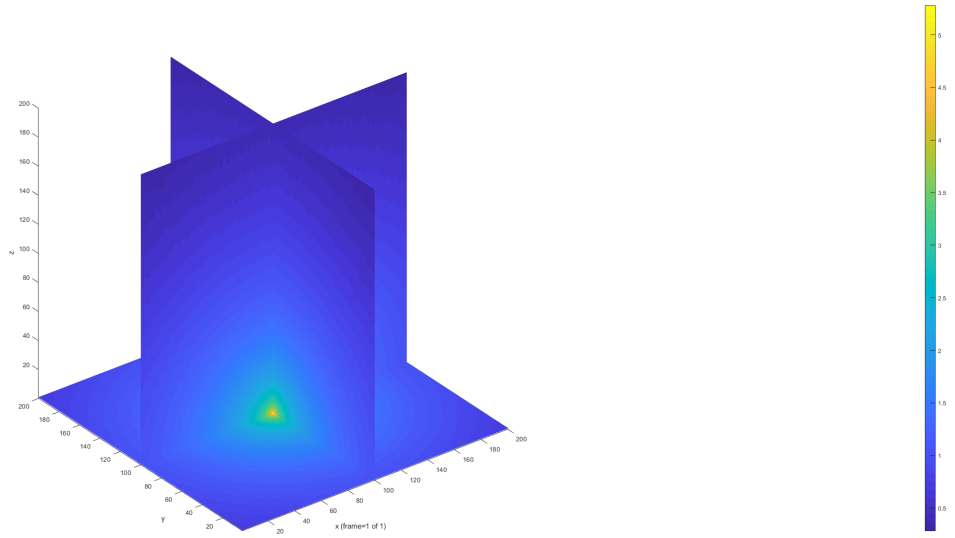


Figure 66. Isotropic point source photon distribution. Simulated using MCX Studio [47].

The detector in the simulation counted 2,540 photons out of the one billion simulated. This led to a solid-angle of 2.54×10^{-6}. This value can be compared to a hand calculation, assuming the point source was within a sphere and the detector was on some part of the surface of the sphere. Details of the formula derivation can be read in Tsoufandis *et al.* and the final equation can be seen in Equation 39. This equation assumed that the radius of the detector was much less than the distance between the source and the detector [145].

$$\Omega = \frac{\pi\ R^2}{4\ \pi\ d^2} \tag{39}$$

Where the variables for Equation 39 are listed below:

- R: radius of the detector (m)
- d: distance from the source to the detector (m)

Using 2 m for the distance and 0.00635 m for the detector's radius, the solid-angle became 2.52×10^{-6}. This value was approximately equal to the MCX Studio simulated value. The slight discrepancy between the two values can be attributed to the fact that Equation 39 was an approximation of the solid-angle. Second, MCX Studio cannot run unless there was some absorption and scattering coefficient added to the simulation. These coefficients were made to be small enough to not have a noticeable effect on the results. The simulation noted that 0.07145% of the energy was absorbed. Third, due to the large volume, more simulated photons would help to reduce the error.

3.5.3 Simulating MCX Studio Results for a Topical Case

The continuous x-ray source was assumed to be a cone source. The angle of this cone source was not known, however to run an example, 0.785 half-angle radians was assumed. This value correlated to a 45° half-angle. One billion photons were simulated. This resulted in the 3D fluence volume model seen in Figure 67.

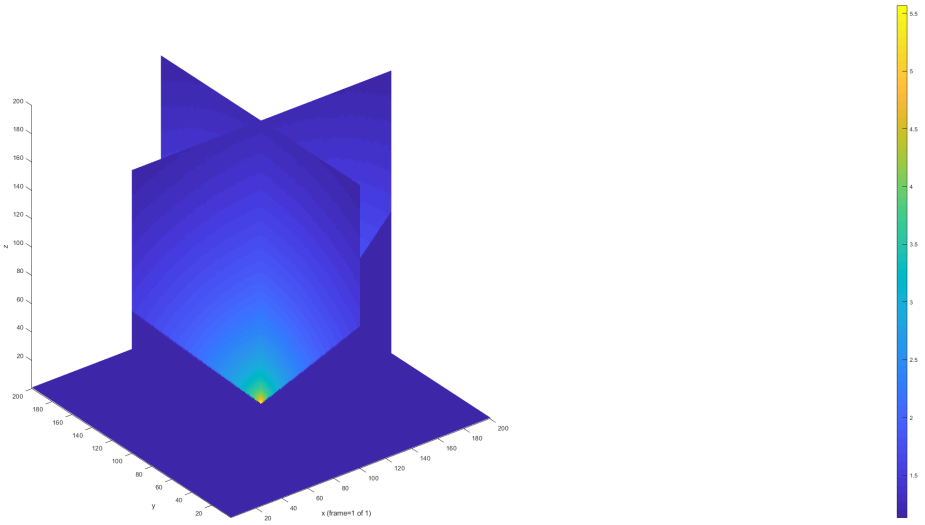


Figure 67. Cone source photon distribution similar to the emission of a bremsstrahlung x-ray tube source. Simulated using MCX Studio [47].

This simulation took 6.04 minutes to complete. The total number of detected photons was 17,286 out of one billion total. These two values yielded a solid angle of 1.7286×10^{-5}. This simulation setup can be used for any x-ray source and detector setup that a team may have used. With the solid angle/geometric efficiency found, this value can be coupled to the detector's efficiency.

3.5.4 Characterizing X-ray Emission

To determine the x-ray flux interacting with the CQD sample, a calibrated NaI(Tl) PMT can be used in current integration mode, with the PMT located exactly where the CQD sample would be located [70] [108]. To calibrate the NaI(Tl) PMT, a characterized planchet disk multi-nuclide source could be used at a prescribed distance from the detector such that it prevents both pile-up and long acquisition times. A best-fit curve could then be made to relate the peaks of the spectra taken with the PMT to the energy emission from the multi-nuclide source. Due to the non-linearity of NaI(Tl) scintillators, some error would be expected [46].

3.5.5 Pulsed X-ray Experimental Setup

Due to the low photon emission of CQDs, the most feasible setup would be to mirror what Turtos *et al.'s* team has done by using a streak camera in single photon counting mode. The x-ray experimental setup can be seen in Figure 68.

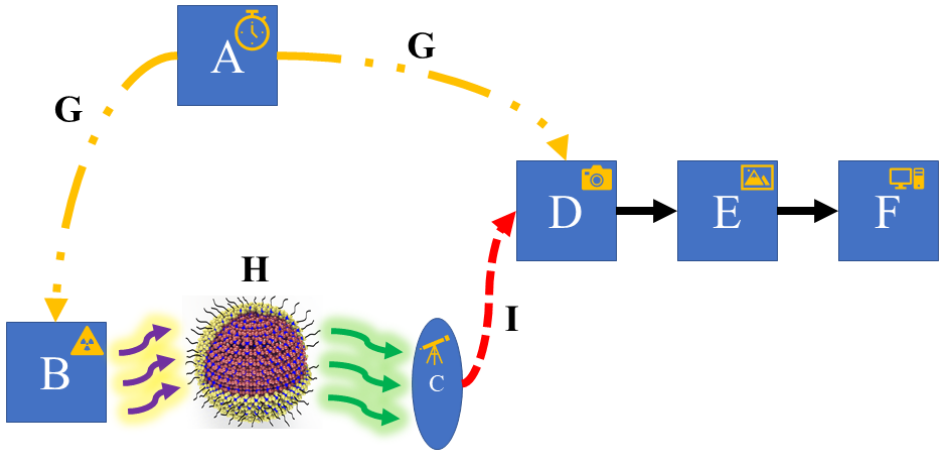


Figure 68. Pulsed x-ray detection setup to test CQD samples.

The equipment and processes seen in Figure 68 are detailed below:

(A) Digital delay generator (DG-645)

(B) X-ray source shutter → Purple arrows with yellow glow going from B to H: x-ray flux

(C) Collimator lens optics guiding light to (I) fiber optic cable

(D) Streak camera with S20 photocathode (Hamamatsu)

(E) Apogee scientific camera

(F) Computer saving streak camera images from Apogee scientific camera

(G) Pulsed timing signal sent to both (B) x-ray source shutter and (D) streak camera

(H) CQD under test → Green arrows with green glow going from H to C: light emitted from CQD

(I) Fiber optic cable guiding light to (D) streak camera

Due to time constraints, the layout of this experiment was written out in this chapter. The experiment would be a part of future work.

3.6 X-ray Lifetime Decay

This experiment would be the last experiment for each material due to the test's destructive nature. A continuous x-ray source would be set to emit on average 100 keV x-rays to irradiate the CQDs towards complete photobleaching. A 451B Ion Chamber Survey Meter with Beta Slide from Fluke would be used. This ion chamber would allow the use of RS-232 communication for real-time data logging of the integrated radiation dose. Both the CQD under test and the ion chamber would be positioned side-by-side. The CQD under test would be emitting to a collimator, fiber coupled to a PMT. A computer would be data logging the optical response of the CQD and the ion chamber at the same time. The equipment setup can be seen in Figure 69.

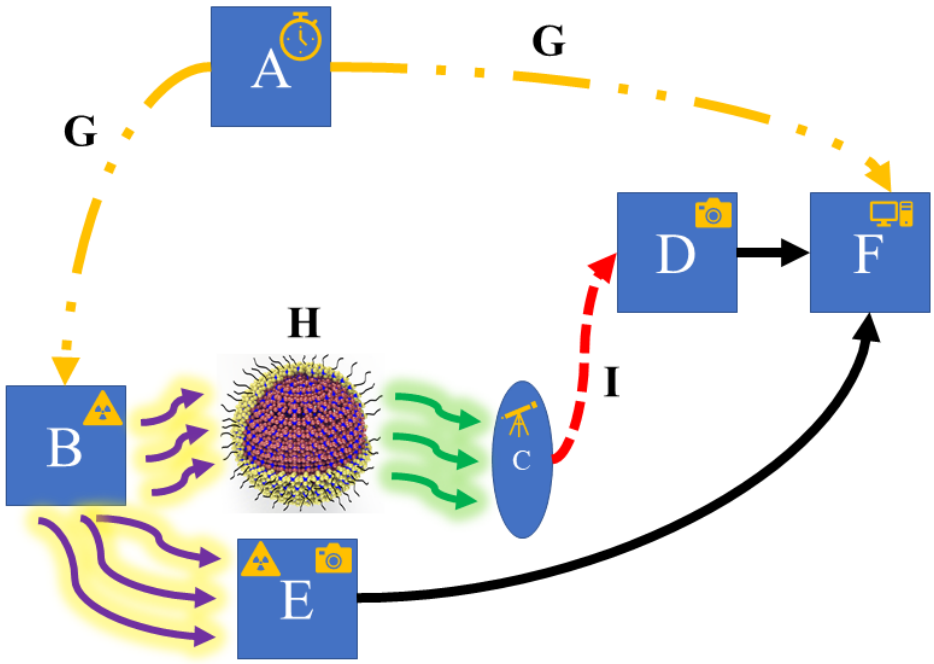


Figure 69. Lifetime x-ray exposure setup to test CQD samples at 100 keV.

The equipment and processes seen in Figure 69 are detailed below:

(A) Digital delay generator (DG-645)

(B) X-ray source shutter → Purple arrows with yellow glow going from B to H and E: x-ray flux

(C) collimator lens optics guiding light to (I) fiber optic cable

(D) PMT

(E) Ion chamber measuring integrated dose sending real time values to (F) computer

(F) Computer acquiring both PMT values and ion chamber

(G) Pulsed timing signal sent to both (B) x-ray source shutter and (E) computer

(H) CQD under test → Green arrows with green glow going from H to C: light emitted from CQD

(I) Fiber optic cable guiding light to (D) PMT

Due to time constraints, the layout of this experiment was detailed in this chapter. This experiment would be a part of future work.

After noticing CT effects, a 3^2 full factorial experiment was done to look into CT controllability by changing the 3D printed structure fabrication process.

3.7 3^2 Two Factor Experimental Setup from PL Spectra and PL Decay Measurements

After conducting the PL spectra experiment, it was noticed that there was a blue-shifted secondary PL peak for a few of the PL spectras using the 3D printed structure. To further investigate what occurred, two 3^2 factorial experiments (PL spectra and PL decay data) were conducted to see how changing the thickness of the 3D printed structure and the amount of CQDs loaded within the 3D printed structure affected both the relative blue-shifted secondary peak intensity and the decay rate of the CQD's main emission peak. It was later determined that both the thickness of the 3D printed structure and the amount of CQDs loaded within the 3D printed scintillator had an effect on CT. A CT peak occurred at $\approx 460\ nm$. This peak only occurred when CQDs were loaded as the control case showed a peak at $\approx 350\ nm$. The PL intensity of the CT peak at $\approx 460\ nm$ was collected for each level for the PL spectra experiment. This factorial experiment was done to find an empirical formula to tune the amount of desired charge transfer and motivate future research into this area. In addition, the PL decay time of the 520 nm-530 nm peak emission wavelengths of the CQDs were measured to determine if the two factors tested had an effect on the PL decay time and if it could be tuned.

Due to a limited supply of CQDs, two CQD materials were used. The primary

CQD used was CdSe/ZnS emitting at 520 nm, while the second CQD was InP/ZnS emitting at 530 nm. Both CQDs were excited with the same excitation wavelength and have similar emissions. Since the QE's were not the same, the photon count cannot be compared. The rationale behind using InP/ZnS compared to the other available CQDs was as follows:

- Similarities in CQD structure to CdSe/ZnS
- Both used a ZnS shell and two elements to make up their core
- Same manufacturer
- Ligands were not the same between the two CQDs, however they were designed to be used in the same material matrix
- Ligand carbon chain lengths were the same

A 3^2 factorial experiment has the following regression model in Equation 40 [92]:

$$y = \beta_0 + \beta_1\ x_1 + \beta_2\ x_2 + \beta_{12}\ x_1\ x_2 + \beta_{11}\ x_1^2 + \beta_{22}\ x_2^2 + \epsilon \tag{40}$$

The nature of this design allows for the following Degrees-of-Freedom (DOF) seen in Table 12.

Source	DOF
A	2
B	2
AB	4
Residuals	$3^2\ (n-1)$
Total	$n\ 3^2 - 1$

Table 12. DOF of each source in a 3^2 factorial experiment where n is the number of replicates.

Where n represented the number of replicates or trials. The replicates for the PL spectra experiment were averaged five times over for further accuracy. The equipment used for the PL spectra experiment was the Horiba-Jobin Fluorolog 3. For the PL decay experiment, no replicates were done due to time-constraints. The equipment used for the PL decay experiment was the PTI Felix 32 Spectrofluorimeter. The 3^2 experimental layout can be seen graphically represented in Table 13 where the material used for each level was noted. In addition, all data collected for both the PL spectra and PL decay experiments were normalized due to the differences in photon counts due to inherent QE of both the CdSe/ZnS and InP/ZnS CQDs.

Factor	240 μm **Thickness**	480 μm **Thickness**	960 μm **Thickness**
40 μL **Concentration**	CdSe/ZnS	InP/ZnS	CdSe/ZnS
80 μL **Concentration**	InP/ZnS	CdSe/ZnS	CdSe/ZnS
160 μL **Concentration**	InP/ZnS	InP/ZnS	CdSe/ZnS

Table 13. 3^2 factorial experiment setup. In addition, the CQD material used for each level was annotated since a lack of resources required using two similar CQDs for this experimental study.

Due to time constraints, this experiment was not conducted in random run order.

3.8 Strain NDT Test

In addition to the x-ray detection application of CQDs, the strain properties of CQDs were investigated as another potential NDT without the need to use radiation.

3.8.1 Micro-Electro-Mechanical Systems (MEMS) Lab-On-A-Chip

A useful way to test the strain PL emission properties of varying CQD materials would be to use MEMS [165]. There are a variety of fabrication methods to develop MEMS devices that can strain CQDs. However, it would be beneficial to

use an affordable, commonly used, easy to design, and easy to mass produce process called PolyMUMPs. A MEMS cantilever, with its physics well defined and ease of design, can be used to strain a thin-film of CQDs within a polymer. In addition, the PolyMUMPs process has not been used to strain CQDs yet, especially as a polymer thin-film. Additional information regarding the theory and the design process behind the PolyMUMPs process can be seen on MEMSCAP's website [88]. MEMSCAP L-Edit software is used to design the masks in this process. Details involving the fabrication process, simulations, and initial results can be seen in Appendix C. An example of one of the masks designed in L-edit can be seen in Figure 70.

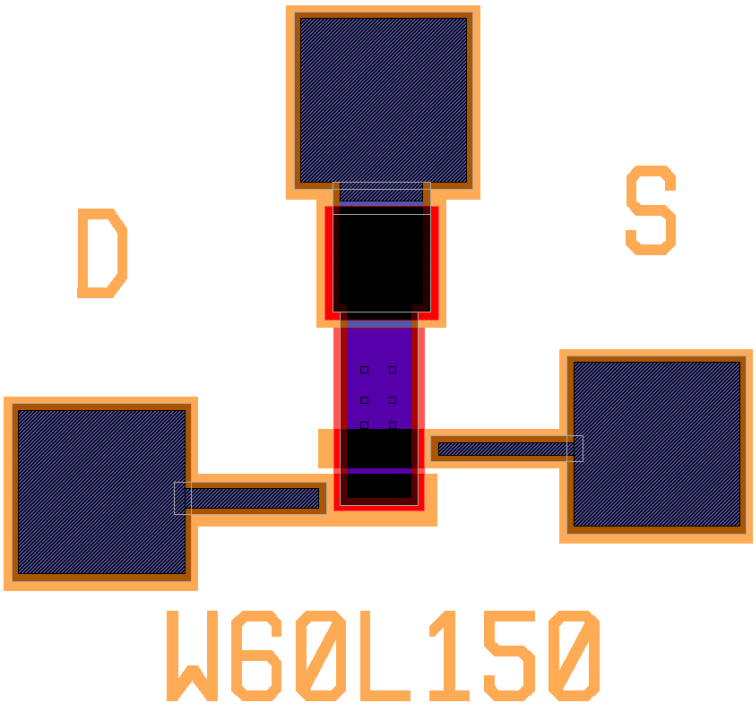


Figure 70. A 150 μm **long and** 60 μm **wide MEMS cantilever designed in L-edit.**

The design was sent to the foundry and the cantilever was released after its arrival in a Class 1000 clean room. A SEM image of the released cantilever can be seen in Figure 71.

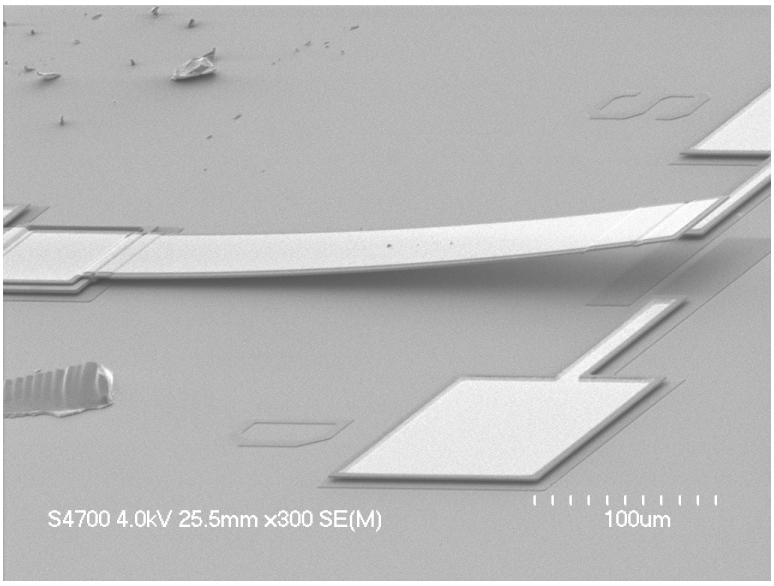


Figure 71. SEM image of one of the multiple cantilevers fabricated to characterize the strain effects of CQDs. SEM settings used in the capturing of this photo were: x300 magnification and 4 kV emission energy.

Bond pads were designed to be 150 μm by 150 μm and were plated with gold. The transmission line between the drive and sense bond pads to the cantilever were also coated in gold in order to minimize resistance. The ground bond pad was located right behind the cantilever to minimize parasitics.

The MEMS cantilever was designed to be as tall as possible in order to maximize strain on the CQDs layer. Dimples were naturally created over the transmission lines coming from the bond pad in order to minimize the effects of stiction while being released. A sacrificial poly1 layer was used to raise up the poly2 layer. It should be noted that in order to ensure the poly2 layer remains attached to the anchor, the poly1 layer was positioned to be as close to the anchor as possible. This resulted in a small trench within the poly2 layer being connected to the anchor as seen in Figure 73. The trench was not an issue for the cantilever.

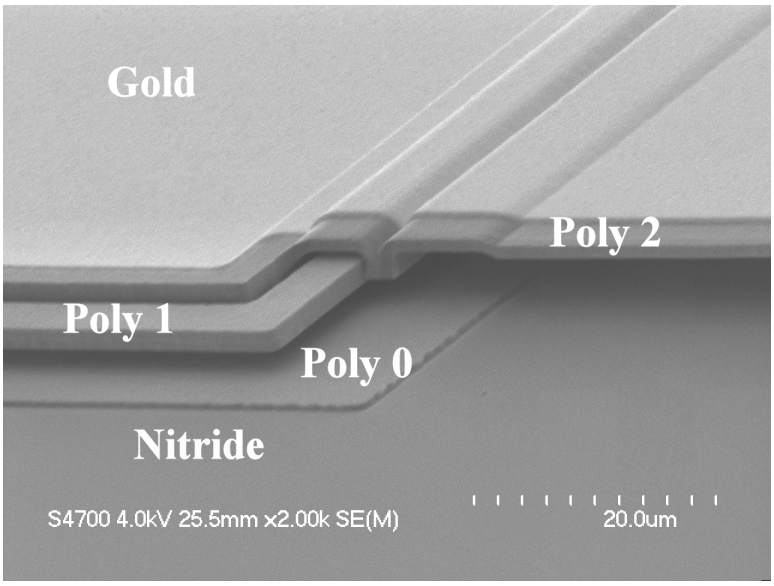


Figure 72. SEM image showing all the layers used in the PolyMUMPs processed and taken at the connection point between the poly2 layer and the anchor. SEM settings used in the capturing of this photo were: x2000 magnification and 4 kV emission energy.

An unintended consequence of maintaining sacrificial poly1 layer consistency underneath under the poly2 layer was difficulty in removing it during the release process. A clear example of a release failure mode can be seen in Figure 73.

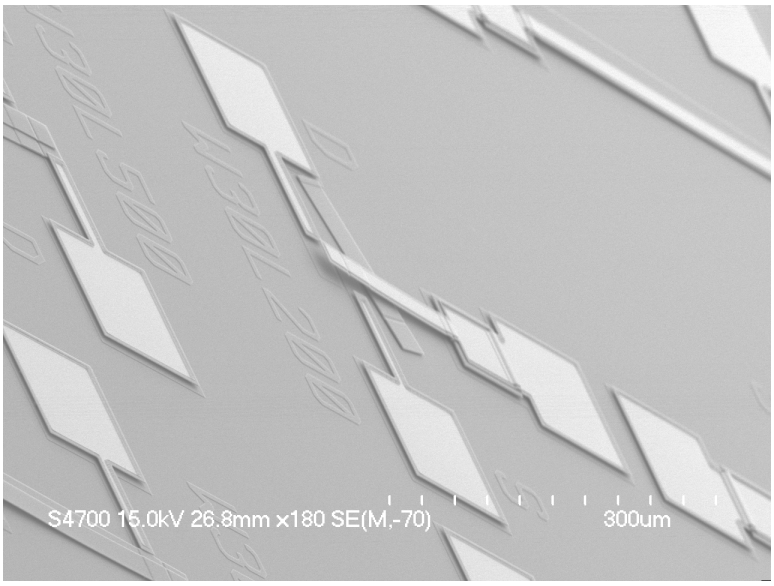


Figure 73. This SEM image showed a release failure mode of the sacrificial poly1 layer. The poly1 layer was unable to get fully out from under the cantilever poly2 layer. SEM settings used in the capturing of this photo were: x180 magnification and 15 kV emission energy.

Fortunately, there was a way to remove the stuck sacrificial poly1 layer by using a probe to carefully drag it away from the cantilever. This was not always successful, however this led to a recommendation for a future design of this MEMS chip to break apart the poly1 layer underneath the poly2 layer instead of using a continuous slab. While there was not enough time to conduct the post-processing steps, there would, in actuality, be both the CQD layer and the gold capping layer to protect the CQD layer from the Hydrofluoric Acid (HF) release. Both of these layers would be fabricated after the MEMS wafer was fabricated using PolyMUMPs, and before release of the MEMS device.

3.8.2 Macro Scale Dog-Bone Test

Due to the MEMS based Lab-On-A-Chip concept requiring significant amounts of additional work to properly make, it was decided to do a macro scale test to evaluate the feasibility of optically sensing strain with CQDs. InP/ZnS CQDs supplied

by NN-Labs were used. A CQD emission wavelength of 530 nm was selected due to the color green being friendly for the majority of readily available optical equipment. InP/ZnS was also chosen because of environmental concerns of cadmium and lead exposure if used as a coating for airplanes [122].

The InP/ZnS CQDs were loaded into a proprietary polymer 10% by weight made by NN-Labs (can be thought of as PMMA in similarity). They were coated as a thin-film onto three Solvay BR 6747-1 coated 301 stainless steel dog-bone samples. This was done by using one side of a metal tweezer and coating about one inch in length and the entire width of the dog-bone on one side. The polymer was applied approximately in the middle of each dog-bone. They were then placed in a convection oven and baked at 121.11 $^{\circ}C$ for 23 minutes and 30 seconds. This resulted in a hardened and cured polymer thin-film. A Leica DVM6 microscope was used to characterize the thickness of the polymer matrix thin-film. A 3D surface image taken with the microscope can be seen in Figure 74.

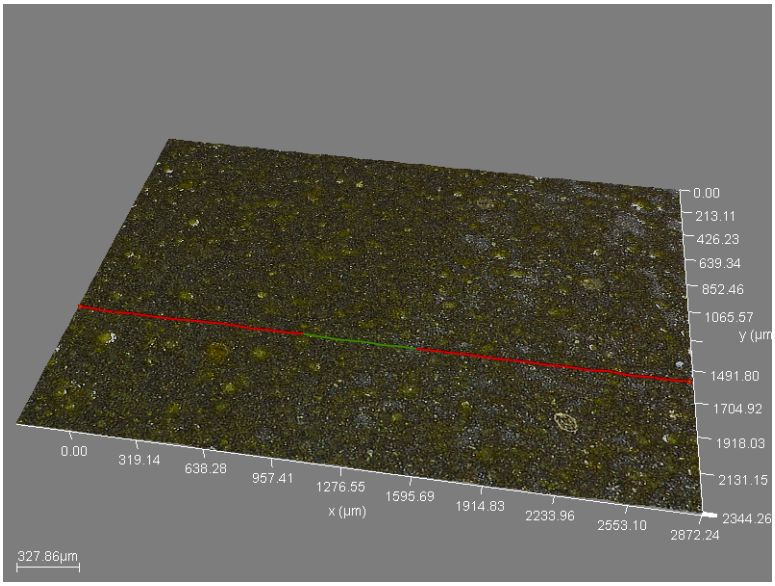
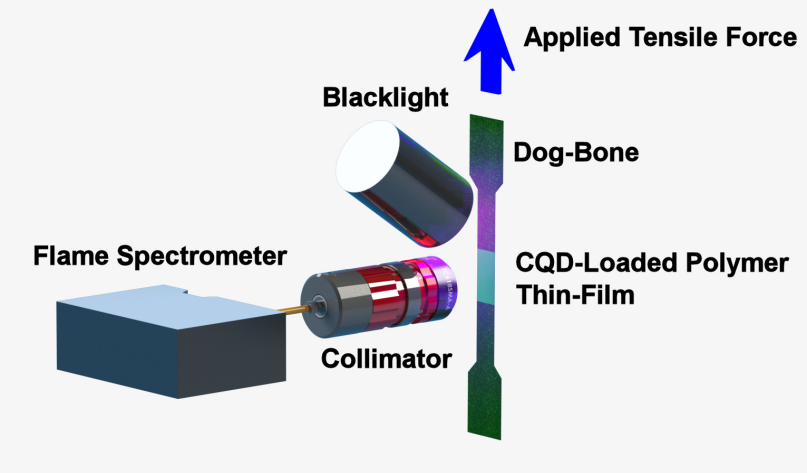


Figure 74. 3D surface model of the coated 301 stainless steel dog-bone with CQD polymer matrix applied. Taken with the Leica DVM6 microscope. Left half of the image contained the CQD-loaded polymer matrix coating while the right half was only the pre-coating (Solvay BR 6747-1) on top of the 301 stainless steel. Microscope settings: 0° tilt, Z-step size of $0.25\ \mu m$, and a FOV3.6 lens.

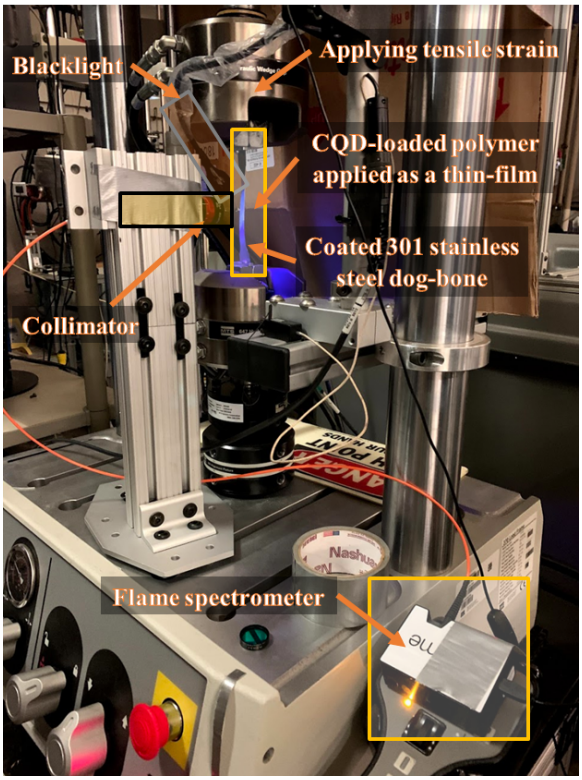
The surface was observed to be rough, which helped the polymer better adhere to a metallic surface. The Leica microscope calculated the maximum/minimum thickness across the CQD polymer matrix and no CQD polymer matrix boundary as $14.10\ \mu m \pm 0.125\ \mu m$ and $5.42\ \mu m \pm 0.125\ \mu m$ respectively. The mean thickness across this section was $9.25\ \mu m \pm 0.177\ \mu m$. There appeared to be no clear section that had a thicker area and a thinner area of CQD-loaded polymer, thus what most likely occurred was that the CQD polymer matrix was applied within the grooves and valleys of the pre-coating on the surface of the 301 stainless steel dog-bone.

Tensile force to the dog-bone was applied by using a stress-strain machine made by MTS Systems Corporation. The load frame's model number was 370.02. Its rated capacity was 25 kN, actuator force capacity was 25 kN, actuator dynamic stroke was 100 mm, actuator total stroke was 114 mm, actuator rated flow was 57 lpm, manifold

rated flow was 57 lpm, and bearing type was standard. The force transducer's model number was 661.19H-04. The experimental setup can be seen in Figure 75.



(a) Illustration of experimental setup.



(b) Labeled photo of experimental setup.

Figure 75. A flame fiber optic spectrometer (model: FLAME-S-VIS-NIR) sold by Ocean Optics was secured to the load frame and fiber optically connected to a Thorlabs zoom fiber collimator ZC618APC-A. A standard blacklight was clamped to the load frame. A dog-bone cured with a sample of InP/ZnS CQDs loaded in a proprietary polymer was placed between the load frame's clamps. A piece of cardboard was used to help lessen the intensity of the overhead lights (background noise) in the laboratory. (a) illustration of the experimental setup. (b) labeled photo of the experimental setup.

The Flame spectrometer's software was set to integrate light over one second increments. Start time between the load frame and the spectrometer acquisition was done by two researchers coordinating in pressing the start button on their piece of equipment. This would result in a error to the timing of at most one second. The applied pulling distance rate on the dog-bone was $0.00087750\frac{in}{s}$. A program was written in order to import the numerous text files created by the Flame spectrometer's software and the stress-strain excel data. It then created a video of the stress-strain curve correlated to the PL emission spectra of the CQDs to find trends. This code can be seen in Appendix Z.8.

IV. Results and Analysis

This chapter focused in on the results of each of the models and experiments discussed in the previous chapter. The results obtained will be provided for: x-ray attenuation thickness and QE modeling using MATLAB, PL spectra experiment, PL decay time experiment, 3D Print 3^2 Factorial Experiment, and CQD strain experiment.

4.1 X-ray Attenuation Thickness and QE Modeling Using MATLAB

4.1.1 Incident X-ray Attenuation Experiment Written in MATLAB Results

Four cases were tested and used in the weighted scoring of each CQD material. The four cases being:

- 100 keV with 99% of incident x-rays absorbed/scattered
- 100 keV with 10% of incident x-rays absorbed/scattered
- 10 keV with 99% of incident x-rays absorbed/scattered
- 10 keV with 10% of incident x-rays absorbed/scattered

Each of the four cases contained different rankings. Thus, thickness values for each CQD material for each case would need to be discussed; not just the final comparison results. Keep in mind that in this experiment, the thickness for getting a certain probability of x-rays to initially interact with the scintillating material was considered. Secondary and tertiary effects were not considered, which in turn may require a larger thickness to fully stop the incident photon flux. However, this experiment works to show in general how much more effective one material would be compared

to another when it comes to having an x-ray interact with it.

Results of the first case of 100 keV with 99% of incident x-rays absorbed/scattered can be seen in Table 14.

Material	**Thickness (μm)**	**Ranking**
PbS	4,414.19	8
PbSe	5,165.11	7
CdSe	20,925.43	6
CdS	23,609.74	5
InP/ZnS	43,216.95	4
Sapphire	45,488.01	3
CdSe/ZnS	49,145.35	2
CuInS/ZnS	52,224.74	1

Table 14. Modeled thickness of CQDs within a PMMA polymer at 10% loading by volume. 100 keV incident x-rays were sent through and thickness set to have 99% of the incident x-rays absorbed/scattered. Scores range from 1-8, with 8 being the best material for this experiment.

From Table 14, PbS had the smallest thickness, while CuInS/ZnS had the largest thickness. What was also of interest was that the additional ZnS shell made their respective materials require a larger thickness than their core-only counterparts. This was due in part to Zn having a lower Z value than the core material Cd. However, it would also be partly due to the size of the CQD as well. When considering a loading volume of 10% within a PMMA matrix, the entire cubic volume of the CQD within the PMMA matrix would be larger length wise than a smaller core only CQD. Thus, more higher Z material can be packed in a given volume with core only CQDs than the larger core/shell CQDs which have about half of the CQD's volume in lower Z material. An unexpected result was also seen where CQDs containing sulfides had

a lower thickness than the ones containing the higher Z selenide. This was because of CQD size. Unlike adding ZnS shell (which causes a larger diameter CQD) causes a larger thickness, having a larger core geometry does not mean a larger thickness. This makes sense as both the high Z lead atoms and the low Z sulfide atoms would contribute to the mass attenuation coefficient throughout the entire core geometry. Conversely in CQDs with shells, both the low Z materials zinc and sulfide would only contribute throughout their portion of the volume of a CQD. Thus, x-ray interaction would be dependent on how much of the overall volume of a CQD contains a high Z material. Notice that the difference between PbS and PbSe for example was small. However, this difference in thickness may matter for applications which have limited space with which to work with.

The results of the second case of 100 keV with 10% of incident x-rays absorbed/scattered can be seen in Table 15.

Material	**Thickness (μm)**	**Ranking**
PbS	100.99	8
PbSe	118.17	7
CdSe	478.75	6
CdS	540.16	5
InP/ZnS	988.75	4
Sapphire	1,040.71	3
CdSe/ZnS	1,124.38	2
CuInS/ZnS	1,194.84	1

Table 15. Modeled thickness of CQDs within a PMMA polymer at 10% loading by volume. 100 keV incident x-rays were sent through and thickness set to have 10% of the incident x-rays absorbed/scattered. Scores range from 1-8, with 8 being the best material for this experiment.

It can be seen that in Table 15 the ranking of each CQD material did not change from Table 14. While the rankings of the materials did not change, the difference in values between the thickest and thinnest values became significantly closer. Going from 99% interaction probability to 10% made the spread from thickest to thinnest values 44x smaller. This matters since CdSe/ZnS would definitely not be a good choice for interacting with 99% of the incident x-ray flux, but becomes more viable when the interaction percent is lowered.

The results of the third case of 10 keV with 99% of incident x-rays absorbed/scattered can be seen in Table 16.

Material	**Thickness (μm)**	**Ranking**
PbS	186.71	8
CuInS/ZnS	205.95	7
PbSe	213.12	6
CdSe/ZnS	217.47	5
InP/ZnS	224.11	4
CdSe	273.05	3
CdS	324.20	2
Sapphire	381.22	1

Table 16. Modeled thickness of CQDs within a PMMA polymer at 10% loading by volume. 10 keV incident x-rays were sent through and thickness set to have 99% of the incident x-rays absorbed/scattered. Scores range from 1-8, with 8 being the best material for this experiment.

From Table 16, lowering the incident x-ray energy from 100 keV to 10 keV changed the material rankings. ZnS shells now make their respective CQDs better at interacting with the incident x-ray. Despite the Sapphire CQD having numerous shells which should now make it more effective, the size of the CQD still makes it harder to

pack more CQDs in a given volume. However, the spread between the thickest and thinnest material became $\approx 100\ \mu m$.

The results of the fourth and final case of 10 keV with 10% of incident x-rays absorbed/scattered can be seen in Table 17.

Material	**Thickness** (μm)	**Ranking**
PbS	4.27	8
CuInS/ZnS	4.71	7
PbSe	4.88	6
CdSe/ZnS	4.98	5
InP/ZnS	5.13	4
CdSe	6.25	3
CdS	7.42	2
Sapphire	8.72	1

Table 17. Modeled thickness of CQDs within a PMMA polymer at 10% loading by volume. 10 keV incident x-rays were sent through and thickness set to have 10% of the incident x-rays absorbed/scattered. Scores range from 1-8, with 8 being the best material for this experiment.

Table 17 did not change the rankings from the 99% case, however the spread became even smaller. From PbS to CdSe/ZnS, nanometers of material now show their differences. From Sapphire to PbS, the difference is $\approx 4\ \mu m$.

Taking all of the above tables and incorporating them into a final weighted score, the standard deviation of each table was calculated. Then, the score of each material was multiplied by how much of the standard deviation percentage a test had over all four tests. This places more emphasis on the scores with a greater difference than the scores with less of a difference instead of treating each test equally. The standard

deviation table and the percentages used to calculate the weight percent can be seen in Table 18.

Test	Standard Deviation	Weight (%)
100keV - 99% Absorption	18,260.08	97.42
100keV - 10% Absorption	417.77	2.23
10keV - 99% Absorption	63.45	0.34
10keV - 10% Absorption	1.45	0.0077

Table 18. Standard deviation of each test and the weight importance as a percentage for each test resulting from the standard deviation.

The weighted scores from this experiment can be seen in Table 19.

Material Score	**Weighted Score**
PbS	8.00
PbSe	7.00
CdSe	5.99
CdS	4.99
InP/ZnS	4.00
Sapphire	2.99
CdSe/ZnS	2.01
CuInS/ZnS	1.02

Table 19. Weighted scores of each CQD material for the x-ray absorption/scattering thickness experiment. Final scores range from 1-8, with 8 being the best material for this experiment.

What would be apparent from Table 19 would be the even divide between core materials and core/shell materials. The smaller diameter CQDs were able to be packed into a denser configuration than the larger counterparts, resulting in a higher probability to interact with an incident x-ray. This experiment by itself does not

properly rank the CQDs. For example, the QE of each material would need to be considered when looking at photon emission from the CQDs. This was what the monolayer QE experiment examined.

4.1.2 Monolayer QE Experiment Written in MATLAB Results

It was found that the MC simulation was repeatable using a 8×10^3 nm diameter monolayer of CQDs at 10 keV. For 100 keV, it was found that a 22×10^3 nm diameter simulated an acceptable amount of error.

To show repeatability of the 10 keV case, two tests were done and their respective QE values can be seen in Table 20.

Material	QE Test 1 (%)	QE Test 2 (%)	% Difference
Sapphire	2.860	2.912	1.818
PbS	1.672	1.652	1.238
CdSe/ZnS	1.450	1.473	1.559
PbSe	1.037	1.027	0.928
CuInS/ZnS	0.889	0.885	0.445
InP/ZnS	0.779	0.782	0.417
CdS	0.544	0.550	0.959
CdSe	0.348	0.350	0.665

Table 20. Repeatability test of the MC simulation with 10 keV incident x-rays. Percent difference between the two tests were $< 2\%$ which was good enough to confidently rank the different CQD materials.

The materials were then scored in terms of their QE from 1-8 with 8 being the highest. The scores can be seen in Table 21.

Material	QE (%)	Score
Sapphire	2.860	8
PbS	1.672	7
CdSe/ZnS	1.450	6
PbSe	1.037	5
CuInS/ZnS	0.889	4
InP/ZnS	0.779	3
CdS	0.544	2
CdSe	0.348	1

Table 21. MC simulation using 10% loading by volume of CQDs in a PMMA polymer matrix as a monolayer. The monolayer was set to be a 8×10^3 nm diameter disk. Incident x-ray energy was set to 10 keV. QE values in % were collected. Scores range from 1-8, with 8 being the best material for this experiment.

Next, the scores from the 100 keV case were collected. To show repeatability of the 100 keV case, two tests were done and their respective QE values can be seen in Table 22.

Material	QE Test 1 (%)	QE Test 2 (%)	% Difference
PbS	0.06781	0.06756	0.376
PbSe	0.04129	0.04131	0.065
Sapphire	0.01992	0.02043	2.516
CdS	0.00549	0.00559	1.803
CdSe/ZnS	0.00434	0.00473	8.182
CdSe	0.00418	0.00398	5.028
InP/ZnS	0.00234	0.00280	16.742
CuInS/ZnS	0.00176	0.00188	6.081

Table 22. Repeatability test of the MC simulation with 100 keV incident x-rays. Percent difference between most of the two tests were $< 10\%$ which was not ideal, but still useful to rank the different CQD materials. A lower percent error would mean running each CQD over a period of days in simulation time.

The materials were then scored in terms of their QE from 1-8 with 8 being the highest. The scores can be seen in Table 23.

Material	QE (%)	Score
PbS	0.0678	8
PbSe	0.0413	7
Sapphire	0.0199	6
CdS	0.0055	5
CdSe/ZnS	0.0043	4
CdSe	0.0042	3
InP/ZnS	0.0023	2
CuInS/ZnS	0.0018	1

Table 23. MC simulation using 10% loading by volume of CQDs in a PMMA polymer matrix as a monolayer. The monolayer was set to be a 22×10^3 nm diameter disk. Incident x-ray energy was set to 100 keV. QE values in % were collected. Scores range from 1-8, with 8 being the best material for this experiment.

In order to make one list of materials that reflects the QE for both the 10 keV and 100 keV cases, the standard deviation of the QE for each case was calculated. Then, the percent weight of the combined standard deviations from both the 10 keV and 100 keV cases were multiplied by the score of each material and added together. The standard deviation and percent weight of each case can be seen in Table 24.

Test	Standard Deviation	Weight (%)
100 keV Monolayer	0.0226	2.920
10 keV Monolayer	0.7497	97.080

Table 24. Standard deviation of each test and the weight importance as a percentage for each test resulting from the standard deviation.

From here, the weighted score of each material can be seen in Table 25.

Material	Weighted Score
Sapphire	7.94
PbS	7.03
CdSe/ZnS	5.94
PbSe	5.06
CuInS/ZnS	3.91
InP/ZnS	2.97
CdS	2.09
CdSe	1.06

Table 25. Weighted scores of each CQD material for the monolayer MC simulation x-ray QE experiment. Final scores range from 1-8, with 8 being the best material for this experiment.

From Table 25, it can be seen that Sapphire CQDs had the highest QE overall compared to the other tested materials. What was notable from the results presented here was how a lower Z material (S) had a higher QE than a higher Z material (Se). Upon further inspection, this was due to sulfide CQDs being larger in diameter. With a larger diameter, there was more volume for the x-ray to interact with. In addition, since the lower 10 keV test had a large standard deviation compared to the 100 keV test, lower Z materials had less of an effect. However, even at 100 keV, a lower Z material like Sapphire still performed on the same order of magnitude as the lead-based dots. The other conventional CQDs were all at least an order of magnitude lower in their QE. The overall modeled QE of Sapphire CQDs at 10 keV was double that of the lead-based dots and four times more than other conventional CQDs. This high modeled QE of Sapphire CQDs was due to their inherent dot QE of at least 80% while the other CQDs were 40% or less. In addition, the large diameter of the Sapphire CQD gave it more space for x-ray interaction when comparing loading by percent volume from one side of the cubic voxel model. Even at 100 keV, the lead-based

CQDs under investigation were only slightly better in their modeled overall QE than the Sapphire CQDs because of their low inherent dot QE of 40%.

These results motivate further research into alloy based CQD technology. The technology is not relegated to cadmium based materials and has been shown to work in both indium-based and lead-based materials as well [77][76].

4.2 PL Spectra Experiment

The focus of this thesis was to look at the PL spectra of each nanomaterial under test. Due to this focus, the PLE spectra will not be mentioned in this document. The manufacturer provided PL and absorption spectra and it was known that CQDs can absorb lower wavelengths. Measuring the CQD's wavelengths shift or lack of shift after fabrication into a structure was useful for engineering these CQDs to work with a photocathode or a semiconductor sensor.

Each nanomaterial tested is explained in this section, with additional analysis about the appearance of non-expected spectra. Each nanomaterial is plotted with the PL spectra in each structure it is applied to.

The first material examined here was CdS with its manufactured emission at 400 nm. The PL spectra for CdS as a thin-film, within a 3D printed structure, and within a CQD-loaded polymer can be seen in Figure 76.

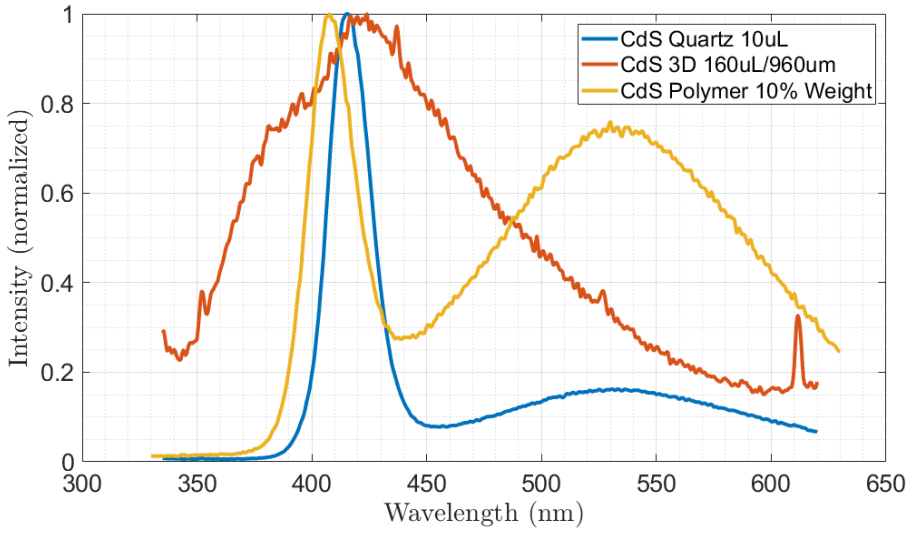


Figure 76. PL spectra of CdS CQDs applied to: thin-film, 3D printed structure, and CQD-loaded polymer structure. Data collected using a Horiba-Jobin Fluorolog-3. Data taken with the following attributes: 320 nm excitation, 1 nm excitation slit width, 1 nm emission slit width, 1 nm wavelength steps, right angle configuration at 30°, 1200/500 emission grating, 1200/330 excitation grating. Data in this plot was averaged over five trials.

The closest spectra to the manufactured peak PL wavelength of 400 nm was the CdS within the CQD-loaded polymer matrix. However, it also emitted a secondary peak at around 530 nm and the same peak also occurred in the thin-film structure. When referenced to the control case in Figure 84, this secondary peak does not align with any of the control peaks. FRET could be ruled out since the CdS CQDs emitting at 530 nm do not have a donor for them to have resonance, thus this secondary peak occurred most likely from oxidation. It was observed that oxidation in both the CdS thin-film and CdS CQD-loaded polymer matrix had a wider FWHM secondary (oxidation) PL emission peak than the main PL emission peak. The peak intensity was the greatest observable change between the CdS in CQD-loaded polymer versus that in a thin-film layer. Inferentially this was due to more CdS CQDs within the CQD-loaded polymer compared to the thin-film and the amount of oxidation was more pronounced during the fabrication process of the CQD-loaded polymer.

A PL emission continuum occurred at lower wavelengths than the main peak PL emission wavelength in the 3D printed structure. As would be discussed with the CdSe/ZnS and InP/ZnS materials, this continuum was most likely due to CT between the CQDs and the surrounding polymer materials. The SU-8-5 photoresist used to cap the CQDs within the 3D structure was the most likely cause of this CT. According to the PL emission spectra measured, the reason why the CdS CQD-loaded polymer did not show this continuum trend was most likely due to the CQD-loaded polymer being specifically designed to keep charge within the CQDs.

The next material examined was CdSe with its manufactured emission at 460 nm. The PL spectra for CdSe as a thin-film, within a 3D printed structure, and within a CQD-loaded polymer can be seen in Figure 77.

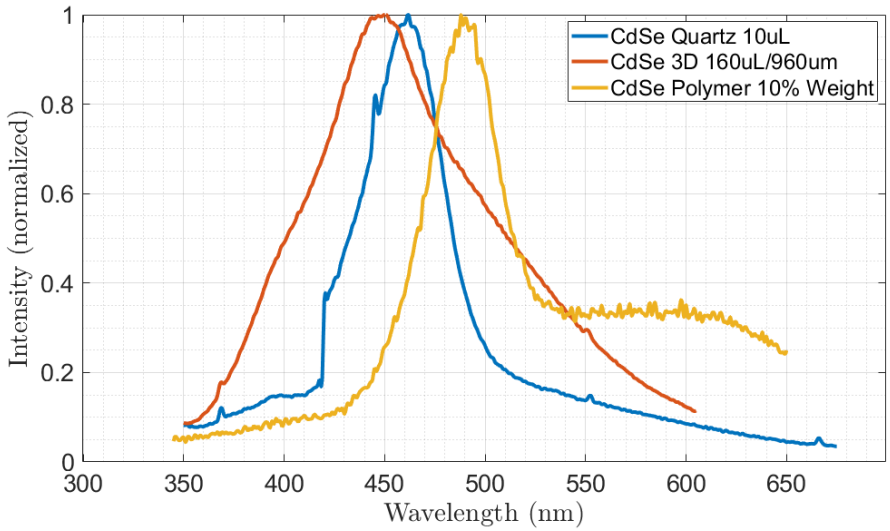


Figure 77. PL spectra of CdSe CQDs applied to: thin-film, 3D printed structure, and CQD-loaded polymer structure. Data collected using a Horiba-Jobin Fluorolog-3. Data taken with the following attributes: 335 nm excitation, 1 nm excitation slit width, 1 nm emission slit width, 1 nm wavelength steps, right angle configuration at 30°, 1200/500 emission grating, 1200/330 excitation grating. Data in this plot was averaged over five trials.

The CdSe CQDs showed less oxidation indicators than the CdS CQDs. An ox-

idation peak did start to occur at a≈ 600 nm for the CQD-loaded polymer. The CdSe within the CQD-loaded polymer was red-shifted while the CdSe within the 3D printed structure was blue-shifted. The 3D printed structure showed possible evidence of CT due to the spectral broadening. The thin-film of CdSe was on the targeted manufactured PL emission peak wavelength at ≈ 460 nm. However, it also shown a discontinuity at 420 nm. The sample was measured five times over, thus this discontinuity was not due to a faulty measurement. It would be possible for the thin-film of CdSe to oxidize in such a way that the CQDs emitting at around 420 nm were the ones mostly affected. However, with oxidation, it would have been expected to see a red-shifted peak within the thin-film PL spectra. It may also be possible that the ligands surrounding the CdSe when exposed to air could be absorbing or collecting the charge of the CQDs that emit around 420 nm. It would be recommended to fabricate another thin-film CdSe structure to confirm if this discontinuity is a unique physical phenomenon that warrants further investigation or was a structural defect.

The next material examined was CdSe NPL with its targeted manufactured emission at 400 nm. The PL spectra for CdSe NPL as a thin-film, within a 3D printed structure, and within a NPL-loaded polymer can be seen in Figure 78.

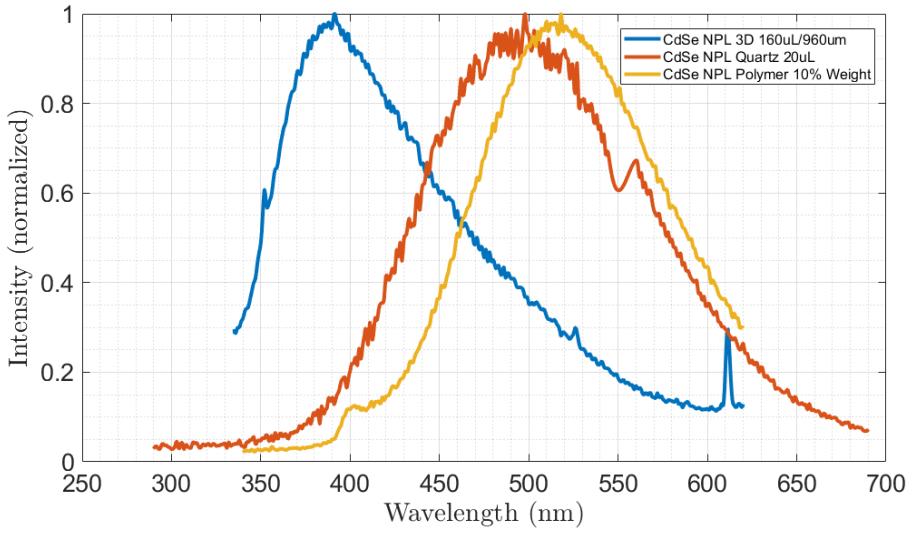


Figure 78. PL spectra of CdSe NPL CQDs applied to: thin-film, 3D printed structure, and NPL-loaded polymer structure. Data collected using a Horiba-Jobin Fluorolog-3. Data taken with the following attributes: 275 nm excitation, 1 nm excitation slit width, 1 nm emission slit width, 1 nm wavelength steps, right angle configuration at 30°, 1200/500 emission grating, 1200/330 excitation grating. Data in this plot was averaged over five trials.

The NPLs dispersed in the 3D printed structure were the closest to the targeted manufactured peak PL emission wavelength. No clearly defined CT peaks occurred for the 3D printed structure, however the spectral broadening could be a possible indicator of CT. The NPLs within the NPL-loaded polymer structure showed a small emission peak at 400 nm, but then the rest of the NPLs heavily red-shifted to $\approx$ 515 nm. Since the NPLs did emit a small amount at 400 nm, this meant that the NPLs were not stable and heavily oxidized during the fabrication process. Since the NPLs were experimental, manufacturing defects could be the reason, but this could be ruled out since the 3D printed structure showed a clear emission peak at $\approx$ 400 nm. The red-shifted peak was not material dependent due to the oxidation peaks occurring in the core-only materials. Inferentially, this occurred while hard baking the NPL-loaded polymer up to $180°C$ which contributed to a rapid rate of oxidation. In the future, hard baking at a lower temperature, but for a longer period

of time would be recommended. The thin-film of NPLs PL spectra showed that the NPLs emitted at ≈ 500 nm. This was also expected since the manufacturer could not guarantee 400 nm and most likely oxidation due to being a core-only material.

The next material examined was CdSe/ZnS with its manufactured emission at 520 nm. The PL spectra for CdSe/ZnS as a thin-film, within a 3D printed structure, and within a CQD-loaded polymer can be seen in Figure 79.

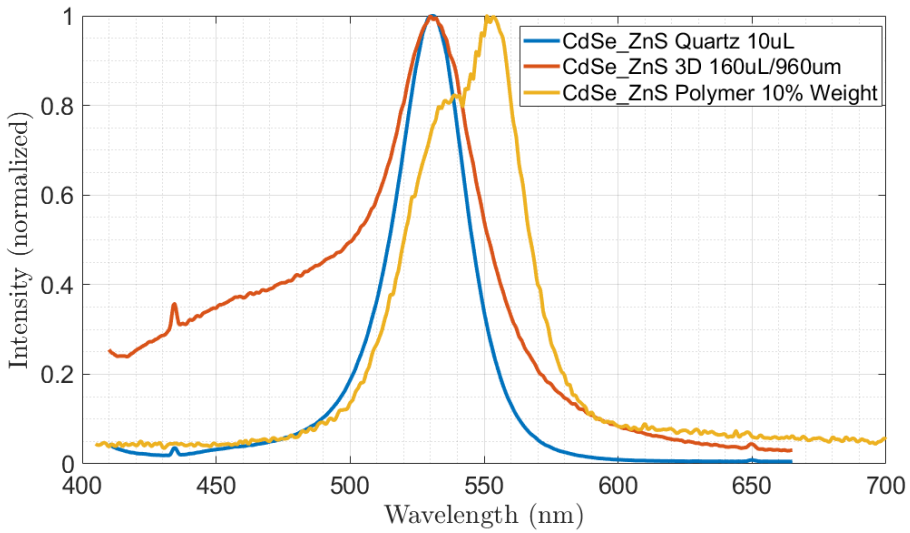


Figure 79. PL spectra of CdSe/ZnS CQDs applied to: thin-film, 3D printed structure, and CQD-loaded polymer structure. Data collected using a Horiba-Jobin Fluorolog-3. Data taken with the following attributes: 395 nm excitation, 1 nm excitation slit width, 1 nm emission slit width, 1 nm wavelength steps, right angle configuration at 30°, 1200/500 emission grating, 1200/330 excitation grating. Data in this plot was averaged over five trials.

Out of all the materials tested, CdSe/ZnS was the most stable and closest to the manufactured peak PL emission wavelength for all three structures. As seen with the previous materials such as seen in Figure 76 and Figure 77, a secondary PL peak occurred in the CQD-loaded polymer structure spectra. This would show more evidence that the fabrication process caused instability to the CQD material. Since a ZnS shell was used, it was unlikely this secondary peak was due to oxidation as the ZnS was known to prevent or limit oxidation [74]. Instead, FRET could be

the reason for this secondary peak. It was observed during the fabrication process that the overall volume of the CQD-loaded polymer shrunk by at least half its original volume. NN-Labs stated this was most likely due to polymer shrinkage which can vary between CQD-loading materials. This would in turn shorten the distance between CQDs and enhance FRET efficiency. The location of the secondary peak would also suggest this was FRET due to both the donor and acceptor spectra overlapping each other. As brought up with the CdS test, the CdSe/ZnS test showed signs of CT with the left slope of the peak PL emission wavelength in the 3D printed structure being a continuum. This property was further investigated and a 3^2 factorial experiment was conducted by changing both the thickness of the 3D printed structure and the amount of CQDs dispersed within the structure to see if this CT could be controlled using the same fabrication process. The results can be seen in Section 4.4.

The next material examined was CuInS/ZnS with its manufactured emission at 530 nm. The PL spectra for CuInS/ZnS as a thin-film, within a 3D printed structure, and within a CQD-loaded polymer can be seen in Figure 80.

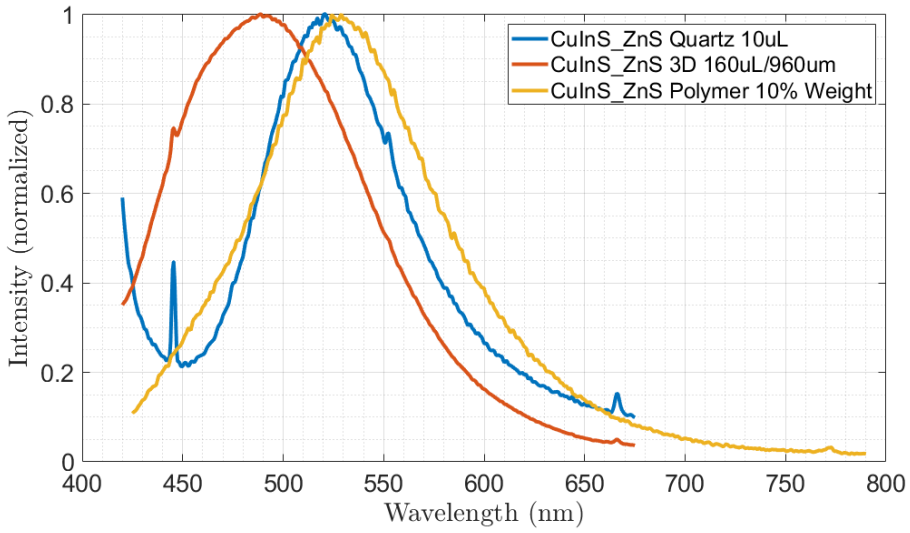


Figure 80. PL spectra of CuInS/ZnS CQDs applied to: thin-film, 3D printed structure, and CQD-loaded polymer structure. Data collected using a Horiba-Jobin Fluorolog-3. Data taken with the following attributes: 405 nm excitation, 1 nm excitation slit width, 1 nm emission slit width, 1 nm wavelength steps, right angle configuration at 30°, 1200/500 emission grating, 1200/330 excitation grating. Data in this plot was averaged over five trials.

Out of all the materials tested, CuInS/ZnS showed to have the greatest FWHM. The CQD-loaded polymer structure showed no secondary peak, and was right on the manufactured peak PL wavelength of 530 nm. With no FRET signature present, this would suggest that the CQDs were spaced far enough apart to prevent FRET from occurring. However, CQD-loaded polymer shrinkage was also observed and another reason why FRET was suppressed could be due to the different ligands passivating CuInS/ZnS compared to CdSe/ZnS. The CuInS/ZnS CQDs used a 9:1 mixture of oleic acid and oleyamine. The mixing of two ligands for CuInS/ZnS could have kept the CQDs far enough apart to subdue FRET. The blue-shifted PL emission peak for the 3D printed structure could be attributed to both incompatibility of the ligands with the fabrication process to cause the entire peak to blue-shift and CT of the surrounding SU-8-5 to cause a continuum at lower wavelengths. Despite a relatively wide FWHM, CuInS/ZnS would be the most stable in preventing additional CT

peaks, oxidation, and FRET when fabricating all three of the structures.

The next material examined was InP/ZnS with its manufactured emission at 530 nm. The PL spectra for InP/ZnS as a thin-film, within a 3D printed structure, and within a CQD-loaded polymer can be seen in Figure 81.

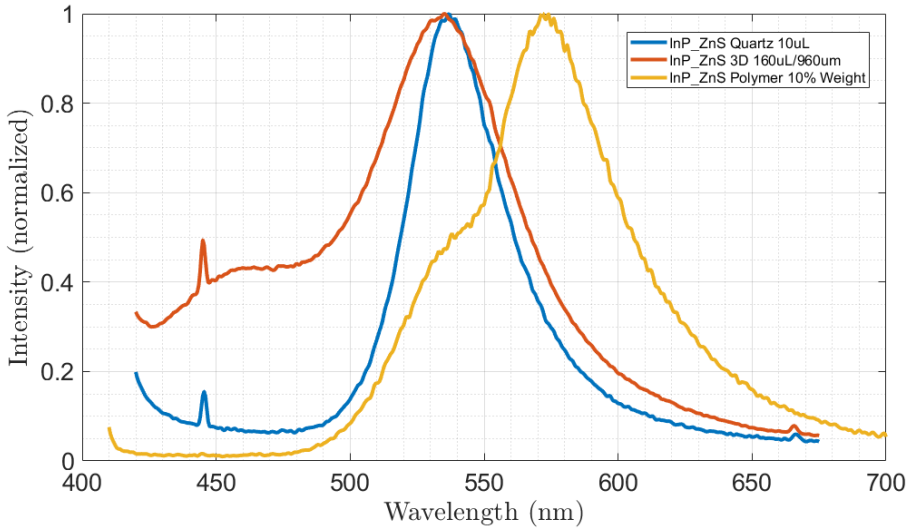


Figure 81. PL spectra of InP/ZnS CQDs applied to: thin-film, 3D printed structure, and CQD-loaded polymer structure. Data collected using a Horiba-Jobin Fluorolog-3. Data taken with the following attributes: 405 nm excitation, 1 nm excitation slit width, 1 nm emission slit width, 1 nm wavelength steps, right angle configuration at 30°, 1200/500 emission grating, 1200/330 excitation grating. Data in this plot was averaged over five trials.

The stability of InP/ZnS was good for both the 3D printed structure and the thin-film structure with a peak PL wavelength at ≈ 530 nm, matching the manufactured peak PL wavelength. There appeared to be a slight 530 nm peak in the CQD-loaded polymer structure, but the majority of the intensity occurred in a secondary peak near 530 nm at ≈ 575 nm. Compared to the previous analysis made, CdSe/ZnS showed a similar spectra. With a ZnS shell, oxidation would be highly unlikely. It also appeared that the PL emission intensity difference between the manufactured peak PL wavelength and the secondary peak was greater in the InP/ZnS sample than the CdSe/ZnS sample. This means the FRET efficiency was higher in the InP/ZnS

sample. From the Leica microscope Z measurements, InP/ZnS was 100 μm thicker than the CdSe/ZnS sample and by observation there was more thickness in the InP/ZnS sample. The InP/ZnS sample was also jelly-like in consistency versus the more liquid CdSe/ZnS sample. The most feasible hypothesis would be that a thicker CQD-loaded poly-mer sample allowed for more emission and re-absorption of the CQD PL emission wavelength, which allowed more photons to enter into CQDs that were experiencing FRET. However, perhaps a more likable scenario would be the percent weight loading. CdSe would be heavier than InP, thus there would have been more InP/ZnS CQDs in the same amount of applied CQD-loaded polymer material, increasing the likelihood for FRET. A TEM image would be able to confirm which of these scenarios occurred.

Additionally, the 3D printed structure for InP/ZnS showed a CT peak like CdSe/ZnS. CuInS/ZnS with a similar PL emission wavelength may have CT as well, and from Figure 80, a slight change in the expected Gaussian curve of the 3D printed structure showed some evidence of CT at 460 nm as well. These three separate materials showed the same CT peak which helped to show that the SU-8-5 photoresist used during the fabrication process of the 3D printed structure was able to emit a statistically significant wavelength intensity with the help of adjacent CQDs.

The next material examined was PbS with its manufactured emission at 1200 nm. The PL spectra for PbS as a thin-film, within a 3D printed structure, and within a CQD-loaded polymer can be seen in Figure 82.

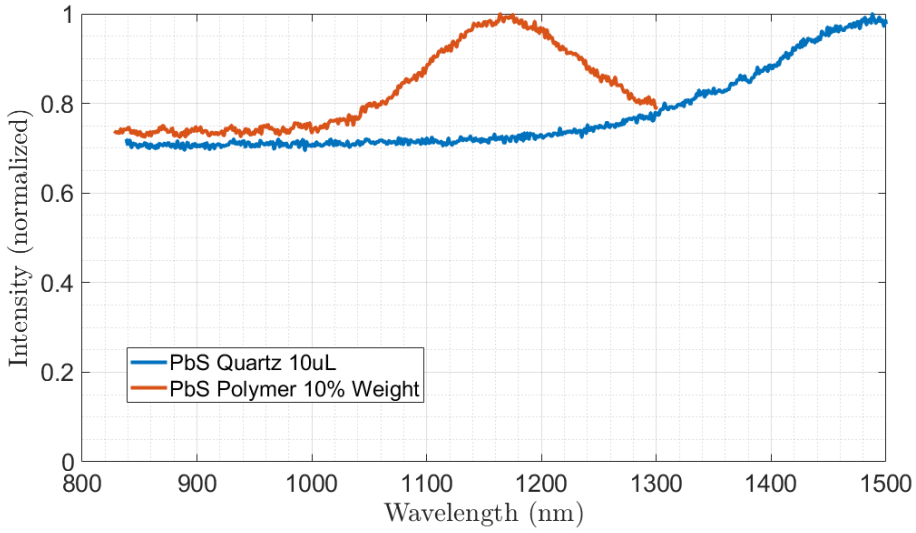


Figure 82. PL spectra of PbS CQDs applied to: thin-film, 3D printed structure, and CQD-loaded polymer structure. Data collected using a Horiba-Jobin Fluorolog-3. Data taken with the following attributes: 823 nm excitation, 1 nm excitation slit width, 1 nm emission slit width, 1 nm wavelength steps, right angle configuration at 30°, 1200/500 emission grating, 1200/330 excitation grating. Data in this plot was averaged over five trials.

A 3D printed structure spectra was not possible to collect with the equipment available. For a greater spectral resolution, a more sensitive detector would need to be used. However, both the CQD-loaded polymer structure and thin-film structure were measurable. The CQD-loaded polymer structure with its peak PL emission at $\approx 1,135$ nm was close to the manufacturer supplied 1,200 nm. Oxidation degradation may have occurred, but with the available data, it was unknown if any other spectral activity occurred after 1,300 nm for this sample. However, a future test using an upgraded NIR spectrometer with at least a 2,000 nm upper measurement limit would be able to confirm if oxidation did occur. However, it could be inferred that all of the materials without a ZnS shell experienced oxidation, and the thin-film case for PbS showed heavy oxidation with its peak PL wavelength at least 1,500 nm. A secondary peak for the CQD-loaded polymer structure would be expected here. Compared to PbSe in Figure 84, PbS performed worse relative intensity-wise. In addition, note the

relative intensity of the base of the PL spectra to the relative intensity of the peak. The Signal-to-Noise Ratio (SNR) was low for both samples due to the low excitation flux from the lamp used at these higher NIR wavelengths. From the lamp spectra, the peaks seen in the NIR were used for determining the excitation peak and they were of less intensity than the lower wavelengths. The lamp spectra of the Horiba-Jobin Fluorlog-3 used can be seen in Appendix Y.

The next material examined here was PbSe with its manufactured emission at 1200 nm. The PL spectra for PbSe as a thin-film, within a 3D printed structure, and within a CQD-loaded polymer can be seen in Figure 83.

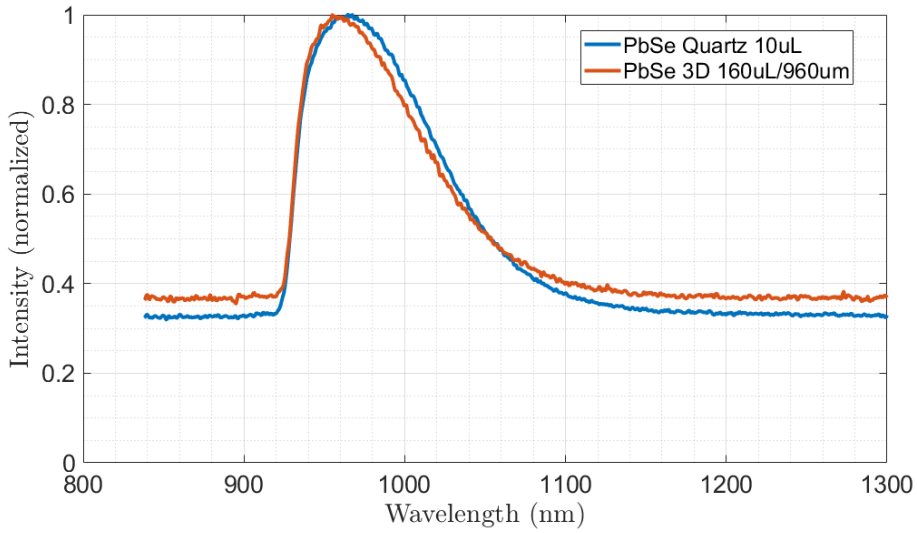


Figure 83. PL spectra of PbSe CQDs applied to: thin-film, 3D printed structure, and CQD-loaded polymer structure. Data collected using a Horiba-Jobin Fluorolog-3. Data taken with the following attributes: 823 nm excitation, 1 nm excitation slit width, 1 nm emission slit width, 1 nm wavelength steps, right angle configuration at 30°, 1200/500 emission grating, 1200/330 excitation grating. Data in this plot was averaged over five trials.

The CQD-loaded polymer structure for PbSe was not possible to collect due to a low amount of CQDs available within the sample. This was because the supplied PbSe CQD-loaded polymer matrix had too low of a viscosity. Thus, during the fabrication process, most of the material oozed out from in between the aluminum

ring and quartz disc holding structure. However, the spectra was collected from both the 3D printed structure and thin-film structure. Already, the SNR was better than PbS due to a larger difference between the base line emission and the peak emission intensities. In addition, both the 3D printed structure and the thin-film structure emitted at approximately the same wavelength, and both were heavily blue-shifted from the manufactured 1,200 nm peak PL emission wavelength. This could suggest that the PbSe CQDs supplied were not manufactured as desired. Of interest was that the thin-film of PbSe CQDs did not experience oxidation as the spectra was similar to the 3D printed structure which protected the CQDs from oxidation. In addition, CT in the 3D printed structure was not evident, however a longer slope on the right side of the PbSe peak occurred. This could be either because of the manufacturing process used, or more likely a small amount of FRET was raising the spectral slope. A TEM image of the PbSe CQDs would be able to confirm whether it was due to FRET or a manufacturing process if the CQD diameters were proportionally larger or not. In addition, a TEM image would be able to confirm if the CQDs were manufactured differently from the desired 1,200 nm wavelength or if another process was causing them to heavily blue-shift.

The final material examined was the control with its manufactured emission at 1200 nm. The PL spectra for the control as a thin-film, within a 3D printed structure, and within a polymer can be seen in Figure 84.

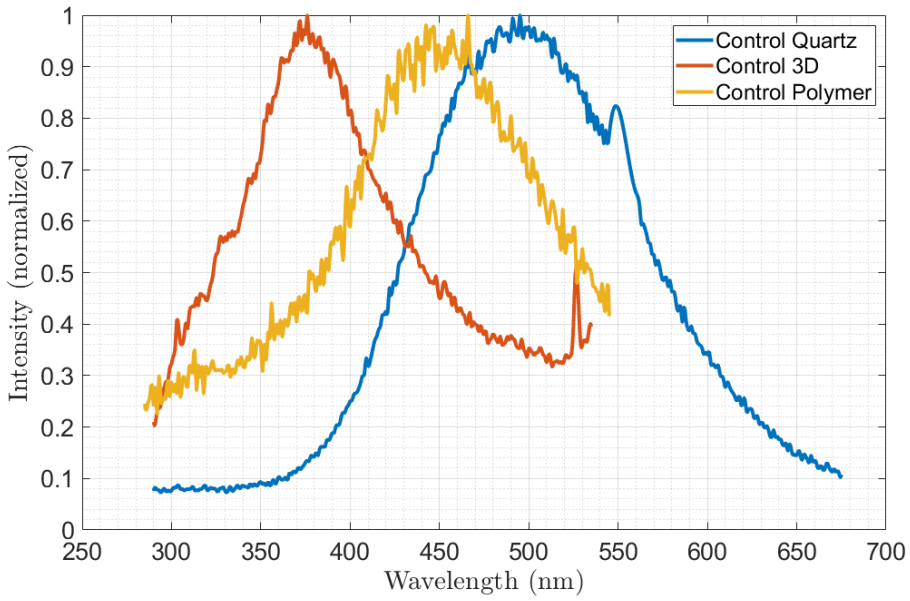


Figure 84. PL spectra of the control case applied to: thin-film, 3D printed structure, and polymer structure. Data collected using a Horiba-Jobin Fluorolog-3. Data taken with the following attributes: 275 nm excitation, 1 nm excitation slit width, 1 nm emission slit width, 1 nm wavelength steps, right angle configuration at 30°, 1200/500 emission grating, 1200/330 excitation grating. Data in this plot was averaged over five trials.

The control cases for each of the three structures was able to show what material mechanism of the secondary CT peak occurred in the 3D printed structures. The control polymer case emitted at $\approx$ 460 nm which was the peak wavelength for where the CT peaks occurred in the 3D printed structures. However, the 3D printed structure with the SU-8-5 capping it already only emitted at $\approx$ 365 nm. This helps to show that CT was occurring in the 3D printed structures when the CQDs were loaded into it. In addition, all three control structures emitted orders of magnitude fewer photons than the structures loaded with CQDs, which helped to confirm that the structures by themselves were not skewing the measurements.

4.3 PL Decay Time Experiment

There were clear differences between the thin-film, 3D printed structure, and polymer CQD samples in terms of their PL decay times. CINT was able to provide all the pre-exponential and decay constant components for use with the bi-exponential model in order to plot the PL decays. The components values used in the making of the figures in this section can be seen in Appendix U.

PL decay bi-exponential curve-fitted models for the thin-film structure can be seen in Figure 85.

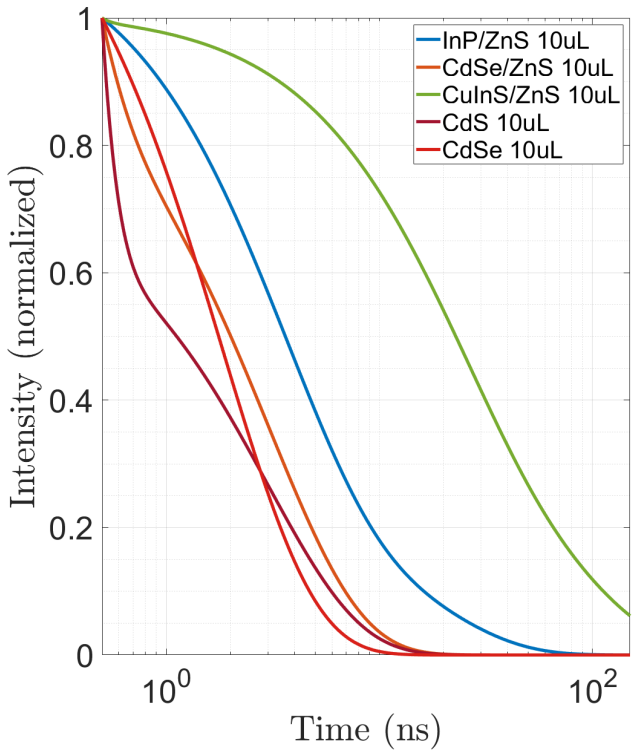


Figure 85. Bi-exponential model curve fitting of PL decay of CQDs applied as a thin-film structure. Data averaged over three trials and a 0.5 s integration time for each data point before curve fitting. Plot begins at 0.5 ns (temporal resolution limit of equipment used). Data collected using a PTI Felix 32 Spectrofluorimeter.

The fastest decaying CQD applied as a thin-film structure was CdS with a Time-

to-Half-Amplitude (THA) of 1.13 ns and the shortest overall PL lifetime decay of 13.11 ns to 0.1% of the original intensity was CdSe. Next, PL decay bi-exponential curve-fitted models for the 3D printed structure can be seen in Figure 86.

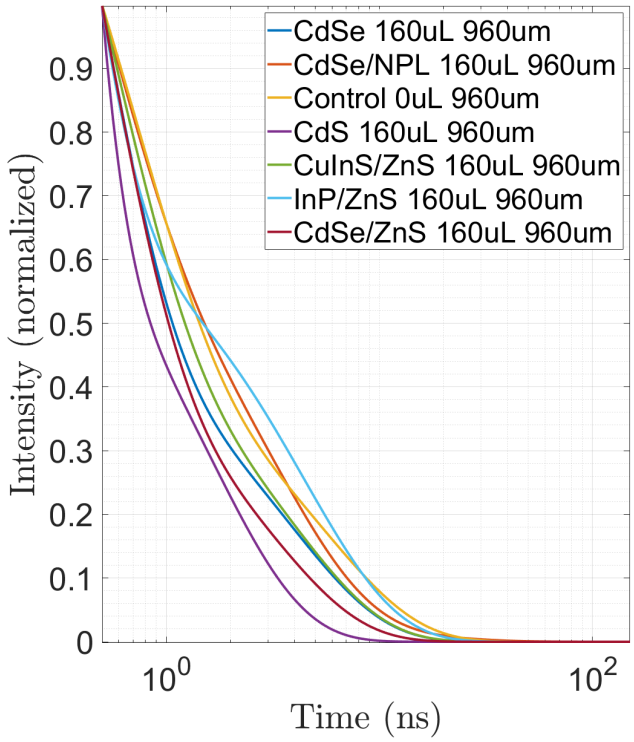


Figure 86. Bi-exponential model curve fitting of PL decay of CQDs applied as a 3D printed structure. Data averaged over three trials and a 0.5 s integration time for each data point before curve fitting. Plot begins at 0.5 ns (temporal resolution limit of equipment used). Data collected using a PTI Felix 32 Spectrofluorimeter.

Unlike the thin-film structure, the CQDs dispersed within the 3D printed structure have a closer grouping in terms of their PL decay time. Since CT was noticed on a few of the CQDs, it would be possible that the PL decay for the 3D printed structure was more of a signature of SU-8-5 than the CQDs themselves. However, the 3D printed structure did cause all of the CQDs to reduce their PL decay time from the thin-film case. The question that needed to be answered was why there was a shift in decay time. Since the shift in decay time was across all of the materials, this was not due to a specific CQD geometric make-up (spherical versus NPL) nor due to

the elemental composition of the materials. Hence, the best hypothesis was that this shift was due to CT exciting the faster decaying SU-8-5 polymer molecules. This was most likely not FRET due to no red-shifting of the peaks. The 3D printed structure PL decay results were similar to Au *et al.'s* research due to CT effects [19].

While the presence of CT may not be desirable in terms of overall QE, it happened to be a useful tool to lower PL decay times. As long as the CQD structure was efficient enough to be measurable by a scientific grade camera, it helps make CQD scintillators more viable for achieving faster temporal resolutions than their bulk counterparts. The main benefit of CT was that the longer phosphorescent emissions appeared to be suppressed. With overall decay times greatly shortened (usually by at least a factor of two), this would help to mitigate the effects of the gating (e.g. pile-up) needed to achieve less than 100 ps temporal response measurements. The mechanisms such as CT that caused the fast decay with the 3D printed structure could be used to enhance fast plastic scintillators like Polyvinyl Toluene (PVT) and even integrated with a 3D printed system [25] [67].

Finally, PL decay bi-exponential curve-fitted models for the CQD-loaded polymer structure can be seen in Figure 87.

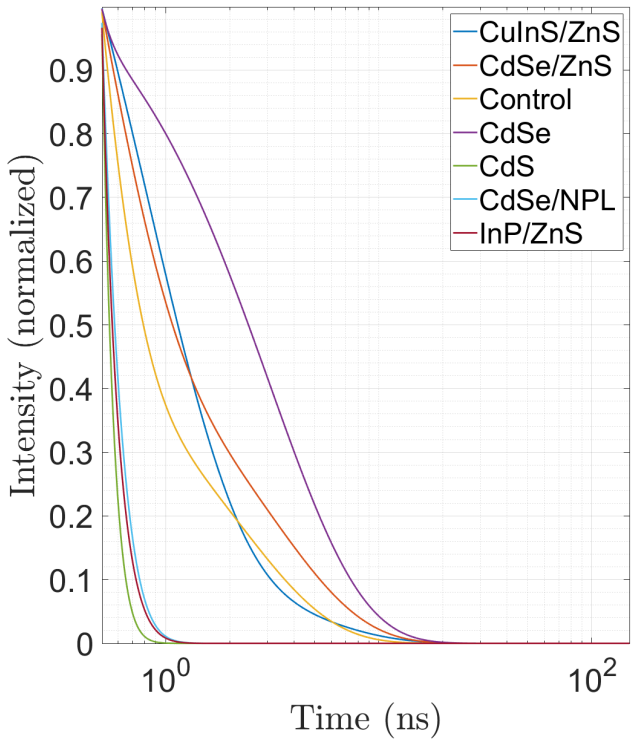


Figure 87. Bi-exponential model curve fitting of PL decay of CQDs applied as a CQD-loaded polymer structure. CdSe NPL had a modified pre-exponential for A_1 to 0.00 since the component was a negative value, thus this line may not be fully representative of the collected data. Data averaged over three trials and a 0.5 s integration time for each data point before curve fitting. Plot begins at 0.5 ns (temporal resolution limit of equipment used). Data collected using a PTI Felix 32 Spectrofluorimeter.

The CQD-loaded polymer structure using the proprietary CQD-loaded polymer from NN-Labs demonstrated PL decays with some materials having under 1 ns overall PL decay lifetime. CT was not seen with the CQD-loaded polymer samples, but FRET was seen, which can help lower PL decay time of the emission wavelength of interest. The PL decay curves were not closely grouped like the 3D printed structure, showing support to the hypothesis that the 3D printed structure may have been more of the SU-8-5 PL decay time versus the CQDs actual PL decay.

Another PL decay measurement was taken to observe how FRET effects the PL decay time of both the donor and acceptor peak emission wavelengths. This mea-

surement was done off of InP/ZnS CQDs and can be seen in Figure 88.

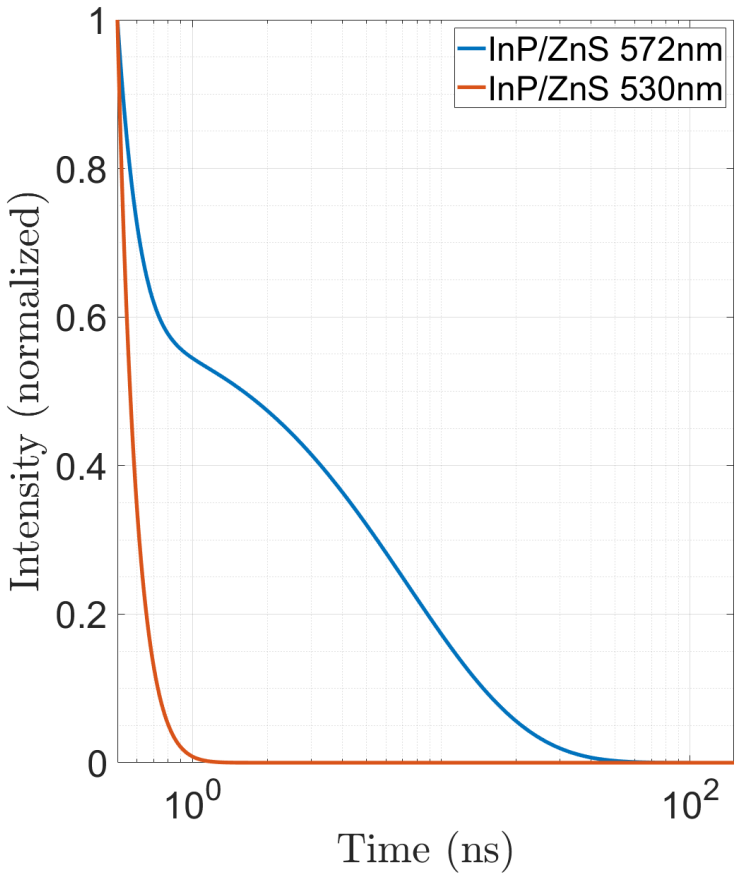


Figure 88. Bi-exponential model curve fitting of PL decay of InP/ZnS CQDs applied as a CQD-loaded polymer structure. One PL decay line represented the 572 nm FRET acceptor peak and the other PL decay line represented the 530 nm donor peak. Data averaged over three trials and a 0.5 s integration time for each data point before curve fitting. Plot begins at 0.5 ns (temporal resolution limit of equipment used). Data collected using a PTI Felix 32 Spectrofluorimeter.

There was clear evidence of FRET occurring from Figure 88. The donor emission which was the regular CQD peak emission wavelength of 530 nm quickly decayed in $\approx 1\ ns$ while the acceptor peak wavelength of emission at 572 nm was drawn out for $\approx 60\ ns$. This could be useful for x-ray detection to quickly look at the prompt photon emission of the 530 nm peak while possibly being able to use the acceptor PL decay for energy resolution.

Tying in all of the results from the thin-film, 3D printed, and CQD-loaded polymer structures, Figure 89 was created to compare all three structures.

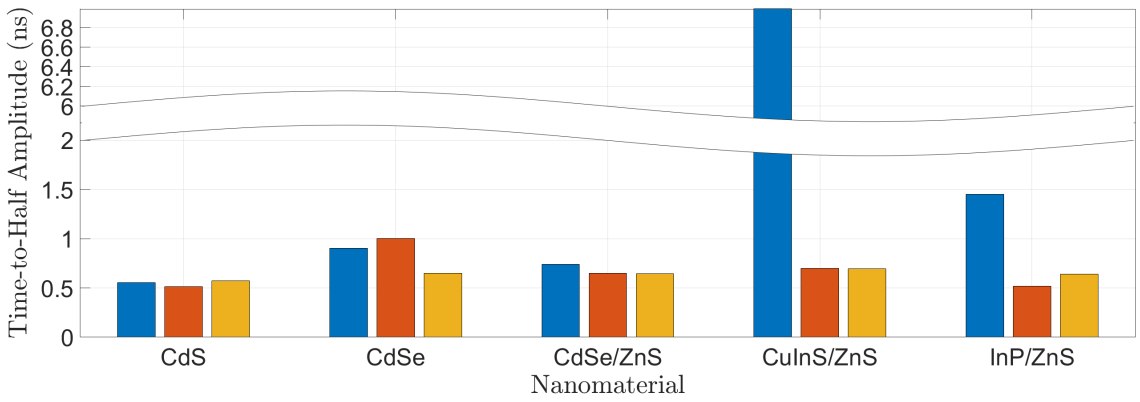


Figure 89. Bar graph comparing the THA values in nanoseconds for each structure experimented in this thesis. The left most bar (blue) for each nanomaterial category represented the thin-film structure. The middle bar (orange) for each nanomaterial category represented the CQD-loaded polymer structure. Finally, the right most bar (yellow) for each nanomaterial category represented the 3D printed structure.

The CQD-loaded polymer structure improved the PL decay times to get the THA for both CdS and InP/ZnS, however it was the same for CdSe/Zns and CuInS/ZnS. Both the 3D printed structure and the CQD-loaded polymer structure had lower PL decay times than the thin-film structure other than the polymer structure decaying slower for CdSe. The polymer material possibly made the PL decay time worse for CdSe due to oxidation. The CdSe NPLs were not included in this bar plot since no good thin-film PL decay measurement was taken due to an insufficient QE.

4.4 3D Print CT Relative Intensity and CT PL Decay Experiments

The PL spectra 3^2 experiment would ideally use five separate samples for each level, but there were not enough materials to do such experiment. End results here should be treated as a guide for controlling CT with the 3D printed structure. It was

determined that both the 3D printed thickness and the amount of CQDs loaded within the 3D printed structure allowed for tuning the relative intensity of the 460 nm CT peak. In addition, there was an optimal 3D printed thickness and amount of CQDs loaded within the 3D printed structure for the main CQD emission peak in order to achieve the fastest decay time as possible. Both of these findings were summarized as contour plots later in this section.

The averaged PL spectra for each level in the two factor analysis test can be seen in Figure 90.

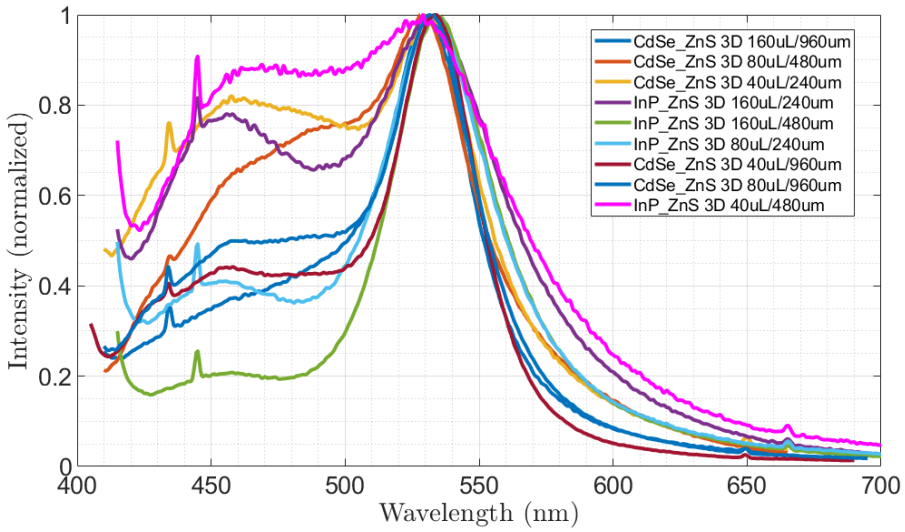


Figure 90. Two factor test showing PL spectra between all of the different levels used. It was observed that the intensity of the CT peak at 460 nm can be controlled.

The relative intensity of the CT peak could be tuned using the available levels at hand anywhere between approximately 0.2 to 0.8. This would be useful to know since if the goal would be to use CQDs as an intermediary step to collect charge and then release it to the surrounding polymer matrix material, it would be desired to make the amount of CT as high as possible. In addition, this CT was acting as an up-converting mechanism. This mechanism would be useful in both scintillators

and photonics to take a higher wavelength emitting CQD and tune the wavelength emission property of the entire system in order to better couple nanomaterial systems to photocathodes or photodiodes for example.

The relative intensity of the 460 nm peak was measured for each level and can be seen in Appendix W. A statistical software called Minitab was used to analyze the data. The Analysis of Variance (ANOVA) table generated within Minitab can be seen in Table 26.

Source	DF	Adj SS	Adj MS	F-Value	P-Value
Model	8	2.01591	0.251988	139.84	0.000
Linear	4	0.90239	0.225597	125.19	0.000
CQD Amount (μL)	2	0.50592	0.252959	140.38	0.000
3D Thickness (μm)	2	0.39647	0.198236	110.01	0.000
2-Way Interactions	4	1.11352	0.278379	154.48	0.000
CQD Amount (μL)*3D Thickness (μm)	4	1.11352	0.278379	154.48	0.000
Error	36	0.06487	0.001802		
Total	44	2.08078			

Table 26. ANOVA table from the 3^2 PL spectra factorial experiment. The amount of CQDs applied to the 3D structure had slightly more importance than changing the thickness of the 3D printed structure. Both factors were significant. The p-value for all sources in this table was more than 16 zeros, which was less than the significance value of 0.05.

As expected, the p-value for all sources in this experiment was much less than the significant value threshold of 0.05, thus the repeated tests were valid. These p-values only shows that the spectrometer used was reliable in taking repeated measurements of the same sample. Additional information from Table 26 showed that the amount of CQDs within the 3D printed structure had more significance on the relative intensity of the secondary peak than the thickness of the 3D printed structure. However, both

factors were significant in the relative intensity of the secondary peak.

The Pareto chart of the standardized effects can be thought of as the equivalent of a half-normal probability plot, except in bar graph form. This chart was generated for the experiment and can be seen in Figure 91.

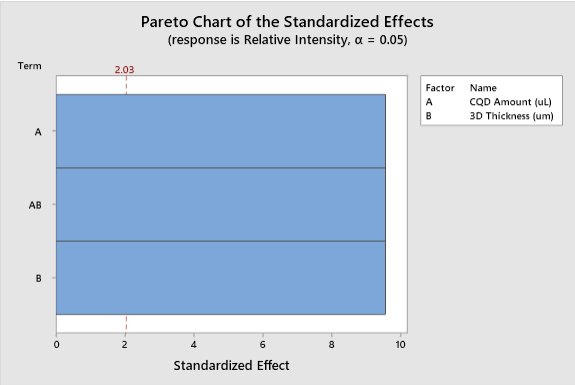


Figure 91. Pareto chart which showed that both the thickness of the 3D printed structure and the amount of loaded CQDs had a significant effect on the CT peak intensity measured at 460 nm.

From the Pareto chart, any term or factor greater than the critical value of 2.03 would be considered significant and should be kept when making calculations and future experiments. In this case this Pareto chart confirms that the amount of CQDs within the 3D printed structure, the thickness of the 3D printed structure, and the interaction between the two were all significant.

The residual plots for relative intensity can be seen in Figure 92.

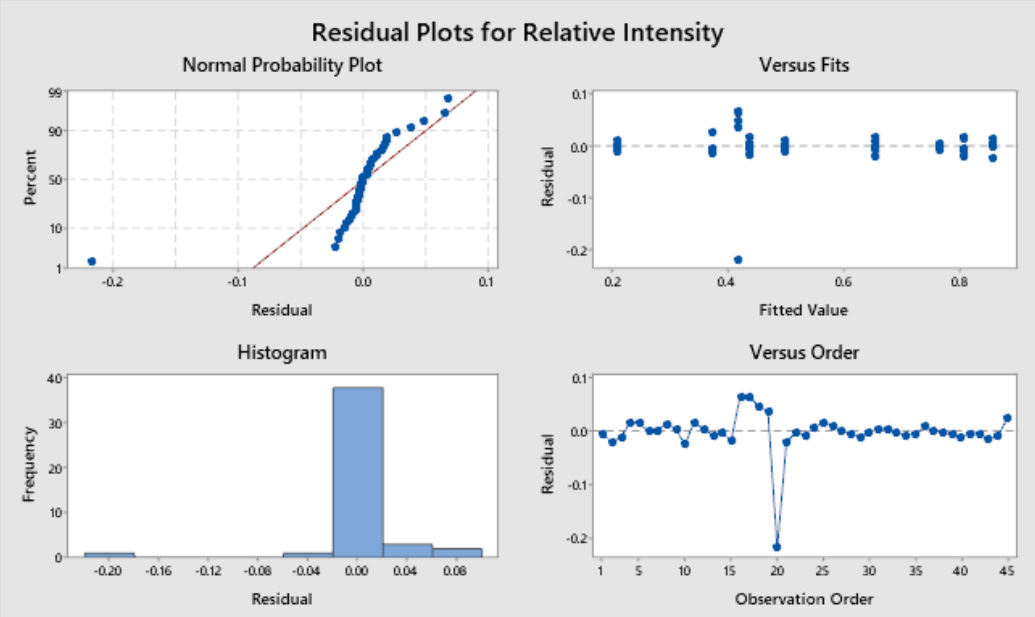


Figure 92. Residual plots showed that this 3^2 experimental data was not taken in randomized manner. This was due to time constraints, however a future study could incorporate a random ordering of runs.

From Figure 92, the run order of this experiment was not ideal. The data points in the normal probability plot should be closely following the red line in a linear trend, but does not. The versus fits plot appeared linear. The histogram had a heavily scaled normal distribution at the 0.00 value, which was not an ideal normal distribution. The versus order fit also helped to confirm that the experiment was not truly random due to a periodic trend across the observation order. This does not come as a surprise since the experiment tested the same sample five times over in material order, thus not random. As stated before, this experiment was not ideal, but more of a feasibility study into an unexpected effect seen during the experiment. It would be encouraged to redo this experiment in the future as a 3^2 experiment with using the same CQD material for all levels. Since the reason for the secondary peak with a high probability comes from the SU-8-5 photoresist used, it would be needed to keep the amount of SU-8-5 photoresist applied to glue the 3D printed structure consistent across all levels. In addition, testing out one sample using NN-Labs proprietary poly-

mer that does not show CT in the 3D printed structure would help to confirm that the secondary peak was indeed coming from SU-8-5 and not the 3D printed structure itself.

Despite not being an ideal experiment, the data could still be of use for engineering up-conversion for x-ray scintillation using the aforementioned 3D printed honeycomb device. Minitab was used to generate the following regression formula with an R^2 value of 43.39% seen in Equation 41. Additional terms could be added to make a better fit, however this would go beyond what the 3^2 model was designed for and may end up modeling unintentional effects. It would be best to redo this experiment with better resources and multiple replicates to be confident that there may be additional terms to add.

$$\begin{aligned} I(\mu L, \mu m) =& 1.190 - 0.000472\ \beta(\mu m) \\ & - 0.00804\ \alpha(\mu L) + 0.000029\ \alpha(\mu L)^2 \end{aligned} \tag{41}$$

Where α was the amount of CQDs in μL dispersed into the 3D printed structure and β was the thickness of the 3D printed structure in μm. This resulted in the following contour plot as seen in Figure 93.

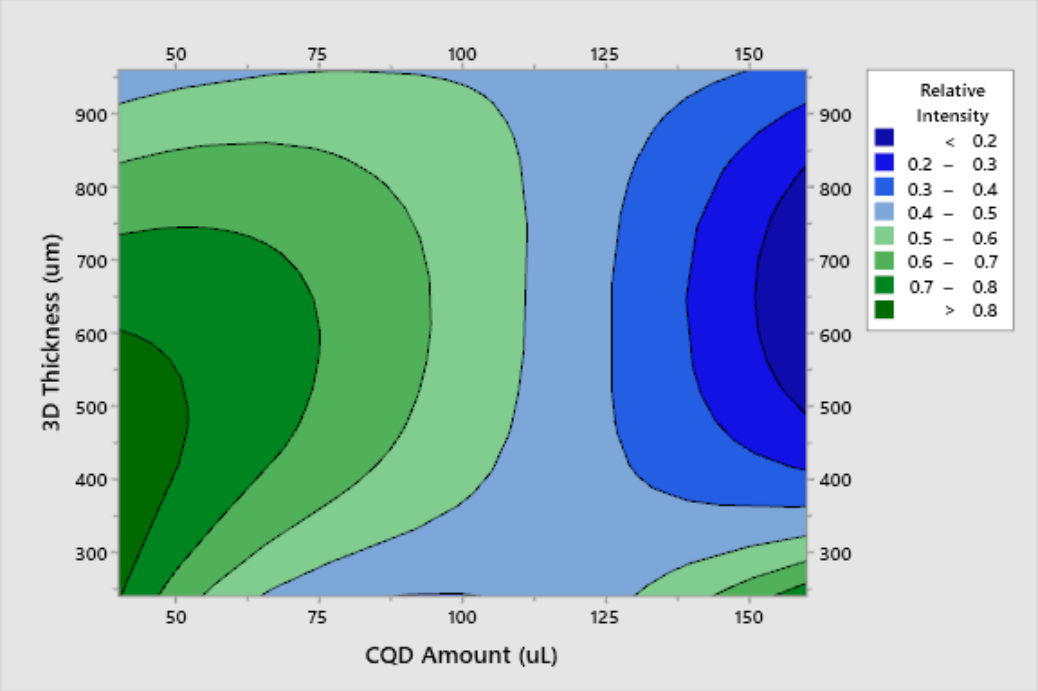


Figure 93. Contour plot showing how both the amount of CQDs loaded and the thickness of the 3D printed structure factors can be tuned to create a desired relative intensity of the secondary peak at approximately 460 nm.

From Figure 93, the relationship between the two factors used would appear to follow a trend where the highest amount of CT occurred with the least amount of CQDs applied and the lowest amount of CT with the most amount of CQDs applied. Going with the hypothesis that the SU-8-5 was responsible for the emission peak at approximately 460 nm, the high relative intensity at the 150 μL and 300 μm data point could be an optimal amount of CQDs in that having a higher concentration of CQDs would transfer more charge to the 460 nm peak than it would reabsorb from that peak. This hypothesis can also be visualized in Figure 94.

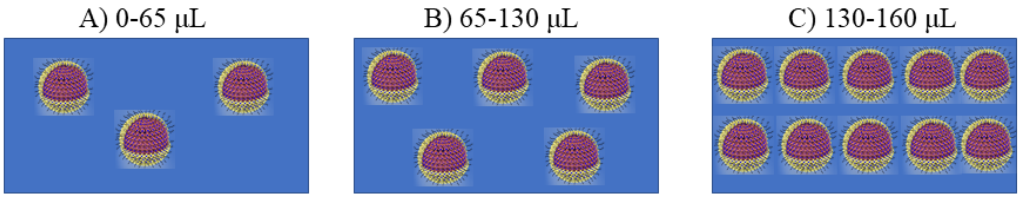


Figure 94. Graphic showing increasing concentrations of CQDs from Figure 93 when going along the x-axis at under 300 μm 3D printed structure thickness. a) low concentration of CQDs mitigate reabsorption of the 460 nm wavelength, thus increasing its intensity. b) a higher concentration of CQDs would start allowing reabsorption of the 460 nm while not adding enough CT to the polymer matrix, thus lowering its intensity. c) a critical concentration of CQDs would cause reabsorption of the 460 nm, but this effect would be less pronounced than the additional energy being transferred into the overall polymer matrix system, thus an increase in the 460 nm wavelength intensity could occur.

Seeing that this anomaly in the contour plot only occurred with the thin 3D printed structures showed that this would be a complex relationship with the amount of CT and the amount of reabsorption since the thicker the structure, the more reabsorption that could occur. This concept can be visualized in Figure 95.

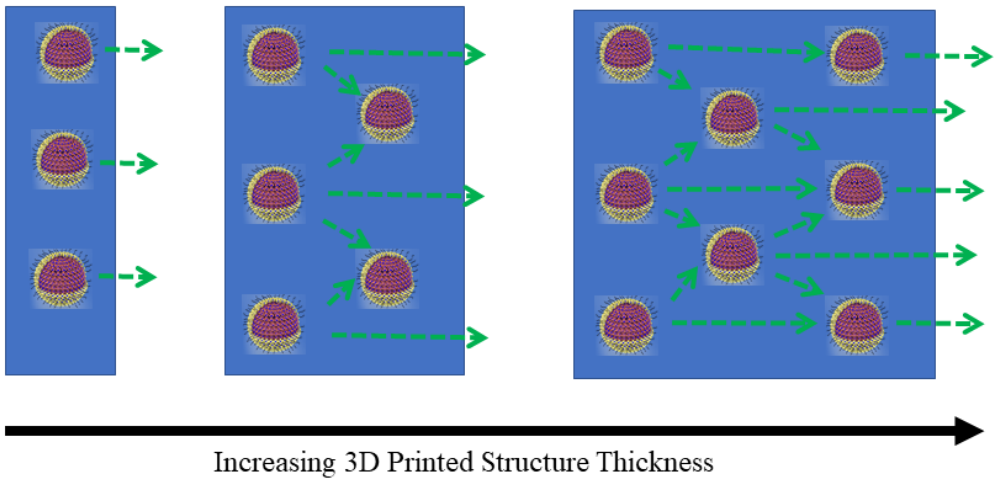


Figure 95. Graphic which shows increasing the thickness of the CQD structure would increase the probability of absorbing the 460 nm wavelength emission as the photon travels through the structure. This was represented by the dashed green arrows. When the 460 nm photon was reabsorbed, it would emit in this case a 520 nm-530 nm characteristic photon from the light absorbing CQD. This graphic also correlated with Figure 93 at 160 μL on the x-axis and going up the y-axis. The inverse could also occur at lower concentrations of CQDs such as while looking at 40 μL along the y-axis. With such a low concentration of CQDs, the thicker the structure, the less likely the 460 nm photon would get reabsorbed by another CQD along the way. However, across all of the CQD concentrations, the intensity of the 460 nm peak begun to greatly decrease at the thickest structure of 960 μm. This was most likely due to photons being lost within the 3D printed structure since it was not designed to be waveguiding and the thicker the amount of SU-8-5 a visible photon travels through, the more it will attenuate. Thus, the lower intensity of the 460 nm wavelength occurred from structural geometry, rather than from the CQDs themselves.

The trend going across the x-axis becomes more linear as the thickness of the 3D printed structure increases. This could be due to less SU-8-5 going throughout the entire 3D printed structure (e.g. coating the channels that the CQDs dispersed into). However, what would be more likely would be that the taller the structure, the better the probability for reabsorption to occur. The 460 nm emission photon could be absorbed by the higher emitting 520 nm-530 nm CQDs. This means the taller the structure, the more CQDs that would be excited and hence the absorption of more secondary CT peak 460 nm photons. The thinner the structure, the better the chance for the CT emission peak to escape without being reabsorbed by the CQDs. Thus,

this data supported the hypothesis that fewer CQDs within the structure would encourage a higher intensity up-converted emission wavelength from the structure due to a lower chance of reabsorption from the CQDs themselves. This finding would be important to consider when integrating CQDs with a polymer scintillator in an up-converting manner.

Since there were no replicates for the PL decay experiment, no p-values could be collected using 3^2 factorial analysis. Instead, a regression equation analysis was done in order to create an empirical formula. The PL decay lines for each level can be seen in Figure 96.

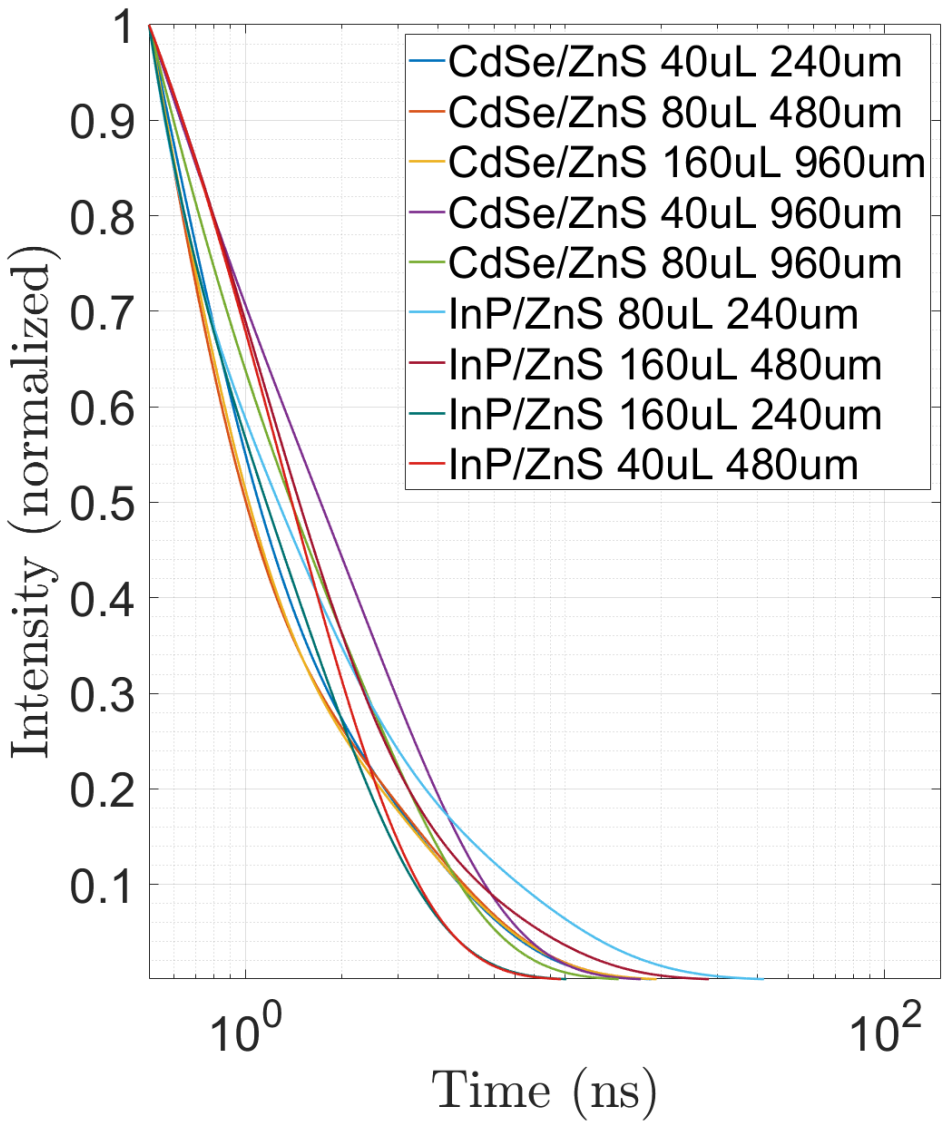


Figure 96. Bi-exponential model curve fitting of PL decay of CQDs applied as a 3D printed structure for the 3^2 factorial experiment. Data averaged over three trials and a 0.5 s integration time for each data point before curve fitting. Plot begins at 0.5 ns (temporal resolution limit of equipment used). Data collected using a PTI Felix 32 Spectrofluorimeter.

Slight fluctuations of the PL decay time was observed for each level, which would be useful for further optimizing the 3D printed scintillator. The THA was measured from each of the modeled PL decay curves and can be seen in Appendix X. The regression equation that mirrors Equation 40 was generated using Minitab and can

be seen in Equation 42. It has a R^2 value of 66.48%. As stated before with the PL spectra experiment additional terms could be added to make a better fit, however this would go beyond what the 3^2 model was designed for and may end up modeling unintentional effects. It would be best to redo this experiment with better resources and multiple replicates to be confident that there may be additional terms to add.

$$\begin{aligned} I(\mu L, \mu m) =& 0.972 + 0.00162\ \beta(\mu m) - 0.0041\ \alpha(\mu L) \\ &+ 0.000038\ \alpha(\mu L)^2 - 0.000009\ \beta(\mu m)\ \alpha(\mu L) \end{aligned} \tag{42}$$

Where α was the amount of CQDs in μL dispersed into the 3D printed structure and β was the thickness of the 3D printed structure in μm. This resulted in the following contour plot as seen in Figure 97.

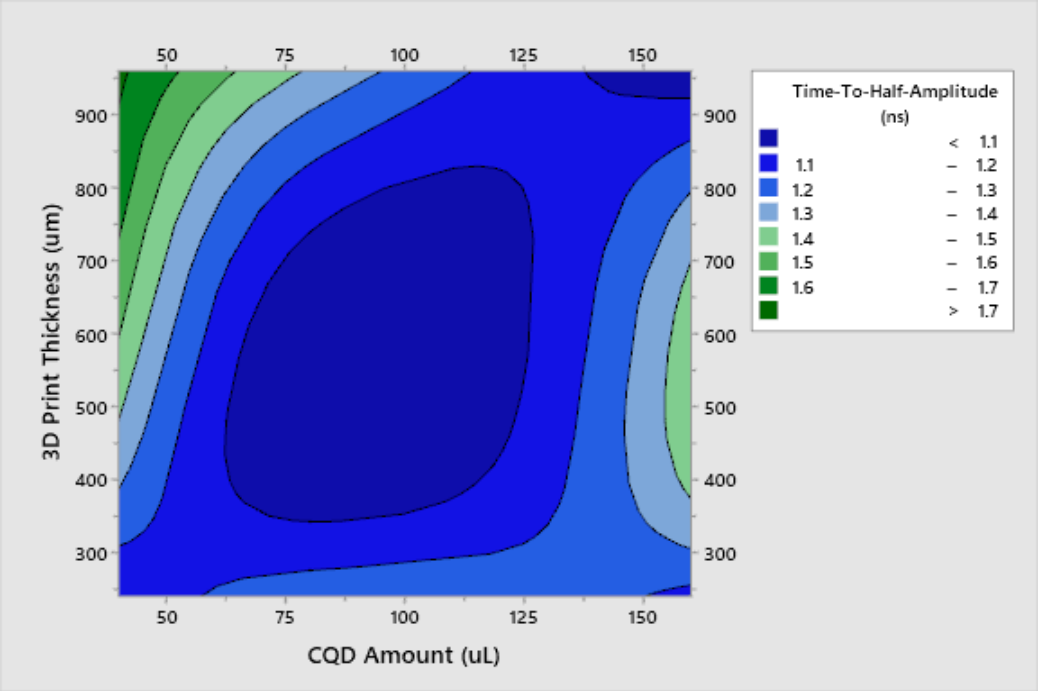


Figure 97. Contour plot showing how both the amount of CQDs loaded and the thickness of the 3D printed structure factors can be tuned to create a desired PL decay THA of the CQDs peak emission wavelength of 520 nm-530 nm.

There appeared to be an optimal amount of CQDs loaded into the 3D printed structure and the 3D printed structure's thickness. This represented a parabolic trend going along either the x-axis or the y-axis. In general, the thicker the 3D printed structure, the more time it took for the CQD to decay, which was expected. However, this effect could be offset by having additional CQDs loaded into the structure. It also was observed that having a high amount of CQDs would cause the decay time to become longer, which as described in Figure 95 would occur from the absorption and re-absorption of the CQD emission.

4.5 CQD Strain Experiment

It can be seen in Figure 98 that the optical spectra experiences shifts in wavelength around the peak wavelength of 530 nm when strain was applied. The secondary peak was most likely from the fluorescence of the polymer or ligands of the CQDs. However, this peak did not change in intensity across the entire test. This further suggested that the wavelength changes at around 530 nm came from the CQDs themselves.

Fortunately, measuring the difference between the plateau and the base of the plateau caused a measurable trend in strain which had not been publicly seen before. The stress-strain trend was found by first observing both the optical spectra and the stress-strain measurement over time. This can be seen in Figure 98.

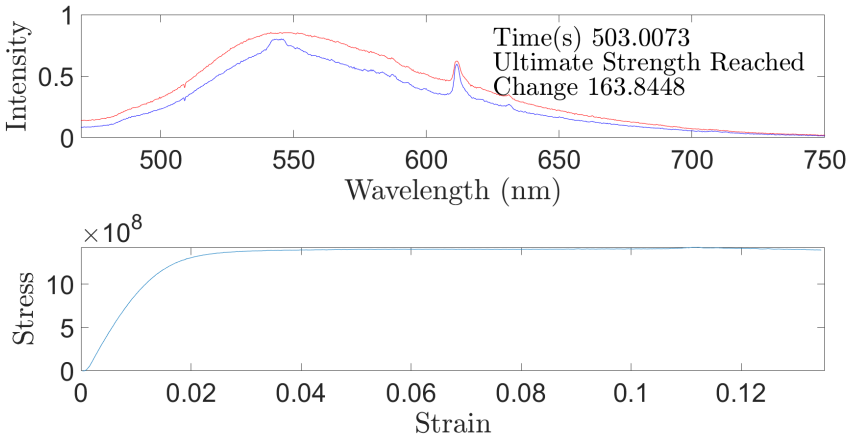


Figure 98. Figure showing both the optical spectra being emitted from the CQDs and the stress-strain curve. The optical spectra was located in the top sub-figure and the stress-strain curve was located on the bottom sub-figure. For the optical spectra, the intensity is normalized. An orange curve signified the first data point which could then be compared against the blue line which represented the data at the present time. The optical spectra plot showed the experimental time in seconds, when the ultimate strength had been reached by being added to the plot, and percent change of the present optical spectra in relation to the plateau rising from the peak of the spectra.

The percent change in intensity between the side of the present peak of the optical spectra and the plateau rising above it can be seen in greater detailed in Figure 99.

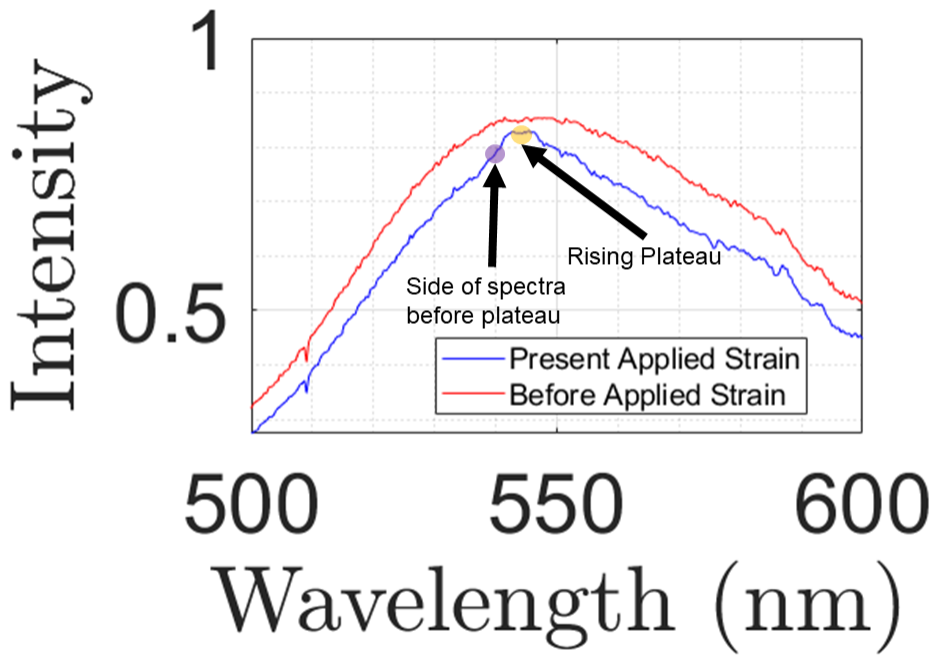


Figure 99. A magnified version of Figure 98. The percent change in intensity in order to get stress-strain measurements for this sample was taking as the percent difference between the rising plateau (yellow dot) and the side of the plateau (purple dot). It was observed that the side of the plateau remained relatively consistent with the rest of the present optical spectra as more strain was applied, but the rising plateau continued to climb higher.

Figure 100 shows the change in the PL spectra due to the applied strain to the dog-bone sample over time.

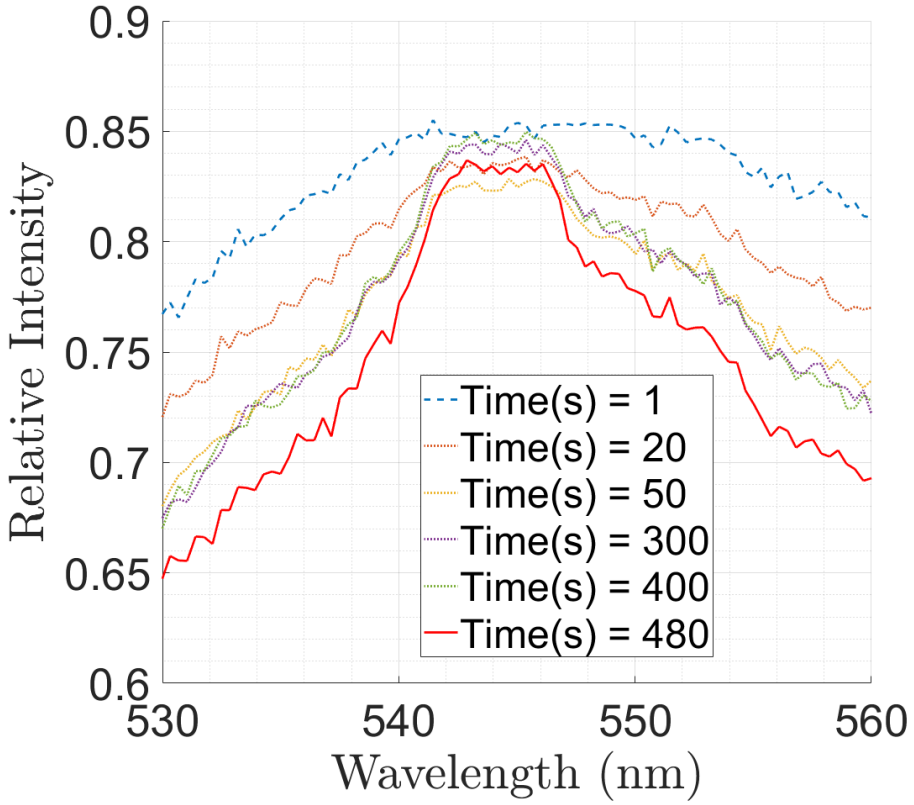


Figure 100. A magnified version of Figure 98 with PL spectra changing over time due to applied strain to the dog-bone sample.

The percent change in intensity was plotted against the strain and this resulted in two trendlines as seen in Figure 101. One trendline occurred from 0.00 to ≈ 0.001846. The second trendline goes from ≈ 0.001846 until a strain of 0.134, after which the dog-bone sample broke.

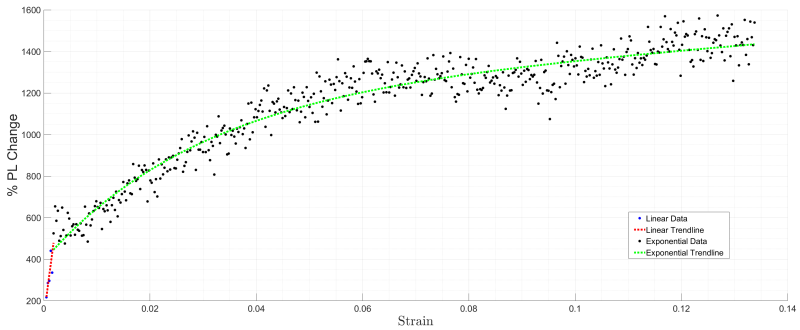


Figure 101. Two trendlines were noticed as the sample was strained.

The first trendline from 0.00 to ≈ 0.001846 along the strain axis in Figure 101 has the following linear relation within the 95% confidence interval bounds in Equation 43.

$$F(x) = 1.94 \times 10^5 x + 120.9 \tag{43}$$

A stress-strain curve plot was created by both Major John Brewer and Major Ronald Aung to come up with the yield strain point which can be seen in Figure 102. Their code used to create this plot can be seen in Appendix Z.14 and Appendix Z.15.

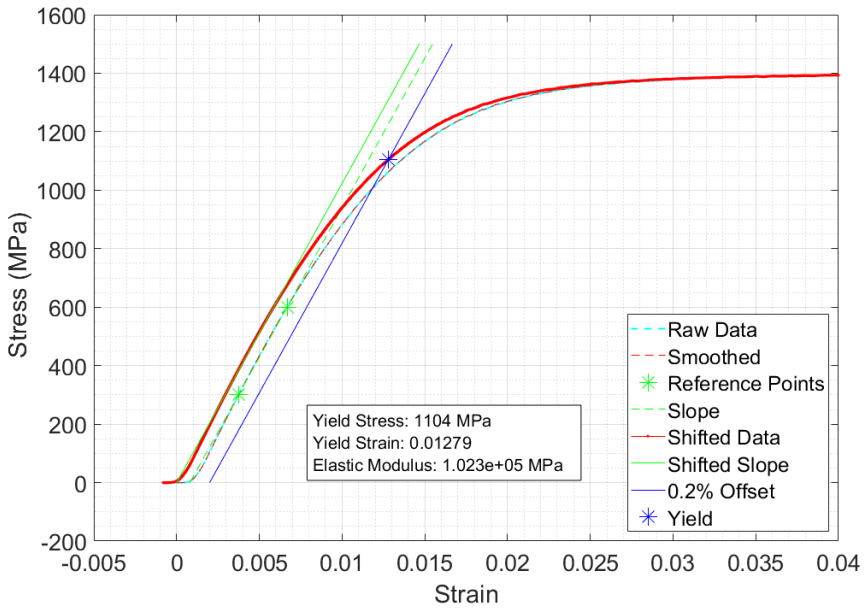


Figure 102. Stress-strain curve highlighting the following: yield stress point, yield strain point, and the elastic modulus. Plot created by Major John Brewer and Major Ronald Aung.

At the ≈ 0.001846 point, the dog-bone sample reaches its yield strength point, where the yield strain was calculated to be 0.01279 with a 2% offset. However, when comparing to the true stress-strain curve, the yield strength becomes 0.0018. The linear trendline change at the ≈ 0.001846 point can be used to optically detect the yield strength of the material. It was difficult to tell exactly where the trendlines change due to a limit number of data points around this yield strength area, however

a future experiment ran at a slower speed could increase the number of available data points and make the optical results more accurate. For the second trendline after ≈ 0.001846, it can be described by the following exponential relation within the 95% confidence interval bounds in Equation 43.

$$F(x) = 1210\ e^{1.319x} - 816.3\ e^{-34.02x} \tag{44}$$

One could then use the fitted lines in both Equation 43 and Equation 44 to determine the strain on a piece of metal from the percent change difference between the rising plateau and the side of the plateau as was seen in Figure 99. The reason for the fluctuations of the data in Figure 101 could be due to not having a high enough excitation flux to get a better signal-to-noise ratio, but mainly it would be due to CQD blinking. This InP/ZnS CQD did not contain the special ligands nor alloying to suppress blinking. It was well known in literature, and especially in the time span of minutes, that CQDs would have periods of high intensities and low intensities due to blinking. Therefore, by using a better designed CQD to suppress blinking, the variation of the data could be minimized. Figure 101 also shows the spread of percent PL change becomes more pronounced as the dog-bone sample is further strained, which shows that strain can increase CQD blinking's change in intensity. However, an upward exponential trend in strain could still be seen and shows that this technique could be used as a NDT technique.

4.6 Decision Matrix for CQDs

The four tested experiments with data were used to score the CQDs under investigation. The final scores can be seen in Table 27.

Experiments	CdS	CdSe	CdSe NPL	CdSe/ZnS	CuInS/ZnS	InP/ZnS	PbSe	PbS	Sapphire
MATLAB X-ray Attenuation Experiment (1-8) W20%	4.99	5.99	5.99	2.01	1.02	4.00	7.00	8.00	2.99
MATLAB X-ray Monolayer MC Experiment (1-8) W20%	2.09	1.06	1.06	5.94	3.91	2.97	5.06	7.03	7.94
UV PL Experiment (1-7) 3D Print FWHM W10%	1.00	2.00	4.00	7.00	3.00	6.00	5.00	0.00	0.00
UV PL Decay Experiment (Polymer Structure) (1-6) W50%	6.00	1.00	4.00	3.00	2.00	5.00	0.00	0.00	0.00
Weighted Total	4.52	2.11	3.81	3.79	2.29	4.49	2.91	3.01	2.19

Table 27. Scoring rubric used to evaluate the most promising CQD for future work. The reasoning for no scores for the of the CQDs were the following: PL spectra data was not possible to collect for the PbS in the 3D printed structure due to equipment limitations, sapphire CQDs did not arrive from the manufacturer, thus could not be experimentally tested, and PL decay from UV excitation was not possible for the NIR CQDs.

It can be seen from Table 27 that both CdS and InP/ZnS would be the best CQDs to look into for future work out of the materials tested. Since their weighted scores were both close, the final decision on the scoring would be with regards to both their stability and ease of fabrication within a loading structure. This led to InP/ZnS being the best choice to go forward with for future work since the stability of the material due to its ZnS shell makes it easier to work with in scintillating structures. In addition, InP/ZnS does not contain cancerous cadmium nor toxic lead. It was also important to note the emission wavelengths of both nanomaterials, where CdS had a 400 nm emission and InP/ZnS had a 530 nm emission. The more blue the emission wavelength the better it would be for use with a S20 photocathode within a streak camera, however since CdS showed oxidation within the polymer material, it had an additional red-shifted peak which took away from the QE of just the 400 nm emission wavelength and nulls its advantage over the green emitting InP/ZnS.

Since the manufacturer for the Sapphire CQD was unable to deliver, no data was available and was thus given a zero score. It was kept in the scoring rubric to show how strong it performed in the monolayer MC experiment. The alloyed CQD technology showed a strong promise for x-ray scintillation and thus, should not be discounted for future work. Also, since both the PbSe and PbS CQDs emit in the NIR, there

were equipment limitations in properly taking the PL spectra and the unavailability of equipment to take a PL decay response. These limitations caused the zero scores in the respective experiments it effected for both the PbSe and PbS CQDs. With the high Z content of lead-based dots, it would be worthwhile to determining what the PL decay spectra looks like for the lead-based dots used within various loading structures.

V. Conclusion and Future Work

5.1 Overview

This chapter discusses: research conclusions, significance and contributions to the community, and future work.

5.2 Research Conclusions

This thesis characterized eight nanomaterials within three tested structures: thin-film, 3D printed, and CQD-loaded polymer. Four experiments were conducted to evaluate the capability of each nanomaterial for x-ray related applications while an additional experiment was conducted to evaluate the strain sensing properties of CQDs.

There was a need for a new fast temporal resolution x-ray diagnostic tool for MSX at LANL. It was determined that investing time into researching and developing CQDs as scintillators would be the best route into creating a faster x-ray scintillator pushing towards 100 ps temporal resolution. The CQD scintillator would be coupled to a streak camera which was capable of imaging such a fast response. CQDs by themselves would not be able to do much for x-ray detection unless they were stacked to be able to detect higher energy x-rays. Thus, four structures were fabricated and three were tested. The four being: CQDs within a polymer matrix, CQDs dispersed into a 3D printed honeycomb structure, CQDs drawn through a PCF, and CQDs dispersed as a thin-film on top of quartz. The PCF structure was not tested due to equipment constraints to properly evaluate it. However, an old fabrication recipe from NASA was brought back from being lost in drawing CQDs through a PCF.

Results from modeling showed that alloyed CQDs would be almost as effective as lead-based CQDs in terms of their QE. This was due to alloyed CQD's superior QE which was stated to be $\geq 80\%$ compared to the conventional CQDs with QEs $\leq 40\%$. It was found that CQDs without any shell required a smaller structural thickness than shelled CQDs when exposed to 100 keV x-rays. This was in part due to the ability to load more CQDs per unit area when within a polymer matrix. However, when analyzing lower energy 10 keV x-rays, CQDs with a shell required a smaller structural thickness.

The PL spectra for all of the CQDs showed a mix of oxidation degradation peaks for the CQDs without a ZnS shell, FRET for the CQDs with ZnS shells, and CT peaks for the CQDs in the 3D printed structure. This was important to consider since the stated wavelength of emission for CQDs may not be the same as when they were experimentally measured after being loaded within a structure.

CT was noticed during the PL spectra experiments using the 3D printed structure. This was especially such for both the CdSe/ZnS and InP/ZnS CQDs due to the location of their peak emission wavelength in relation to the CT peak emission wavelength of ≈ 460 nm. This CT peak most likely occurred from the SU-8-5 polymer used in the fabrication process. A 3^2 factorial experiment was performed which demonstrated that the relative intensity of the CT peak could be controlled by changing both the amount of CQDs dispersed into the 3D printed structure and the thickness of the 3D printed structure.

Due to logistical and time constraints, x-ray tests were not conducted, however UV data was available. The best temporal resolution experiment available at the

time was 500 ps. The PL decay data showed that the 3D printed structures reduced the decay time by at least half for most of the CQD thin-film samples. The CQDs like CdS that were already decaying quickly did not have much of a decrease in their decay time. This was most likely caused by charge transferring from the CQDs to the SU-8-5 polymer matrix capping the 3D printed structure (which also bled into the holes containing the CQDs. The fastest CQD tested within the 3D printed structure under UV excitation was CdS with a THA of 830 ps. The second best material was CdSe/ZnS with a THA of 1.023 ns. CdSe NPLs did not perform well with a THA of 1.508 ns. However, it was unknown how the CdSe NPLs would perform with faster temporal resolution equipment. Within the CQD-loaded polymer matrix structures, CdS showed the fastest THA of 545 ps with Inp/ZnS coming in second demonstrating 562 ps. In addition, PL responses from x-rays may change how fast each of the CQDs would initially decay.

Both lead-based CQDs were not able to be tested for their PL decay due to equipment availability, however results from prior work suggests they would decay slowly due to lead's dense hold on electrons [78] [36]. Their QE under x-rays on the other hand may be superior than the other materials due to having an inherently higher QE than the other materials and the high Z lead material would give them the best probability of interaction with an incident x-ray. However, this advantage could be challenge by the use of alloyed CQDs with far higher QE.

Overall, InP/ZnS performed highly through all of the experiments in the evaluation rubric used while also considering CQD stability. This was also because the alloyed CQDs never arrived from the supplier, thus this type of CQD technology should not be discounted. However, when it comes to narrowing down to one CQD technology, InP/ZnS would be recommended at this point. Future x-ray experiments

may change this recommendation.

In addition, the optical stress-strain response of InP/ZnS CQDs within a polymer matrix showed promise. This experiment was performed with a pre-coating applied to the surface of an aluminum structure before applying the polymer CQD material. There was both a clear linear and exponential trend in the wavelength shift of the InP/ZnS CQDs to the applied strain. The two trends seen in the change of optical response for the CQDs deviate at the yield strength point of the material under strain. Overall, the CQD strain sensor was able to show a PL percent change of $\approx 1,573\%$ from the two points of measurement over the time it took to strain the 301 stainless steel dog-bone sample till failure. Furthermore, CQD blinking was observed as the data was acquired over time. This could be mitigated through the use of OPV ligands and the use of alloyed CQDs. However, if blinking is a desired property, this experiment also showed that applied strain to CQDs will cause them to blink with a higher change in intensity.

5.3 Research Significance

The experiments for using CQDs as fast x-ray scintillators pointed toward the need to look into utilizing CT effects. CQD emission could be up-converting when in the proximity of a polymer designed to take their charge. This could have implications for photonics and improve the QE of CQDs scintillator systems which cannot emit in the blue spectrum. This up-converting property could be useful for Air Force sensors and technologies such as NVG. In addition, the up-conversion of CQDs using SU-8-5 could be used in Quantum Information Science (QIS) to help tune the CQDs for single photon emission. This in turn would help the Air Force's strategic capabilities in quantum communications, which ensures fully secured communication, and

quantum computing which would help the Air Force lead on the cutting edge of cyber and computational simulations.

The InP/ZnS CQDs show promise in being used as a x-ray detection scintillator for the MSX project at LANL which has implications for the NNSA. In turn, this would benefit the Air Force with a more secured nuclear arsenal. In addition, two patents were filed from the work in this thesis: one for the 3D printed structure and the other for the stress-strain NDT using CQDs. With additional improvements, these devices would have wide and impactful implications for DoD, Department of Energy (DoE), and NASA x-ray detection capabilities, other sensing capabilities, and a more reliable way to optically check for defects on any structure. In addition, the ability to sense strain with CQDs would allow for mixing of CQDs within 3D printed materials to check for defects in 3D printed structures. This is possible by using high thermal tolerance CQDs such as the Sapphire CQD. Such integration of CQDs within 3D printed materials would greatly help any research group to quickly diagnose structural issues with their 3D printed designs or even issues in their 3D printing process.

5.4 Future Work

Suggestions for future work are listed below:

- Redo the 3^2 factorial experiment with enough material to cover all the levels. For example, only using CdSe/ZnS for all the levels. In addition, run the experiment in random order and have enough material to create five separate replicates of the structure for each level.
- For the 3D printed structures, redo the experiments with the second iteration

of the design that is further discussed later in this section. This is because warping was an issue with the samples which could make replicability harder.

- Look into using PVT scintillating polymer to load CdSe/ZnS into. Design the ligands for the CdSe/ZnS to efficiently transfer charge to the PVT in order to enhance its QE.

- Look into dispersing CQDs into broken micro-channel plates as a possible CQD loading structure.

- Splice PCF fiber into a larger fiber to be coupled into a fast photodiode. Test PCF in the same experiments as the other structures.

- Test CQDs loaded into PCF as a new tool for temperature sensing, strain sensing, and magnetic field sensing.

- Test the CdSe/ZnS CQDs with the salt-bridge structure method and determine if this structure improves temporal decay response and FWHM.

- Further developing the PolyMUMPS based MEMS cantilever chip to characterize the stress-strain properties of various CQDs within a polymer matrix under conditions that an aircraft would experience during its flight. It is envisioned that this chip would be placed within a vacuum chamber with the ability to both heat and cool the chip.

- Look into using CQDs drawn through a PCF and add reflectors on both ends as another option to cause lasing. This could allow for better guide lasers used by both the DoD and NASA for imaging in space.

- Utilize the shrinkage factor of polymers to various CQD-loaded polymers on MEMS devices as a possible way to tune CQD peak emission wavelengths for photonic systems.

- Look at utilizing CQDs within 3D printed structures or coated onto them as an optical NDT
- Investigate the use of salt-bridge scintillators. By using the acidic ligands encapsulating a CQD, monolayer deposition control could occur by dipping a layer of CQDs into a basic solution, then back into the CQD solution to form a salt bridge between each monolayer. This would be a stronger bond than van der Waals forces. Theoretically, one could create thick and dense blocks of CQDs with higher efficiency.
- Collect PL decay data for both PbSe and PbS CQDs.
- Investigate if lead-based CQDs can efficiently show CT to SU-8-5 as a way absorb NIR and emit blue light.
- Collect PL decay data for a core-crown CdSe NPLs applied as a thin-film.

In addition, there are numerous future ideas for both the 3D printed honeycomb structure and the CQD optical NDT invention.

5.4.1 3D Printed Structure Future Ideas

There are several ways to improve the 3D printed structure loaded with CQDs. Using more advanced 3D printing can result in the same function, but better capability as seen in Figure 103.

- Alternative A

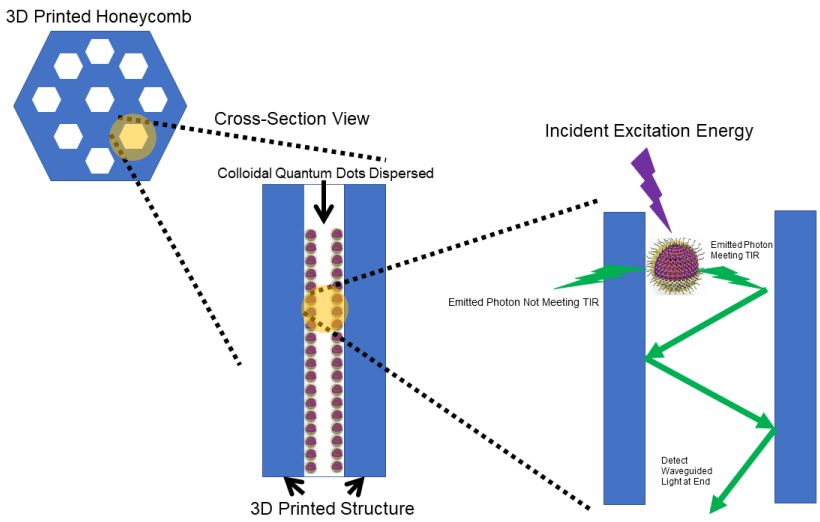


Figure 103. The invention can be modified by using a two-photon polymerization 3D printer to create about 100 nm sized holes in the 3D printed structure. The exact diameter of this hole can be designed to waveguide emitted light from the CQD down to the bottom of the structure.

In addition, spin coating a thin-film of UV curable photoresist on both sides of the 3D printed structure would be possible without the photoresist going right through the CQD channels in the honeycomb structure. With the right viscosity, the nanometer scale holes would discourage photoresist from entering the channel and affecting the waveguiding performance.

- Alternative B

  The 3D printed scintillator, due to having a low Z polymer makeup in the structure, could work as a neutron detector. This could occur by using proton recoil within the low Z polymer, which further interactions would eventually excite the CQDs dispersed within the 3D printed scintillator.

- Alternative C

  Instead of using standard 3D printing materials for this invention, it would be ideal to use a scintillating 3D polymer which can encourage charge transfer

towards the CQDs, or even light themselves to increase the quantum efficiency of the overall scintillator. In addition, this alternative could be coupled with alternative A to make use of waveguiding. This alternative can be visualized in Figure 104.

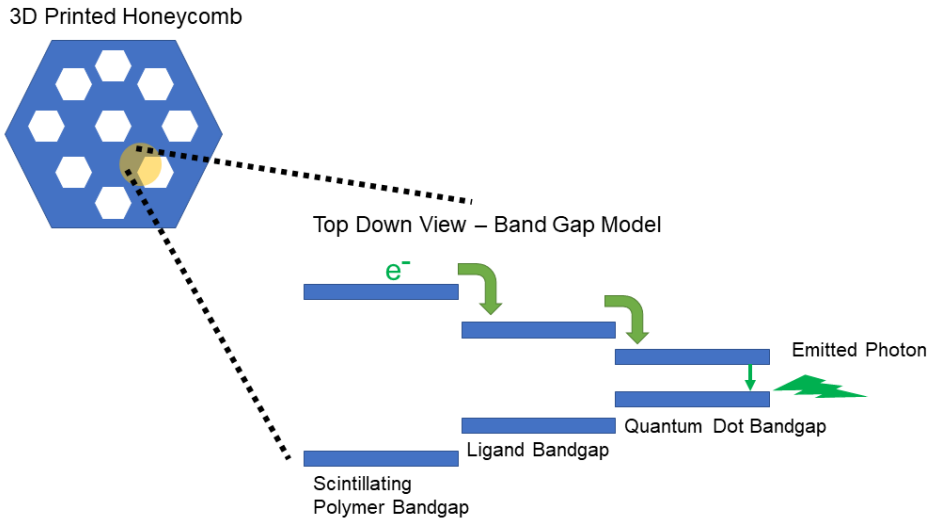


Figure 104. An engineering 3D printed scintillating polymer can charge transfer energy deposited into it over to nearby CQDs to emit additional photons and increase quantum efficiency.

- Alternative D

  Without any modifications from the prototype CQD 3D printed scintillator described in this patent, an improvement would be to 3D print about 200 µm thick structures and load them with CQDs. Then, it would be possible to stack the 3D printed structures in a sandwiched manner with another transparent medium such as quartz or a specially designed polymer. This medium could be designed to be a waveguide in between the 3D printed structures. This improves the original design by preventing photons from being greatly attenuated by a thick amount SU-8-5 photoresist before reaching a detector. The detector could then be placed at the side of the scintillator to detect emitted photons from the CQDs. This method would be useful for higher energy x-rays as lower energy

x-rays on the order of 1 keV would not be able to transmit through thin layers of quartz, unless the transparent layer is a polymer layer. This alternative is better explained in Figure 105.

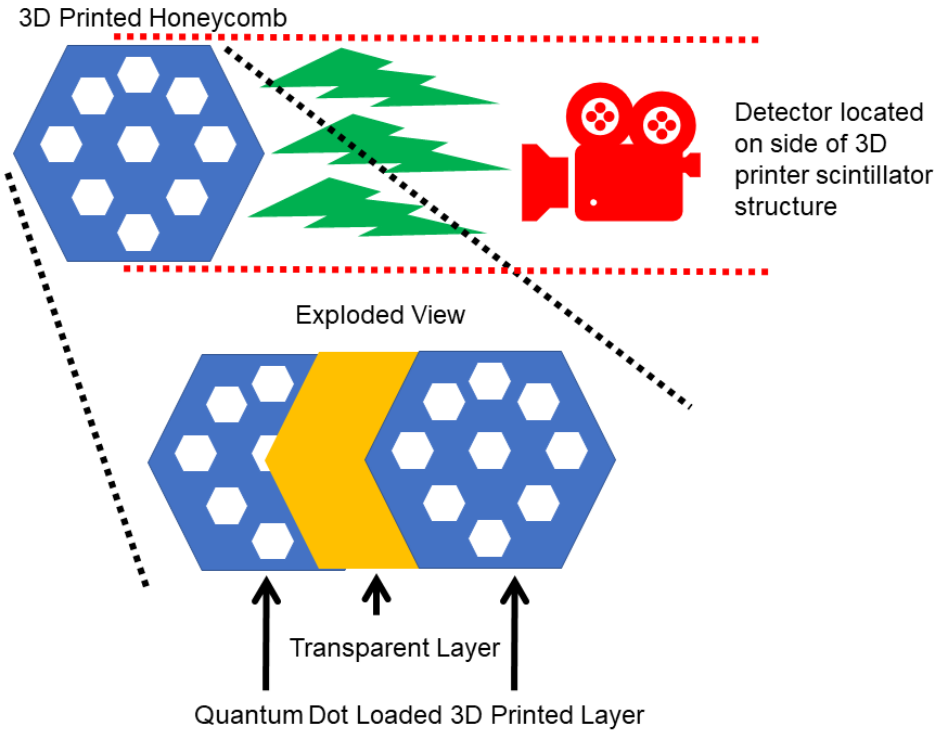


Figure 105. Instead of one single thick 3D printed structure, this alternative slices up the structure into thinner slices. In between each 3D printed slice would be a transparent medium to guide light emitted by the CQDs out to a detector located to the side of the entire structure. This medium could be quartz or even a polymer.

- Alternative E During the fabrication process of the original prototype, it was noticed that the IPA and toluene caused warping of the 3D printed structure's edges which made curing the structure flat to a piece of quartz difficult. This could be avoided by using water-based CQDs and avoid the IPA step altogether, however not every CQD material is available in water and toluene must be used. In this case, an improvement would be to add a metal support structure around the entire circumference of the 3D printed structure after printing and cleaning of any support material. The metal structure would be in two pieces (one for

each side of the 3D printed structure) and snap together. This would prevent the structure from warping during fabrication when using CQDs suspended in toluene. Orthographic drawings of this new design can be seen in Appendix B. A 3D model of this improved design can be seen in Figure 106.

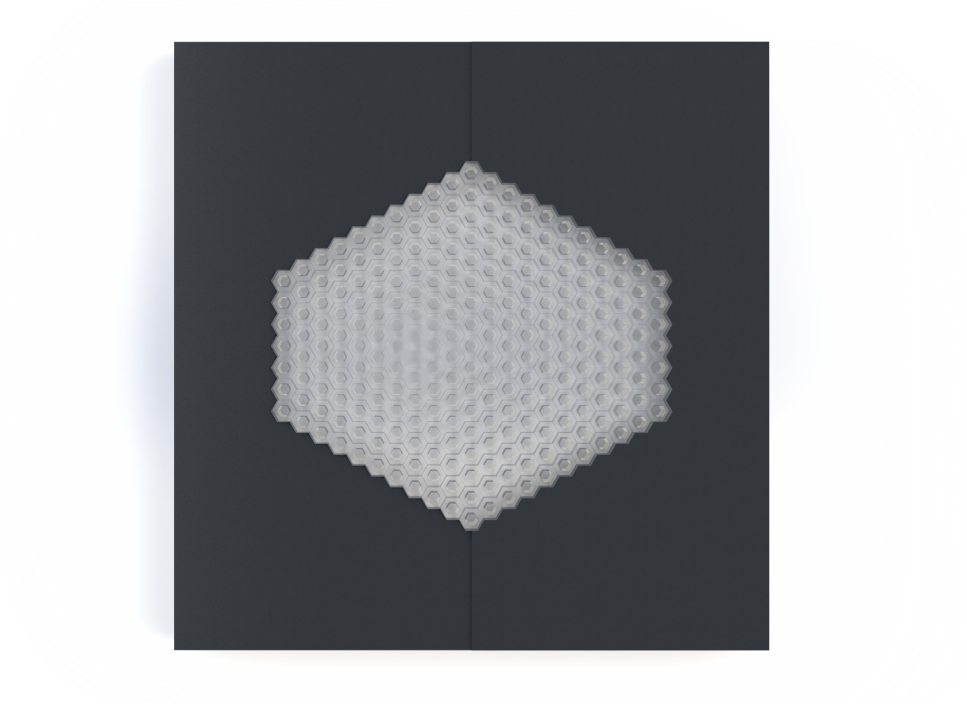


Figure 106. Metal surrounding the 3D printed honeycomb will prevent warping during fabrication.

An exploded view showing how the metal rim comes into place around the 3D printed part can be seen in Figure 107.

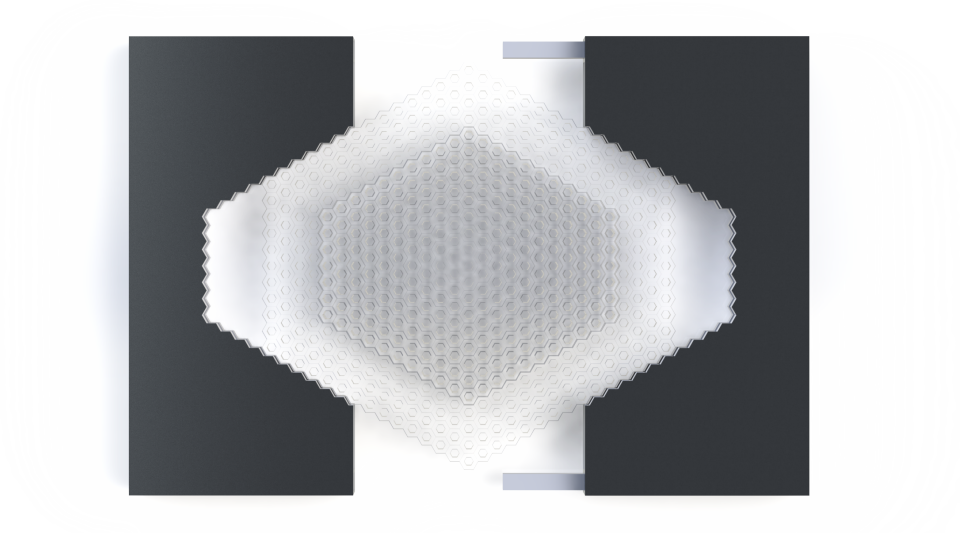


Figure 107. Two metal pieces are pushed into each other to surround the 3D printed honeycomb.

5.4.2 Stress-Strain Future Ideas

There are additional ways to improve the stress-strain CQD NDT concept.

- CQD Layers Embedded Within Structure and Fiber Optically Excited Alternative This concept does not use optics, but instead does all functions within, for example, an airframe. It would require a new composite material with the CQD layer within the composite material. Multiple CQD layers could be used as well depending on structural integrity. The overall concept can be seen in Figure 108.

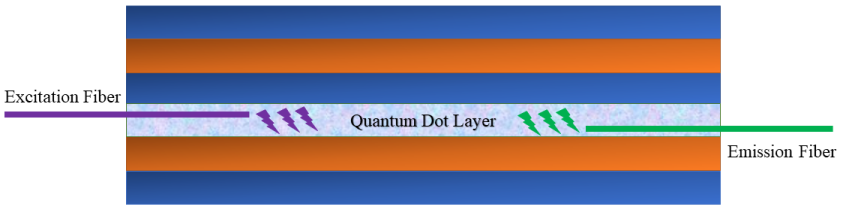


Figure 108. Graphic showing alternative which applies the stress-strain wavelength changes from the main invention within an aircraft frame.

Taking advantage of the evanescent fiber enables CQD excitement. However, it is possible to also use the end of individual fibers to shine light into a CQD-loaded polymer layer. This concept is explained by Figure 111.

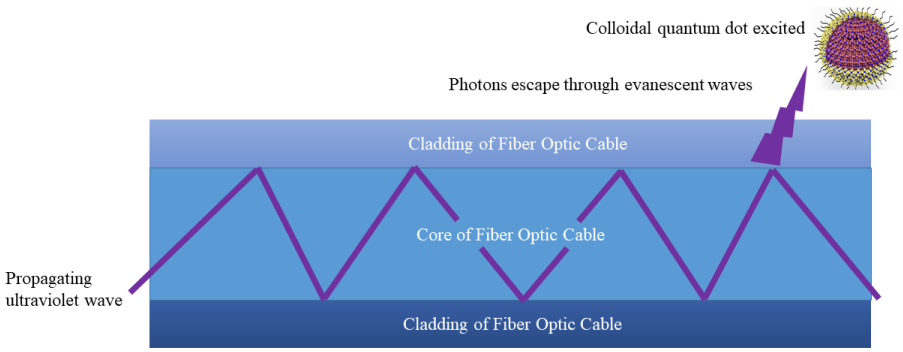


Figure 109. Evanescent waves from the fiber optic can be used to excite nearby CQDs.

Sensing the emission of CQDs would be possible through collecting their photons which meet the TIR angle criteria for the fiber. When the photon meets the TIR

angle, it can be waveguided back to a spectrometer to be measured. Ideally a dedicated fiber would be used for collecting the emitted photons from the CQDs. This concept is also explained by Figure 110.

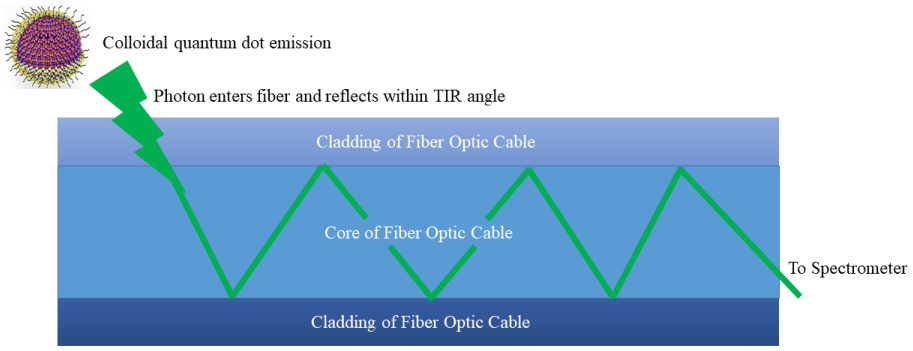


Figure 110. Excited CQDs emitting their photons can be sensed by collecting photons that enter a nearby fiber optic cable and meeting the TIR angle criteria.

If both the excitation wavelengths and the emission wavelengths are far enough apart, it could be possible to do both Figure 111 and Figure 110 within the same fiber optic cable.

- Fabrication This approach integrates a thin-film layer of CQD-loaded polymer. This integration may require coatings on the composite material layers adjacent to the CQD-loaded polymer layer. The first half of the composite material would be made, then the CQD-loaded polymer would be added on top of it. Next, at least two fiber optic cables would be routed along the length of the CQD-loaded polymer. Then, the remaining half of the composite material would be added to the top of the CQD-loaded polymer to finish the composite structure. Note, there could be multiple CQD-loaded polymer layers to measure stress-strain at different

thicknesses within a composite structure.

  - How To Use A network of sensing fibers would be embedded in the areas of interest. It may be possible to use the speed of light to calculate how far down a fiber the cracks occur in order to use a single fiber to sense multiple points around an airframe. However, the easiest way would be to have multiple fibers embedded at important points of interest and run a fiber optic multiplexer to have a single spectrometer measure the wavelengths of emission across all the sensing fibers. The CQD-loaded polymer matrix would be excited by another set of fibers which would, by design, allow evanescent waves to disperse far enough away from the core to excite the CQDs.

- CQD Emission Transmission Through Material Alternative This concept operates in the same manner as the main invention, but also can be used within a new composite material. The main difference is that the new composite material must be designed to allow for the transmission of both the excitation wavelength and the emission of the CQD photon wavelength. This concept is explained by Figure 111.

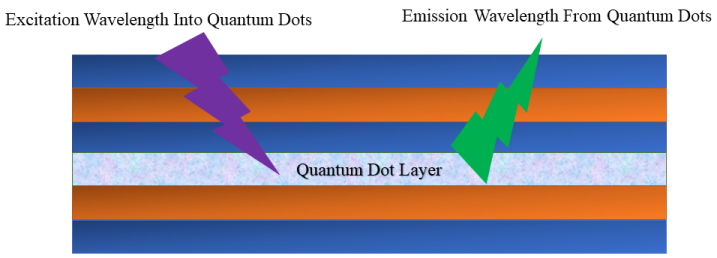


Figure 111. Graphic showing alternative design which is an improved modification. Here, the composite material must be designed to allow both the excitation wavelength of light to the layer of CQDs within a polymer and the excited emission of the CQDs.

The overall system configuration to make use of this concept is explained by Figure 112.

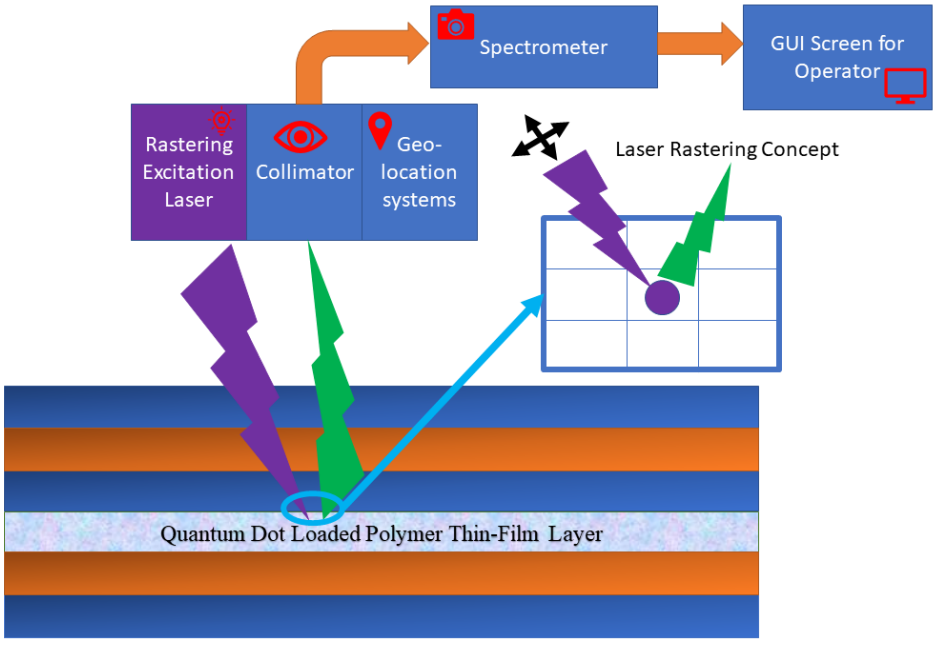


Figure 112. Overall system setup to use for CQD emission transmission through material alternative.

– Fabrication

  A future experimental composite material could integrate a thin-film layer of CQD-loaded polymer. The composite material must be designed in order to transmit both the wavelength of excitation for the CQD-loaded polymer layer and the CQD-loaded polymer layer's emission wavelength. This integration may require coatings on the composite material layers adjacent to the CQD-loaded polymer layer. The first half of the composite material would be made, then the CQD-loaded polymer would be added on top of it. Then, the remaining half of the composite material would be added to the top of the CQD-loaded polymer to finish the composite structure. Note, there could be multiple CQD-loaded polymer layers to measure stress-strain at different thicknesses within a composite structure. Different CQD materials/diameters could be used at different layers which emit different wavelengths of light in order to measure the stress-strain of varying thicknesses within a composite structure.

– How To Use Sensing wavelength changes in this concept would be the same as in the stress-strain experiment as discussed in Chapter **??**. The differences would be the possible changes in the excitation wavelength used and the emission wavelengths to be sensed. This may also require infrared emitting CQDs that are still cadmium free such as lead-based CQDs.

Appendix A. Leica DVM6 Colored Surface Maps of Polymer Scintillators

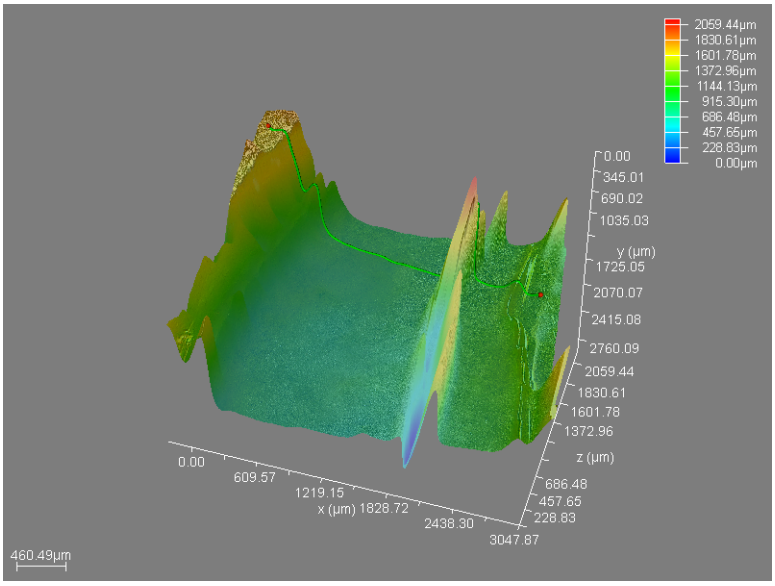


Figure 113. CdSe NPL polymer colored surface map taken with a 10° tilt.

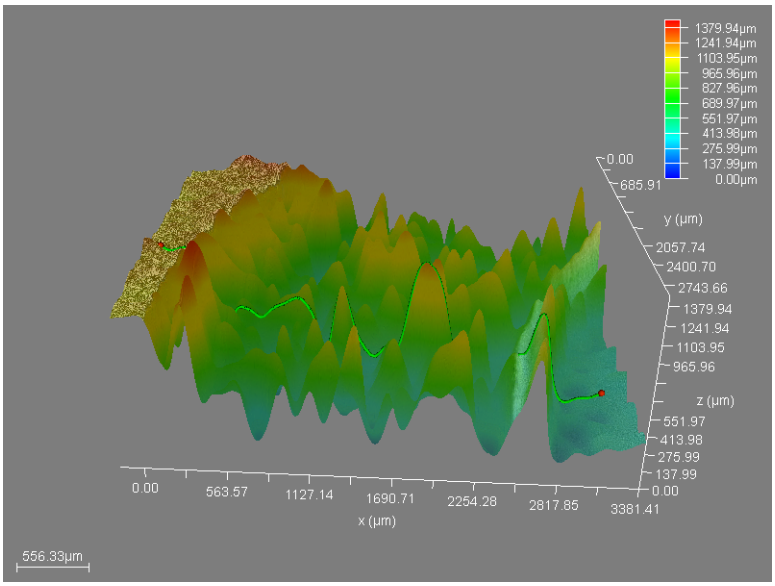


Figure 114. CuInS/ZnS polymer colored surface map taken with a 10° tilt.

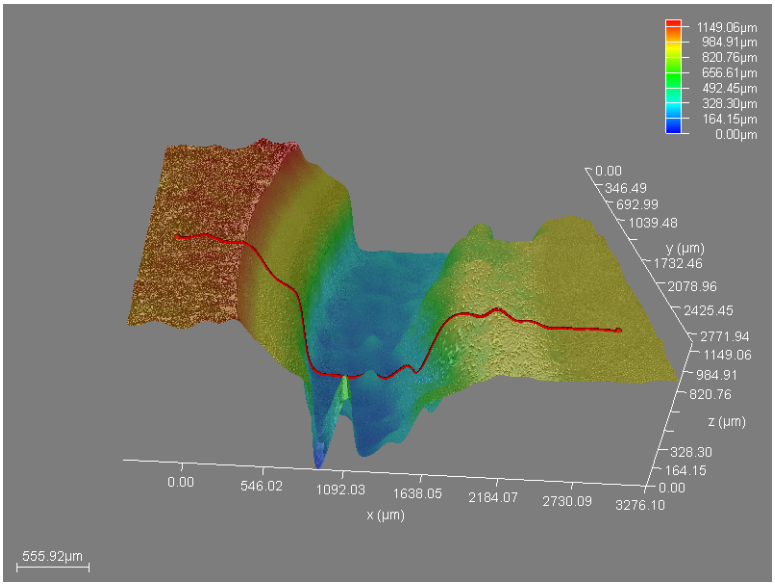


Figure 115. Control polymer colored surface map taken with a 9° tilt.

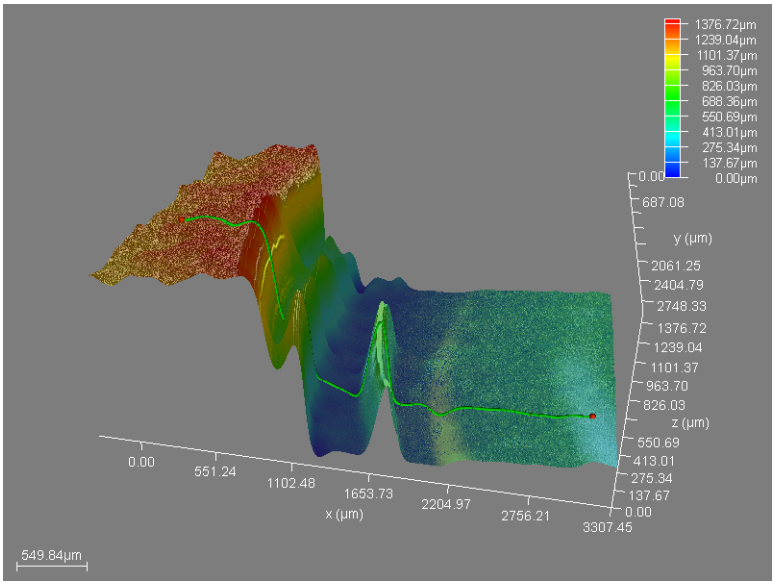


Figure 116. CdSe polymer colored surface map taken with a 9° tilt.

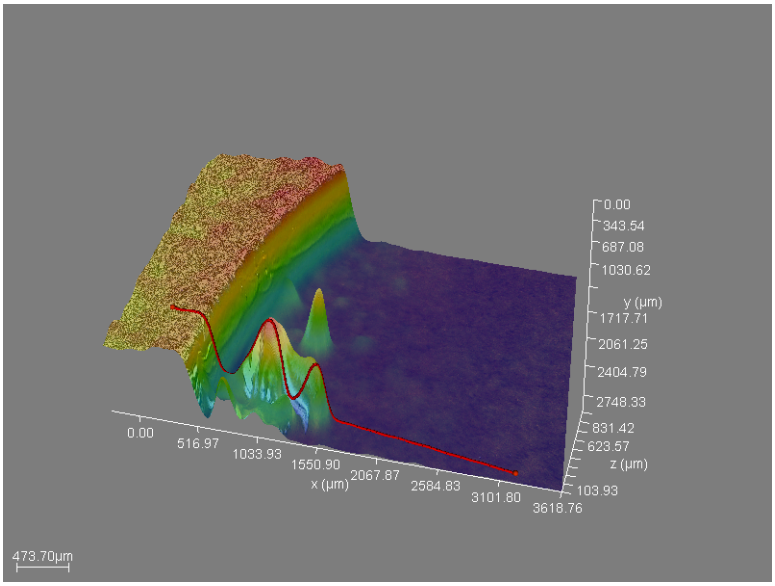


Figure 117. CdSe/ZnS polymer colored surface map taken with a 5° tilt.

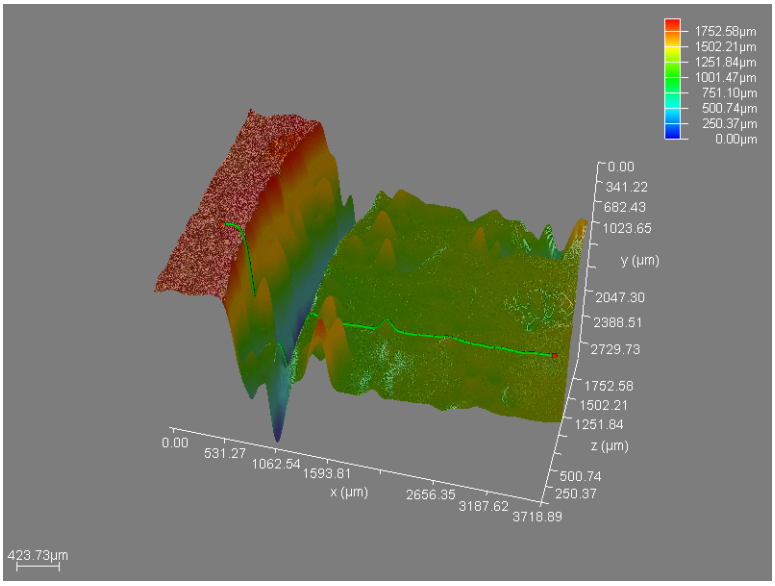


Figure 118. InP/ZnS polymer colored surface map taken with a 5° tilt.

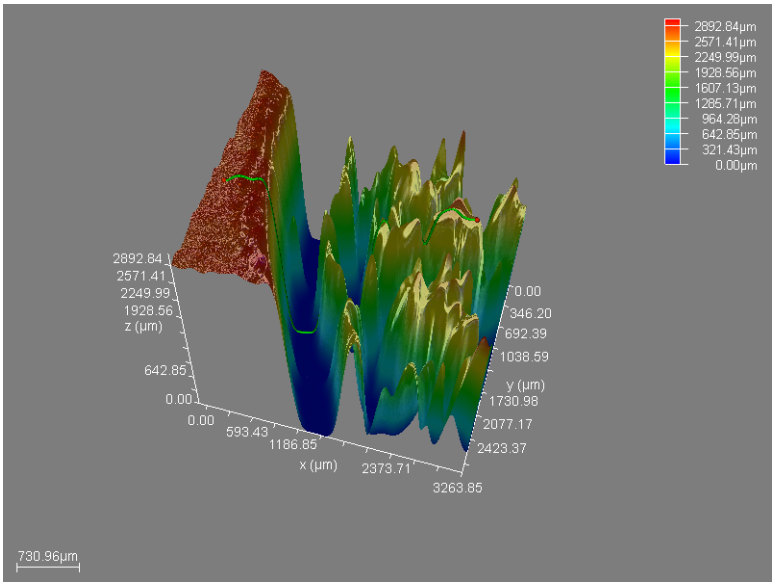


Figure 119. PbS polymer colored surface map taken with a 10° tilt.

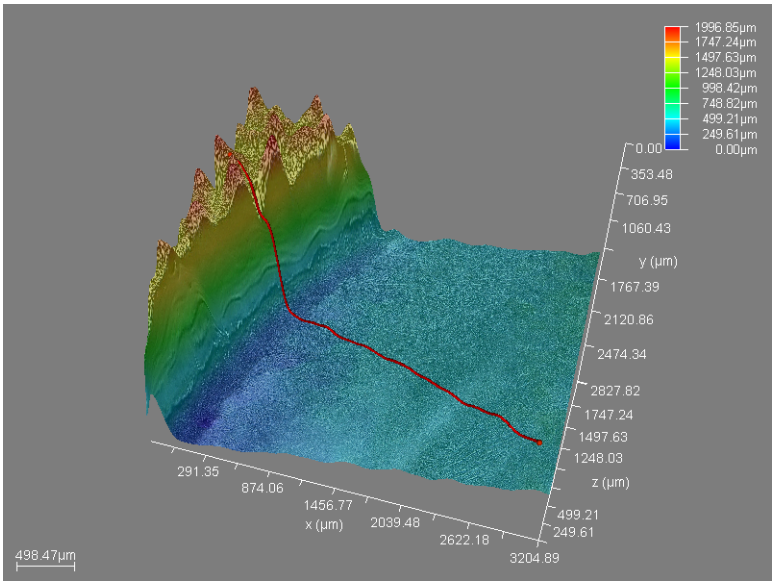


Figure 120. PbSe polymer colored surface map taken with a 10° tilt.

Appendix B. 3D Printed Structure Version Two

An orthographic drawing of the 3D printed structure can be seen in Figure 121.

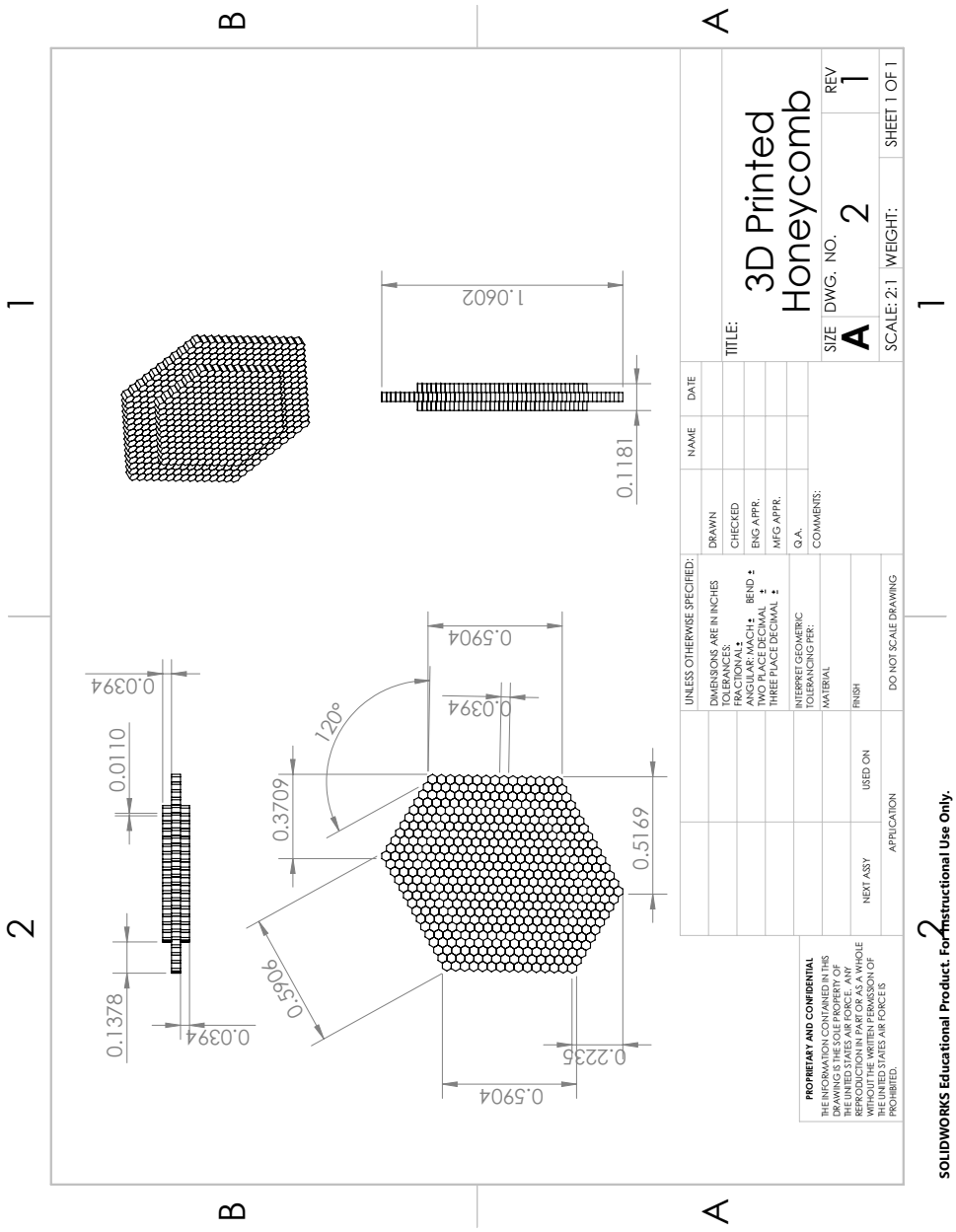


Figure 121. Orthographic drawing of version two of the 3D printed honeycomb structure. Drawn within SolidWorks.

An orthographic drawing of the right metal support to surround the right side of

the 3D printed honeycomb structure can be seen in Figure 122.

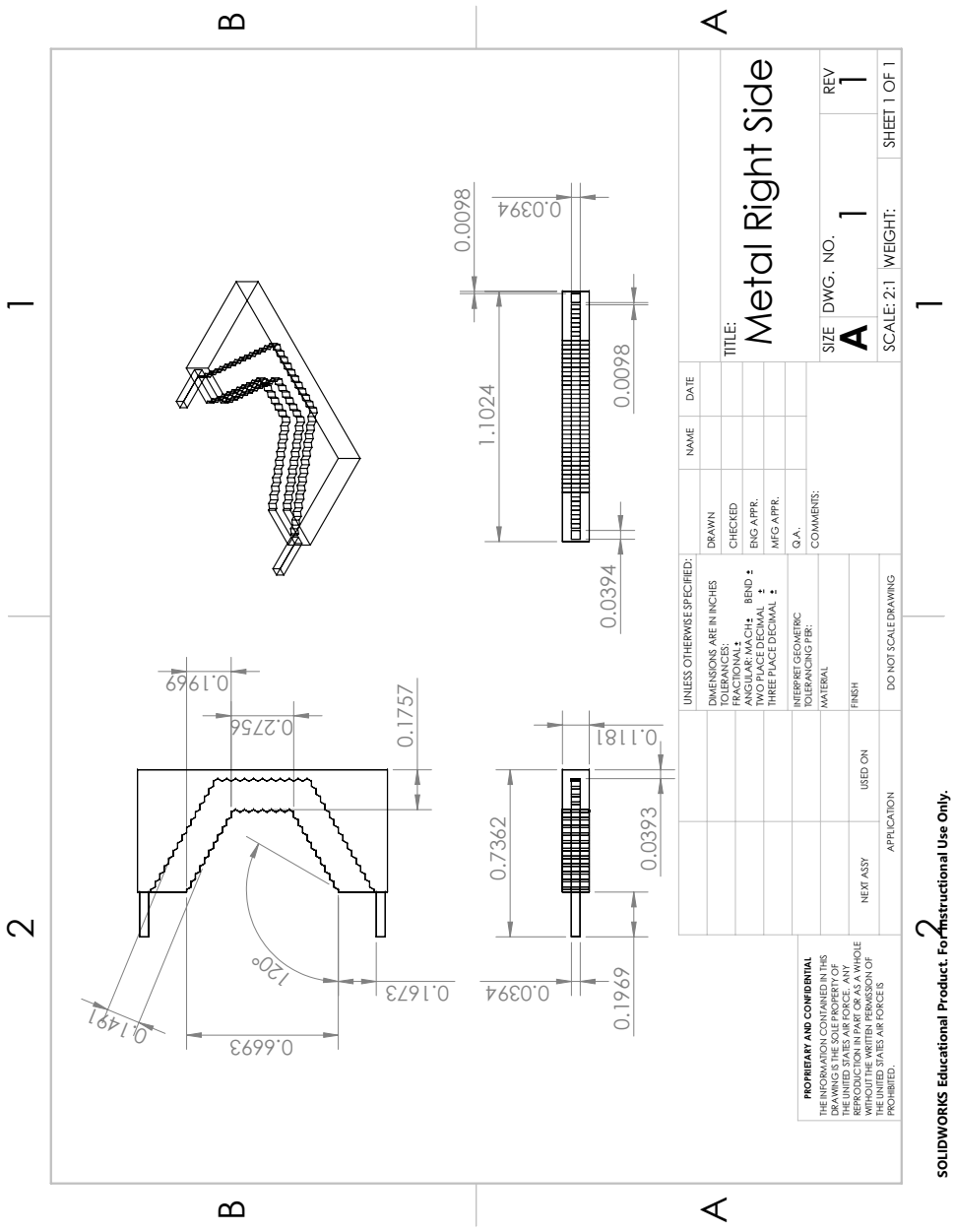


Figure 122. Orthographic drawing of the right metal support that slides onto the 3D printed honeycomb structure. Drawn within SolidWorks.

An orthographic drawing of the left metal support to surround the left side of the 3D printed honeycomb structure can be seen in Figure 123.

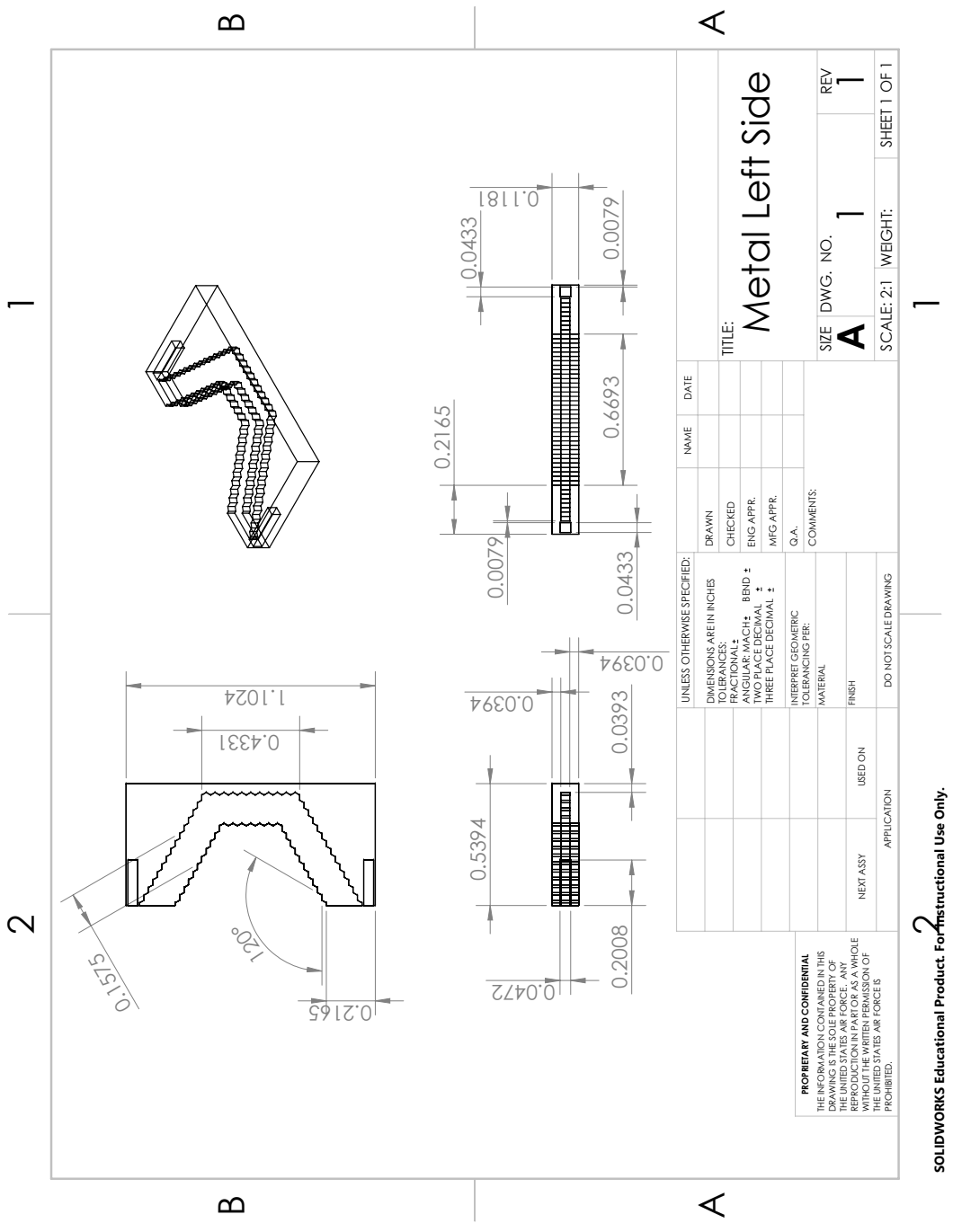


Figure 123. Orthographic drawing of the left metal support that slides onto the 3D printed honeycomb structure. Drawn within SolidWorks.

Appendix C. Design and Initial Testing of MEMS Cantilever Chip

C.1 MATLAB Calculations

MATLAB was utilized to do a quick check on the following parameters:

- Fundamental Frequency
- Applied AC voltage needed for resonance excitation
- RLC Equivalent Circuit
- Pull-In Voltage
- Max Strain

The formulas used to solve for each parameter will be discussed in the following subsections.

C.2 Fundamental Frequency

The fundamental frequency was calculated by using $f_0 = \frac{1}{2\ \pi} \times \sqrt{\frac{K_{eff}}{m_{eff}}}$. Where K_{eff} was calculated after taking both the total mechanical stiffness and electrostatic stiffness [32]. m_{eff} was $\frac{33}{140}\ m_{eff}$ [33]. In the case of a cantilever, the electrostatic stiffness brings down the overall effective stiffness. This calculation was given by: $K_{eff} = K_{mech} - K_e$. Where the calculation for K_e can be seen by using: $K_e = \frac{\epsilon \times A_{eff}\ {V_{dc}}^2}{{d_0}^3}$. Finally, for K_{mech}, this calculation was given by: $K_{mech} = \frac{E\ W\ H^3}{4\ L^3}$. This stiffness was added three times, each for the stiffness of the polysilicon layer, the gold layer, and the CQDs polymer layer [32].

C.3 Applied Alternating Current (AC) voltage needed for resonance excitation

The applied AC voltage was found by using the displacement transfer function and running it in a loop until the optimal AC voltage was found. This optimal value was one-third the of the difference of the gap between the height of the cantilever and the electrode and the displacement caused by the applied Direct Current (DC) voltage. Which in this case the applied DC voltage was modeled as one-third of the pull-down voltage. This AC value was calculated to prevent the displacement of the cantilever beam from hitting the electrode and remain stable during resonance.

C.4 RLC Equivalent Circuit

The equations for getting the RLC equivalent circuit for a MEMS cantilever were well known. The resistance was given by: $R = \frac{\sqrt{K_{eff}\ m}}{Q\ \eta^2}$. The inductance was given by: $L = \frac{m}{\eta^2}$. Finally, the capacitance was given by: $C = \frac{\eta^2}{K_{eff}}$. From the RLC equations, the electrical coefficient η^2 was calculated by using: $\eta^2 = \frac{\epsilon\ A_{eff}\ V_{dc}}{{d_0}^2}$ [32].

C.5 Pull-In Voltage

The pull-in voltage was found by using the total effective stiffness before considering the electrostatic stiffness effect. This is because the required V_{dc} needed to calculate the electrostatic stiffness was dependent on the pull-in voltage value first. The formula used is: $V_{pi} = \sqrt{\frac{8}{27}\ \frac{K_{mech}\ {d_0}^3}{\epsilon\ A_{eff}}}$ [32].

C.6 Max Strain

The maximum strain experience by the cantilever can be found by first finding the electrostatic force pulling the cantilever down at its pull-in voltage. This formula

was as follows: $F_{es} = \frac{1}{2} \frac{\epsilon \ A_{eff} \ {V_{pi}}^2}{{d_0}^2}$. Then, the following formula was used to calculate the strain: $\epsilon_{max} = \frac{F_{es}}{A_{cross} \ E}$. Where A_{cross} was the cross-sectional area of the cantilever beam [31].

C.7 LTSpice Simulations

From the calculated values found with the MATLAB calculations, an electrically equivalent model was drawn in LTSpice. This layout can be seen in Figure 124.

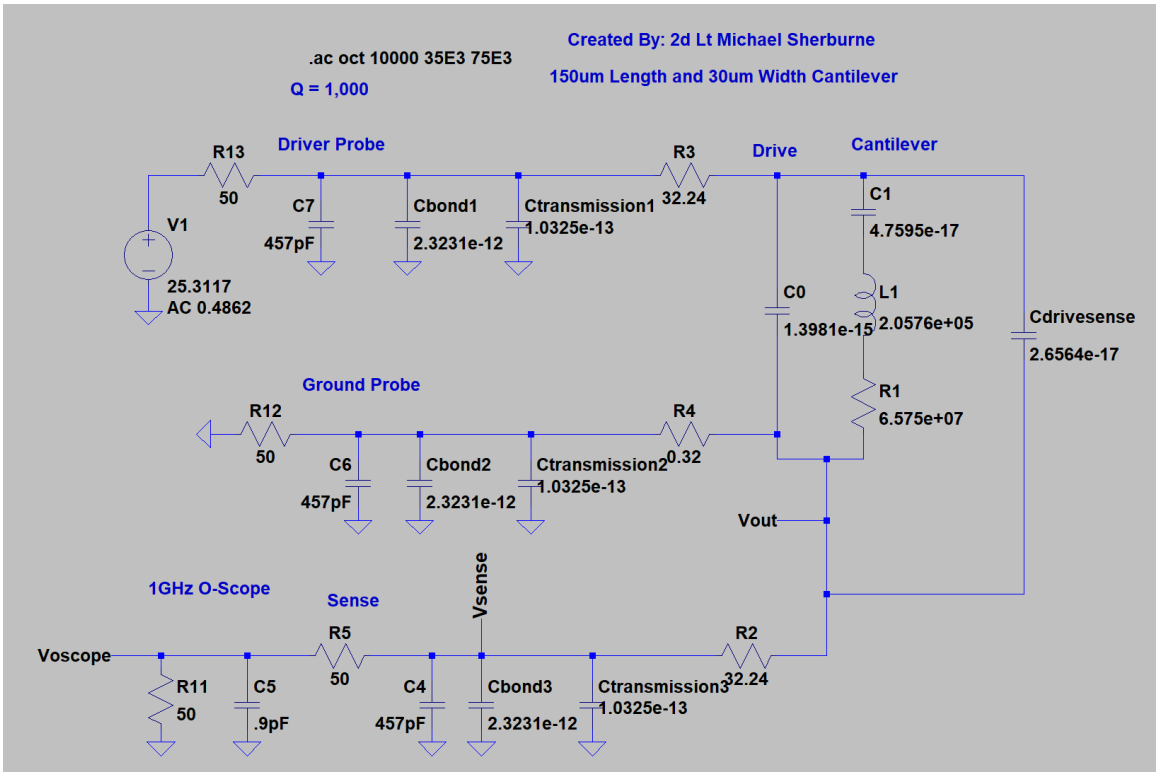


Figure 124. LTSpice model drawn with RLC equivalent cantilever and all associated transmission line effects to drive and sense the cantilever.

As can be seen in Figure 124, the MEMS RLC equivalent circuit is embedded in the middle of the circuit, and all associated transmission line affects were applied. A frequency sweep was then applied around the fundamental frequency of the cantilever.

C.8 COMSOL Finite-Element Analysis (FEA) Simulations

A model, shown in Figure 125, was drawn in COMSOL that had accurate dimensions of the cantilever anchor, electrodes, and cantilever beam. The Au layer was not included as it was assumed that it contributed a negligible effect to the mechanical system as a whole, and further complicates the FEA.

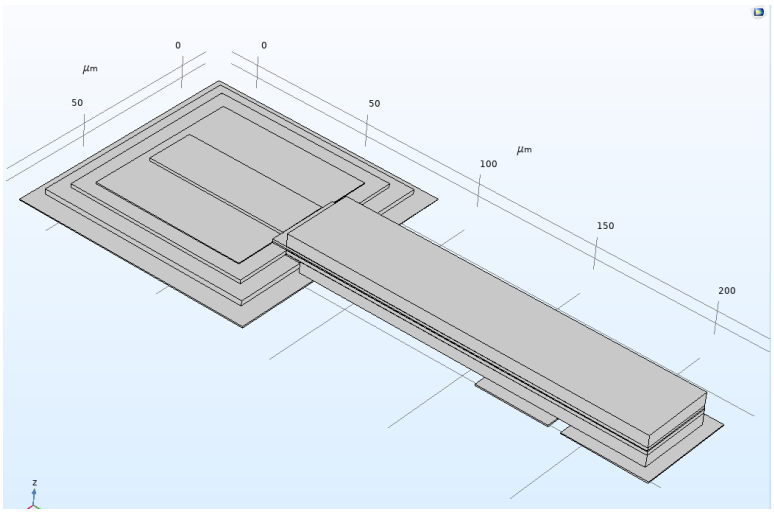


Figure 125. 3D model made in COMSOL to simulate a MEMS cantilever with a PMMA layer used to simulate the CQDs layer.

C.8.1 Empirical Calculations and FEA Results

MATLAB calculations can be seen in Table 28.

Parameter	Value (MKS)
R (Ω)	6.575e+07
L (H)	2.0576e+05
C (F)	4.7595e-17
C_0 (F)	1.3981e-15
Cdrivesense (F)	2.6564e-17
η^2 (N/V)	5.5507e-17
Cbondpad (F)	2.3231e-12
V_{pi} (V)	75.9351
V_{dc} (V)	25.3117
V_{ac} (V)	0.4862
Electrostatic Force (DC) (N)	8.4860e-07
f_0 (used for circuit) (Hz)	50,858
K_{eff} (K_{mech} – K_{es}) (N/m)	1.1662
Strain at V_{pi}	1.0139e-07

Table 28. Calculated values using a Q = 1,000 and a 150 μm **Length and** 30 μm **cantilever.**

These values were then plugged into the LTSpice simulation. The LTSpice simulaton results can be seen in Figure 126.

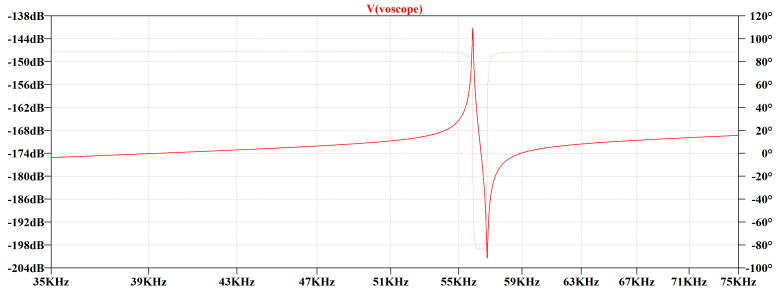


Figure 126. LTSpice simulation as seen from oscilloscope probe.

As can be seen, a resonant and anti-resonant response would be expected around

the fundamental frequency of the cantilever. The simulated frequency versus cantilever beam lengths from the COMSOL simulation can be seen in Figure 127.

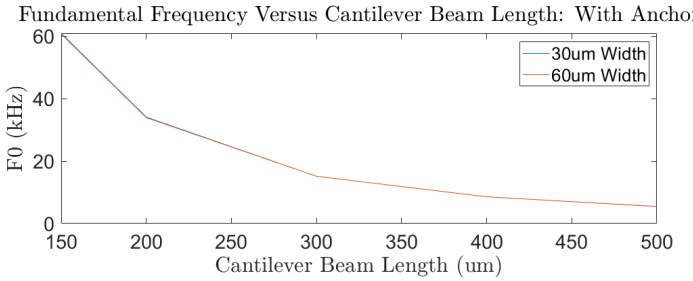


Figure 127. f_0 **over cantilever beam lengths.**

The pull-in voltage versus cantilever beam lengths can be seen in Figure 128.

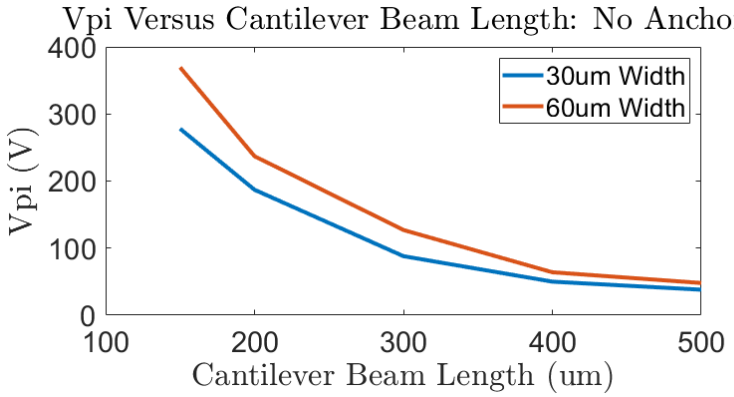


Figure 128. V_{pi} **over cantilever beam lengths.**

The MATLAB calculated f_0 in Table 28 and simulated in LTSpice in Figure 126 were within 10 kHz from the COMSOL simulation results in Figure 127. However, there was a few hundred volt difference from the V_{pi} in the MATLAB calculation versus COMSOL's results in Figure 128 for the respective cantilever dimensions. There were sources of error in the MATLAB calculations not considered such as the fringe field effects. The varying materials used along the cantilever beam could be one of the more major causes for the large discrepancy when considering fringe field effects.

C.9 Prepping the Cantilever for CQDs Layer

Polymers usually have a difficult time adhering to a smooth metal surface such as gold, or even polysilicon. However, sometimes pre-treating a metallic surface with a treatment such as Hexamethyldisalazane (HMDS) does not always ensure better adhesion as learned in the laboratory. Thus, no pre-treatment was done to the gold coated cantilver in this design.

C.10 CQDs Layer

CQDs loaded within a UV-curable polymer were then applied. The application steps were shown below:

1. Use light field masks (additive pattern process)
2. Apply 1 μm thick CQDs layer using a spin coater
3. Soft bake at 100°C to enhance adhesion
4. UV cure, then develop with metal-ion free MF-319 developer

C.10.1 Photoresist Layer Before Au Sputtering

The following steps were done to prepare the wafer for Au sputtering in order to cap the CQDs layer:

1. Use SU-1818 photoresist (positive resist) and use a light field mask
2. Softbake at 115°C for 60 s [4]
3. Use MF-319 MIF developer

C.11 Au Sputtering Layer

After the application of the CQDs layer, Au was used to protect the CQDs from HF release. Low temperature application of the protecting layer was important since the polymer was rated to about 200°C. It was found that Au had the best resistance to HF etching [113]. The application of the Au was done through low temperature sputtering. An example process can be seen by Malinský *et al.* [83]. Using this process would require ≈ 4.38 s of sputtering to deposit a 6 nm Au layer.

C.12 Removal of Excess Au

After applying Au through sputtering, the excess would need to be removed. The steps to do this were shown below:

1. Use SU-1818 positive photoresist to pattern layer
2. Softbake photoresist at 115°C for 60 s
3. Use MF-319 metal-ion free developer to remove uncured photoresist
4. Use GE-8110 to remove excess Au
5. Run this process for ≈ 4 s at 25°C [42]
6. Use Microposit Remover 1165 to remove cured photoresist

After the removal of the excess Au, the release of the MEMS device can commence. It was found that the dry-HF release was not good for this design which was unfortunate since dry-HF has no stiction [34]. Wet-HF release was used instead.

C.13 Releasing the MEMS Cantilever

Due to time constraints, no CQDs were applied to the cantilever. Instead, the cantilever's actuation was tested. Upon delivery from the foundry, the MEMS chips had a layer of protective photoresist. This layer served to protect the chips when diced into smaller pieces. The photoresist removal recipe was as followed:

- Set spin speed to 1,000 rpm
- 30 s of acetone
- 30 s of methanol
- 30 s of DI water
- Repeat once more

A summary of the different HF release processes can be seen in Table 29.

Method	CO_2 Dry Used?	CO_2 Chamber Chip Orientation	Release Time	Condition Of Chip	Sacrificial Layer Removed?	Stiction?
Dry HF	No	Horizontal	2.5 hours	Lots of residual debris	No	No
Buffered Oxide Etch (BOE)	No	Horizontal	5 hours	Parts gone	No	N/A
49% HF w/ water	No	Horizontal	9 minutes	Clean	No	Yes
49% HF only methanol	Yes	Horizontal	9 minutes	Clean	Few	Partial
49% HF only methanol	Yes	Vertical	9 minutes	Some debris	Yes (only for gold devices)	No

Table 29. Table of various release processes used on MEMS chip.

The steps used in the most successful release process from Table 29 can be seen in the recipe below:

- Dip in 49% HF beaker for 9 minutes
- Dip in methanol beaker for 5 minutes
- Dip in 2nd methanol beaker for 10 minutes
- CO_2 critical point dry vertically within basket

C.13.1 Zygo Profilometer Measurements

The 3D profile of one of the cantilevers that worked can be seen in Figure 129.

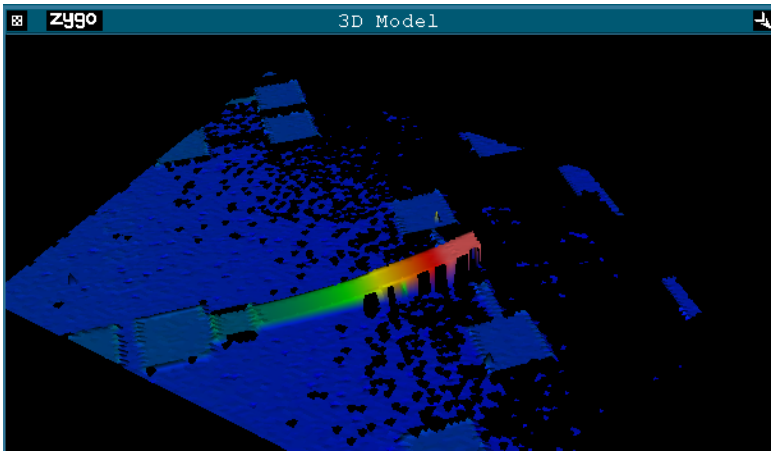


Figure 129. 3D profile of a 500 μm length and 60 μm width cantilever with gold on top

The measurement data from the Zygo can be seen across the cross-section of the cantilever in Figure 130.

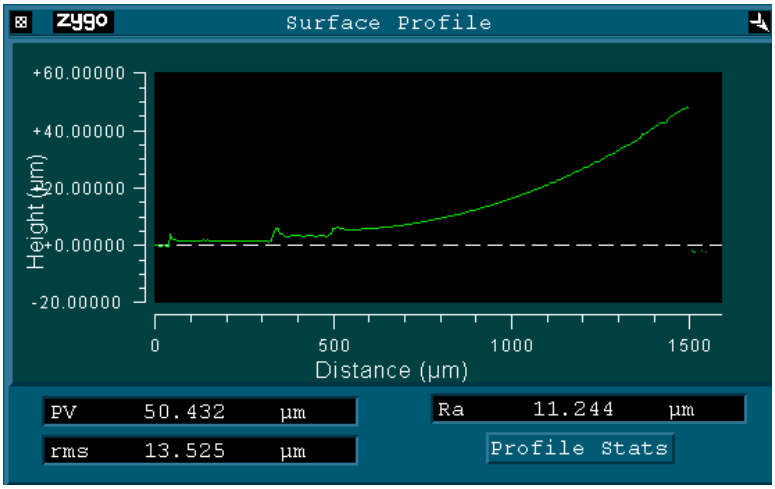


Figure 130. Height data of the MEMS cantilever using a Zygo profilometer.

It can seen that the cantilever released to a height of 50.432 μm.

C.14 Experimental Results

The number of data points were limited due to only a few of the cantilevers being fully released. The experimental setup used probes on both the ground and drive pads, a 50 Ω shunt in between the ground and probe station ground, a high voltage power supply, and a volt meter measuring resistance with a probe connected to the sense pad.

C.14.1 Calculating Residual Stress

The residual stress seen in Figure 129 was calculated by using Equation 45 [134].

$$\sigma = \frac{2\ y\ E\ t}{(1-\nu)\ L^2} \tag{45}$$

The variables seen in Equation 45 can be seen in the list below:

- t: Thin film thickness (0.5 μm) gold
- E: Young's modulus (169 GPa) [71]
- y: Height of deflection
- ν: Poisson ratio (0.23) [71]
- L: Cantilever length

Equation 45 was applied to the data taken from both the Zygo and the SEM. The deflection height was mapped to the residual stress. This can be seen in Table 30.

Beam Length	Max Height ± 2.5 (μ m)	Stress (GPa)
1.50E-04	5.00E-06	4.88E-02
2.00E-04	9.75E-06	5.35E-02
3.00E-04	1.48E-05	3.60E-02
4.00E-04	2.28E-05	3.12E-02
5.00E-04	3.48E-05	3.05E-02

Table 30. Table of residual stress values for varying gold thin-film coated cantilever lengths with 30 μ m **width.**

C.14.2 Resistance Measurements of PolyMUMPs Layers

With most of the cantilevers not showing any actuation under the microscope, an idea was that the line resistances were too high across the PolyMUMPs materials. A Fluke volt meter was placed upon the test structures already on the PolyMUMPs device and the results were summarized below:

- Each test structure has about same dimension as probe entrance
- Used a 57.34 Ω shunt when measuring and actuating
- Poly0: 1.5687 kΩ after removing shunt value
- Poly2: 198.96 Ω after removing shunt value
- Poly2/Gold: 7.52 Ω after removing shunt value

Seeing that the gold greatly decreased the line resistance, the current flow through the cantilevers was not of a concern for their actuation. If a cantilever was not released, it showed a resistance on an ohm meter, thus it will not actuate normally. A non-released cantilever would actuate, but it would be seen as a buckling near the anchor while the tip was stuck to the Poly0 layer and eventually failed. Since the shorter cantilevers had a lower deflection height, it was possible actuation was occurring on those cantilevers, but not noticeable to the human eye. Due to using

high voltages (up to over 200 V) and prevention of damaging the profilometer, the actuation could not be done under the Zygo. This would be another benefit of having CQDs layered on top of the cantilevers, since a cheap optical method could be used to determine actuation, versus testing devices under a more expensive diagnostic system.

C.14.3 Pull-In Voltage of Working Cantilevers

Only four samples of the gold cantilevers released or successfully poked back to release that resulted in good voltage pull-in test data. This data can be seen in Table 31.

Length (μm)	**Width** (μm)	**Deflection Height** (μm)	**Theory** (V_{pi})	**Measured** (V_{pi})	**Double Pad** (V_{pi})
300	30	19.1	175	160	123.7
200	60	13.3	169	172	119.5
400	60	32.5	276.5	213.9	195.5
500	60	50	394.2	244	278.7

Table 31. Table of pull-in voltages of four gold thin-film coated MEMS cantilevers of varying lengths and widths.

For the cantilevers with pull-in voltages of under 200 V, their pull-in voltage results were close to theoretical values. However, for the cantilevers with pull-in voltages of over 200 V, the theoretical calculation broke down. This was because fringe effects were not considered. One thought was that the electric field became strong enough to make the second actuation pad conductive, thus effectively doubling the available area for actuation. While not perfect, this brought the theoretical voltages much closer to experimental. Additional analytical models either did not have the right assumptions to be useful or still gave similar results to the conventional model. These models were also not designed for as high of a deflection as this experiment had measured [102] [37].

An interesting find also occurred during the 500 μm length and 60 μm width

cantilever test. The current monitor on the high voltage supply started to display 6 mA of current at about 10 V before pull-in. This could be a useful method to pull down the cantilever as much possible, but without causing a pull-in that resulted in the expected rapid disassembly of the MEMS cantilever. In addition, a RC time delay was evident in the video footage of the actuation of the MEMS cantilever. There was a delay in both pulling in the cantilever and turning off the voltage to the cantilever for it to come back up. The shunt in between the ground of the MEMS chip and the probe station was limiting the entrance and escape of current through the cantilever. It could be possible one could use this delay property to determine the resistance of a device that connects to the ground end of the MEMS cantilever.

C.15 Comparing Experimental Results to Theory

Another method in fitting the analytical model to the experimental data was to find the effective actuation area until the pull-in voltage matches the measured result. This was a rearrangement of the pull-in voltage formula and can be seen in Equation 46.

$$A_{eff} = \frac{K_{eff} * d_0^3}{\epsilon_0 \ \epsilon_r \ V_{pi}^2 \ \frac{27}{8}} \tag{46}$$

The original A_{eff} was found to be $1,500\ \mu m^2$. The effective area more than doubled to $5,094.3\ \mu m^2$ when considering the 500 μm long and 60 μm gold thin-film cantilever case. For the same cantilever beam, but for the 400 μm case, the effective area became $2,588.6\ \mu m^2$, which was still a bit more than the original effective area. When correcting the algorithm to analytically determine the pull-in voltage, doubling the actuation area plus an additional 30% in that area gave out the measured pull-in voltage for the 500 μm length cantilever. However, for the 400 μm length cantilever, only the original actuation area plus an additional 35% in that area gave the measured value. This led to the conclusion that there was a complex non-linear relationship

between the drive and sense pads on top of fringing field effects. Even if a best-fit line was made to account for the deflection height as the beam becomes longer, fringe field effects were seen to be non-linear and would throw off the analytical calculation.

Appendix D. Cherenkov Radiation Calculations

Starting with Equation 47, which showed the relativistic kinetic energy of a particle [89]:

$$T = mc^2 \times (\frac{1}{\sqrt{1-\beta^2}} - 1) \tag{47}$$

It was known that $\beta = \frac{v}{c}$. The refractive index n was well known as $\frac{c}{v}$. Rearranging β in terms of n led to Equation 48.

$$E_{thres}(n, m) = mc^2 \times (\frac{1}{\sqrt{1-\frac{1}{n^2}}} - 1) \tag{48}$$

In order to help academia, two types of energy thresholds were found for Cherenkov radiation. One of the forms which was found in multiple publications can be found in Quintero's thesis [114]. This energy threshold was given by Equation 49.

$$E_{thres}(n, m) = mc^2 \times (\frac{n}{^2 - 1}) \tag{49}$$

There was a fundamental difference between Equation 48 and Equation 49, where one had a smaller value in the energy threshold than the other. Upon further inspection, the two equations deviate by a subtraction of one. One idea about this deviation was a difference between the center of mass frame of reference or lab frame of reference being used. This was not the case, but instead goes back further into the fundamentals of Einstein's theory of relativity. Going back to the beginning, Einstein asserted that velocity and mass have an energy according to Equation 50.

$$E = m_0 \ c^2 \tag{50}$$

Equation 50 considered the energy of a particle at rest. However, when a charged

particle (which has mass) was moving at a measurable fraction of the speed of light, relativistic kinematics played a role. A Lorentz factor of γ must be used to correct the observed energy when the charged particle's velocity was compared to the speed of light. The Lorentz factor was given by Equation 51.

$$\gamma = \frac{1}{\sqrt{1 - \frac{v^2}{c^2}}} = \frac{1}{\sqrt{1 - \beta^2}} \tag{51}$$

Using the Lorentz factor was useful as when the velocity of a particle was at low speeds, no correction took place as γ was approximately one. When the particle's velocity becomes a measurable fraction of the speed of light, γ would have a corrective effect. The Lorentz factor in Equation 51 could then be applied to Einstein's energy formula in Equation 50. This relativistic factor correction was given by Equation 52.

$$E = \gamma \; m_0 \; c^2 \tag{52}$$

It was important to note that the formula in Equation 52 was used in Equation 49. However, this energy from Einstein's equation was the total energy of a moving particle with rest mass [3]. When considering both the rest mass energy and kinetic energy, this led to Equation 53.

$$E = E_{kin} + m_0 \; c^2 \tag{53}$$

From here, E in Equation 53 could be replaced with Equation 52. Rearranging the formula to be in terms of E_{kin}, the resulting work could be seen in Equation 54.

$$E_{kin} = \gamma \; m_0 \; c^2 - m_0 \; c^2 \tag{54}$$

This equation also fell in line with what Einstein envisioned for a kinetic particle.

When the particle's velocity goes to zero, the resulting formula would be Equation 50. Further simplification yielded Equation 55.

$$E_{kin} = m_0 \, c^2 \, (\gamma - 1) \tag{55}$$

It could be seen that Equation 55 would be Equation 48 when the Cherenkov threshold condition was accounted for. When solving for the threshold energy for Cherenkov, a moving charged particle was considered. This was its kinetic energy, not its rest energy. Thus, it would be best to not use Equation 49.

Equation 48 would determine if Cherenkov radiation could be a viable scintillating method in the range of 10 keV to 100 keV. The main limiting factor was the material to be used as the refractive media. The threshold n value could be found by solving for E_{thres}. An electron $\frac{MeV}{c^2}$ was 0.511 MeV. The MATLAB code to model the threshold energy can be seen in Appendix Z.1. The plot below in Figure 131 showed the results.

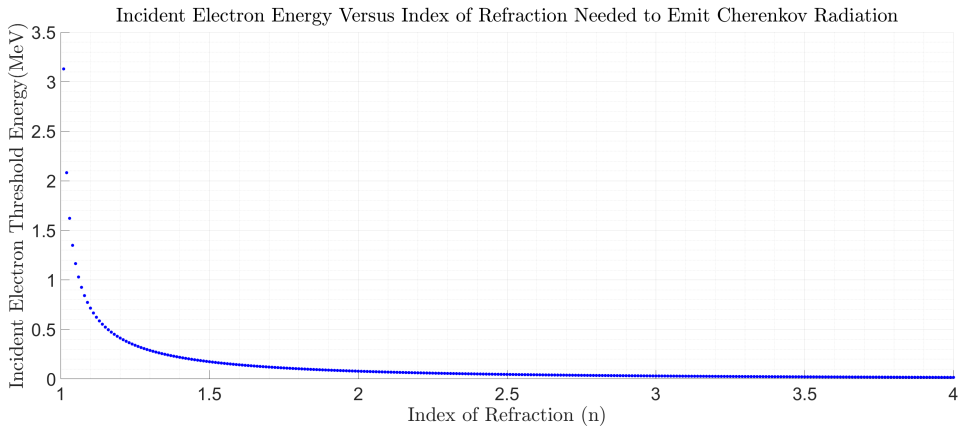


Figure 131. MATLAB modeling for electron threshold energy versus refractive index.

Figure 131 showed that Cherenkov could be emitted down to $\approx$ 47 keV at an index of refraction of 2.5 (index of refraction of diamond). Knowing where Cherenkov radiation was possible, the Frank-Tamm formula was used to approximate the total

amount of energy radiated per unit length. The energy radiated coming through the surface of a cylinder was defined. This formula could be seen in Equation 56 [62].

$$\frac{dE}{dx}_{rad} = \frac{z^2\ e^2}{c^2} \int_{\epsilon(\omega) > \frac{1}{\beta^2}} \omega(1 - \frac{1}{\beta^2\ \ \epsilon(\omega)})\ d\ \omega \tag{56}$$

There was fortunately a simplification of Equation 56. The following assumptions were made [89]:

- $\sigma = 0$ within medium
- $\mu = 1$ within medium
- Zero absorption of Cherenkov radiation
- Charged particle does not change its velocity within medium
- The medium goes on infinitely
- Cylinder length l should be much greater than the wavelength of emitted radiation

This could be seen in Equation 57.

$$M = 2\ \pi\ \alpha\ (\frac{1}{\lambda_2} - \frac{1}{\lambda_1}) \int_{\frac{1}{n}}^{max} (\frac{1}{(\beta(l)\ n)^2} - 1)\ dl \tag{57}$$

Equation 57 derived from Frank and Tamm had the following variables:

- M: number of photons emitted between wavelengths λ_1 and λ_2
- λ_2: upper wavelength of particles considered in total photon count
- λ_1: lower wavelength of particles considered in total photon count
- α: fine structure constant ($\frac{e^2}{\hbar\ c}$)

An additional modification was made in the simplified Frank-Tamm formula. Instead of integrating across all beta values, one could iterate over a few beta value changes. In this case, MeVcm was used as the unit for electron stopping power. A 3 cm long medium would be modeled which would still be both ergonomic and viable to use in front of a streak camera. The simplified Frank-Tamm formula was applied in a MATLAB code. To confirm how to use the formula, contact was established with Mr. Matthew Millard who wrote a thesis on Cherenkov radiation and the $\beta(l)$ value in his thesis was the beta value dependent on the distance the electron traveled down a medium. The values can be approximated by using the Beth-Bloche formula [89].

One iteration of calculating the electron stopping power in a diamond medium would be discussed. Starting with the material properties, a standard diamond had the following properties and coefficients:

- Elemental material: Carbon-12
- Number of protons: 6
- Density of diamond: 3.5 $(\frac{g}{cm^3})$
- Molar mass: 12 (amu)
- Index of Refraction: 2.5

The collisional stopping power for an electron was given by the simplified Beth-Bloche formula given by Equation 58.

$$(-\frac{dE}{dX})^{-}_{col} = \frac{5.08 \times 10^{-31}\, n}{\beta^2}\, [G^{-}(\beta) - ln(I_{eV})](\frac{MeV}{cm}) \tag{58}$$

The $G^{-}(\beta)$ term was calculated in Equation 59.

$$G^{-}(\beta) = ln(3.61 \times 10^{5} \tau \sqrt{\tau + 2}) + F^{-}(\beta) \tag{59}$$

The $F^{-}(\beta)$ term was calculated in Equation 60.

$$F^{-}(\beta) = \frac{1 - \beta^{2}}{2} [1 + \frac{\tau^{2}}{8} - (2 \tau + 1) ln(2)] \tag{60}$$

The $F\tau$ term was calculated in Equation 61.

$$\tau = \frac{T}{mc^{2}} \tag{61}$$

In addition, the I_eV term still needed to be calculated. A good approximation of this value could be seen in Equation 62. These equations related to the Z number of the medium.

$$19.0eV, Z = 1(hydrogen)11.2 + 11.7 \; ZeV, 2 <= \; Z \; <= 1352.8 + 8.87 \; ZeV, Z > 13 \tag{62}$$

First, β was solved by back calculating the incident electron using relativistic kinematics. Then, solve for its kinetic velocity. Next, the values from diamond were used with the found β value to solve for the above equations. Upon finding the stopping power, the initial incident energy of the photon was subtracted by this value. Then, β was recalculated and the process started over again. Since diamond would be the best case scenario for seeing if Cherenkov was feasible or not without going into exotic materials, this case was applied across a range of 1 keV to 100 keV incident energy values. 3 cm length of material was used and then calculated the total photon emission from the material generated by Cherenkov. The upper wavelength was determined by knowing the highest QE of a S20 photocathode was $\approx$ 400 nm

before starting to lose its QE. The lower wavelength was the transmission limit of diamond ($\approx$ 200 nm). Cherenkov would emit photons of lower wavelengths, but these would not be transmitted by the diamond. The MATLAB code used in the calculations can be seen in Appendix Z.2. The resulting plot from the MATLAB code could be seen in Figure 132.

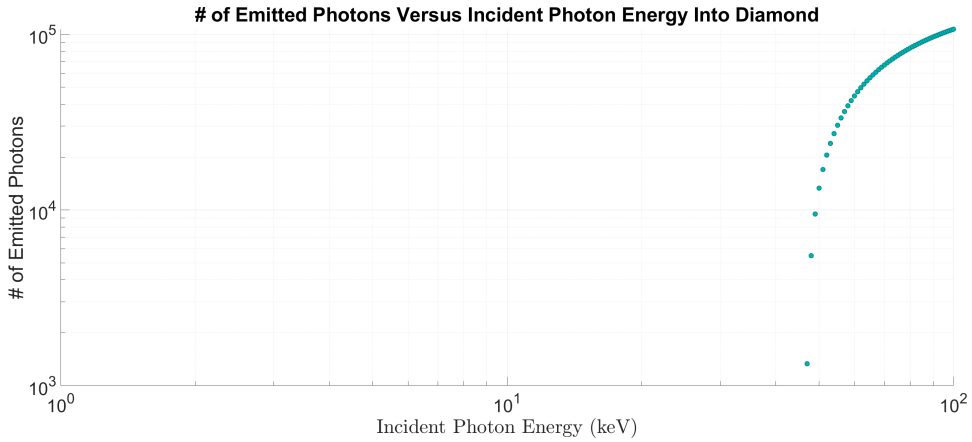


Figure 132. Cherenkov photon emission versus incident x-ray energy in a diamond medium.

This plot showed that at 47 keV using a diamond crystal as the Cherenkov material, there were 1,333 photons emitted through the diamond. At 50 keV, there were 13,310 photons. At this point, Cherenkov would be a viable x-ray detection tool. Going to the upper energy range of 100 keV, resulted in 106,900 photons.

Appendix E. Loading CQDs as a Sol-Gel Procedure

1. Hydrolysis and polycondensation of Tetraethyl Orthosilicate (TEOS) ($Si(OC_2H_5)_4$)
2. Dissolving TEOS in ethanol
   (a) This makes SiO_2 sol as a glassy solution
3. Add in CdSe CQD stabilized with the ODA ligands in toluene
4. Once mixture shows a gel formation, apply it as a spin coat onto desired surface

Appendix F. Explanation of the Nuclear Shell Model

An example of the shell model in a nucleus can be seen in Figure 133.

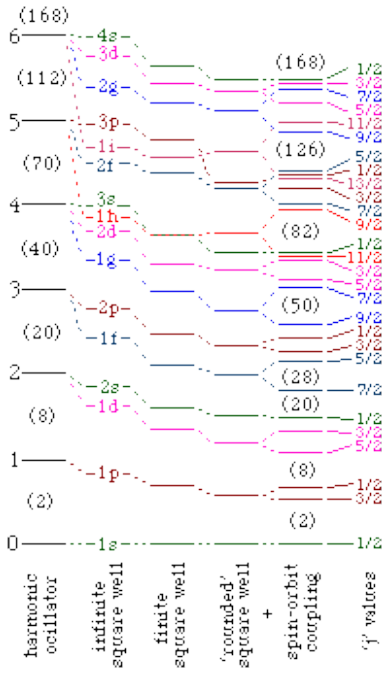


Figure 133. An example of multiple shell models, where going all the way to spin-orbit coupling gives the best approximation of the different energy states available within a nucleus. Image from Combley *et al.* [41]

It can be seen from Figure 133 that a few properties of the nucleus can be predicted, such as: angular momentum, magnetic moments, and electric quadrupole moments. The shell model has larger differences between energy levels towards the bottom of the structure, and it becomes more and more narrow between energy levels as the energy levels increase. The larger jumps between energy levels are caused by the magic numbers: 2, 8, 20, 28, 50, 82, 126, and 184. If the number of nucleons matches a magic number, it becomes more stable, thus has a higher binding energy. A nucleus can be known as "doubly magic" if both the number of protons and neutrons are magic numbers. In this case, the binding energy would be even higher and the nuclei is more stable.

The shell model is not perfect on its own. The nucleus could be in an energy case that is in between energy bands, such as having a momentum that is the same as a magic number. Should the upper or lower band be selected? This could be better explained with the collective model [41]. The Hamiltonian used to create the shell model assumes interactions within an individual nucleon, however, there exists nucleons outside the last closed shell that could have an affect on the nuclear structure. For instance, the addition of a proton or a neutron to the next energy level could complete a nucleon pair, which would in turn cause the energy of the former level to have less energy due to being an unpaired nucleon.

Appendix G. VESTA Crystal Structures of Quantum Dots

G.1 ZnS

ZnS was a common shell material to enhance quantum yield and to cause a stokes shift in the optical properties of the CQDs. The ZnS crystal structure shown in Figure 134 had its crystal data referenced from Kisi *et al.* [68].

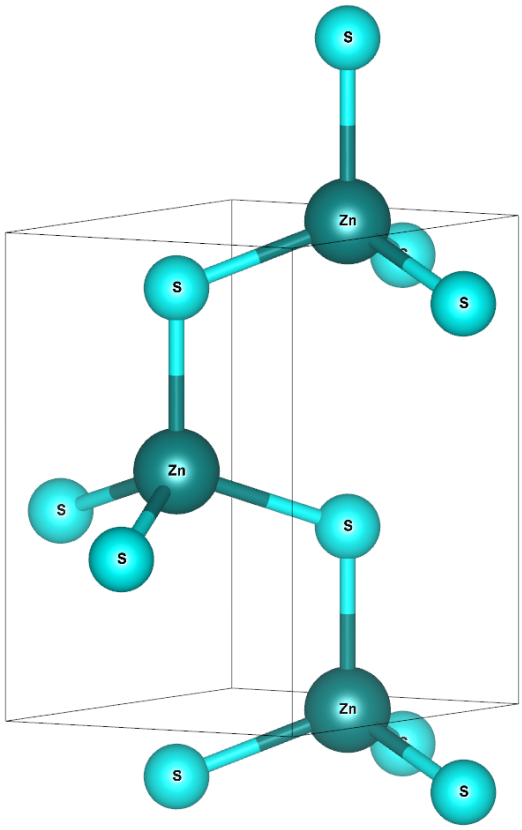


Figure 134. 3D crystal structure model of ZnS. Figure created in VESTA [91].

G.2 InP

The InP crystal structure shown in Figure 135 had its crystal data referenced from from Lopez-Perez *et al.* [79].

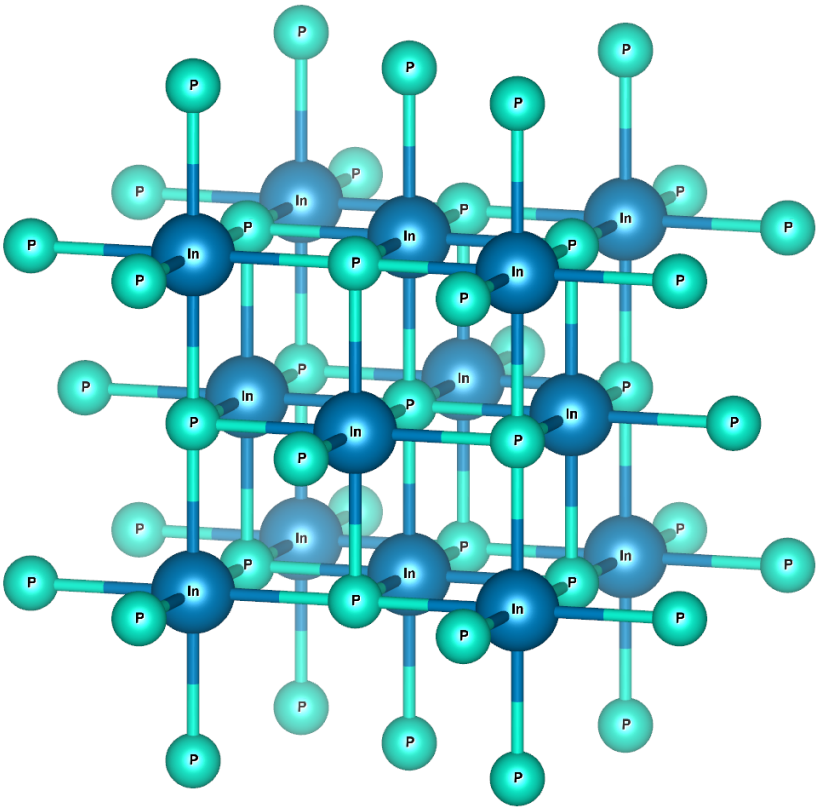


Figure 135. 3D crystal structure model of InP. Figure created in VESTA [91].

G.3 PbS

The PbS crystal structure shown in Figure 136 had its crystal data referenced from from Ramsdell [116].

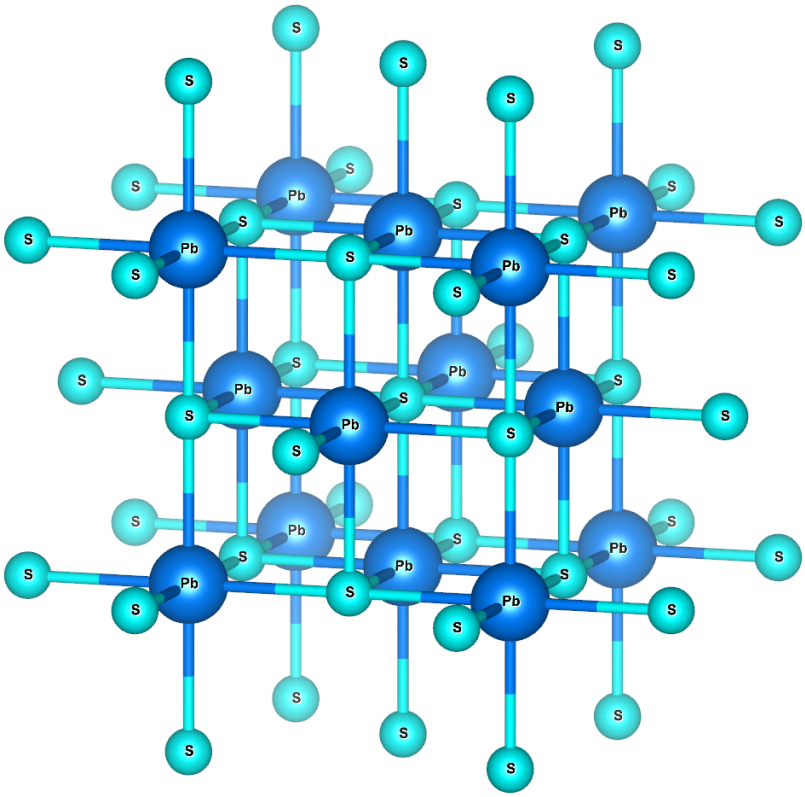


Figure 136. 3D crystal structure model of PbS. Figure created in VESTA [91].

G.4 CdS

The CdS crystal structure shown in Figure 137 had its crystal data referenced from from Ulrich *et al.* [150].

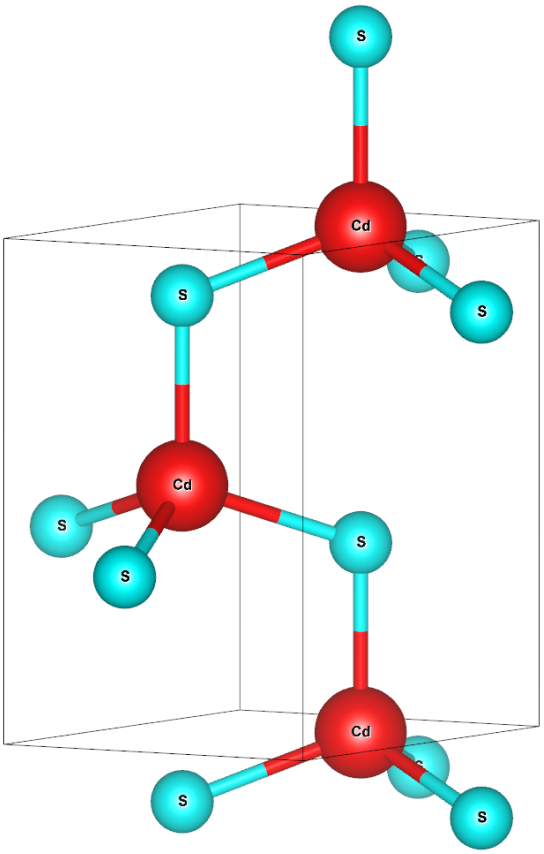


Figure 137. 3D crystal structure model of CdS. Figure created in VESTA [91].

G.5 CuInS

The $CuInS_2$ crystal structure shown in Figure 138 had its crystal data referenced from from Yao *et al.* [159].

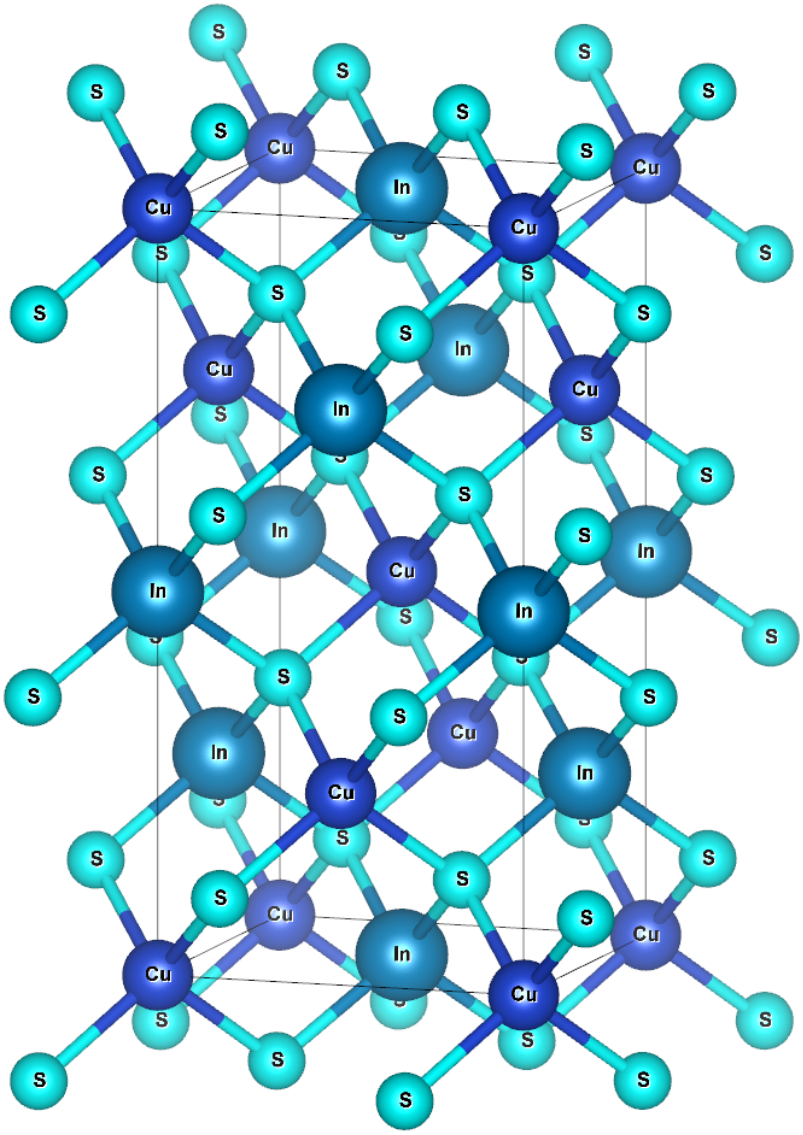


Figure 138. 3D crystal structure model of $CuInS_2$. Figure created in VESTA [91].

G.6 PbSe

The PbSe crystal structure shown in Figure 139 had its crystal data referenced from from Noda *et al.* [97].

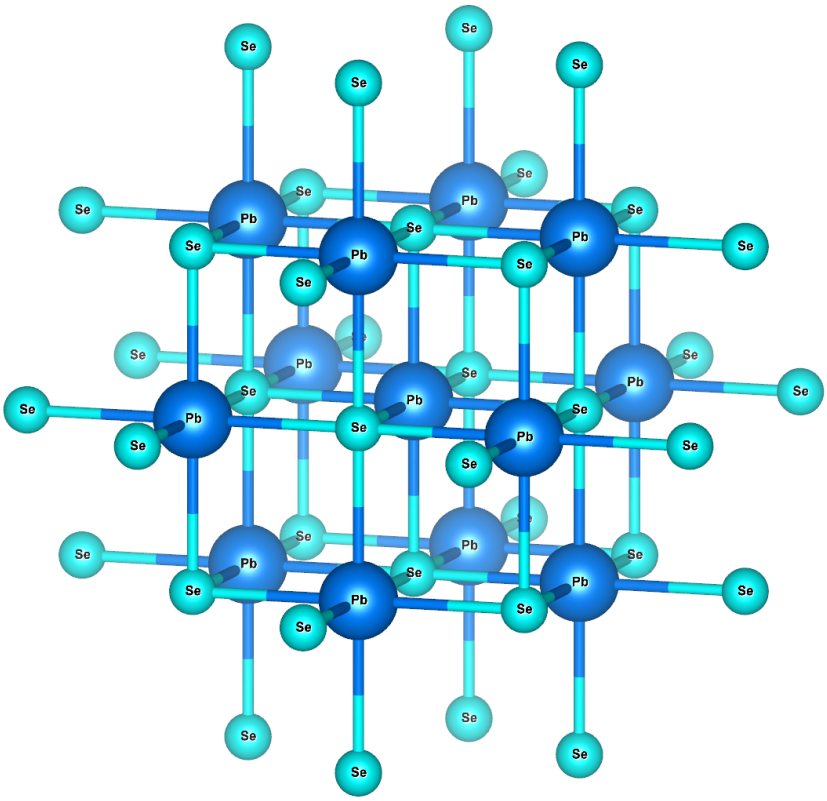


Figure 139. 3D crystal structure model of PbSe. Figure created in VESTA [91].

Appendix H. Leica DVM6 Quantum Dot Loaded Polymer Scintillator Images

Note that CdS overview image was already discussed in Chapter III as an example image and would not be reiterated here. There was a local tone mapping function in Corel Paintshop Pro X8 that greatly enhanced contrast effects. It became easy to see the capillary channels in the samples. A local tone mapping image was also shown with each overview image in this appendix.

H.1 CdS

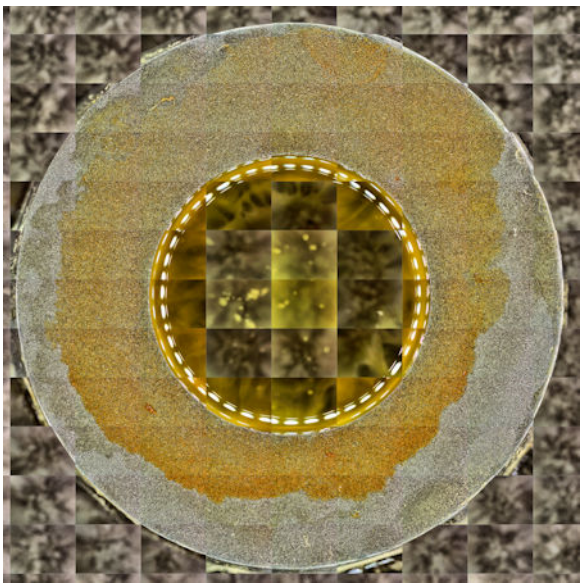


Figure 140. CdS top down overview image with local tone mapping enhancement.

H.2 CdSe NPL

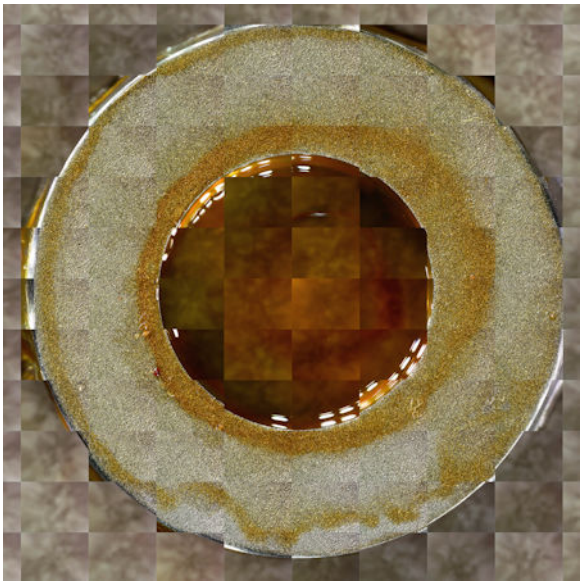


Figure 141. CdSe NPL top down overview image.



Figure 142. CdSe NPL top down overview image with local tone mapping enhancement.

H.3 CuInS/ZnS

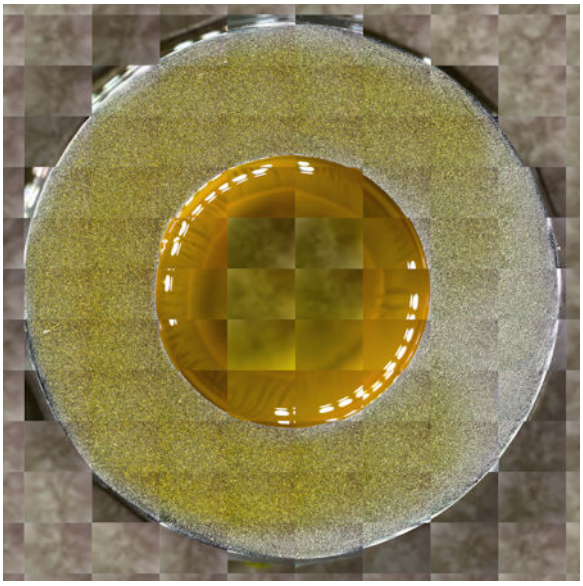


Figure 143. CuInS/ZnS top down overview image.

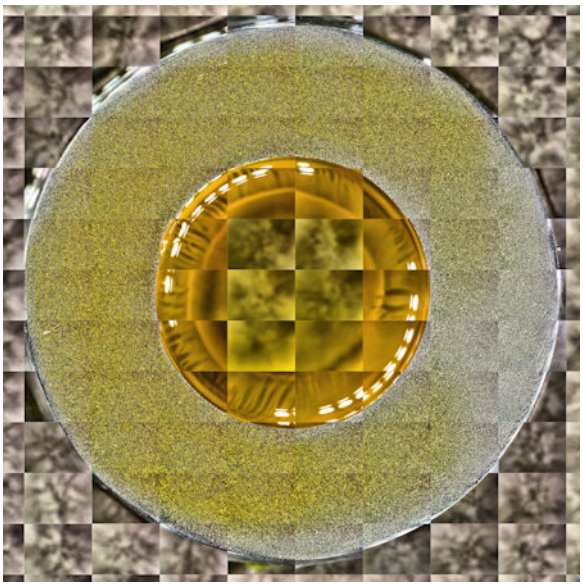


Figure 144. CuInS/ZnS top down overview image with local tone mapping enhancement.

H.4 CdSe

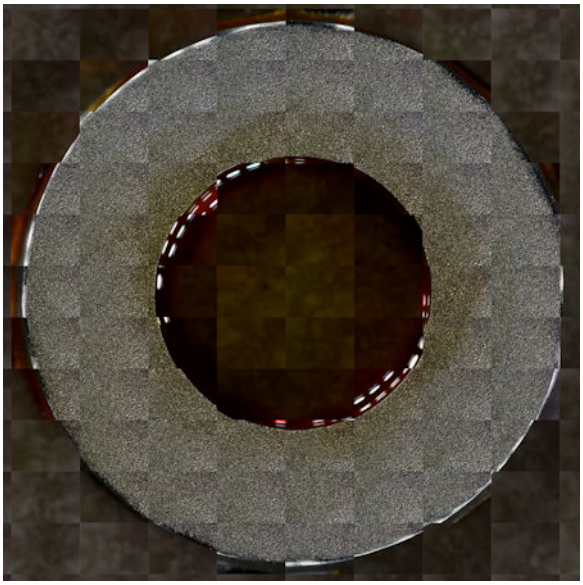


Figure 145. CdSe top down overview image.

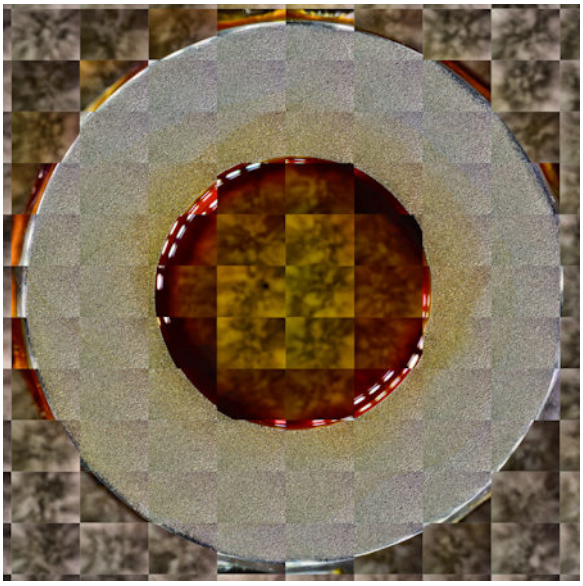


Figure 146. CdSe top down overview image with local tone mapping enhancement.

H.5 InP/ZnS

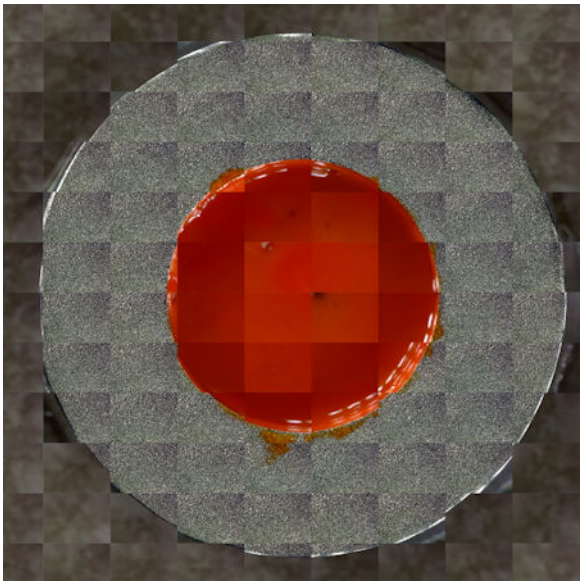


Figure 147. InP/ZnS top down overview image.

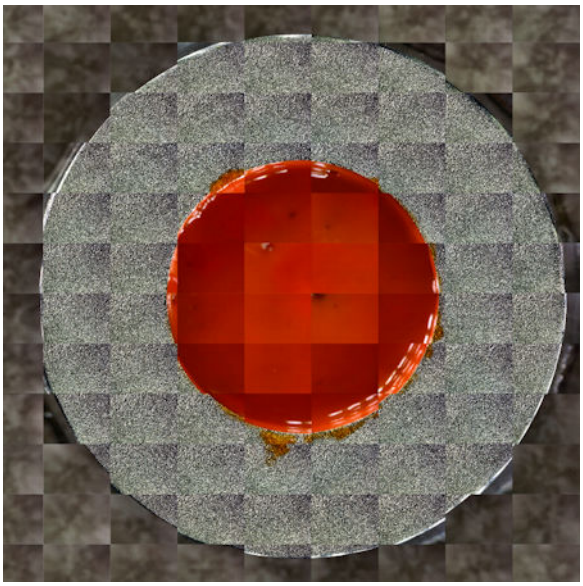


Figure 148. InP/ZnS top down overview image with local tone mapping enhancement.

H.6 PbS

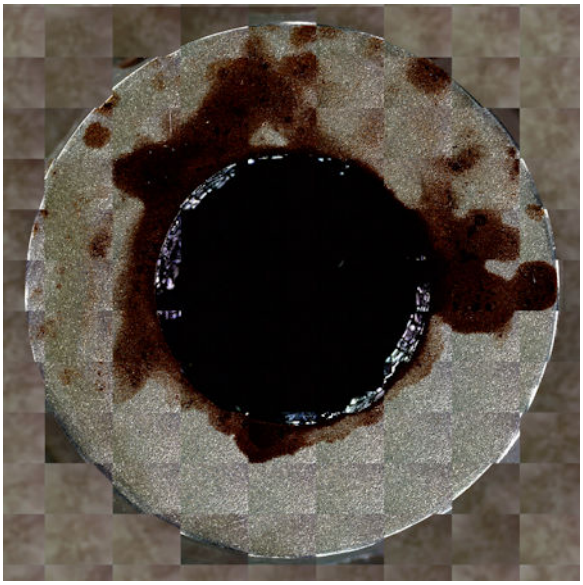


Figure 149. PbS top down overview image.

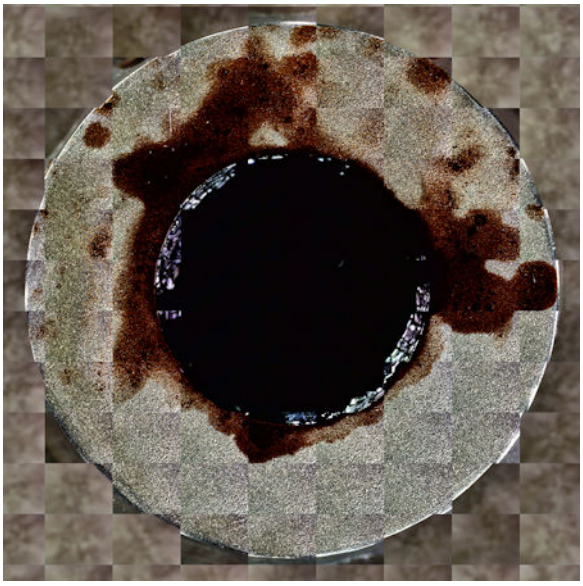


Figure 150. PbS top down overview image with local tone mapping enhancement.

H.7 PbSe

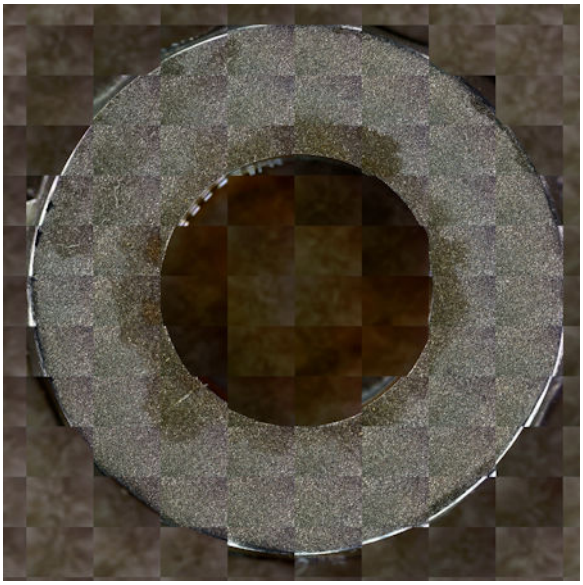


Figure 151. PbSe top down overview image.

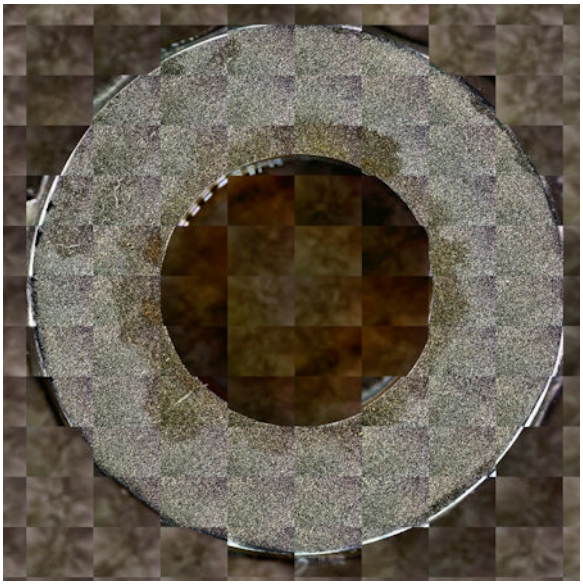


Figure 152. PbSe top down overview image with local tone mapping enhancement.

H.8 CdSe/ZnS

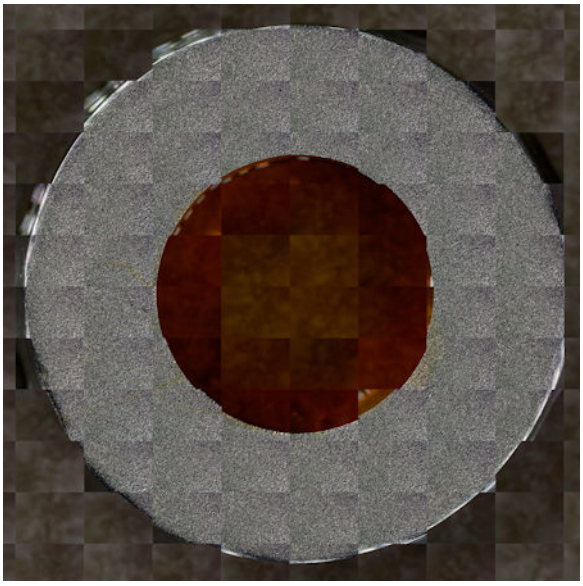


Figure 153. CdSe/ZnS top down overview image.

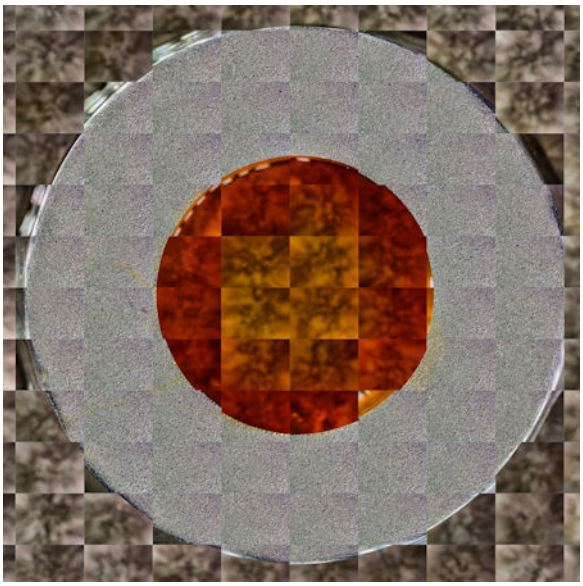


Figure 154. CdSe/ZnS top down overview image with local tone mapping enhancement.

H.9 Control (Blank Polymer)

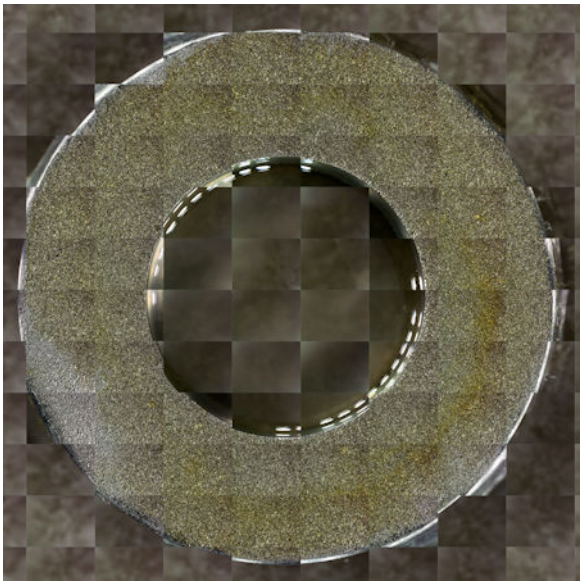


Figure 155. Blank polymer top down overview image.

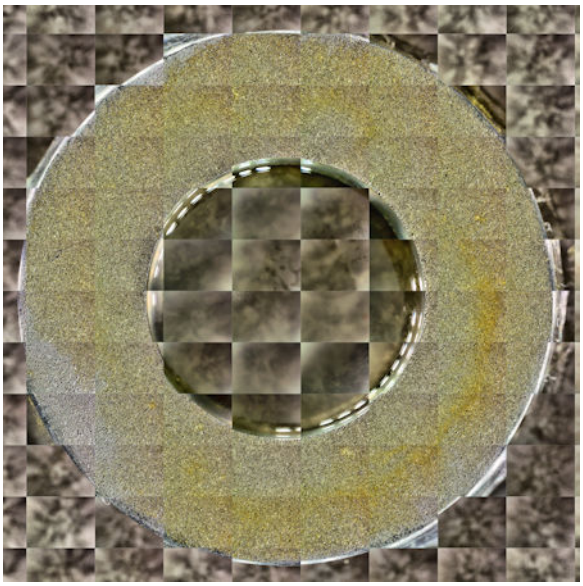


Figure 156. Blank polymer top down overview image with local tone mapping enhancement.

H.10 No Polymer

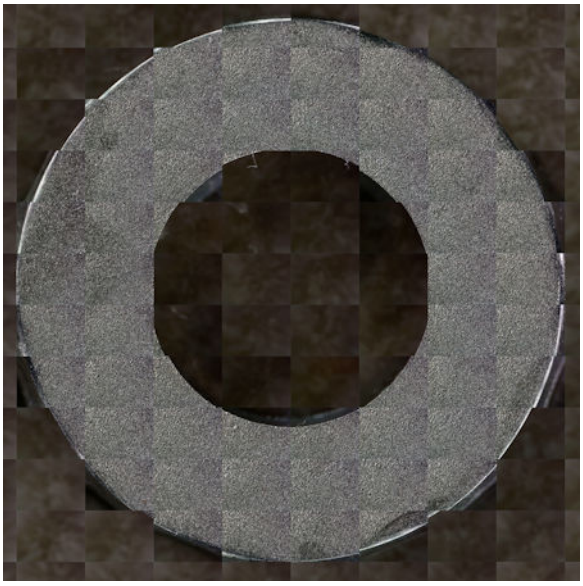


Figure 157. No polymer top down overview image.

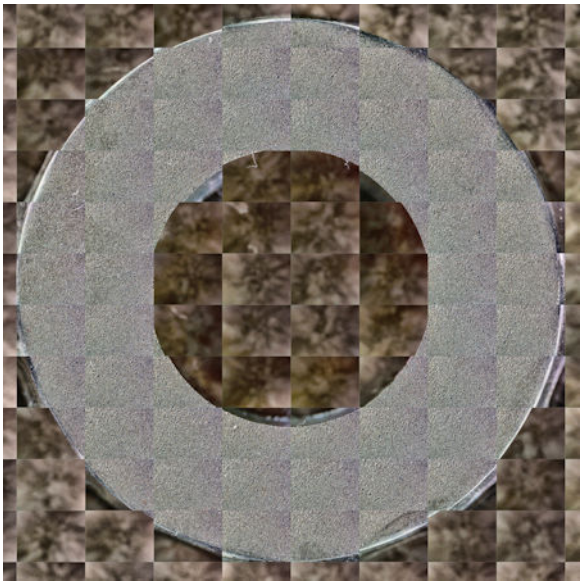


Figure 158. No polymer top down overview image with local tone mapping enhancement.

Appendix I. Gluing Aluminum Ring to Quartz Disc

1. Using SU-8-5, lightly apply a ring of the material around the circumference under the 0.05″ aluminum disc
2. Use a sponge tipped wand, gently go over the applied SU-8-5 and ensure entire surface under the 0.05″ thick aluminum disc is coated with SU-8-5 (ensure there is no material dripping)
3. Pick up the aluminum disc in one hand and a quartz disc in the other, carefully place them together onto the SU-8-5 side
4. Gently apply pressure on the back of the quartz disc into the aluminum disc along the ring to have the SU-8-5 get onto the quartz disc
5. Use a foam brush soaked in acetone to remove any excess SU-8-5 that got onto the other side of the quartz disc
6. UV cure the SU-8-5 from the quartz side for 10 minutes
7. Set a hot plate to 180°C
8. Place structure onto a small aluminum pie tin and place onto hot plate and let hard bake for ten minutes
9. Carefully remove structure in the aluminum pie tin while keeping it as flat to the surface as possible (to prevent the quartz slide from shifting under the aluminum ring) and place onto an aluminum block to cool
10. Let structure cool on aluminum block for one minute
11. Check quartz side for any photoresist on the outside of the quartz disc

12. If photoresist is seen where it is not supposed to be, wet a piece of cloth with acetone and gently rub the cloth over the area till clean

Appendix J. Polymer Scintillator Fabrication Procedure

1. Using scissors, cut off tape sealing the centrifuge container holding the CQD-loaded polymer
2. Take a micropipette and insert a sterile aerosol micropipette tip
3. Set micropipette to 15 μL
4. Open centrifuge container and insert micropipette tip into polymer
5. Carefully load micropipette and disperse into aluminum disc structure onto the quarts disc within the 0.5″ diameter hole
6. Continue dispersing CQD-loaded polymer until CQD-loaded polymer is level with the top of the aluminum disc
7. Hold micropipette over a trash can and eject the micropipette tip
8. Set hot plate to 120°C
9. Place structure onto a small pie tin and place onto hot plate
10. Let structure bake for 20 minutes
11. Carefully place structure onto an aluminum block and cool for one minute
12. Change temperature of the hot plate to 140°C
13. Place structure back onto hot plate
14. Let structure bake for 20 minutes
15. Carefully place structure onto an aluminum block and cool for one minute
16. Change temperature of the hot plate to 180°C

17. Place structure back onto hot plate
18. Let structure bake for 40 minutes
19. Carefully place structure onto an aluminum block and cool for one minute
20. Set convection oven to $135°C$
21. Place sample into convection oven and let bake for 30 minutes
22. Remove sample from convection oven and let cool for five minutes
23. Hold structure sideways and ensure no polymer is oozing out
24. If polymer is still oozing, place sample back in the convection oven and let bake for ten minutes
25. Label and store structure in a nitrogen purged box

Appendix K. Leica Digital Microscope Taking Thickness Measurement Procedure

1. Lower platform to allow placement of a sample
2. Tilt microscope head to desired angle
3. Place sample onto specimen platform
4. Ensure LED light is on
5. Line up sample within the circle of the LED light on the platform
6. Raise up platform till sample becomes visible on the microscope
7. Move platform till washer can be seen on microscope
8. Either raise or lower platform enough to get washer mostly in focus
9. Right click on the image window and select autofocus
10. Bring up the tilescan image window
11. Move platform to find the boundary between the aluminum ring and the polymer located at the left side of the sample
12. Place viewing box in the tilescan image window on the boundary
13. Click on Z-stack and select custom
14. Lower stage until sample is blurry, click on begin
15. Raise stage until sample becomes in focus and begins to become blurry again, click on end

16. Set Z-step size as $0.25\mu m$

17. Click begin experiment

18. Once finished, go to the right side of the screen and look for 3D

19. Click on the 3D image, and a new window will appear

20. Thickness measurements can be taken in this window by selecting a line that goes across the desired measurement area

21. A new graph will appear towards the bottom of the screen that shows the thickness going across the length of the line

Appendix L. Removal of 3D Printed Wax Structural Support Procedure

1. Print out 3D printed structure
2. Heat structure in hot oven at $70°C$ for 30 minutes on top of a perforated aluminum sheet
3. Remove structure by wiping it across the perforated aluminum sheet onto a kimwipe to mostly clean off of wax
4. Boil water in a glass beaker to $250°C$ on a hot plate
5. Using metal tweezers, submerge 3D print into boiling water and shake back and forth a few times
6. Quickly pull out 3D print and let air dry on a metal surface (we have found that laying ontop of kimwipes attaches fibers to the print and sometimes the print attaches to the kimwipe and breaks coming off)
7. Hold 3D print to a light and check for any blocked holes, if there are many blockages, redo the last two steps. If only a few, resubmerge 3D print in boiling water then use pressurized nitrogen gas to dry off the 3D print.
8. Check the 3D print again under light, if blockages remain, redo the last step, otherwise do one final submersion of the 3D print into boiling water, then quickly drop into a glass jar filled with water to keep it hydrophilic

Appendix M. Application of CQDs into 3D Printed Structure Procedure

1. Drop IPA onto top of honeycomb structure
2. Apply CQDs using a micropipette to top of structure
3. Let dry for 5 minutes
4. Place honeycomb structure on top of quartz slide and center with the quartz slide on top of a kimwipe
5. Apply SU-8-5 around circumference of 3D printed honeycomb structure allowing excess SU-8-5 onto the kimwipe to avoid saturating the structure with the photoresist
6. UV cure for 1000 s
7. Apply SU-8-5 to top of honeycomb structure on top of a spin coater after UV curing edges
8. Ramp up speed: 500 RPM
9. Spin speed: 3000 RPM
10. UV cure for 1000 s
11. Place structure upside down onto a kimwipe and use a foam tip to remove excess photoresist using acetone
12. Use another foam tip with IPA and then again with water to remove the solvents
13. Nitrogen blow dry the sample
14. Store sample in a nitrogen purged and dry environment

Appendix N. Dispersing Thin-Film of CQDs onto Quartz Procedure

1. Set heat plate to 120°C
2. Place aluminum ring structure onto a small pie tin
3. Using a micropipette, draw out 10 μL of CQD solution
4. Carefully disperse CQD solution onto the exposed quartz side of the aluminum ring structure
5. Pick up the pie tin and carefully place onto hot plate
6. Let structure bake for ten minutes
7. Pick up the pie tin and place onto aluminum block
8. Cool off for 1 minute

Appendix O. Loading CQDs within PCF Procedure

1. Strip fiber optic using 125 μm stripper, 1″ on each side
2. Moisten a kimwipe with IPA and gently but firmly wipe each stripped end of the fiber
3. Place fiber optic in a manual fiber cleaver like pictured in Figure 159, ensure stripped part fully goes over each rubber pad

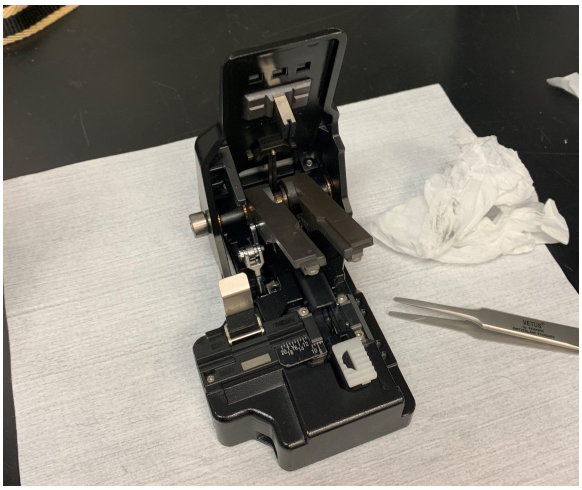


Figure 159. A Fujikura CT-20 fiber cleaver.

4. Slowly push down anvil of cleaver
5. When cleaver is about 1″ over the fiber, apply a quick striking force to cleave the fiber
6. Tape one end of the fiber to a block, with fiber tip just above the side of block as in Figure 160

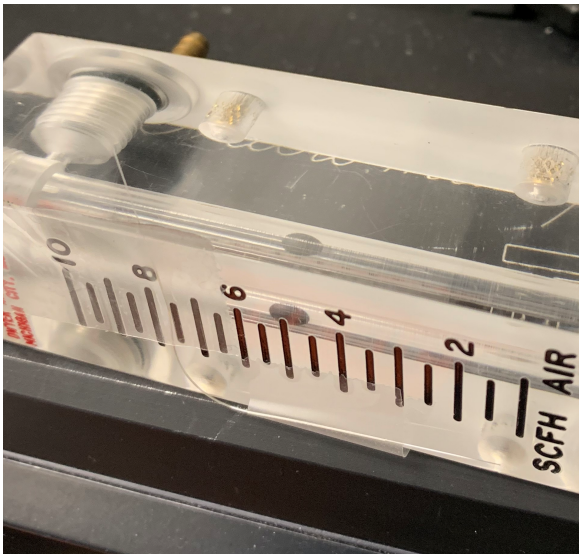


Figure 160. PCF taped at an angle and point straight up on a block.

7. Using a microscope, apply 10x magnification to find fiber tip

8. Apply 50x magnification and check for cleave defects, if small holes within core are not covered, fiber tip is good, mark good end of fiber using a sharpie

9. Repeat steps 5-7 on the other end of fiber

10. Carefully store fibers in container (tape over a glass slide) to ensure tips do not touch anything

11. If desired for better quality control, place fiber within a SEM to check for any blocked holes

12. The fiber preparation before placing it into the SEM can be seen in Figure 161

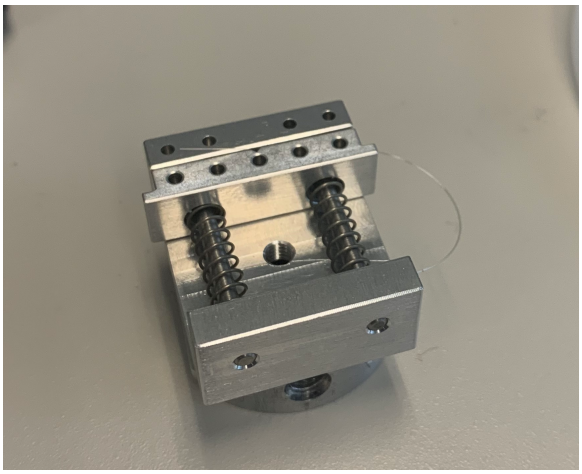


Figure 161. PCF wrapped in a U-shape within a SEM holder.

13. If blocked holes are seen, redo fiber end from step 1

14. If blockage is affecting only a few holes and this is acceptable, use ImageJ from the SEM image to assist in automatically counting the number of usable holes as seen in Figure 162

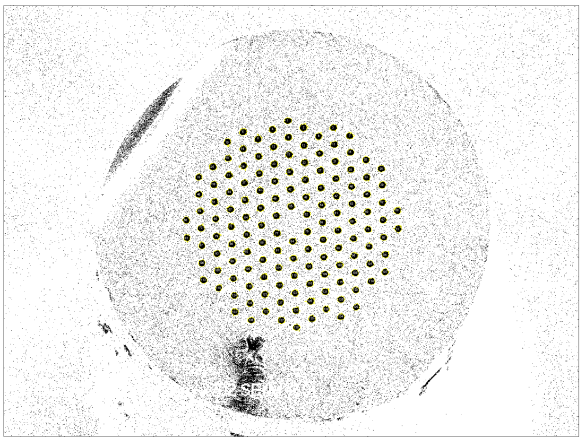


Figure 162. ImageJ used to automatically count the number of good holes on the tip of a PCF

15. Apply some putty around one end of the fiber

16. Slide putty side fiber through the tip of a syringe with the syringe pump fully in the down position

17. Under a fume hood, apply the open end of the fiber into desired solution of CQD through a micropipette tip to prevent bending the fiber

18. Pull on the syringe and place two rolls of electrical tape to keep the syringe in a vacuum state

19. The setup should look like Figure 163

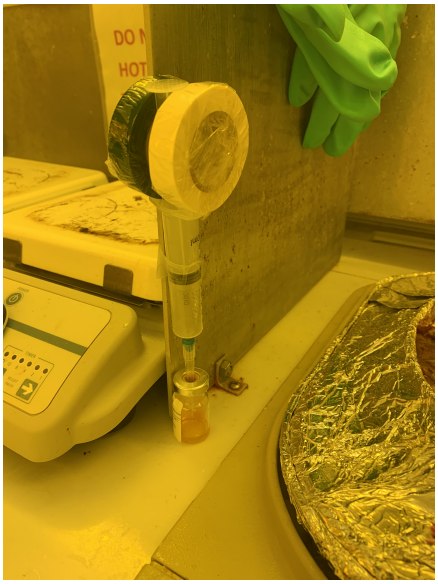


Figure 163. Vacuum system using a syringe, putty, and electrical tape to hold the vacuum.

20. Wait for 20 minutes

21. Remove fiber from toluene solution

22. Carefully pull off syringe from fiber

23. If desired to fully remove toluene within the fibers, place fiber within a glass petri dish with a lid and place within a convention oven

24. Bake fiber for eight hours at $40^{\circ}C$

25. While over a chemical drain, use water to clean out the glass petri dish that the fiber was sitting in while baking

26. Clean out tip of syringe by drawing up IPA three times and dispensing into chemical drain

27. Store fiber in a nitrogen box and on top of a glass slide with tape to secure the fiber

Appendix P. PCF Tip Shock Wave SEM Image

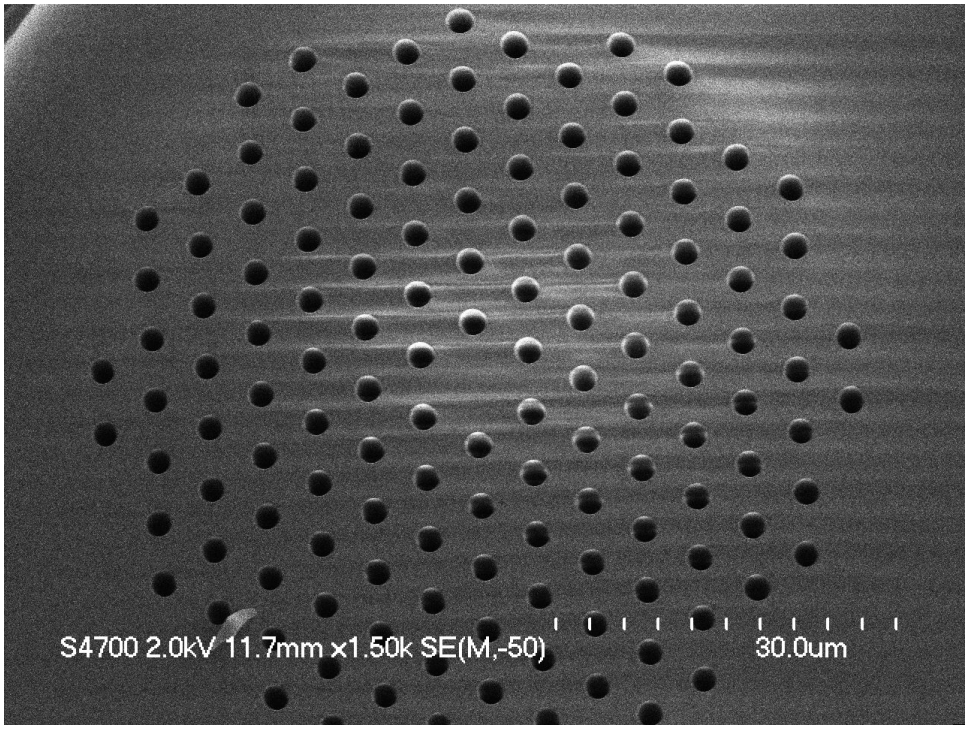


Figure 164. Rippling on top of a fiber tip that occurred during the shock wave that occurred during the cleaving process when viewed in a SEM

Appendix Q. Structural Support for Polymer Scintillator

Orthographic Drawing

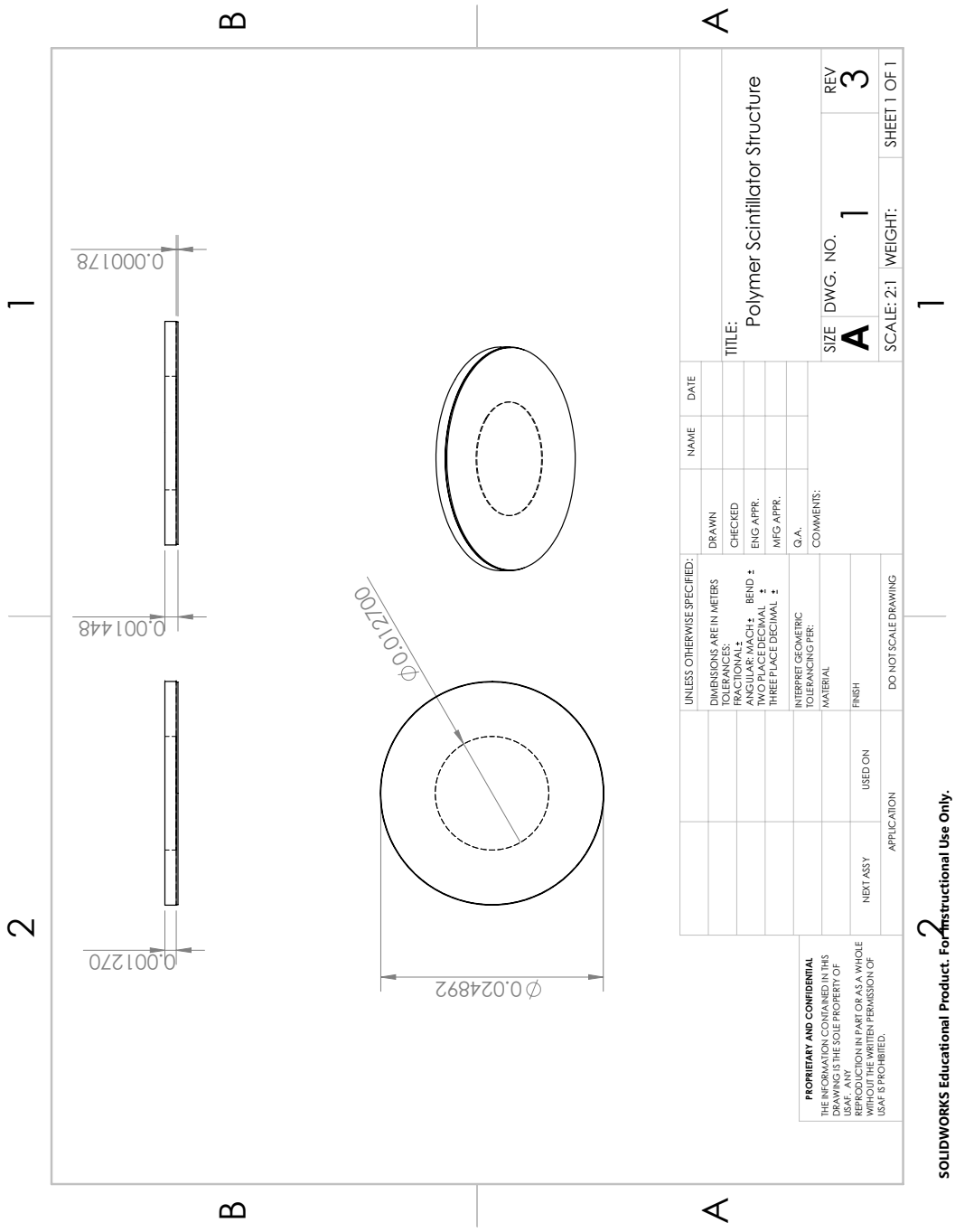


Figure 165. Orthographic drawing of supporting structure for polymer. Drawn within SolidWorks.

Appendix R. 3D Printed Honeycomb Scintillator

Orthographic Drawing

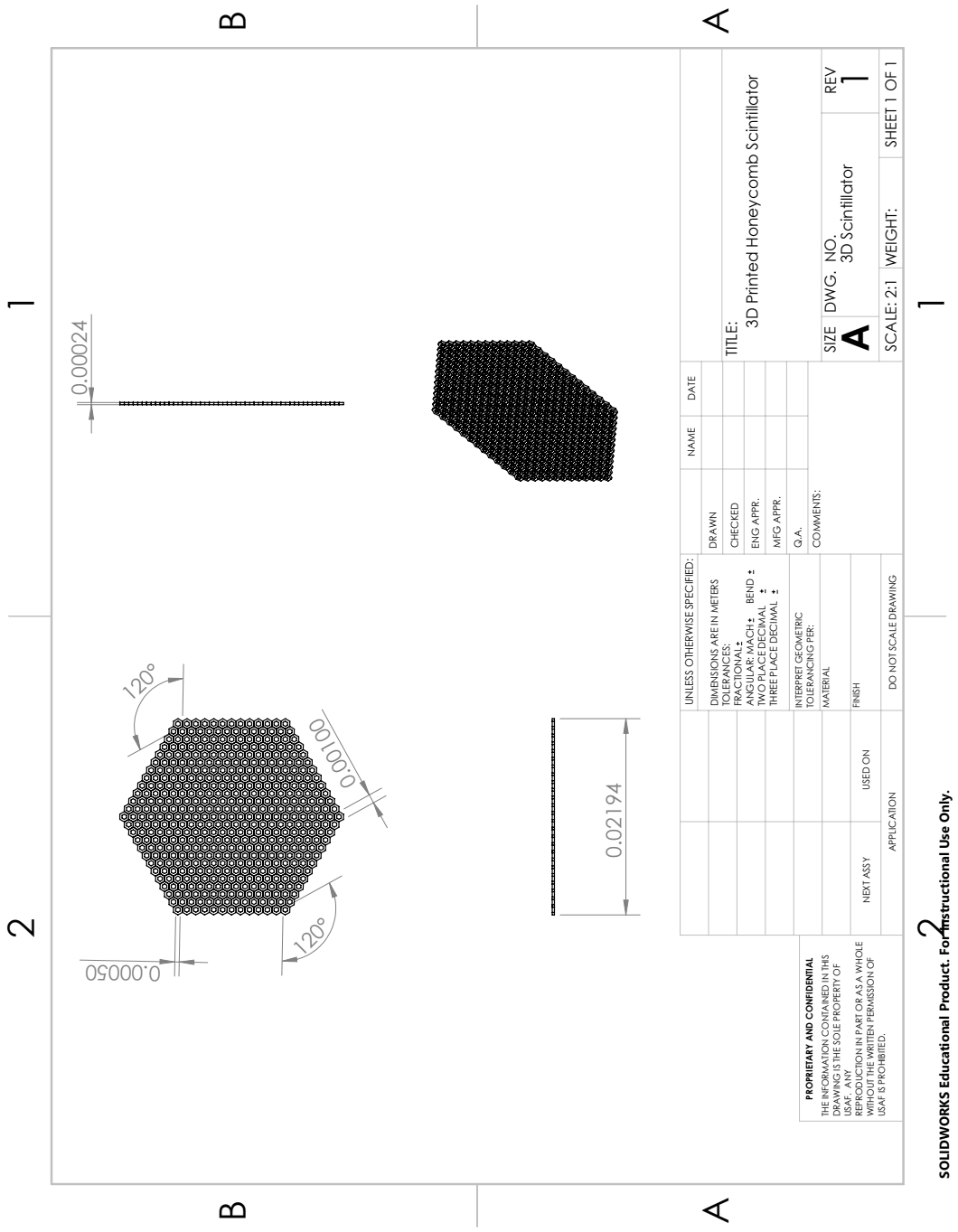


Figure 166. Orthographic drawing of 3D printed honeycomb. Drawn within SolidWorks.

Appendix S. Structural Support for 3D Printed Scintillator

Orthographic Drawing

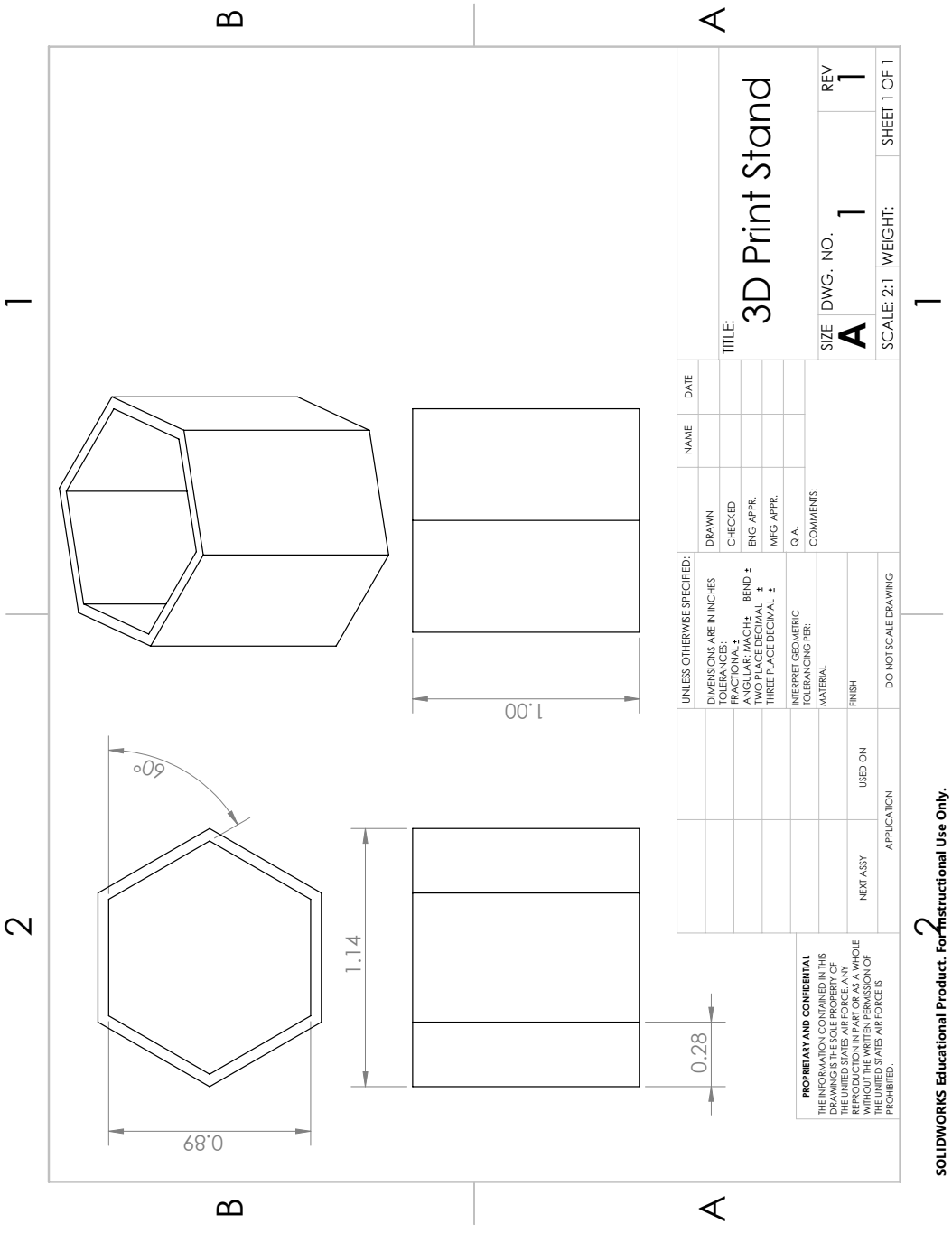


Figure 167. Orthographic drawing of 3D printed stand. Drawn within SolidWorks.

Appendix T. CQD Ligand 3D Models

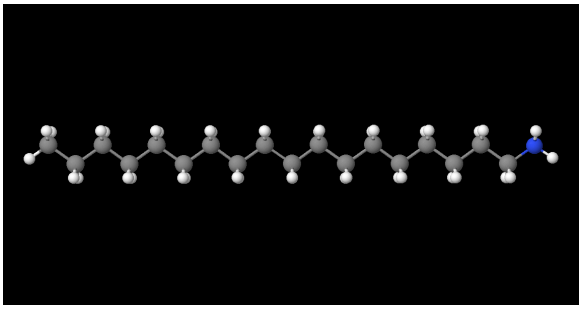


Figure 168. Organic polymer chain 3D model. Image information from PubChem [109] and 3D rendered in MolView v2.4 [24].

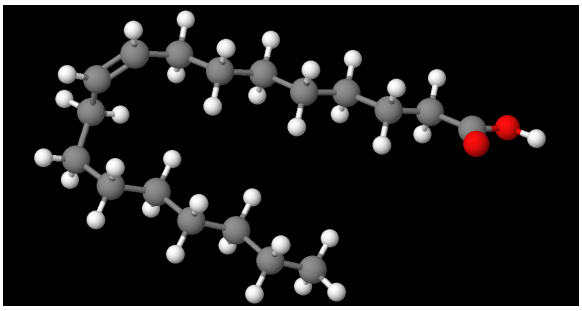


Figure 169. Organic polymer chain 3D model. Image from PubChem [110] and 3D rendered in MolView v2.4 [24].

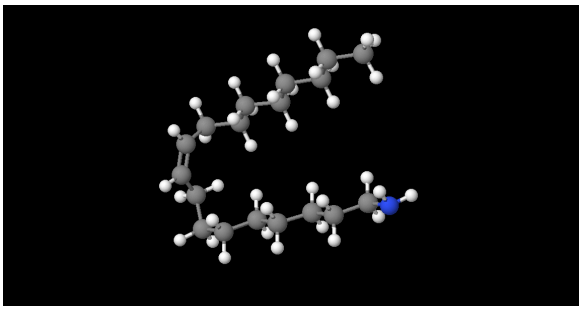


Figure 170. Organic polymer chain 3D model. Image from PubChem [111] and 3D rendered in MolView v2.4 [24].

Appendix U. PL Decay Bi-Exponential Components for Main Experiment

Nanomaterial	Structure	Pre-Exponential Components (A1,A2,A3,A4)	Decay Constants Components (T1,T2,T3,T4) in ns
CdSe	3D	1.235, 0.2876, 0, 0	0.3797, 3.884, 0, 0
CdSe/ZnS	3D	0.6481, 0.148, 0, 0	0.4056, 3.049, 0, 0
CdS	3D	2.015, 0.09432, 0, 0	0.1359, 1.62, 0, 0
CdSe (NPL)	3D	2.121, 0.5805, 0.6623, 0.06273	0.4375, 3.728, 2.851, 13.38
CuInS/ZnS	3D	1.256, 0.4243, 0, 0	0.4932, 3.884, 0, 0
InP/ZnS	3D	1.362, 0.2593, 0, 0	0.2219, 4.454, 0, 0
CdSe	Thin-Film	0.7866, 0.006337, 0, 0	0.04341, 1.827
CdSe/ZnS	Thin-Film	2.238, 0.5446, 0, 0	0.1612, 3.044, 0, 0
CdS	Thin-Film	4.564, 0.0205, 0, 0	0.08263, 3, 0, 0
CuInS/ZnS	Thin-Film	9.103, 0, 0.03857, 0.02466	0.05056, 0, 20.62, 80.46
InP/ZnS	Thin-Film	0.08652, 0.02379, 0, 0	3.391, 16.73, 0, 0
CdSe	Polymer	22.33, 0.09231, 0, 0	0.05928, 3.075, 0, 0
CdSe/ZnS	Polymer	2.02, 0.539, 0, 0	0.3705, 3.117, 0, 0
CdS	Polymer	5.915, 4.819, 0, 0	0.06462, 0.06676, 0, 0
CdSe (NPL)	Polymer	-6.094, 16.32, 0, 0	0.1618, 0.1113, 0, 0
CuInS/ZnS	Polymer	1.499, 0.1365, 0, 0	0.7973, 4.004, 0, 0
InP/ZnS	Polymer	12.58, 0.1626, 0, 0	0.05034, 0.1113, 0, 0

Table 32. Temporal resolution of PL decay is 0.5 ns, thus any values less than 0.5 ns may not be the response of the CQD under test. CQD loaded into the three following structures: 3D, thin-film, and polymer are all shown in this table.

Appendix V. PL Decay Bi-Exponential Components for 3^2 Factorial Experiment

Amount of CQDs	Thickness	Pre-Exponential Components (A1,A2,A3,A4)	Decay Constants Components (T1,T2,T3,T4) in ns
40	240	0.1044, 0.3576, 0, 0	2.92, 0.4632, 0, 0
40	480	0.7814, 8.146, 0, 0	1.299, 0.05143, 0, 0
40	960	1.983, 2.469, 0, 0	0.3359, 2.434, 0, 0
80	240	0.2796, 12.82, 1.671, 0.4066	8.175, 0.1466, 1.028, 4.808
80	480	0.3034, 1.405, 0, 0	3.029, 0.3656, 0, 0
80	960	3.051, 2.377, 0, 0	0.3252, 2.093, 0, 0
160	240	0.7216, 10.31, 4.368, 0.7317	1.386, 0.07859, 0.1726, 1.411
160	480	1.671, 0.4066, 0, 0	1.028, 4.808, 0, 0
160	980	0.6481, 0.148, 0, 0	0.4056, 3.049, 0, 0

Table 33. Temporal resolution of PL decay is 0.5 ns, thus any values less than 0.5 ns may not be the response of the CQD under test.

Appendix W. PL Relative Intensity Values at $\approx 460\ nm$ for 3^2 Factorial Experiment Raw Data

Material	Factor 1	Factor 2	R1	R2	R3	R4	R5
CdSe/ZnS	40	240	0.80421	0.78882	0.79611	0.82364	0.82406
InP/ZnS	40	480	0.79874	0.80095	0.81312	0.80236	0.77461
CdSe/ZnS	40	960	0.45298	0.44006	0.42922	0.43325	0.41914
InP/ZnS	80	240	0.42188	0.41911	0.40215	0.39197	0.13625
CdSe/ZnS	80	480	0.63588	0.65485	0.65018	0.66337	0.67477
CdSe/ZnS	80	960	0.50884	0.50157	0.49443	0.48872	0.49747
InP/ZnS	160	240	0.71038	0.71104	0.70258	0.69822	0.69938
InP/ZnS	160	480	0.1559	0.14874	0.14491	0.14094	0.13625
CdSe/ZnS	160	960	0.36816	0.36656	0.3568	0.36449	0.39682

Table 34. PL relative intensity measurements at $460\ nm$ for each level in the 3^2 factorial experiment.

Appendix X. PL Decay Bi-Exponential Component 3^2 Factorial Experiment Raw Data

Material	CQD Amount (μL)	3D Print Thickness (μm)	THA (ns)
CdSe/ZnS	40	240	1.101
InP/ZnS	40	480	1.398
CdSe/ZnS	40	960	1.72
InP/ZnS	80	240	1.268
CdSe/ZnS	80	480	1.005
CdSe/ZnS	80	960	1.392
InP/ZnS	160	240	1.163
InP/ZnS	160	480	1.474
CdSe/ZnS	160	960	1.026

Table 35. PL decay times for each level in the 3^2 factorial experiment. The THA for each level was measured.

Appendix Y. Lamp Spectra

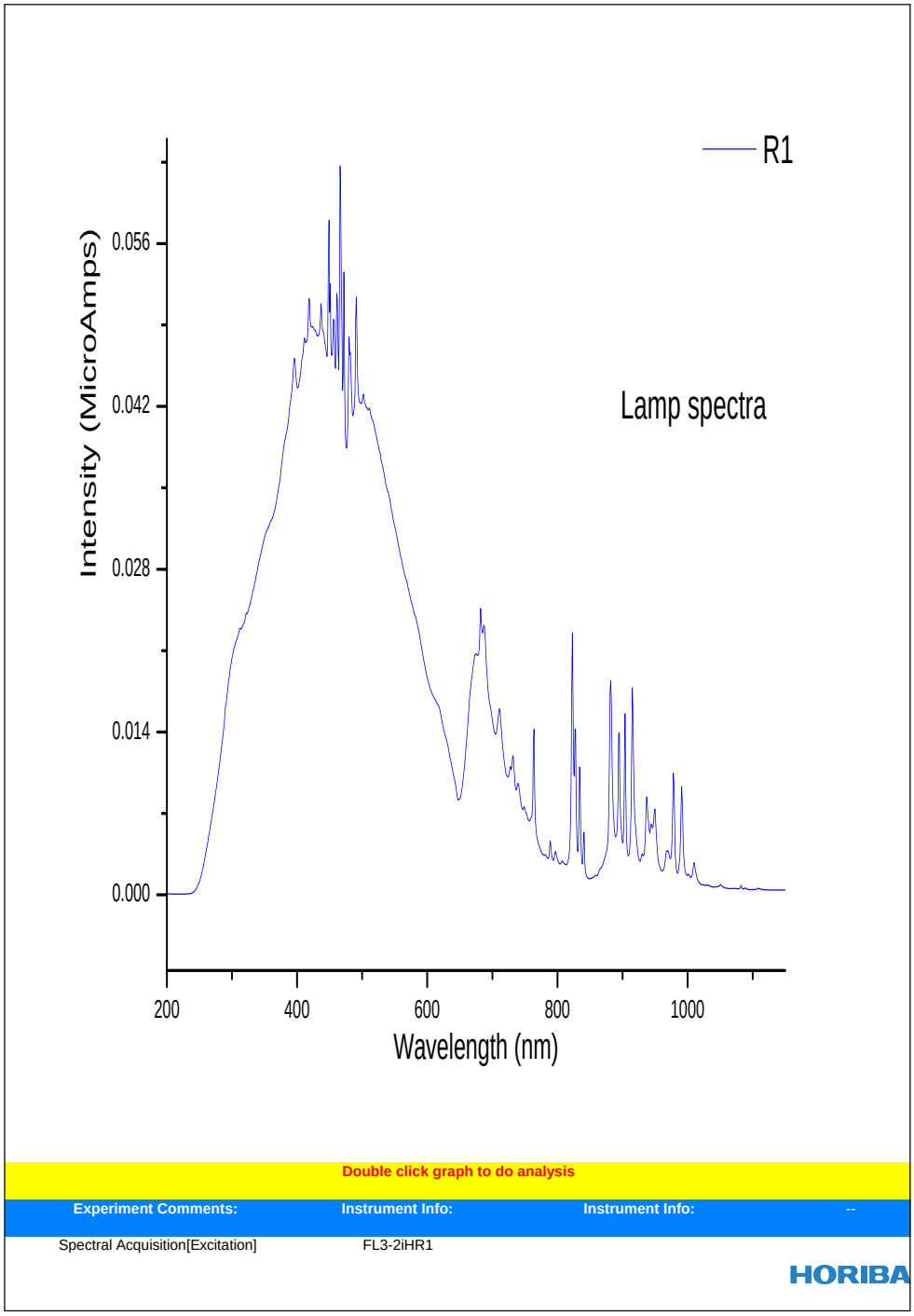


Figure 171. Lamp spectra of the Horiba-Jobin Fluorolog-3 used. Peaks in the NIR wavelengths were used to excite the lead-based CQDs.

Appendix Z. MATLAB Codes

Z.1 Cherenkov Feasibility Code

```
%Created By: 2d Lt Michael Sherburne
%Date Created: 12/26/2018
%Description: Estimate refractive index needed for Cherenkov radiation

indexSweep = 100:1:400;
[~,plotsize] = size(indexSweep);
refractiveindex = zeros(1,plotsize);

for i = indexSweep
 refractiveindex(i) = i/100;
 incidentEnergy(i) = 0.511.*((1/sqrt(1-(1/refractiveindex(i).^2)))-1);
end

%Plot Information
set(0, 'DefaultLineLineWidth' ,0.5)
set(0, 'DefaultLineMarkerSize' ,15)
set(0, 'DefaultAxesFontSize' ,22)
set(0, 'DefaultFigureColor' ,[1,1,1])
set(0, 'DefaultTextFontSize' ,26)
set(0, 'DefaultTextInterpreter' , 'latex' )
set(0, 'DefaultTextFontName' , 'Arial' ) %Times-Roman')
set(0, 'DefaultAxesFontName' , 'Arial' ) %Times-Roman')

figure(1)
scatter(refractiveindex,incidentEnergy,5,'b');
hold on
grid on
grid(gca,'minor')
hAx=gca;
set(hAx,'xminorgrid','on','yminorgrid','on')
hold on
xlabel('Index of Refraction (n)');
ylabel('Incident Electron Threshold Energy(MeV)');
xlim([1 inf])
title(strcat('Incident Electron Energy Versus Index of Refraction',...
    'Needed to Emit Cherenkov Radiation'),'FontSize', 20)

%Auto Save Plot as PNG
orient(figure(1),'landscape','rotated')
fig1 = figure(1);
pos_fig1 = [0 0 2500 1200];
set(fig1,'Position',pos_fig1)
saveas(gcf,'cherenkovviabilityplot.fig');
print('cherenkovviabilityplot','-dpng');
```

Z.2 Frank-Tamm Photon Count Code

```
%Created By: 2d Lt Michael Sherburne
%Date Created: 1/23/2019
%Description: Apply Frank-Tamm formula to determine feasibility
format long
clc
clear
set(0, 'DefaultLineLineWidth' ,0.5)
set(0, 'DefaultLineMarkerSize' ,10)
set(0, 'DefaultAxesFontSize' ,40)
set(0, 'DefaultFigureColor' ,[1,1,1])
set(0, 'DefaultTextFontSize' ,40)
set(0, 'DefaultTextInterpreter' , 'latex' )
set(0, 'DefaultTextFontName' , 'Arial' ) %Times-Roman')
set(0, 'DefaultAxesFontName' , 'Arial' ) %Times-Roman')
%Enter In Threshold Energy and Maximum Energy to Plot
lowenergy = 1E3; %eV
maxenergy = 100E3; %eV
energyStep = 1E3; %eV
%Enter in length of medium (must be a whole number)
mediumLength = 3; %cm
%Wavelength Range (limited by cherenkov material)
%Diamond transmission limit is 200nm
%Photocathodes are sensitive to 400nm, then drop at higher wavelengths
L1 = 200E-9; %m
L2 = 400E-9; %m
wavelengthdiff = (1/L2 - 1/L1);
%Constants
c = 3E8; %m/s
FSC = 0.0072973525664;%1.439976;%(e^2/(hbar*c)) MeV*fm or a
Na = 6.022E23; %Avogadro's number
e = 1.602E-19; %coulombs
%Refractive Index of Media
nr = 2.5;
%Solving for I, material of interest is diamond (carbon) z=6
%Diamond Properties
Z = 6; %proton #
%https://www.engineeringtoolbox.com/density-solids-d_1265.html
p = 3.5; %density g/cm^3
Mmatl = 12; %molar mass of matl
n = ((p*Na)/Mmatl)*Z; %electron density
%I approximation formulas dependent on Z value
if Z == 1
    I = 19;
elseif Z>1 && Z<14
    I = 11.2+11.7*Z;
elseif Z>13
    I = 52.8+8.87;
end
for k = lowenergy:energyStep:maxenergy
```

```
    EnergyScale(k) = k;
    E = k;
    E = E*1E-6; %convert to MeV
    m = 9.11e-31; %mass of electron in kg
    Ej = E*1E6 * 1.6e-19; %eV to Joules conversion
    gamma = (Ej/(m*c^2))+1;
    beta = sqrt(1-(1/(gamma^2)));
    intmax = vpa(beta);
    intmin = 1/nr;
    Tau = E/0.511; %MeV electrons
    i = 0;
    if beta > (1/nr)
        while beta > (1/nr) && i < mediumLength
            i = i + 1;
            Ej = E*1E6 * 1.6e-19; %eV to Joules conversion
            gamma = (Ej/(m*c^2))+1;
            beta = sqrt(1-(1/(gamma^2)));
            betabb(i) = vpa(beta);
            %Solving for F(b)
            F(i) = ((1-betabb(i)^2)/2)*(1+((Tau^2)/8)-(2*Tau+1)*log(2));
            G(i) = log(3.61E5*Tau*sqrt(Tau+2))+F(i);
            %Beth-Bloch solution for electrons (simplified)
            dedx(i) = ((5.08E-31*n)/(betabb(i)^2))*(G(i)-log(I)); ...
                %MeV/cm
            E = E - dedx(i); %MeV/cm
        end
        betabb(end) = [];
        M(k) = 2*pi*FSC*(wavelengthdiff)*sum((1./((betabb.*nr).^2))-1);
    else
        %If Cherenkov threshold is not met, return 0
        M(k) = 0;
    end
end
scatter(EnergyScale/1E3,M,'MarkerEdgeColor',[0 .5 .5],...
    'MarkerFaceColor',[0 .7 .7],'LineWidth',1.5)
set(gca,'xscale','log')
set(gca,'yscale','log')
xlabel('Incident Photon Energy (keV)')
ylabel('# of Emitted Photons')
title('# of Emitted Photons Versus Incident Photon Energy Into Diamond')
grid on
grid minor
```

Z.3 Gathering X-ray Data Code

```
%Created By: 2d Lt Michael Sherburne
%Date Created: 12/4/2018
%Description: Collect X-ray coefficient data and elemental data from an
%Excel file
function [density,mass,energy,attencoef,absorbcoef] = ...
    collectxraydata(material)
    [~, ~, raw]  = ...
       xlsread('NISTMATERIALXRAYCOEFFICIENTS.xlsx',material);
    nrows = size(raw,1) - 4; %read in number of data points
    density = ...
       xlsread('NISTMATERIALXRAYCOEFFICIENTS.xlsx',material,'B1');
    mass  = xlsread('NISTMATERIALXRAYCOEFFICIENTS.xlsx',material,'B2');
    energy  = xlsread('NISTMATERIALXRAYCOEFFICIENTS.xlsx',material,...
        strcat('A5:A',int2str(nrows)));
    attencoef  = ...
       xlsread('NISTMATERIALXRAYCOEFFICIENTS.xlsx',material,...
        strcat('B5:B',int2str(nrows)));
    absorbcoef = ...
       xlsread('NISTMATERIALXRAYCOEFFICIENTS.xlsx',material,...
        strcat('C5:C',int2str(nrows)));
end
```

Z.4 X-ray Absorption and Attenuation Calculation Code

```
%Created By: 2d Lt Michael Sherburne
%Date Created: 11/4/2019
%Description: Take X-ray coefficient data and calculate thickness of a
%thin film needed based upon the elements in the colloidal quantum dot
%used
function [attenuationthickness,absorptionthickness ] = ...
    xraycalc(d1,m1,...
     e1,atc1,abc1,d2,m2,e2,atc2,abc2,d3,m3,e3,atc3,abc3,d4,m4,e4,atc4,...
     abc4,material1,material2,material3,incidentxrayenergy,...
     xrayabsorptionattenuation,loadingdensity,user,coreinnerdiameter,...
     coreshelldiameter)

if (user == 1)

%Collect material 1 data
Index = find(e1 == incidentxrayenergy);
if isempty(Index)

x = incidentxrayenergy;
MINindex = max(find(e1 < incidentxrayenergy));
x0 = e1(MINindex);
MAXindex = min(find(e1>incidentxrayenergy));
x1 = e1(MAXindex);

y0atc = atc1(MINindex);
y0abc = abc1(MINindex);
y1atc = atc1(MAXindex);
y1abc = abc1(MAXindex);

mat1atc1 = y0atc+(x-x0)*((y1atc-y0atc)/(x1-x0));
mat1abc1 = y0abc+(x-x0)*((y1abc-y0abc)/(x1-x0));
else
%If not find is not empty
mat1atc1 = atc1(Index);
mat1abc1 = abc1(Index);
end

atc1calcvalue = d1*mat1atc1;
abc1calcvalue = d1*mat1abc1;

%Applying Beer-Lambert Law (I/I0) = exp(-u/p*p*x)

%Solving for Attenuation
attenuationthickness = -1*log(xrayabsorptionattenuation)/atc1calcvalue;
attenuationthickness = attenuationthickness+(attenuationthickness*...
    loadingdensity);
%Solving for Absorption
absorptionthickness = -1*log(xrayabsorptionattenuation)/abc1calcvalue;
absorptionthickness = absorptionthickness+(absorptionthickness*...
```

```
49      loadingdensity);
50
51  elseif (user == 2)
52
53  %Collect material 1 data
54  Index = find(e1 == incidentxrayenergy);
55  if isempty(Index)
56
57  x = incidentxrayenergy;
58  MINindex = max(find(e1 < incidentxrayenergy));
59  x0 = e1(MINindex);
60  MAXindex = min(find(e1>incidentxrayenergy));
61  x1 = e1(MAXindex);
62
63  y0atc = atc1(MINindex);
64  y0abc = abc1(MINindex);
65  y1atc = atc1(MAXindex);
66  y1abc = abc1(MAXindex);
67
68  mat1atc1 = y0atc+(x-x0)*((y1atc-y0atc)/(x1-x0));
69  mat1abc1 = y0abc+(x-x0)*((y1abc-y0abc)/(x1-x0));
70  else
71  %If not find is not empty
72  mat1atc1 = atc1(Index);
73  mat1abc1 = abc1(Index);
74  end
75
76
77  %Collect material 2 data
78  Index = find(e2 == incidentxrayenergy);
79  if isempty(Index)
80
81  x = incidentxrayenergy;
82  MINindex = max(find(e2 < incidentxrayenergy));
83  x0 = e2(MINindex);
84  MAXindex = min(find(e2>incidentxrayenergy));
85  x1 = e2(MAXindex);
86
87  y0atc = atc2(MINindex);
88  y0abc = abc2(MINindex);
89  y1atc = atc2(MAXindex);
90  y1abc = abc2(MAXindex);
91
92  mat2atc2 = y0atc+(x-x0)*((y1atc-y0atc)/(x1-x0));
93  mat2abc2 = y0abc+(x-x0)*((y1abc-y0abc)/(x1-x0));
94  else
95  %If not find is not empty
96  mat2atc2 = atc2(Index);
97  mat2abc2 = abc2(Index);
98  end
99
100 %Calculate Mass Percentages
```

```
masspercent1 = m1/(m1+m2);
masspercent2 = m2/(m1+m2);

atc1calcvalue = d1*masspercent1*mat1atc1;
abc1calcvalue = d1*masspercent1*mat1abc1;

atc2calcvalue = d2*masspercent2*mat2atc2;
abc2calcvalue = d2*masspercent2*mat2abc2;

totalatcvalue = atc1calcvalue + atc2calcvalue;
totalabcvalue = abc1calcvalue + abc2calcvalue;

%Applying Beer-Lambert Law (I/I0) = exp(-u/p*p*x)

%Solving for Attenuation
attenuationthickness = -1*log(xrayabsorptionattenuation)/totalatcvalue;
attenuationthickness = attenuationthickness+(attenuationthickness*...
    loadingdensity);

%Solving for Absorption
absorptionthickness = -1*log(xrayabsorptionattenuation)/totalabcvalue;
absorptionthickness = absorptionthickness+(absorptionthickness*...
    loadingdensity);

elseif (user == 3)

%Collect material 1 data
Index = find(e1 == incidentxrayenergy);
if isempty(Index)

x = incidentxrayenergy;
MINindex = max(find(e1 < incidentxrayenergy));
x0 = e1(MINindex);
MAXindex = min(find(e1>incidentxrayenergy));
x1 = e1(MAXindex);

y0atc = atc1(MINindex);
y0abc = abc1(MINindex);
y1atc = atc1(MAXindex);
y1abc = abc1(MAXindex);

mat1atc1 = y0atc+(x-x0)*((y1atc-y0atc)/(x1-x0));
mat1abc1 = y0abc+(x-x0)*((y1abc-y0abc)/(x1-x0));
else
%If not find is not empty
mat1atc1 = atc1(Index);
mat1abc1 = abc1(Index);
end


%Collect material 2 data
Index = find(e2 == incidentxrayenergy);
```

```
153 if isempty(Index)
154
155 x = incidentxrayenergy;
156 MINindex = max(find(e2 < incidentxrayenergy));
157 x0 = e2(MINindex);
158 MAXindex = min(find(e2>incidentxrayenergy));
159 x1 = e2(MAXindex);
160
161 y0atc = atc2(MINindex);
162 y0abc = abc2(MINindex);
163 y1atc = atc2(MAXindex);
164 y1abc = abc2(MAXindex);
165
166 mat2atc2 = y0atc+(x-x0)*((y1atc-y0atc)/(x1-x0));
167 mat2abc2 = y0abc+(x-x0)*((y1abc-y0abc)/(x1-x0));
168 else
169 %If not find is not empty
170 mat2atc2 = atc2(Index);
171 mat2abc2 = abc2(Index);
172 end
173
174 %Collect material 3 data
175 Index = find(e3 == incidentxrayenergy);
176 if isempty(Index)
177
178 x = incidentxrayenergy;
179 MINindex = max(find(e3 < incidentxrayenergy));
180 x0 = e3(MINindex);
181 MAXindex = min(find(e3>incidentxrayenergy));
182 x1 = e3(MAXindex);
183
184 y0atc = atc3(MINindex);
185 y0abc = abc3(MINindex);
186 y1atc = atc3(MAXindex);
187 y1abc = abc3(MAXindex);
188
189 mat3atc3 = y0atc+(x-x0)*((y1atc-y0atc)/(x1-x0));
190 mat3abc3 = y0abc+(x-x0)*((y1abc-y0abc)/(x1-x0));
191 else
192 %If not find is not empty
193 mat3atc3 = atc3(Index);
194 mat3abc3 = abc3(Index);
195 end
196
197 %Calculate Mass Percentages
198 masspercent1 = m1/(m1+m2+m3);
199 masspercent2 = m2/(m1+m2+m3);
200 masspercent3 = m3/(m1+m2+m3);
201
202 atc1calcvalue = d1*masspercent1*mat1atc1;
203 abc1calcvalue = d1*masspercent1*mat1abc1;
204
```

```
atc2calcvalue = d2*masspercent2*mat2atc2;
abc2calcvalue = d2*masspercent2*mat2abc2;

atc3calcvalue = d3*masspercent3*mat3atc3;
abc3calcvalue = d3*masspercent3*mat3abc3;

totalatcvalue = atc1calcvalue + atc2calcvalue + atc3calcvalue;
totalabcvalue = abc1calcvalue + abc2calcvalue + atc3calcvalue;

%Applying Beer-Lambert Law (I/I0) = exp(-u/p*p*x)

%Solving for Attenuation
attenuationthickness = -1*log(xrayabsorptionattenuation)/totalatcvalue;
attenuationthickness = attenuationthickness+(attenuationthickness*...
    loadingdensity);

%Solving for Absorption
absorptionthickness = -1*log(xrayabsorptionattenuation)/totalabcvalue;
absorptionthickness = absorptionthickness+(absorptionthickness*...
    loadingdensity);

elseif (user == 4)

%Collect material 1 data
Index = find(e1 == incidentxrayenergy);
if isempty(Index)

x = incidentxrayenergy;
MINindex = max(find(e1 < incidentxrayenergy));
x0 = e1(MINindex);
MAXindex = min(find(e1>incidentxrayenergy));
x1 = e1(MAXindex);

y0atc = atc1(MINindex);
y0abc = abc1(MINindex);
y1atc = atc1(MAXindex);
y1abc = abc1(MAXindex);

mat1atc1 = y0atc+(x-x0)*((y1atc-y0atc)/(x1-x0));
mat1abc1 = y0abc+(x-x0)*((y1abc-y0abc)/(x1-x0));
else
%If not find is not empty
mat1atc1 = atc1(Index);
mat1abc1 = abc1(Index);
end


%Collect material 2 data
Index = find(e2 == incidentxrayenergy);
if isempty(Index)

x = incidentxrayenergy;
```

```
MINindex = max(find(e2 < incidentxrayenergy));
x0 = e2(MINindex);
MAXindex = min(find(e2>incidentxrayenergy));
x1 = e2(MAXindex);

y0atc = atc2(MINindex);
y0abc = abc2(MINindex);
y1atc = atc2(MAXindex);
y1abc = abc2(MAXindex);

mat2atc2 = y0atc+(x-x0)*((y1atc-y0atc)/(x1-x0));
mat2abc2 = y0abc+(x-x0)*((y1abc-y0abc)/(x1-x0));
else
%If not find is not empty
mat2atc2 = atc2(Index);
mat2abc2 = abc2(Index);
end

%Collect ZnS material data
%Collect material 3 data
Index = find(e3 == incidentxrayenergy);
if isempty(Index)

x = incidentxrayenergy;
MINindex = max(find(e3 < incidentxrayenergy));
x0 = e3(MINindex);
MAXindex = min(find(e3>incidentxrayenergy));
x1 = e3(MAXindex);

y0atc = atc3(MINindex);
y0abc = abc3(MINindex);
y1atc = atc3(MAXindex);
y1abc = abc3(MAXindex);

mat3atc3 = y0atc+(x-x0)*((y1atc-y0atc)/(x1-x0));
mat3abc3 = y0abc+(x-x0)*((y1abc-y0abc)/(x1-x0));
else
%If not find is not empty
mat3atc3 = atc3(Index);
mat3abc3 = abc3(Index);
end

%Collect material 3 data
Index = find(e4 == incidentxrayenergy);
if isempty(Index)

x = incidentxrayenergy;
MINindex = max(find(e4 < incidentxrayenergy));
x0 = e4(MINindex);
MAXindex = min(find(e4>incidentxrayenergy));
x1 = e4(MAXindex);

```

```
y0atc = atc4(MINindex);
y0abc = abc4(MINindex);
y1atc = atc4(MAXindex);
y1abc = abc4(MAXindex);

mat4atc4 = y0atc+(x-x0)*((y1atc-y0atc)/(x1-x0));
mat4abc4 = y0abc+(x-x0)*((y1abc-y0abc)/(x1-x0));
else
%If not find is not empty
mat4atc4 = atc4(Index);
mat4abc4 = abc4(Index);
end


%Calculate Core Volume
corevolume = (4/3)*pi*(coreinnerdiameter/2)^3;

%Calculate Shell Volume
shellvolume = (4/3)*pi*(coreshelldiameter/2)^3;

%Core volume material percentage over shell volume material
corevolumepercent = corevolume /(corevolume+shellvolume);

%Shell volume material percentage over core volume material
shellvolumepercent = shellvolume /(corevolume+shellvolume);

%Calculate Mass Percentages of Core
masspercent1 = m1/(m1+m2);
masspercent2 = m2/(m1+m2);

%Calculate Mass Percentages of Shell
masspercent3 = m3/(m3+m4);
masspercent4 = m4/(m3+m4);

atc1calcvalue = d1*masspercent1*mat1atc1;
abc1calcvalue = d1*masspercent1*mat1abc1;

atc2calcvalue = d2*masspercent2*mat2atc2;
abc2calcvalue = d2*masspercent2*mat2abc2;

atc3calcvalue = d2*masspercent3*mat3atc3;
abc3calcvalue = d2*masspercent3*mat3abc3;

atc4calcvalue = d2*masspercent4*mat4atc4;
abc4calcvalue = d2*masspercent4*mat4abc4;

totalatcvalue = (atc1calcvalue + atc2calcvalue)*corevolumepercent+...
    (atc3calcvalue + atc4calcvalue)*shellvolumepercent;
totalabcvalue = (abc1calcvalue + abc2calcvalue)*corevolumepercent+...
    (abc3calcvalue + abc4calcvalue)*shellvolumepercent;

%Applying Beer-Lambert Law (I/I0) = exp(-u/p*p*x)
```

```
361
362 %Solving for Attenuation
363 attenuationthickness = -1*log(xrayabsorptionattenuation)/totalatcvalue;
364 attenuationthickness = attenuationthickness+(attenuationthickness*...
365     loadingdensity);
366
367 %Solving for Absorption
368 absorptionthickness = -1*log(xrayabsorptionattenuation)/totalabcvalue;
369 absorptionthickness = absorptionthickness+(absorptionthickness*...
370     loadingdensity);
371
372 end
373 end
```

Z.5 User Input and Presentation Code

```
%Created By: 2d Lt Michael Sherburne
%Date Created: 11/4/2019
%Description: Calculate needed thickness of a material to absorb a ...
    desired
%amount of energy. Uses Beer-Lambert's law to solve.
%Coefficient Data:
%https://physics.nist.gov/PhysRefData/XrayMassCoef/tab3.html
%Density Data:
%http://periodictable.com/Properties/A/Density.al.html

%References
%https://www.mathworks.com/matlabcentral/answers/375710-find-nearest-
%value-to-specific-number
%https://stackoverflow.com/questions/28741747/change-the-symbols-size-
%in-matlab-legend
%https://www.mathworks.com/matlabcentral/answers/26174-break-title-into-
%multiple-lines

%Available Materials
%Cd,Se,Zn,S,Mn,Ga,As,Pb,Al,O

%Excel Information
%Row A: Energy in MeV
%Row B: Attenuation Coefficient
%Row C: Absorption Coefficient

%User Parameter Input:
%incidentxrayenergy = 100; %in keV
[~, ~, raw]  = xlsread('XRAYPROJECTLOADER.xlsx','Loader');
nrows = size(raw,1);
rows = nrows - 3;

for projectTask = 1:1:rows

cell = projectTask + 3;
user  = xlsread('XRAYPROJECTLOADER.xlsx','Loader',...
    strcat('A',int2str(cell)));
[~,material1,~]  = xlsread('XRAYPROJECTLOADER.xlsx','Loader',...
    strcat('B',int2str(cell)));
material1 = char(material1);
[~,material2,~]  = xlsread('XRAYPROJECTLOADER.xlsx','Loader',...
strcat('C',int2str(cell)));
material2 = char(material2);
[~,material3,~]  = xlsread('XRAYPROJECTLOADER.xlsx','Loader',...
    strcat('D',int2str(cell)));
material3 = char(material3);
coreinnerdiameter  = xlsread('XRAYPROJECTLOADER.xlsx','Loader',...
    strcat('E',int2str(cell)));
coreshelldiameter  = xlsread('XRAYPROJECTLOADER.xlsx','Loader',...
```

```
    strcat('F',int2str(cell)));
loadingdensity  = xlsread('XRAYPROJECTLOADER.xlsx','Loader',...
    strcat('G',int2str(cell)));
xrayabsorptionattenuation  = xlsread('XRAYPROJECTLOADER.xlsx',...
    'Loader',strcat('H',int2str(cell)));

%Conversions...
%incidentxrayenergy = incidentxrayenergy/1E3; %convert to MeV
xrayabsorptionattenuation = (100-xrayabsorptionattenuation)/100; ...
    %convert
%to fractional value
loadingdensity = (100-loadingdensity)/100; %convert to fractional value

format long

%Define Variables
d1 = 0;
m1 = 0;
e1 = 0;
atc1 = 0;
abc1 = 0;
d2 = 0;
m2 = 0;
e2 = 0;
atc2 = 0;
abc2 = 0;
d3 = 0;
m3 = 0;
e3 = 0;
atc3 = 0;
abc3 = 0;
d4 = 0;
m4 = 0;
e4 = 0;
atc4 = 0;
abc4 = 0;

%Core Single Material
if (user == 1)
[d1,m1,e1,atc1,abc1] = collectxraydata(material1);

%Core Compound
elseif (user == 2)
[d1,m1,e1,atc1,abc1] = collectxraydata(material1);
[d2,m2,e2,atc2,abc2] = collectxraydata(material2);

%Core Three Compound
elseif (user == 3)

[d1,m1,e1,atc1,abc1] = collectxraydata(material1);
[d2,m2,e2,atc2,abc2] = collectxraydata(material2);
[d3,m3,e3,atc3,abc3] = collectxraydata(material3);
```

```
100
101 %Core Compound/Shell
102 elseif (user == 4)
103
104 [d1,m1,e1,atc1,abc1] = collectxraydata(material1);
105 [d2,m2,e2,atc2,abc2] = collectxraydata(material2);
106 [d3,m3,e3,atc3,abc3] = collectxraydata('Zn');
107 [d4,m4,e4,atc4,abc4] = collectxraydata('S');
108
109 end
110
111 %Plot Values (1keV-100keV)
112 attenuationthickness = zeros(100,1);
113 absorptionthickness = zeros(100,1);
114
115 %Need to convert X-ray values from keV to MeV to use NIST Values
116 for I = 1:1:100
117    incidentxrayenergy(I) = I/1E3;
118    [attenuationthickness(I),absorptionthickness(I)] = xraycalc(d1,m1,...
119        e1,atc1,abc1,d2,m2,e2,atc2,abc2,d3,m3,e3,atc3,abc3,d4,m4,e4,...
120        atc4,abc4,material1,material2,material3,incidentxrayenergy(I),...
121        xrayabsorptionattenuation,loadingdensity,user,coreinnerdiameter,...
122        coreshelldiameter);
123 end
124
125 %Plot Information
126
127 %%%%%%%%%%%%%%%%%%%%%%%%%%%%%%%%%%%%%%%%%%%%%%%
128 %Set plot stuff:
129 set(0, 'DefaultLineLineWidth' ,0.5)
130 % set(0,'DefaultLineColor',[1,1,1])
131 set(0, 'DefaultLineMarkerSize' ,15)
132 set(0, 'DefaultAxesFontSize' ,22)
133 set(0, 'DefaultFigureColor' ,[1,1,1])
134 set(0, 'DefaultTextFontSize' ,26)
135 set(0, 'DefaultTextInterpreter' , 'latex' )
136 set(0, 'DefaultTextFontName' , 'Arial' ) %Times-Roman')
137 set(0, 'DefaultAxesFontName' , 'Arial' ) %Times-Roman')
138 %%%%%%%%%%%%%%%%%%%%%%%%%%%%%%%%%%%%%%%%%%%%%%%
139
140 figure(1)
141 scatter(incidentxrayenergy.*1E3,attenuationthickness.*1E4,500,'b.');
142 hold on
143 scatter(incidentxrayenergy.*1E3,absorptionthickness.*1E4,500,'r.');
144
145 set(gca,'xscale','log','yscale','log')
146 grid on
147 grid(gca,'minor')
148 hAx=gca;
149 set(hAx,'xminorgrid','on','yminorgrid','on')
150 hold on
151 xlabel('Incident X-Ray Energy (keV)');
```

```
ylabel('Thickness ($\mu$m)');

%Change title of plot accordingly
if (user == 1)
STR = strcat(material1, ...
    ' Quantum Dot Thickness Over Incident X-Ray ...Energy and ',{' ...
      '},...
    int2str(100-xrayabsorptionattenuation*100),...
    ' % Absorption/Attenuation with ',{' '},...
    int2str(100-loadingdensity*100), '% Quantum Dot Loading Density');
elseif (user == 2)
STR = strcat(material1,material2,...
    ' Quantum Dot Thickness Over Incident X-Ray Energy and ',{' '},...
    int2str(100-xrayabsorptionattenuation*100),...
    ' % Absorption/Attenuation with ',{' '},...
    int2str(100-loadingdensity*100), '% Quantum Dot Loading Density');
elseif (user == 3)
STR = strcat(material1,material2,material3,...
    ' Quantum Dot Thickness Over Incident X-Ray Energy and ',{' '},...
    int2str(100-xrayabsorptionattenuation*100),...
    ' % Absorption/Attenuation with ',{' '},...
    int2str(100-loadingdensity*100), '% Quantum Dot Loading Density');
elseif (user == 4)
STR = strcat(material1,material2,...
' ZnS Core Shell Quantum Dot Thickness Over Incident X-Ray Energy ...
   and ',...
    {' '},int2str(100-xrayabsorptionattenuation*100),...
    ' % Absorption/Attenuation with ',{' '},...
    int2str(100-loadingdensity*100), '% Quantum Dot Loading Density');
end

title(STR,'FontSize', 20)
[~, objh] = legend('Attenuation','Absorption','location','best');
objhl = findobj(objh, 'type', 'patch');
set(objhl, 'Markersize', 25);

%Auto Save Plot as PNG
orient(figure(1),'landscape','rotated')
fig1 = figure(1);
pos_fig1 = [0 0 2500 1200];
set(fig1,'Position',pos_fig1)
if (user == 1)
out = strcat(material1,'absorb',...
    int2str(100-xrayabsorptionattenuation*100),'loading',...
    int2str(100-loadingdensity*100));
elseif (user == 2)
out = strcat(material1,material2,'absorb',...
    int2str(100-xrayabsorptionattenuation*100),'loading',...
    int2str(100-loadingdensity*100));
elseif (user == 3)
out = strcat(material1,material2,material3,'absorb',...
    int2str(100-xrayabsorptionattenuation*100),'loading',...
```

```
202     int2str(100-loadingdensity*100));
203 elseif (user == 4)
204 out = strcat(material1,material2,'ZnSCoreShell','absorb',...
205     int2str(100-xrayabsorptionattenuation*100),'loading',...
206     int2str(100-loadingdensity*100));
207 end
208
209 filenameprint = out;
210 saveas(gcf,[pwd strcat('/MATLABPLOTS/',strcat(out,'.fig'))]);
211 print(filenameprint,'-dpng');
212 movefile(strcat(filenameprint,'.png'),'G:\Michael\Documents\GrabCAD\Los ...
       Alamos-AFRL-AFIT Streak Camera\XRay Absorption ...
       Calculations\MATLABPNGS')
213
214 clf
215
216 end
217
218 clc
219 clear
```

Z.6 PL and PLE Peak and FWHM Finder Code

```
%Created By: 2d Lt Michael Sherburne
%Date: 10/19/2019
%Description: Plot each individual material data set and find FWHM ...
    for PL
%data
clc
clear
%%%%%%%%%%%%%%%%%%%%%%%%%%%%%%%%%%%%%%%%%%%%%%%%
%Set plot stuff:
set(0, 'DefaultLineLineWidth' ,0.5)
set(0, 'DefaultLineMarkerSize' ,10)
set(0, 'DefaultAxesFontSize' ,40)
set(0, 'DefaultFigureColor' ,[1,1,1])
set(0, 'DefaultTextFontSize' ,40)
set(0, 'DefaultTextInterpreter' , 'latex' )
set(0, 'DefaultTextFontName' , 'Arial' ) %Times-Roman')
set(0, 'DefaultAxesFontName' , 'Arial' ) %Times-Roman')
MarkerSize = 800;
MarkerTransparency = .4;
FONTSIZE = 22;
LABEL_FONTSIZE = 26;
%%%%%%%%%%%%%%%%%%%%%%%%%%%%%%%%%%%%%%%%%%%%%%%%
filename = 'Master_PL_PLE_QD_Spectra.xlsx';
NU = 1; %Select Material Data Set
matlNum = NU; %Select material to import
%Determine size of dataset
t = readtable(filename,'Sheet',int2str(matlNum));
[rows, columns] = size(t);
dataSize = rows+1;
%Import in attributes
[~,Structure(1)]  = xlsread(filename,...
    int2str(matlNum),'D1'); %Material Name
[~,PLType(1)]  = xlsread(filename,...
    int2str(matlNum),'B3'); %Material Name
[~,Material(1)]  = xlsread(filename,...
    int2str(matlNum),'B1') %Material Name
Concentration(1)  = xlsread(filename,...
    int2str(matlNum),'D2'); %Concentration of Material
%Get exact size of dataset
[SIZE,~] = size(xlsread(filename,int2str(matlNum),...
    strcat('A7:A',int2str(dataSize)) )) ;
%Import in wavelength data
Wavelength(1:SIZE,1)= xlsread(filename,int2str(matlNum),...
    strcat('A7:A',int2str(dataSize)) );
%Get exact size of dataset
[SIZE,~] = size(xlsread(filename,int2str(matlNum),strcat...
    ('B7:B',int2str(dataSize)) )) ;
%Import in intensity data
Intensity(1:SIZE,1)= xlsread(filename,int2str(matlNum),...
```

```
49      strcat('B7:B',int2str(dataSize)) );
50  %Normalize Data?
51  NORM = 1; %1 = normalize
52  fig1 = figure
53  compareStruct = string(Structure(1)) == "Quartz";
54  comparePL = string(PLType(1)) == "PL";
55  %compareStruct == 0 means 3D structure
56  %comparePL == 0 means PLE
57  maxPoint = max(nonzeros(Wavelength(:,1)));
58  minPoint = min(nonzeros(Wavelength(:,1)));
59  xq = minPoint:0.5:maxPoint;
60  if NORM == 1
61      vq1 = interp1(nonzeros(Wavelength(:,1)),nonzeros(Intensity(:,1))/...
62          nonzeros(max(Intensity(:,1))),xq,'spline');
63  else
64      vq1 = ...
           interp1(nonzeros(Wavelength(:,1)),nonzeros(Intensity(:,1)),xq...
65          ,'spline');
66  end
67  plot(xq,vq1,'LineWidth',3)
68  if NORM == 1
69       ylim([0 1])
70  else
71       %Do not change yaxis limits
72  end
73  xlabel('Wavelength (nm)')
74  if NORM == 1
75      ylabel('Intensity (normalized)')
76  else
77      if comparePL == 1
78          ylabel('Intensity (cps)')
79      else
80          ylabel('Intensity (cps/uA)')
81      end
82  end
83  %Find FWHM
84  if comparePL == 1
85      [pks,locs,widths] = findpeaks(vq1,xq,'MinPeakProminence',0.05,...
86          'MinPeakHeight',0.8,'Annotate','extents')
87      findpeaks(vq1,xq,'MinPeakProminence',0.05,'MinPeakHeight',0.8,...
88          'Annotate','extents')
89  end
90  set(gca,'FontSize',20);
91  set(findall(gca, 'Type', 'Line'),'LineWidth',3);
92  grid on
93  hAx=gca;  %avoid repetitive function calls
94  set(hAx,'xminorgrid','on','yminorgrid','on')
95  hold on
96  %Save .PNG File
97  orient(fig1,'landscape') %figure(matlNum)
98  pos_fig1 = [0 0 1000 1000];
99  set(fig1,'Position',pos_fig1)
```

```
100 out = strcat(Material(i),Structure(i),PLType(i));
101 s1 = char(strrep(out, ' ', ''))
102 set(fig1,'PaperOrientation','portrait');
103 print(fig1,s1,'-dpng')
```

Z.7 Absorption Thickness Code

```
%Created By: 2d Lt Michael Sherburne
%Date Created: 11/25/2019
%Description: Voxelize an entire quantum dot and assume homogenuity ...
    of dots
%within a polymer matrix to test for x-ray absorption efficiency
format long
clc
clear
close all
incidentxrayenergy = 10; %keV
incidentxrayenergy = incidentxrayenergy/1E3; %Convert keV to MeV to make
polymermatl = 'PMMA'; %Polymer Q-Dots are Suspended In
gridSize = 150; %Voxel Grid Size (Higher # = better resolution but ...
    slower
%performance
N = maxNumCompThreads(8)%maxNumCompThreads %Use maximum number of ...
    CPU cores
%User Parameter Input:
filename = 'XRAYPROJECTLOADER.xlsx';
[~, ~, raw]  = xlsread(filename,'Loader');
nrows = size(raw,1);
rows = nrows - 3;
for projectTask = 1:1:rows
  %Define Global Variables
  tcatc = 0;
  tcabs = 0;
  ts1atc = 0;
  ts1abs = 0;
  ts2atc = 0;
  ts2abs = 0;
  ts3atc = 0;
  ts3abs = 0;
  corediameter = 0;
  shell1diameter = 0;
  shell2diameter = 0;
  shell3diameter = 0;
  cell = projectTask + 3;
  %Gather Core Material Data
  [~,material1,~]  = ...
     xlsread(filename,'Loader',strcat('A',int2str(cell)));
  material1 = char(material1);
  amountm1  = xlsread(filename,'Loader',strcat('B',int2str(cell)));
  [~,material2,~]  = ...
     xlsread(filename,'Loader',strcat('C',int2str(cell)));
  material2 = char(material2);
  amountm2  = xlsread(filename,'Loader',strcat('D',int2str(cell)));
  [~,material3,~]  = ...
     xlsread(filename,'Loader',strcat('E',int2str(cell)));
  material3 = char(material3);
```

```
44  amountm3  = xlsread(filename,'Loader',strcat('F',int2str(cell)));
45  [~,material4,~]  = ...
       xlsread(filename,'Loader',strcat('G',int2str(cell)));
46  material4 = char(material4);
47  amountm4  = xlsread(filename,'Loader',strcat('H',int2str(cell)));
48  %Core Diameter
49  corediameter  = xlsread(filename,'Loader',strcat('I',int2str(cell)));
50  %Gather Shell Level 1 Data
51  [~,shell1m1,~]  = ...
       xlsread(filename,'Loader',strcat('J',int2str(cell)));
52  shell1m1 = char(shell1m1);
53  amounts11  = xlsread(filename,'Loader',strcat('K',int2str(cell)));
54  [~,shell1m2,~]  = ...
       xlsread(filename,'Loader',strcat('L',int2str(cell)));
55  shell1m2 = char(shell1m2);
56  amounts12  = xlsread(filename,'Loader',strcat('M',int2str(cell)));
57  %Shell 1 Diameter
58  shell1diameter  = ...
       xlsread(filename,'Loader',strcat('N',int2str(cell)));
59  %Gather Shell Level 2 Data
60  [~,shell2m1,~]  = ...
       xlsread(filename,'Loader',strcat('O',int2str(cell)));
61  shell2m1 = char(shell2m1);
62  amounts21  = xlsread(filename,'Loader',strcat('P',int2str(cell)));
63  [~,shell2m2,~]  = ...
       xlsread(filename,'Loader',strcat('Q',int2str(cell)));
64  shell2m2 = char(shell2m2);
65  amounts22  = xlsread(filename,'Loader',strcat('R',int2str(cell)));
66  %Shell 2 Diameter
67  shell2diameter  = ...
       xlsread(filename,'Loader',strcat('S',int2str(cell)));
68  %Gather Shell Level 3 Data
69  [~,shell3m1,~]  = ...
       xlsread(filename,'Loader',strcat('T',int2str(cell)));
70  shell3m1 = char(shell3m1);
71  amounts31  = xlsread(filename,'Loader',strcat('U',int2str(cell)));
72  [~,shell3m2,~]  = ...
       xlsread(filename,'Loader',strcat('V',int2str(cell)));
73  shell3m2 = char(shell3m2);
74  amounts32  = xlsread(filename,'Loader',strcat('W',int2str(cell)));
75  %Shell 3 Diameter
76  shell3diameter  = ...
       xlsread(filename,'Loader',strcat('X',int2str(cell)));
77  %Other Parameters
78  loadingdensity  = ...
       xlsread(filename,'Loader',strcat('Y',int2str(cell)));
79  xrayabsorptionattenuation  = xlsread(filename,'Loader', ...
80      strcat('Z',int2str(cell)));
81  %Conversions...
82  xrayabsorptionattenuation = xrayabsorptionattenuation/100; %convert
83  %to fractional value
84  loadingdensity = loadingdensity/100; %convert to fractional value
```

```
%Calculate Attenuation Through PMMA
[d1,m1,e1,atc1,abc1] = collectxraydata(polymermatl);
%Collect material 1 data
Index = find(e1 == incidentxrayenergy);
if isempty(Index)
    x = incidentxrayenergy;
    MINindex = max(find(e1 < incidentxrayenergy));
    x0 = e1(MINindex);
    MAXindex = min(find(e1>incidentxrayenergy));
    x1 = e1(MAXindex);
    y0atc = atc(i,MINindex);
    y0abc = abc(i,MINindex);
    y1atc = atc(i,MAXindex);
    y1abc = abc(i,MAXindex);
    mat1atc1 = y0atc+(x-x0)*((y1atc-y0atc)/(x1-x0));
    mat1abc1 = y0abc+(x-x0)*((y1abc-y0abc)/(x1-x0));
  else
    %If not find is not empty
    mat1atc1 = atc1(Index);
    mat1abc1 = abc1(Index);
end
atc1calcvalue = d1*mat1atc1;
abc1calcvalue = d1*mat1abc1;
tpabs = atc1calcvalue+abc1calcvalue;
mcorecount = 0; %count number of core materials
%Gather Core Materials
if material1 ~= ""
    [d(1),m(1),e(1,:),atc(1,:),abc(1,:)] = collectxraydata(material1);
    mcorecount = mcorecount + 1;
end
if material2 ~= ""
    [d(2),m(2),e(2,:),atc(2,:),abc(2,:)] = collectxraydata(material2);
    mcorecount = mcorecount + 1;
end
if material3 ~= ""
    [d(3),m(3),e(3,:),atc(3,:),abc(3,:)] = collectxraydata(material3);
    mcorecount = mcorecount + 1;
end
if material4 ~= ""
    [d(4),m(4),e(4,:),atc(4,:),abc(4,:)] = collectxraydata(material4);
    mcorecount = mcorecount + 1;
end
shellcount = 0; %count number of shells
%Shell Layer #1 (Compound)
  if shell1m1 ~= ""
    [ds(1),ms(1),es(1,:),atcs(1,:),abcs(1,:)] = ...
        collectxraydata(shell1m1);
    [ds(2),ms(2),es(2,:),atcs(2,:),abcs(2,:)] = ...
        collectxraydata(shell1m2);
    shellcount = shellcount + 1;
end
%Shell Layer #2 (Compound)
```

```
137   if shell2m1 ~= ""
138       [ds(3),ms(3),es(3,:),atcs(3,:),abcs(3,:)] = ...
139           collectxraydata(shell2m1);
140       [ds(4),ms(4),es(4,:),atcs(4,:),abcs(4,:)] = ...
141           collectxraydata(shell2m2);
142       shellcount = shellcount + 1;
143   end
144   %Shell Layer #3 (Compound)
145   if shell3m1 ~= ""
146       [ds(5),ms(5),es(5,:),atcs(5,:),abcs(5,:)] = ...
147           collectxraydata(shell3m1);
148       [ds(6),ms(6),es(6,:),atcs(6,:),abcs(6,:)] = ...
149           collectxraydata(shell3m2);
150       shellcount = shellcount + 1;
151   end
152   %Collect material 1 data
153   for i = 1:1:mcorecount
154       Index = find(e(i,:) == incidentxrayenergy);
155       if isempty(Index)
156           x = incidentxrayenergy;
157           MINindex = max(find(e(i) < incidentxrayenergy));
158           x0 = e(i,MINindex);
159           MAXindex = min(find(e(i)>incidentxrayenergy));
160           x1 = e(i,MAXindex);
161           %Linear Interpolation
162           y0atc = atc(i,MINindex);
163           y0abc = abc(i,MINindex);
164           y1atc = atc(i,MAXindex);
165           y1abc = abc(i,MAXindex);
166           mat1atc(i) = y0atc+(x-x0)*((y1atc-y0atc)/(x1-x0));
167           mat1abc(i) = y0abc+(x-x0)*((y1abc-y0abc)/(x1-x0));
168       else
169           %If not find is not empty
170           mat1atc(i) = atc(i,Index);
171           mat1abc(i) = abc(i,Index);
172       end
173       %If material count > 1, then calculate mass percentages
174       atccalcvalue(i) = d(i)*mat1atc(i);
175       abccalcvalue(i) = d(i)*mat1abc(i);
176       %totalatcvalue(i) = atccalcvalue(i);
177   end
178   %For 1 material core
179   totalabcvalue = atccalcvalue(1)+abccalcvalue(1);
180   if mcorecount == 2
181       masspercent1 = (m(1)*amountm1)/((m(1)*amountm1)+(m(2)*amountm2));
182       masspercent2 = (m(2)*amountm2)/((m(1)*amountm1)+(m(2)*amountm2));
183       atccalcvalue(1) = d(1)*mat1atc(1)*masspercent1;
184       abccalcvalue(1) = d(1)*mat1abc(1)*masspercent1;
185       atccalcvalue(2) = d(2)*mat1atc(2)*masspercent2;
186       abccalcvalue(2) = d(2)*mat1abc(2)*masspercent2;
187       totalabcvalue = atccalcvalue(1)+abccalcvalue(1);
188       totalabcvalue = atccalcvalue(2) + abccalcvalue(2)+ totalabcvalue;
```

```
189   elseif mcorecount == 3
190       masspercent1 = (m(1)*amountm1)/((m(1)*amountm1)+...
191           (m(2)*amountm2)+(m(3)*amountm3));
192       masspercent2 = (m(2)*amountm2)/((m(1)*amountm1)+...
193           (m(2)*amountm2)+(m(3)*amountm3));
194       masspercent3 = (m(3)*amountm3)/((m(1)*amountm1)+...
195           (m(2)*amountm2)+(m(3)*amountm3));
196       atccalcvalue(1) = d(1)*mat1atc(1)*masspercent1;
197       abccalcvalue(1) = d(1)*mat1abc(1)*masspercent1;
198       atccalcvalue(2) = d(2)*mat1atc(2)*masspercent2;
199       abccalcvalue(2) = d(2)*mat1abc(2)*masspercent2;
200       atccalcvalue(3) = d(3)*mat1atc(3)*masspercent3;
201       abccalcvalue(3) = d(3)*mat1abc(3)*masspercent3;
202       totalabcvalue = atccalcvalue(1)+abccalcvalue(1);
203       totalabcvalue = atccalcvalue(2) + abccalcvalue(2)+ totalabcvalue;
204       totalabcvalue = atccalcvalue(3) + abccalcvalue(3) + totalabcvalue;
205   elseif mcorecount == 4
206       masspercent1 = (m(1)*amountm1)/((m(1)*amountm1)+...
207           (m(2)*amountm2)+(m(3)*amountm3)+(m(4)*amountm4));
208       masspercent2 = (m(2)*amountm2)/((m(1)*amountm1)+...
209           (m(2)*amountm2)+(m(3)*amountm3)+(m(4)*amountm4));
210       masspercent3 = (m(3)*amountm3)/((m(1)*amountm1)+...
211           (m(2)*amountm2)+(m(3)*amountm3)+(m(4)*amountm4));
212       masspercent4 = (m(4)*amountm4)/((m(1)*amountm1)+...
213           (m(2)*amountm2)+(m(3)*amountm3)+(m(4)*amountm4));
214       atccalcvalue(1) = d(1)*mat1atc(1)*masspercent1;
215       abccalcvalue(1) = d(1)*mat1abc(1)*masspercent1;
216       atccalcvalue(2) = d(2)*mat1atc(2)*masspercent2;
217       abccalcvalue(2) = d(2)*mat1abc(2)*masspercent2;
218       atccalcvalue(3) = d(3)*mat1atc(3)*masspercent3;
219       abccalcvalue(3) = d(3)*mat1abc(3)*masspercent3;
220       atccalcvalue(4) = d(4)*mat1atc(4)*masspercent4;
221       abccalcvalue(4) = d(4)*mat1abc(4)*masspercent4;
222       totalabcvalue = atccalcvalue(1)+abccalcvalue(1);
223       totalabcvalue = atccalcvalue(2) + abccalcvalue(2) + totalabcvalue;
224       totalabcvalue = atccalcvalue(3) + abccalcvalue(3)+ totalabcvalue;
225       totalabcvalue = atccalcvalue(4) + abccalcvalue(4) + totalabcvalue;
226   end
227   %Calculate Shell Material
228   if shellcount > 0
229       for i = 1:1:(shellcount*2)
230           Index = find(es(i,:) == incidentxrayenergy);
231           if isempty(Index)
232               x = incidentxrayenergy;
233               MINindex = max(find(es(i) < incidentxrayenergy));
234               x0 = es(i,MINindex);
235               MAXindex = min(find(es(i)>incidentxrayenergy));
236               x1 = es(i,MAXindex);
237               %Linear Interpolation
238               y0atc = atcs(i,MINindex);
239               y0abc = abcs(i,MINindex);
240               y1atc = atcs(i,MAXindex);
```

```
241                 y1abc = abcs(i,MAXindex);
242                 mat1atcs(i) = y0atc+(x-x0)*((y1atc-y0atc)/(x1-x0));
243                 mat1abcs(i) = y0abc+(x-x0)*((y1abc-y0abc)/(x1-x0));
244             else
245                 %If not find is not empty
246                 mat1atcs(i) = atcs(i,Index);
247                 mat1abcs(i) = abcs(i,Index);
248             end
249             %If material count > 1, then calculate mass percentages
250             atccalcvalues(i) = ds(i)*mat1atcs(i);
251             abccalcvalues(i) = ds(i)*mat1abcs(i);
252         end
253     end
254     %Calculate Shell Parameters
255     if  shellcount > 0
256         %Gather Shell Material Data
257         masspercent1 = (ms(1)*amounts11)/((ms(1)*amounts11)+...
258             (ms(2)*amounts12));
259         masspercent2 = (ms(2)*amounts12)/((ms(1)*amounts11)+...
260             (ms(2)*amounts12));
261         atccalcvalues(1) = ds(1)*mat1atcs(1)*masspercent1;
262         abccalcvalues(1) = ds(1)*mat1abcs(1)*masspercent1;
263         atccalcvalues(2) = ds(2)*mat1atcs(2)*masspercent2;
264         abccalcvalues(2) = ds(2)*mat1abcs(2)*masspercent2;
265         if shellcount > 1
266             masspercent1 = (ms(3)*amounts21)/((ms(3)*amounts21)...
267                 +(ms(4)*amounts22));
268             masspercent2 = (ms(4)*amounts22)/((ms(3)*amounts21)...
269                 +(ms(4)*amounts22));
270             atccalcvalues(3) = ds(3)*mat1atcs(3)*masspercent1;
271             abccalcvalues(3) = ds(3)*mat1abcs(3)*masspercent1;
272             atccalcvalues(4) = ds(4)*mat1atcs(4)*masspercent2;
273             abccalcvalues(4) = ds(4)*mat1abcs(4)*masspercent2;
274             if shellcount > 2
275                 masspercent1 = (ms(5)*amounts31)/((ms(5)*amounts31)...
276                     +(ms(6)*amounts32));
277                 masspercent2 = (ms(6)*amounts32)/((ms(5)*amounts31)...
278                     +(ms(6)*amounts32));
279                 atccalcvalues(5) = ds(5)*mat1atcs(5)*masspercent1;
280                 abccalcvalues(5) = ds(5)*mat1abcs(5)*masspercent1;
281                 atccalcvalues(6) = ds(6)*mat1atcs(6)*masspercent2;
282                 abccalcvalues(6) = ds(6)*mat1abcs(6)*masspercent2;
283             end
284         end
285         %Calculate Shell Proportions
286         shell1volume = 0;
287         shell2volume = 0;
288         shell3volume = 0;
289         %Calculate Core Volume
290         corevolume = (4/3)*pi*(corediameter/2)^3; %nm^3
291         if shellcount > 0
292             shell1volume = (4/3)*pi*(shell1diameter/2)^3;
```

```
293             if shellcount > 1
294                 shell2volume = (4/3)*pi*(shell2diameter/2)^3;
295                 if shellcount > 2
296                     shell3volume = (4/3)*pi*(shell3diameter/2)^3;
297                 end
298             end
299         end
300         %Core volume material percentage over shell volume material
301         corevolumepercent = corevolume /(corevolume+shell1volume+...
302             shell2volume+shell3volume);
303         %Shell 1 volume material percentage over core volume material
304         shell1volumepercent = shell1volume /(corevolume+shell1volume+...
305             shell2volume+shell3volume);
306         %Shell 2 volume material percentage over core volume material
307         shell2volumepercent = shell2volume /(corevolume+shell1volume+...
308             shell2volume+shell3volume);
309         %Shell 3 volume material percentage over core volume material
310         shell3volumepercent = shell3volume /(corevolume+shell1volume+...
311             shell2volume+shell3volume);
312         %Load Shell Values into Voxel
313         %Shell 1
314         if shellcount > 0
315           ts1abs = atccalcvalues(1)+abccalcvalues(1);
316           ts1abs = atccalcvalues(2) + abccalcvalues(2) + ts1abs;
317           if shellcount > 1
318           %Shell 2
319               ts2abs = atccalcvalues(3)+abccalcvalues(3);
320               ts2abs = atccalcvalues(4) + abccalcvalues(4) + ts2abs;
321               if shellcount > 2
322                   %Shell 3
323                   ts3abs = atccalcvalues(5) + abccalcvalues(5);
324                   ts3abs = atccalcvalues(6) + abccalcvalues(6) + ts3abs;
325               end
326           end
327       end
328   else
329     %No shell
330   end
331   %Load Core Values into Voxels
332   tcatc = totalabcvalue;
333   tcabs = totalabcvalue;
334   [CAVGTRANSMITTED,SL] = test(gridSize,tpabs,tpabs,...
335       tcatc,tcabs,...
336       ts1atc,ts1abs,...
337       ts2atc,ts2abs,...
338       ts3atc,ts3abs,...
339       corediameter,shell1diameter,shell2diameter,shell3diameter,...
340       loadingdensity,incidentxrayenergy)
341   %Solve for needed thickness of scintillator material
342   NumberCubes = log(1-xrayabsorptionattenuation)/log(CAVGTRANSMITTED);
343   Thickness(projectTask) = NumberCubes*SL*0.001 %solve for thickness
344   %and convert from nm to um
```

```
345 end
```

Z.8 Import Stress-Strain and Optical Information and Present Information Code

```
%Created By: 2d Lt Michael Sherburne
%Date Created: 3/5/2020
%Description: Import in optical strain data
clc;
clear all;
close all;
set(0, 'DefaultLineLineWidth' ,0.5)
set(0, 'DefaultLineMarkerSize' ,10)
set(0, 'DefaultAxesFontSize' ,40)
set(0, 'DefaultFigureColor' ,[1,1,1])
set(0, 'DefaultTextFontSize' ,40)
set(0, 'DefaultTextInterpreter' , 'latex' )
set(0, 'DefaultTextFontName' , 'Arial' ) %Times-Roman')
set(0, 'DefaultAxesFontName' , 'Arial' ) %Times-Roman')
MarkerSize = 800;
MarkerTransparency = .4;
FONTSIZE = 22;
LABEL_FONTSIZE = 26;
format long
%Cross-Sectional Area of T-Bone Under Test
CA = 1.29032e-6; %m^2
L0 = 83.312; %mm
filename = 'Test3.xlsx'; %Strain Data File Name
tablename = 'Test3';
myFolder = '10282019T3';
filePattern = fullfile(myFolder, '*.txt');
txtFiles    = dir(filePattern);
%https://www.mathworks.com/matlabcentral/answers/57446-faq-how-can-i-process-a-sequence-
for k = 1:length(txtFiles)
  baseFileName = txtFiles(k).name;
  fullFileName = fullfile(myFolder, baseFileName);
  fprintf('Now reading %s\n', fullFileName);
  fidi = fopen(fullFileName,'rt');
  Dc = textscan(fidi, '%f%f%f', 'HeaderLines',2, ...
      'CollectOutput',true, 'EndOfLine','\r\n');
  fclose(fidi);
  D = cell2mat(Dc);
  wavelength(k,:) = D(:,1);
  intensity(k,:) = D(:,2);
end
%Import Strain Data
t = readtable(filename,'Sheet',tablename);
[rows, columns] = size(t);
dataSize = rows+1;
[SIZE,~] = ...
    size(xlsread(filename,tablename,strcat('A6:A',int2str(dataSize)))) ...
    ; %Material Name
Time(1:SIZE)= ...
```

```
    xlsread(filename,tablename,strcat('A6:A',int2str(dataSize)));
AxialDisplacement(1:SIZE)= ...
    xlsread(filename,tablename,strcat('B6:B',int2str(dataSize)));
AxialForce(1:SIZE)= ...
    xlsread(filename,tablename,strcat('C6:C',int2str(dataSize)));
maxEmission = max(intensity(1,:));
%Time Interval: How many seconds between frames
timeInterval = 1;
for z = 1:SIZE
   if mod(Time(z),timeInterval) < 0.0095
       placeHolder(z) = z; %Division by 3
   end
end
placeHolderNZ = nonzeros(placeHolder');
size(placeHolderNZ)
NewTime = Time(placeHolderNZ);
NewDisplacement = AxialDisplacement(placeHolderNZ);
NewForce = AxialForce(placeHolderNZ);
NewStrain = NewDisplacement/L0; %Will need updating
NewStress = NewForce/CA;
[lengthUse,~] = size(placeHolderNZ); %Length to go through from data
width = 2000;
height = 1000;
LOCtext = 625; %nm x-axis location
triggerOn = 0;
triggerOn2 = 0;
Ccheck = 0;
for j = 1:lengthUse%length(txtFiles)
    xA = wavelength(j,:);
    yA = intensity(j,:)/maxEmission;
    %Optical Spectra Plot
    subplot(2,1,1);
    plot(xA,yA,'b')
    hold on
    plot(wavelength(1,:),intensity(1,:)/maxEmission,'r')
    hold off
    %Plot Present Experimental Time
    text(LOCtext,.8,strcat('Time(s)'," ",num2str(NewTime(j))))
    xlim([470 750])
    %xlim([500 600]) %Magnify
    ylabel('Intensity')
    xlabel('Wavelength (nm)')
    %Use these two points
    A = intensity(j,540);
    B = 0;
    for avgW = 550:1:557
        B = intensity(j,avgW)+B;
    end
    B  = B / 8;
    if j == 1
       C(1) = (B-A);
    else
```

```
95          C(j) = (((B-A))/(C(1)))*100; %Percent Change (absolute value)
96          if Ccheck < 1 && j > 50
97                 Ccheck = C(j-1);
98          else
99            Ccheck = C(j);
100         end
101     end
102     text(LOCtext,.4,strcat('Change'," ",num2str(Ccheck)))
103     %Observations
104     %Peak wavelength is not changing!
105     %Check for Ultimate Strength and Plot Once Reached
106     if j > 1
107         ForceCheck = NewForce(j)/NewForce(j-1);
108         if ForceCheck < 1.001 && ForceCheck > 0.99
109             triggerOn = 1;
110         end
111     end
112     if triggerOn == 1
113        text(LOCtext,.6,'Ultimate Strength Reached')
114     end
115     %End of Yield Point Test
116     %Plot Stress-Strain Curve
117     subplot(2,1,2);
118     c = linspace(1,.1,j);
119     plot(NewStrain(1:j),NewStress(1:j))%,50,'filled')
120     ylabel('Stress')
121     xlabel('Strain')
122     ylim([0 max(NewStress)])
123     xlim([0 max(NewStrain)])
124      if triggerOn == 1
125          if triggerOn2 == 0
126              triggerOn2 = 1;
127             StrainPoint = NewStrain(j);
128          end
129      end
130     %Gather a snapshop of each value for video
131     set(gcf,'position',[0 0 width height])
132     M(j) = getframe(gcf,[0 0 width height]);
133 end
134
135 %Strain Change Plot
136 POINTE = lengthUse-4;
137 figure
138 scatter(NewStrain(2:POINTE),C(2:POINTE),50,'r','filled')
139 xlabel('Strain')
140 ylabel('% PL Change')
141 figure
142 thres = 7;
143 hold on
144 F = fit(NewStrain(2:thres)',C(2:thres)','poly1')
145 pp = plot(F,NewStrain(2:thres)',C(2:thres))
146 F2 = fit(NewStrain(thres:POINTE)',C(thres:POINTE)','exp2')
```

```
147 p = plot(F2,':g',NewStrain(thres:POINTE)',C(thres:POINTE),'k.')
148 pp(2).LineWidth = 4;
149 p(2).LineWidth = 4;
150 grid on
151 xlabel('Strain')
152 ylabel('% PL Change')
153 hAx=gca;
154 set(hAx,'xminorgrid','on','yminorgrid','on')
155
156 %Read Movie
157 set(gcf,'position',[0 0 width height])
158 movie(gcf,M,1,2)
```

Z.9 Monolayer X-ray Quantum Efficiency Code

```
%Created By: 2d Lt Michael Sherburne
%Date Created: 11/25/2019
%Description: Voxelize an entire quantum dot and assume homogenuity ...
    of dots
%within a polymer matrix to test for x-ray absorption efficiency
format long
clc
clear
close all
incidentxrayenergy = 100; %keV
incidentxrayenergy = incidentxrayenergy/1E3; %Convert keV to MeV to make
polymermatl = 'PMMA'; %Polymer Q-Dots are Suspended In
gridSize = 40; %Voxel Grid Size (Higher # = better resolution but slower
%performance
N = maxNumCompThreads(8) %Use maximum number of CPU cores
%User Parameter Input:
filename = 'XRAYPROJECTLOADER.xlsx';
[~, ~, raw]  = xlsread(filename,'Loader');
nrows = size(raw,1);
rows = nrows - 3;
FPOC = zeros(1,rows);
for projectTask = 1:1:rows
  %Define Global Variables
  tcatc = 0;
  tcabs = 0;
  ts1atc = 0;
  ts1abs = 0;
  ts2atc = 0;
  ts2abs = 0;
  ts3atc = 0;
  ts3abs = 0;
  corediameter = 0;
  shell1diameter = 0;
  shell2diameter = 0;
  shell3diameter = 0;
    cell = projectTask + 3;
    %Gather Core Material Data
    [~,material1,~]  = xlsread(filename,'Loader',...
        strcat('A',int2str(cell)));
    material1 = char(material1);
    amountm1  = xlsread(filename,'Loader',strcat('B',int2str(cell)));
    [~,material2,~]  = xlsread(filename,'Loader',...
        strcat('C',int2str(cell)));
    material2 = char(material2);
    amountm2  = xlsread(filename,'Loader',strcat('D',int2str(cell)));
    [~,material3,~]  = xlsread(filename,'Loader',...
        strcat('E',int2str(cell)));
    material3 = char(material3);
    amountm3  = xlsread(filename,'Loader',strcat('F',int2str(cell)));
```

```
49      [~,material4,~]  = xlsread(filename,'Loader',...
50          strcat('G',int2str(cell)));
51      material4 = char(material4);
52      amountm4  = xlsread(filename,'Loader',strcat('H',int2str(cell)));
53      %Core Diameter
54      corediameter  = ...
           xlsread(filename,'Loader',strcat('I',int2str(cell)));
55      %Gather Shell Level 1 Data
56      [~,shell1m1,~]  = ...
           xlsread(filename,'Loader',strcat('J',int2str(cell)));
57      shell1m1 = char(shell1m1);
58      amounts11  = xlsread(filename,'Loader',strcat('K',int2str(cell)));
59      [~,shell1m2,~]  = ...
           xlsread(filename,'Loader',strcat('L',int2str(cell)));
60      shell1m2 = char(shell1m2);
61      amounts12  = xlsread(filename,'Loader',strcat('M',int2str(cell)));
62      %Shell 1 Diameter
63      shell1diameter  = ...
           xlsread(filename,'Loader',strcat('N',int2str(cell)));
64      %Gather Shell Level 2 Data
65      [~,shell2m1,~]  = ...
           xlsread(filename,'Loader',strcat('O',int2str(cell)));
66      shell2m1 = char(shell2m1);
67      amounts21  = xlsread(filename,'Loader',strcat('P',int2str(cell)));
68      [~,shell2m2,~]  = ...
           xlsread(filename,'Loader',strcat('Q',int2str(cell)));
69      shell2m2 = char(shell2m2);
70      amounts22  = xlsread(filename,'Loader',strcat('R',int2str(cell)));
71      %Shell 2 Diameter
72      shell2diameter  = ...
           xlsread(filename,'Loader',strcat('S',int2str(cell)));
73      %Gather Shell Level 3 Data
74      [~,shell3m1,~]  = ...
           xlsread(filename,'Loader',strcat('T',int2str(cell)));
75      shell3m1 = char(shell3m1);
76      amounts31  = xlsread(filename,'Loader',strcat('U',int2str(cell)));
77      [~,shell3m2,~]  = ...
           xlsread(filename,'Loader',strcat('V',int2str(cell)));
78      shell3m2 = char(shell3m2);
79      amounts32  = xlsread(filename,'Loader',strcat('W',int2str(cell)));
80      %Shell 3 Diameter
81      shell3diameter  = ...
           xlsread(filename,'Loader',strcat('X',int2str(cell)));
82      %Other Parameters
83      loadingdensity  = ...
           xlsread(filename,'Loader',strcat('Y',int2str(cell)));
84      xrayabsorptionattenuation  = xlsread(filename,'Loader', ...
85          strcat('Z',int2str(cell)));
86      quantumefficiency  = xlsread(filename,'Loader', ...
87          strcat('AA',int2str(cell)));
88      %Conversions...
89      xrayabsorptionattenuation = xrayabsorptionattenuation/100; %convert
```

```
90      %to fractional value
91      loadingdensity = loadingdensity/100; %convert to fractional value
92      %Calculate Attenuation Through PMMA
93      [d1,m1,e1,atc1,abc1] = collectxraydata(polymermatl);
94      %Collect material 1 data
95      Index = find(e1 == incidentxrayenergy);
96      if isempty(Index)
97          x = incidentxrayenergy;
98          MINindex = max(find(e1 < incidentxrayenergy));
99          x0 = e1(MINindex);
100         MAXindex = min(find(e1>incidentxrayenergy));
101         x1 = e1(MAXindex);
102         y0atc = atc(i,MINindex);
103         y0abc = abc(i,MINindex);
104         y1atc = atc(i,MAXindex);
105         y1abc = abc(i,MAXindex);
106         mat1atc1 = y0atc+(x-x0)*((y1atc-y0atc)/(x1-x0));
107         mat1abc1 = y0abc+(x-x0)*((y1abc-y0abc)/(x1-x0));
108     else
109         %If not find is not empty
110         mat1atc1 = atc1(Index);
111         mat1abc1 = abc1(Index);
112     end
113   atc1calcvalue = d1*mat1atc1;
114   abc1calcvalue = d1*mat1abc1;
115   tpabs = atc1calcvalue+abc1calcvalue;
116   mcorecount = 0; %count number of core materials
117     %Gather Core Materials
118     if material1 ~= ""
119         [d(1),m(1),e(1,:),atc(1,:),abc(1,:)] = ...
              collectxraydata(material1);
120         mcorecount = mcorecount + 1;
121     end
122
123     if material2 ~= ""
124         [d(2),m(2),e(2,:),atc(2,:),abc(2,:)] = ...
              collectxraydata(material2);
125         mcorecount = mcorecount + 1;
126     end
127
128     if material3 ~= ""
129         [d(3),m(3),e(3,:),atc(3,:),abc(3,:)] = ...
              collectxraydata(material3);
130         mcorecount = mcorecount + 1;
131     end
132
133     if material4 ~= ""
134         [d(4),m(4),e(4,:),atc(4,:),abc(4,:)] = ...
              collectxraydata(material4);
135         mcorecount = mcorecount + 1;
136     end
137
```

```
138     shellcount = 0; %count number of shells
139     %Shell Layer #1 (Compound)
140     if shell1m1 ~= ""
141         [ds(1),ms(1),es(1,:),atcs(1,:),abcs(1,:)] = ...
142             collectxraydata(shell1m1);
143         [ds(2),ms(2),es(2,:),atcs(2,:),abcs(2,:)] = ...
144             collectxraydata(shell1m2);
145         shellcount = shellcount + 1;
146     end
147
148     %Shell Layer #2 (Compound)
149     if shell2m1 ~= ""
150         [ds(3),ms(3),es(3,:),atcs(3,:),abcs(3,:)] = ...
151             collectxraydata(shell2m1);
152         [ds(4),ms(4),es(4,:),atcs(4,:),abcs(4,:)] = ...
153             collectxraydata(shell2m2);
154         shellcount = shellcount + 1;
155     end
156
157     %Shell Layer #3 (Compound)
158     if shell3m1 ~= ""
159         [ds(5),ms(5),es(5,:),atcs(5,:),abcs(5,:)] = ...
160             collectxraydata(shell3m1);
161         [ds(6),ms(6),es(6,:),atcs(6,:),abcs(6,:)] = ...
162             collectxraydata(shell3m2);
163         shellcount = shellcount + 1;
164     end
165
166     %Collect material 1 data
167     for i = 1:1:mcorecount
168         Index = find(e(i,:) == incidentxrayenergy);
169         if isempty(Index)
170             x = incidentxrayenergy;
171             MINindex = max(find(e(i) < incidentxrayenergy));
172             x0 = e(i,MINindex);
173             MAXindex = min(find(e(i)>incidentxrayenergy));
174             x1 = e(i,MAXindex);
175
176             %Linear Interpolation
177             y0atc = atc(i,MINindex);
178             y0abc = abc(i,MINindex);
179             y1atc = atc(i,MAXindex);
180             y1abc = abc(i,MAXindex);
181             mat1atc(i) = y0atc+(x-x0)*((y1atc-y0atc)/(x1-x0));
182             mat1abc(i) = y0abc+(x-x0)*((y1abc-y0abc)/(x1-x0));
183         else
184             %If not find is not empty
185             mat1atc(i) = atc(i,Index);
186             mat1abc(i) = abc(i,Index);
187         end
188
189         %If material count > 1, then calculate mass percentages
```

```
190         atccalcvalue(i) = d(i)*mat1atc(i);
191         abccalcvalue(i) = d(i)*mat1abc(i);
192         %totalatcvalue(i) = atccalcvalue(i);
193     end
194     %For 1 material core
195     totalabcvalue = atccalcvalue(1)+abccalcvalue(1);
196     if mcorecount == 2
197         masspercent1 = ...
                (m(1)*amountm1)/((m(1)*amountm1)+(m(2)*amountm2));
198         masspercent2 = ...
                (m(2)*amountm2)/((m(1)*amountm1)+(m(2)*amountm2));
199         atccalcvalue(1) = d(1)*mat1atc(1)*masspercent1;
200         abccalcvalue(1) = d(1)*mat1abc(1)*masspercent1;
201         atccalcvalue(2) = d(2)*mat1atc(2)*masspercent2;
202         abccalcvalue(2) = d(2)*mat1abc(2)*masspercent2;
203         totalabcvalue = atccalcvalue(1)+abccalcvalue(1);
204         totalabcvalue = atccalcvalue(2) + abccalcvalue(2)+ ...
                totalabcvalue;
205     elseif mcorecount == 3
206         masspercent1 = (m(1)*amountm1)/((m(1)*amountm1)+...
207             (m(2)*amountm2)+(m(3)*amountm3));
208         masspercent2 = (m(2)*amountm2)/((m(1)*amountm1)+...
209             (m(2)*amountm2)+(m(3)*amountm3));
210         masspercent3 = (m(3)*amountm3)/((m(1)*amountm1)+...
211             (m(2)*amountm2)+(m(3)*amountm3));
212         atccalcvalue(1) = d(1)*mat1atc(1)*masspercent1;
213         abccalcvalue(1) = d(1)*mat1abc(1)*masspercent1;
214         atccalcvalue(2) = d(2)*mat1atc(2)*masspercent2;
215         abccalcvalue(2) = d(2)*mat1abc(2)*masspercent2;
216         atccalcvalue(3) = d(3)*mat1atc(3)*masspercent3;
217         abccalcvalue(3) = d(3)*mat1abc(3)*masspercent3;
218             totalabcvalue = atccalcvalue(1)+abccalcvalue(1);
219            totalabcvalue = atccalcvalue(2) + abccalcvalue(2)+ ...
220                totalabcvalue;
221           totalabcvalue = atccalcvalue(3) + abccalcvalue(3) + ...
222               totalabcvalue;
223     elseif mcorecount == 4
224         masspercent1 = (m(1)*amountm1)/((m(1)*amountm1)+...
225             (m(2)*amountm2)+(m(3)*amountm3)+(m(4)*amountm4));
226         masspercent2 = (m(2)*amountm2)/((m(1)*amountm1)+...
227             (m(2)*amountm2)+(m(3)*amountm3)+(m(4)*amountm4));
228         masspercent3 = (m(3)*amountm3)/((m(1)*amountm1)+...
229             (m(2)*amountm2)+(m(3)*amountm3)+(m(4)*amountm4));
230         masspercent4 = (m(4)*amountm4)/((m(1)*amountm1)+...
231             (m(2)*amountm2)+(m(3)*amountm3)+(m(4)*amountm4));
232         atccalcvalue(1) = d(1)*mat1atc(1)*masspercent1;
233         abccalcvalue(1) = d(1)*mat1abc(1)*masspercent1;
234         atccalcvalue(2) = d(2)*mat1atc(2)*masspercent2;
235         abccalcvalue(2) = d(2)*mat1abc(2)*masspercent2;
236         atccalcvalue(3) = d(3)*mat1atc(3)*masspercent3;
237         abccalcvalue(3) = d(3)*mat1abc(3)*masspercent3;
238         atccalcvalue(4) = d(4)*mat1atc(4)*masspercent4;
```

```
239         abccalcvalue(4) = d(4)*mat1abc(4)*masspercent4;
240             totalabcvalue = atccalcvalue(1)+abccalcvalue(1);
241             totalabcvalue = atccalcvalue(2) + abccalcvalue(2) + ...
242                 totalabcvalue;
243             totalabcvalue = atccalcvalue(3) + abccalcvalue(3)+ ...
244                 totalabcvalue;
245            totalabcvalue = atccalcvalue(4) + abccalcvalue(4) + ...
246                totalabcvalue;
247     end
248     %Calculate Shell Material
249     if shellcount > 0
250         for i = 1:1:(shellcount*2)
251             Index = find(es(i,:) == incidentxrayenergy);
252             if isempty(Index)
253                 x = incidentxrayenergy;
254                 MINindex = max(find(es(i) < incidentxrayenergy));
255                 x0 = es(i,MINindex);
256                 MAXindex = min(find(es(i)>incidentxrayenergy));
257                 x1 = es(i,MAXindex);
258                 %Linear Interpolation
259                 y0atc = atcs(i,MINindex);
260                 y0abc = abcs(i,MINindex);
261                 y1atc = atcs(i,MAXindex);
262                 y1abc = abcs(i,MAXindex);
263                 mat1atcs(i) = y0atc+(x-x0)*((y1atc-y0atc)/(x1-x0));
264                 mat1abcs(i) = y0abc+(x-x0)*((y1abc-y0abc)/(x1-x0));
265             else
266                 %If not find is not empty
267                 mat1atcs(i) = atcs(i,Index);
268                 mat1abcs(i) = abcs(i,Index);
269             end
270             %If material count > 1, then calculate mass percentages
271             atccalcvalues(i) = ds(i)*mat1atcs(i);
272             abccalcvalues(i) = ds(i)*mat1abcs(i);
273         end
274     end
275     %Calculate Shell Parameters
276     if  shellcount > 0
277         %Gather Shell Material Data
278         masspercent1 = (ms(1)*amounts11)/((ms(1)*amounts11)+...
279             (ms(2)*amounts12));
280         masspercent2 = (ms(2)*amounts12)/((ms(1)*amounts11)+...
281             (ms(2)*amounts12));
282         atccalcvalues(1) = ds(1)*mat1atcs(1)*masspercent1;
283         abccalcvalues(1) = ds(1)*mat1abcs(1)*masspercent1;
284         atccalcvalues(2) = ds(2)*mat1atcs(2)*masspercent2;
285         abccalcvalues(2) = ds(2)*mat1abcs(2)*masspercent2;
286         if shellcount > 1
287             masspercent1 = (ms(3)*amounts21)/((ms(3)*amounts21)...
288                 +(ms(4)*amounts22));
289             masspercent2 = (ms(4)*amounts22)/((ms(3)*amounts21)...
290                 +(ms(4)*amounts22));
```

```
291             atccalcvalues(3) = ds(3)*mat1atcs(3)*masspercent1;
292             abccalcvalues(3) = ds(3)*mat1abcs(3)*masspercent1;
293             atccalcvalues(4) = ds(4)*mat1atcs(4)*masspercent2;
294             abccalcvalues(4) = ds(4)*mat1abcs(4)*masspercent2;
295             if shellcount > 2
296                 masspercent1 = (ms(5)*amounts31)/((ms(5)*amounts31)...
297                     +(ms(6)*amounts32));
298                 masspercent2 = (ms(6)*amounts32)/((ms(5)*amounts31)...
299                     +(ms(6)*amounts32));
300                 atccalcvalues(5) = ds(5)*mat1atcs(5)*masspercent1;
301                 abccalcvalues(5) = ds(5)*mat1abcs(5)*masspercent1;
302                 atccalcvalues(6) = ds(6)*mat1atcs(6)*masspercent2;
303                 abccalcvalues(6) = ds(6)*mat1abcs(6)*masspercent2;
304             end
305         end
306         %Calculate Shell Proportions
307         shell1volume = 0;
308         shell2volume = 0;
309         shell3volume = 0;
310         %Calculate Core Volume
311         corevolume = (4/3)*pi*(corediameter/2)^3; %nm^3
312         if shellcount > 0
313             shell1volume = (4/3)*pi*(shell1diameter/2)^3;
314             if shellcount > 1
315                 shell2volume = (4/3)*pi*(shell2diameter/2)^3;
316                 if shellcount > 2
317                     shell3volume = (4/3)*pi*(shell3diameter/2)^3;
318                 end
319             end
320         end
321         %Core volume material percentage over shell volume material
322         corevolumepercent = corevolume /(corevolume+shell1volume+...
323             shell2volume+shell3volume);
324         %Shell 1 volume material percentage over core volume material
325         shell1volumepercent = shell1volume /(corevolume+shell1volume+...
326             shell2volume+shell3volume);
327         %Shell 2 volume material percentage over core volume material
328         shell2volumepercent = shell2volume /(corevolume+shell1volume+...
329             shell2volume+shell3volume);
330         %Shell 3 volume material percentage over core volume material
331         shell3volumepercent = shell3volume /(corevolume+shell1volume+...
332             shell2volume+shell3volume);
333         %Load Shell Values into Voxel
334         %Shell 1
335         if shellcount > 0
336
337                 ts1abs = atccalcvalues(1)+abccalcvalues(1);
338
339                 ts1abs = atccalcvalues(2) + abccalcvalues(2) + ts1abs;
340
341             if shellcount > 1
342             %Shell 2
```

```
343                     ts2abs = atccalcvalues(3)+abccalcvalues(3);
344                     ts2abs = atccalcvalues(4) + abccalcvalues(4) + ...
                            ts2abs;
345                 if shellcount > 2
346                 %Shell 3
347                         ts3abs = atccalcvalues(5) + abccalcvalues(5);
348                         ts3abs = atccalcvalues(6) + abccalcvalues(6) ...
                                +...
349                             ts3abs;
350                 end
351             end
352         end
353     else
354         %No shell
355     end
356     %Load Core Values into Voxels
357     tcatc = totalabcvalue;
358     tcabs = totalabcvalue;
359     ND = 0;
360     COREVALUES = 0;
361     [CAVGTRANSMITTED,SL,POC,COREVALUES] = QDXvoxelize(gridSize,tpabs,...
362         tpabs,tcatc,tcabs,ts1atc,ts1abs,ts2atc,ts2abs,...
363         ts3atc,ts3abs,corediameter,shell1diameter,shell2diameter,...
364         shell3diameter,loadingdensity,incidentxrayenergy);
365
366     %Diameter of Hole in nm: 1.27e+7
367     ParticlesNumber = round((pi*(22E3/2)^2)/(SL^2),0);
368     TotalCounts = 0;
369     tic
370     for loop = 1:1:ParticlesNumber
371         [POC] = photoncount(gridSize,quantumefficiency,COREVALUES);
372         TotalCounts = POC + TotalCounts;
373     end
374     toc
375     FPOC(1,projectTask) = (TotalCounts/ParticlesNumber)*100; %QE
376     PN(1,projectTask) = ParticlesNumber;
377     TC(1,projectTask) = TotalCounts;
378     FPOC(projectTask)
379 end
```

Z.10 Create 3D Quantum Dot Geometry

```
%Created By: 2d Lt Michael Sherburne
%Date Created: 11/25/2019
%Description: Voxelization function that takes information from ...
   materials
%and assumes a homogeneous distribution of incident x-ray flux into
%quantum dot to determine total x-ray attenuation going through a single
%quantum dot suspended in a polymer. This does not take into ...
   consideration
%scattering effects in its present form.
function [CUBEAvgTransmitted,SideLength,PhotonOpticCount,COREVALUES]...
    = QDXvoxelize(gridSize,tpatc,tpabs,...
     tcatc,tcabs,...
     ts1atc,ts1abs,...
     ts2atc,ts2abs,...
     ts3atc,ts3abs,...
     corediameter,shell1diameter,shell2diameter,shell3diameter,...
     loadingdensity,incidentxrayenergy)
    %Code
    OuterShellDiameterArray = [corediameter,shell1diameter,...
    shell2diameter,shell3diameter];
    OuterShellDiameter = sum(OuterShellDiameterArray); %take largest
    %diameter to determine loading
    SideLength = ...
       geometryfunction(OuterShellDiameter,loadingdensity); %nm
    %Check OuterShellDiameterArray = 1, means coreo only, = 2
    %core-shell, etc.
    [~,sizeDArray] = size(OuterShellDiameterArray);
    if sizeDArray > 0
        Core = corediameter/SideLength;
        if sizeDArray > 1
            Shell1 = (shell1diameter+corediameter)/SideLength;
            if sizeDArray > 2
                Shell2 = (shell2diameter+shell1diameter+corediameter)...
                    /SideLength;
                if sizeDArray > 3
                    Shell3 = (shell3diameter+shell2diameter+...
                        shell1diameter+corediameter)/SideLength;
                end
            end
        end
    end
    %In Nanometers
    Rx = SideLength;
    Ry = SideLength;
    Rz = SideLength;
    %The number 100 means 100 grids across entire cube, not radius
    [X,Y,Z] = ndgrid(linspace(-Rx,Rx,gridSize),...
        linspace(-Ry,Ry,gridSize),linspace(-Rz,Rz,gridSize));
    R = sqrt((X/Rx).^2 + (Y/Ry).^2 + (Z/Rz).^2);
```

```
47      seg = zeros(size(X));
48      %Create 3D Model
49      if sizeDArray > 3
50          seg(R <= Shell3) = 4;
51      end
52      if sizeDArray > 2
53          seg(R <= Shell2) = 3;
54      end
55      if sizeDArray > 1
56          seg(R <= Shell1) = 2;
57      end
58      if sizeDArray > 0
59          seg(R <= Core) = 1;
60      end
61      %shading interp
62      TotalModelHeight = SideLength*2; %For Sphere, all directions the ...
           same
63      HeightPerStep = (TotalModelHeight/gridSize); %200 grid points from
64      %top to bottom (nm)
65      HeightPerStepCM = HeightPerStep*1E-7; %Convert nm to cm
66      %Ydata
67      if sizeDArray > 3
68          SHELL3atten = zeros(gridSize,gridSize,gridSize);
69          SHELL3abs = zeros(gridSize,gridSize,gridSize);
70      end
71      if  sizeDArray > 2
72          SHELL2atten = zeros(gridSize,gridSize,gridSize);
73          SHELL2abs = zeros(gridSize,gridSize,gridSize);
74      end
75      if  sizeDArray > 1
76          SHELL1atten = zeros(gridSize,gridSize,gridSize);
77          SHELL1abs = zeros(gridSize,gridSize,gridSize);
78      end
79      if sizeDArray > 0
80          COREatten = zeros(gridSize,gridSize,gridSize);
81          COREabs = zeros(gridSize,gridSize,gridSize);
82      end
83      %Create probability for both absorption and scattering chart
84      parfor s = 1:1:gridSize %slice step
85          par1 = zeros(gridSize,gridSize);
86          par2 = zeros(gridSize,gridSize);
87          par3 = zeros(gridSize,gridSize);
88          par4 = zeros(gridSize,gridSize);
89          par5 = zeros(gridSize,gridSize);
90          par6 = zeros(gridSize,gridSize);
91          par7 = zeros(gridSize,gridSize);
92          par8 = zeros(gridSize,gridSize);
93          par9 = zeros(gridSize,gridSize);
94          par10 = zeros(gridSize,gridSize);
95
96          %Move slice incrementally from one end to the other
97          StepSlice = ((-1*SideLength)+HeightPerStep*(s-1));
```

```
98          sdata = slice(Y,X,Z,seg,StepSlice,0,0);
99          for i = 1:1:gridSize  %i data goes from -Y to +Y
100             for j = 1:1:gridSize %j data goes from -X to +X
101                 material = sdata(1).CData(i,j);
102                 if material == 0 %PMMA (find transmission
103                     par1(i,j) = exp(-tpatc*HeightPerStepCM); ...
                        %attenuation
104                     par2(i,j) = exp(-tpabs*HeightPerStepCM); %absorption
105                     %of PMMA
106                 elseif material == 1 %Core
107                     par3(i,j) = exp(-tcatc*HeightPerStepCM); ...
                        %attenuation
108                     par4(i,j) = exp(-tcabs*HeightPerStepCM); %absorption
109                 elseif material == 2 %Shell 1
110                     par5(i,j) = exp(-ts1atc*HeightPerStepCM); ...
                        %attenuation
111                     par6(i,j) = exp(-ts1abs*HeightPerStepCM);  ...
                        %absorption
112                 elseif material == 3 %Shell 2
113                     par7(i,j) = exp(-ts2atc*HeightPerStepCM); ...
                        %attenuation
114                     par8(i,j) = exp(-ts2abs*HeightPerStepCM);  ...
                        %absorption
115                 elseif material == 4 %Shell 3
116                     par9(i,j) = exp(-ts3atc*HeightPerStepCM); ...
                        %attenuation
117                     par10(i,j) = exp(-ts3abs*HeightPerStepCM);  ...
                        %absorption
118                 end
119             end
120         end
121         PMMAatc(s,:,:) = par1;
122         PMMAabs(s,:,:) = par2;
123         COREatten(s,:,:) = par3;
124         COREabs(s,:,:) = par4;
125         SHELLatten1(s,:,:) = par5;
126         SHELLabs1(s,:,:) = par6;
127         SHELLatten2(s,:,:) = par7;
128         SHELLabs2(s,:,:) = par8;
129         SHELLatten3(s,:,:) = par9;
130         SHELLabs3(s,:,:) = par10;
131     end
132     if sizeDArray == 1
133         COREVALUES = COREabs;
134     elseif sizeDArray == 2
135         for i = 1:1:gridSize
136             for j = 1:1:gridSize
137                 for k = 1:1:gridSize
138                     COREVALUES(i,j,k) = COREabs(i,j,k)+SHELLabs1(i,j,k);
139                 end
140             end
141         end
```

```
142     elseif sizeDArray == 3
143         for i = 1:1:gridSize
144             for j = 1:1:gridSize
145                 for k = 1:1:gridSize
146                     COREVALUES(i,j,k) = ...
                            COREabs(i,j,k)+SHELLabs1(i,j,k)...
147                          +SHELLabs2(i,j,k);
148                 end
149             end
150         end
151     elseif sizeDArray == 4
152         for i = 1:1:gridSize
153             for j = 1:1:gridSize
154                 for k = 1:1:gridSize
155                     COREVALUES(i,j,k) = ...
                            COREabs(i,j,k)+SHELLabs1(i,j,k)...
156                          +SHELLabs2(i,j,k)+SHELLabs3(i,j,k);
157                 end
158             end
159         end
160     end
161     %PMMA Screen (Need to Do This By Itself to Seperate Out Absorption)
162     s = 1;
163     i = 1;
164     j = 1;
165     PMMAscreenCOM = ones(gridSize,gridSize);
166     PMMAscreenABS = ones(gridSize,gridSize);
167     %s and j values form the screen at backend
168     for s = 1:1:gridSize
169         for j = 1:1:gridSize
170             for i = 1:1:gridSize
171                 %Compton Scattering Case
172                 if PMMAatc(s,i,j)~= 0
173                     PMMAscreenCOM(s,j) = ...
                            PMMAscreenCOM(s,j)*PMMAatc(s,i,j);
174                 end
175                 %Photoelectric Absorption Case
176                 if PMMAabs(s,i,j) ~= 0
177                     PMMAscreenABS(s,j) = ...
                            PMMAscreenABS(s,j)*PMMAabs(s,i,j);
178                 end
179             end
180         end
181     end
182     PMMAscreenCOM2 =  PMMAscreenCOM;
183     PMMAscreenABS2 =  PMMAscreenABS;
184     PMMAscreenCOM2(PMMAscreenCOM2 == 1) = 0;
185     PMMAscreenABS2(PMMAscreenABS2 == 1) = 0;
186     xvalues = 1:1:gridSize;
187     yvalues = 1:1:gridSize;
188
189     if sizeDArray > 3
```

```
190         SHELLscreen3COM = ones(gridSize,gridSize);
191         SHELLscreen3ABS = ones(gridSize,gridSize);
192     end
193
194     if  sizeDArray > 2
195         SHELLscreen2COM = ones(gridSize,gridSize);
196         SHELLscreen2ABS = ones(gridSize,gridSize);
197     end
198
199     if  sizeDArray > 1
200         SHELLscreen1COM = ones(gridSize,gridSize);
201         SHELLscreen1ABS = ones(gridSize,gridSize);
202     end
203
204     if sizeDArray > 0
205         COREscreenCOM = ones(gridSize,gridSize);
206         COREscreenABS = ones(gridSize,gridSize);
207     end
208     %Shell Screen
209     s = 1;
210     i = 1;
211     j = 1;
212     %s and j values form the screen at backend
213     for s = 1:1:gridSize
214         for j = 1:1:gridSize
215             for i = 1:1:gridSize
216                 if sizeDArray > 3
217                     if SHELLatten3(s,i,j)~= 0
218                         SHELLscreen3COM(s,j) = SHELLscreen3COM(s,j)*...
219                             SHELLatten3(s,i,j);
220                     end
221                 if SHELLabs3(s,i,j)~=0
222                     SHELLscreen3ABS(s,j) = SHELLscreen3ABS(s,j)*...
223                         SHELLabs3(s,i,j);
224                 end
225             end
226
227             if  sizeDArray > 2
228                 if SHELLatten2(s,i,j)~= 0
229                     SHELLscreen2COM(s,j) = SHELLscreen2COM(s,j)*...
230                         SHELLatten2(s,i,j);
231                 end
232
233                 if SHELLabs2(s,i,j)~=0
234                     SHELLscreen2ABS(s,j) = SHELLscreen2ABS(s,j)*...
235                         SHELLabs2(s,i,j);
236                 end
237             end
238
239             if  sizeDArray > 1
240                 if SHELLatten1(s,i,j)~= 0
241                     SHELLscreen1COM(s,j) = SHELLscreen1COM(s,j)*...
```

```
                        SHELLatten1(s,i,j);
                end

                if SHELLabs1(s,i,j)~=0
                    SHELLscreen1ABS(s,j) = SHELLscreen1ABS(s,j)*...
                        SHELLabs1(s,i,j);
                end
            end

            if sizeDArray > 0
                 if COREatten(s,i,j)~= 0
                     COREscreenCOM(s,j) = COREscreenCOM(s,j)*...
                         COREatten(s,i,j);
                end

                if COREabs(s,i,j)~=0
                     COREscreenABS(s,j) = COREscreenABS(s,j)*...
                         COREabs(s,i,j);
                end
            end

        end
    end
end
%Take All 2D Slices and Combine Values by Multiplying Probabilities
if sizeDArray == 4
    TotalABS = COREscreenABS.*SHELLscreen1ABS.*SHELLscreen2ABS.*...
        SHELLscreen3ABS;
end

if  sizeDArray == 3
    TotalABS = COREscreenABS.*SHELLscreen1ABS.*SHELLscreen2ABS;
end

if  sizeDArray == 2
    TotalABS = COREscreenABS.*SHELLscreen1ABS;
end
if sizeDArray == 1
    TotalABS = COREscreenABS;
end
%What % of x-rays still transmit through the voxel cube of polymer ...
   and dot
CUBEAvgTransmitted = sum(sum(TotalABS.*PMMAscreenABS2))/(gridSize^2);
PhotonOpticCount = 0;
end
%References
%https://www.mathworks.com/matlabcentral/answers/
%58885-creating-a-spherical-matrix
```

Z.11 Monte Carlo Function for Monolayer X-ray Code

```
%Created By: 2d Lt Michael Sherburne
%Date Created: 11/25/2019
%Calculate Number of Photons from Probability
function [PhotonOpticCount] = photoncount(gridSize,QE,COREVALUES)
    QE = QE/100; %quanutm efficiency %
    PhotonCount = 0;
    PhotonCount2 = 0;
    PhotonTest = 1-COREVALUES;
    PhotonTest(find(PhotonTest == 1)) = 0;
    PhotonTest = PhotonTest-rand(gridSize,gridSize,gridSize);
    [PhotonCount,~] = size(PhotonTest(PhotonTest>=0));
    if PhotonCount > 0
        randNUM = QE-rand(1,PhotonCount);
        [PhotonCount2,~] = size(randNUM(randNUM>=0));
    end
    %Pick Direction for Photon To Go (Assume Isotropic)
    %Six Main Directions (Use #1 for facing towards optics)
    PhotonOpticCount = 0;
    if PhotonCount2 > 0
        randNUM = 0.1667-rand(1,PhotonCount2);
        [PhotonOpticCount,~] = size(randNUM(randNUM>=0));
    end
end
```

Z.12 Geometry Function for X-ray Voxel Codes

```
%Created By: 2d Lt Michael Sherburne
%Date: 3/28/2019
%Quantum Dot Geometry Function
%Input: diameter of quantum dot
%Outputs:
function [SL] = geometryfunction(d,LD) %diameter in cm
    r = d/2; %nm
    Vsphere = (4/3)*pi*r^3; %nm^3
    Vcube = Vsphere/LD; %nm^3
    SL = Vcube^(1/3); %nm (length of one side of cube boundary)
end
```

Z.13 PL Decay Plotter Code

```
%Created By: 2d Lt Michael Sherburne
%Date: 1/16/2020
%Description: Biexponential Model for UV-Vis PL Decay
clc
clear
set(0, 'DefaultLineLineWidth' ,0.5)
set(0, 'DefaultLineMarkerSize' ,40)
set(0, 'DefaultAxesFontSize' ,40)
set(0, 'DefaultFigureColor' ,[1,1,1])
set(0, 'DefaultTextFontSize' ,40)
set(0, 'DefaultTextInterpreter' , 'latex' )
set(0, 'DefaultTextFontName' , 'Arial' ) %Times-Roman')
set(0, 'DefaultAxesFontName' , 'Arial' ) %Times-Roman')
MarkerSize = 800;
MarkerTransparency = .4;
FONTSIZE = 22;
LABEL_FONTSIZE = 26;
filename = 'UVVisDecayMaster.xlsx';
t = 0.5:.001:150; %Set Time Range in Nanoseconds
t = t.*10^(-9);
t0 = 0;
F0 = 0;
step = 1;
for i = 1:30
    matlNum = i; %Select material to import
    [~,Structure(step)]  = xlsread(filename,...
        int2str(matlNum),'D1'); %Material Name
    [~,Material(step)]  = xlsread(filename,...
        int2str(matlNum),'B1') %Material Name
    Concentration(step)  = xlsread(filename,...
        int2str(matlNum),'D2'); %Concentration of Material
    if string(Structure(step)) == '3D' || string(Structure(step)) == ...
       '3D2'
        Thickness(step)  = xlsread(filename,...
            int2str(matlNum),'D3'); %Concentration of Material
    end
    PreExp1(step) = xlsread(filename,int2str(matlNum),'A7');
    tau1(step) = xlsread(filename,int2str(matlNum),'B7')*1E-9;
    PreExp2(step) = xlsread(filename,int2str(matlNum),'C7');
    tau2(step) = xlsread(filename,int2str(matlNum),'D7')*1E-9;
    PreExp3(step) = xlsread(filename,int2str(matlNum),'E7');
    tau3(step) = xlsread(filename,int2str(matlNum),'F7')*1E-9;
    PreExp4(step) = xlsread(filename,int2str(matlNum),'G7');
    tau4(step) = xlsread(filename,int2str(matlNum),'H7')*1E-9;
    step = step + 1;
end
fig1 = figure
maxElements = step-1; %collect number of materials collected in this set
LEG = strings(1,maxElements);
```

```
count = 1;
%Create A Large Color Palette for Plots
C1 = [0 0.4470 0.7410];
C2 = [0.8500 0.3250 0.0980];
C3 = [0.9290 0.6940 0.1250];
C4 = [0.4940 0.1840 0.5560];
C5 = [0.4660 0.6740 0.1880];
C6 = [0.3010 0.7450 0.9330];
C7 = [0.6350 0.0780 0.1840];
C8 = [0 0.4470 0.4410];
C9 = [0.8500 0.1250 0.0980];
C10 = [0.9290 0.4940 0.1250];
C11 = [0.7940 0.1840 0.5560];
C12 = [0.1660 0.5740 0.3880];
line_color = [C1; C2; C3; C4; C5; C6; C7; C8; C9; C10; C11; C12];
for i = 1:1:maxElements
    if (string(Structure(i)) == "Polymer") %Check to ensure desired
        %scintillators are loaded
        F = F0+PreExp1(i)*exp(-1*(t-t0)/tau1(i))+PreExp2(i)*exp(-1*...
            (t-t0)/tau2(i))+PreExp3(i)*exp(-1*(t-t0)...
            /tau3(i))+PreExp4(i)*exp(-1*(t-t0)/tau4(i));
        vq1 = F/max(F);
        semilogx(t/1E-9,vq1,'LineWidth',2,'Color',line_color(count,:))
        ylim([0 1])
        xlabel('Time (ns)')
        ylabel('Intensity (normalized)')
        %Calculate Time to Half Amplitude
        LOC = find(vq1 > 0.4999 & vq1 < 0.8);
        halftime(count) = t(LOC(1))/1E-9;
        grid on
        hAx=gca;
        set(hAx,'xminorgrid','on','yminorgrid','on')
        hold on
        %Populate Legend
        if string(Structure(i)) == 'Quartz'
            LEG(count) = strcat(string(Material(i)),{' '},...
                string(Concentration(i)),'uL');
        elseif string(Structure(i)) == 'Polymer'
            LEG(count) = strcat(string(Material(i)));
        else
            LEG(count) = strcat(string(Material(i)),...
                {' '},string(Concentration(i)),'uL',{' '},...
                string(Thickness(i)),'um');
        end
        count = count + 1;
    end
end
%Add Legend of Used Data
tl = legend(LEG)
set(tl,'Interpreter','none')
hold off
table(LEG',halftime')
```

Z.14 Stress-Strain Yield Point Plotter Code

```
%Created By: Major John Brewer
%%Reading in raw load and displacement
clc
tic
Test1_load=xlsread('Qdots.xlsx','Test1','C6:C100000');
Test1_disp=xlsread('Qdots.xlsx','Test1','b6:b100000');
Test2_load=xlsread('Qdots.xlsx','Test2','C6:C100000');
Test2_disp=xlsread('Qdots.xlsx','Test2','b6:b100000');
Test3_load=xlsread('Qdots.xlsx','Test3','C6:C100000');
Test3_disp=xlsread('Qdots.xlsx','Test3','b6:b100000');
toc
%% Smoothing Test 2 Data
Test2_load_smooth=SmoothData(Test2_load',100);
Test2_disp_smooth=SmoothData(Test2_disp',100);
Test3_load_smooth=SmoothData(Test3_load',100);
Test3_disp_smooth=SmoothData(Test3_disp',100);

%%  Converting to Stresses and Strains
% Inputs
width=0.5*25.4;  % specimen width (inches to mm)
thick=.004*25.4;  % speciment thickness(inches to mm)
gauge_length=3.28*25.4;  % length of the narrow portion of the
%specimen (inches to mm)
% Calculations
Area=width*thick;
Test1_stress=Test1_load/Area;
Test1_strain=Test1_disp/gauge_length;
Test2_stress=Test2_load/Area;
Test2_strain=Test2_disp/gauge_length;
Test2_stress_smooth=Test2_load_smooth/Area;
Test2_strain_smooth=Test2_disp_smooth/gauge_length;
Test3_stress=Test3_load/Area;
Test3_strain=Test3_disp/gauge_length;
Test3_stress_smooth=Test3_load_smooth/Area;
Test3_strain_smooth=Test3_disp_smooth/gauge_length;
%% Plotting All load-disp
figure (1)
plot (Test1_disp,Test1_load,'r')
hold on
plot (Test2_disp_smooth,Test2_load_smooth,'g')
plot (Test3_disp_smooth,Test3_load_smooth,'b')
grid on
xlabel('Displacement (mm)')
ylabel('Load(N)')
legend('Test1','Test2','Test3','location','southeast')
title 'Load v Displacement'
x0=5;
y0=5;
width=800;
```

```
height=500;
set(gcf,'position',[x0,y0,width,height])
%% Plotting All stress-strain
figure (2)
plot (Test1_strain,Test1_stress,'r')
hold on
plot (Test2_strain_smooth,Test2_stress_smooth,'g')
plot (Test3_strain_smooth,Test3_stress_smooth,'b')
grid on
xlabel('Strain')
ylabel('Stress (MPa)')
legend('Test1','Test2','Test3','location','southeast')
title 'Stress v Strain'
x0=200;
y0=100;
width=800;
height=500;
set(gcf,'position',[x0,y0,width,height])
%% Test1 Calculations
clc
disp Test1
low=260; %300 MPa Point
hi=402;%600 MPa Point
figure (3)
offset=.002;
low_strain=Test1_strain(low);
hi_strain=Test1_strain(hi);
low_stress=Test1_stress(low);
hi_stress=Test1_stress(hi);
slope=(hi_stress-low_stress)/(hi_strain-low_strain)
intercept=low_stress-(slope*low_strain);
correction=-(intercept)/slope
yield=[.015823 1118.505];
pt2_1=((1500-intercept)/slope);
pt1=[correction,0];
pt2=[ pt2_1 1500];
% Plotting raw
plot(Test1_strain,Test1_stress,'r--')
hold on
grid on
%plotting line
plot([low_strain hi_strain],[low_stress hi_stress],'g*','markersize',15)
plot([pt1(1) pt2(1)],[pt1(2) pt2(2)],'g--')
% plotting corrected
plot(Test1_strain-correction,Test1_stress,'r.-')
 plot([pt1(1)-correction pt2(1)-correction],[pt1(2) pt2(2)],'g')
 % ploting yield
 plot([pt1(1)+offset-correction pt2(1)+offset-correction],[pt1(2) ...
    pt2(2)],'b')
 plot(yield(1),yield(2),'b*','markersize',15)
xlim([-.004,.04])
title('Test1 Calculations')
```

```
xlabel 'Strain'
ylabel 'Stress (MPa)'
legend ('Raw Data','Reference Points','Slope','Shifted Data',...
    'Shifted Slope','0.2% Offset','Yield','location','southeast')
x0=400;
y0=200;
width=800;
height=500;
set(gcf,'position',[x0,y0,width,height])
line1=[ 'Yield Stress: ' num2str(yield(2),4) ' MPa'];
line2=[ 'Yield Strain: ' num2str(yield(1),4)];
line3=[ 'Elastic Modulus: ' num2str(slope,4) ' MPa'];
annotation('textbox',[.35 .05 .2 .2],'string'...
    ,{line1, line2,line3}...
    ,'FitBoxToText','on','BackgroundColor','w');

%% Test2 Calculations
clc
disp Test2
low=1688;
hi=2828;
figure (4)
offset=.002;
low_strain=Test2_strain_smooth(low);
hi_strain=Test2_strain_smooth(hi);
low_stress=Test2_stress_smooth(low);
hi_stress=Test2_stress_smooth(hi);
slope=(hi_stress-low_stress)/(hi_strain-low_strain)
intercept=low_stress-(slope*low_strain);
correction=-(intercept)/slope
yield=[.012473 1055.0495];
pt2_1=((15e2-intercept)/slope);
pt1=[correction,0];
pt2=[ pt2_1 15e2];
% Plotting raw
plot(Test2_strain,Test2_stress,'c--','linewidth',2)
hold on
plot(Test2_strain_smooth,Test2_stress_smooth,'r--')
grid on
%plotting line
plot([low_strain hi_strain],[low_stress hi_stress],'g*','markersize',15)
plot([pt1(1) pt2(1)],[pt1(2) pt2(2)],'g--')
% plotting corrected
plot(Test2_strain_smooth-correction,Test2_stress_smooth,'r.-')
 plot([pt1(1)-correction pt2(1)-correction],[pt1(2) pt2(2)],'g')
 % plotting yield
 plot([pt1(1)+offset-correction pt2(1)+offset-correction],...
     [pt1(2) pt2(2)],'b')
 plot(yield(1),yield(2),'b*','markersize',15)
xlim([-.005,.04])
title('Test2 Calculations')
xlabel 'Strain'
```

```
ylabel 'Stress (MPa)'
legend ('Raw Data','Smoothed','Reference Points',...
    'Slope','Shifted Data','Shifted Slope','0.2% Offset','Yield',...
    'location','southeast')
x0=600;
y0=300;
width=800;
height=500;
set(gcf,'position',[x0,y0,width,height])

line1=[ 'Yield Stress: ' num2str(yield(2),4) ' MPa'];
line2=[ 'Yield Strain: ' num2str(yield(1),4)];
line3=[ 'Elastic Modulus: ' num2str(slope,4) ' MPa'];
annotation('textbox',[.35 .05 .2 .2],'string'...
    ,{line1, line2,line3}...
    ,'FitBoxToText','on','BackgroundColor','w');
%% Test3 Calculations
clc
disp Test3
low=2612;
hi=1491;
figure (5)
offset=.002;
low_strain=Test3_strain_smooth(low);
hi_strain=Test3_strain_smooth(hi);
low_stress=Test3_stress_smooth(low);
hi_stress=Test3_stress_smooth(hi);
slope=(hi_stress-low_stress)/(hi_strain-low_strain)
intercept=low_stress-(slope*low_strain);
correction=-(intercept)/slope
yield=[.012793 1104.116];
pt2_1=((15e2-intercept)/slope);
pt1=[correction,0];
pt2=[ pt2_1 15e2];
% Plotting raw
plot(Test3_strain,Test3_stress,'c--','linewidth',1.5)
hold on
plot(Test3_strain_smooth,Test3_stress_smooth,'r--')
grid on
%plotting line
plot([low_strain hi_strain],[low_stress hi_stress],'g*','markersize',15)
plot([pt1(1) pt2(1)],[pt1(2) pt2(2)],'g--')
% plotting corrected
plot(Test3_strain_smooth-correction,Test3_stress_smooth,'r.-')
 plot([pt1(1)-correction pt2(1)-correction],[pt1(2) pt2(2)],'g')
 % ploting yield
 plot([pt1(1)+offset-correction pt2(1)+offset-correction],...
     [pt1(2) pt2(2)],'b')
 plot(yield(1),yield(2),'b*','markersize',15)
xlim([-.005,.04])
title('Test3 Calculations')
xlabel 'Strain'
```

```
ylabel 'Stress (MPa)'
legend ('Raw Data','Smoothed','Reference Points','Slope',...
    'Shifted Data','Shifted Slope','0.2% Offset','Yield',...
    'location','southeast')
x0=800;
y0=400;
width=800;
height=500;
set(gcf,'position',[x0,y0,width,height])
line1=[ 'Yield Stress: ' num2str(yield(2),4) ' MPa'];
line2=[ 'Yield Strain: ' num2str(yield(1),4)];
line3=[ 'Elastic Modulus: ' num2str(slope,4) ' MPa'];
annotation('textbox',[.35 .05 .2 .2],'string'...
    ,{line1, line2,line3}...
    ,'FitBoxToText','on','BackgroundColor','w');
```

Z.15 Smoothing Function for Stress-Strain Yield Point Plotter Code

```
%Created By: Major Ronald Aung
function smoothed_data = SmoothData(original_data, smooth_window_size)

%% function smoothed_data = SmoothData(original_data, ...
    smooth_window_size)
%  INPUTS:
%    original_data     : 1xN data, (do not use Nx1)
%    smooth_window_size: the number of data points to be averaged.  Use
%                        integer value.
%  OUTPUT:
%    smoothed_data: 1xN data with rolling 'smooth_window_size' average.
data_size = length(original_data);
% Pad data so that the last few data points won't get averaged with the
% first data points.
original_data = [original_data, zeros(1,smooth_window_size*10)];
% Create a rolling average window function.
smooth_function = zeros(1, data_size+(smooth_window_size*10));
smooth_function(1:smooth_window_size) = 1/smooth_window_size;
% Smooth the data using Fast-Fourier-Transform method
smoothed_data = real(ifft(fft(original_data).*fft(smooth_function)));
% Remove the zero padding so that the return data has the same size ...
    as the
% original data.
smoothed_data = smoothed_data(1:data_size);
% Thanks to Maj Ron Aung AFIT PhD class 21s for writing this.
% He was too humble to put his own name on it.
end
```

Bibliography

1. Design and performance of a selectable-rate streak-camera deflection ramp generator. *LLE Review*, 85:21–28.

2. The sol-gel process. Online.

3. The theory of special relativity (ners 311). Online.

4. Microposit s1800 series photoresist. Technical report, Rohm and Haas, February 2006.

5. Guide to streak cameras. Technical report, Hamamatsu, 2008.

6. Streak camera tubes. techreport, Photek Limited, 26 Castleham Road, St Leonards on Sea, East Sussex, TN38 9NS, United Kingdom, October 2014.

7. History of quantum dots. Online, 2016.

8. History of the high speed camera, May 2016.

9. High-speed photography. Online, July 2017.

10. Photochron 5. Technical report, Photek Limited, April 2017.

11. Density of the elements. Online, 2018.

12. NNSE 618. Lecture contents. Lecture.

13. Ashraf Almahwasi. "does hadron therapy offer enough effectiveness in treating cancer to be worth the cost?". Master's thesis, University of Surrey, September 2011.

14. Yemliha Altıntas, Mohammad Younis Talpur, and Evren Mutlugun. The effect of ligand chain length on the optical properties of alloyed core-shell inpzns/zns quantum dots. *Journal of Alloys and Compounds*, 711:335–341, March 2017.

15. Jonatan Alvelid. Investigation of the photophysical properties of quantum dots for super-resolution imaging. Master's thesis, KTH Royal Institute of Technology, 2016.

16. D.L. Andrews. A unified theory of radiative and radiationless molecular energy transfer. *Chemical Physics*, 135(2):195–201, August 1989.

17. ARPANSA. Gamma radiation. Online.

18. J.C. Ashley, C.J. Tung, and R.H. Ritchie. Electron inelastic mean free paths and energy losses in solids. *Surface Science*, 81(2):409–426, March 1979.

19. Thi Huong Au, Stéphanie Buil, Xavier Quélin, Jean-Pierre Hermier, and Ngoc Diep Lai. Photostability and long-term preservation of a colloidal semiconductor-based single photon emitter in polymeric photonic structures. *Nanoscale Advances*, 1(8):3225–3231, 2019.

20. Wan Ki Bae, Lazaro A. Padilha, Young-Shin Park, Hunter McDaniel, Istvan Robel, Jeffrey M. Pietryga, and Victor I. Klimov. Controlled alloying of the core–shell interface in CdSe/CdS quantum dots for suppression of auger recombination. *ACS Nano*, 7(4):3411–3419, April 2013.

21. S.L. Baldochi and I.M. Ranieri. Alkali halide crystals: Growth. In *Encyclopedia of Materials: Science and Technology*, pages 74–78. Elsevier, 2001.

22. M G Bawendi, M L Steigerwald, and L E Brus. The quantum mechanics of larger semiconductor clusters ("quantum dots"). *Annual Review of Physical Chemistry*, 41(1):477–496, October 1990.

23. V.S. Belolipetski, P.B. Gornostaev, V.I. Lozovoi, and M. Ya. Schelev. 10 ps x-ray streak camera. In *28th International Congress on High-Speed Imaging and Photonics*, volume 7126, February 2009.

24. Herman Bergwerf. Molview v2.4. Online, 2015.

25. Ozdal Boyraz, Alan Tam, and Mikael Nilsson. Plastic scintillator enhancement through quantum dot. In Michael Fiederle, Arnold Burger, Larry Franks, Ralph B. James, and Stephen A. Payne, editors, *Hard X-Ray, Gamma-Ray, and Neutron Detector Physics XIX*. SPIE, August 2017.

26. Garnett W. Bryant, M. Zieliński, Natalia Malkova, James Sims, W. Jaskólski, and Javier Aizpurua. Effect of mechanical strain on the optical properties of quantum dots: Controlling exciton shape, orientation, and phase with a mechanical strain. *Physical Review Letters*, 105(6), August 2010.

27. Eric Burke, Phillip Williams, Stan Dehaven, Mool Gupta, and Dennis Waldron III. Scintillating quantum dots for imaging x-rays (sqdix) for aircraft inspection. Technical report, NASA LaRC Non-Destructive Sciences Branch, 2014.

28. Raffaela Busse. Characterisation of a photocathode for a monoenergetic electron source for the katrin experiment. Bachelors Thesis, Westfalische Wilhelms-Universitat Munster, 2014.

29. Mike Cate. Interview with mike cate. private communication, November 2018.

30. Celeroton. Motors. Online, 2018.

31. Hengky Chandrahalim. Lecture 10: Electrostatic mems. Lecture, February 2019.

32. Hengky Chandrahalim. Lecture 12: Electrical equivalent circuit. Lecture, February 2019.

33. Hengky Chandrahalim. Lecture 13: Q-factors, electrostatic sensing, thermal actuators. Lecture, March 2019.

34. Hengky Chandrahalim. Lecture 13: Q-factors, electrostatic sensing, thermal actuators. Lecture, March 2019.

35. Thomas G. Chasteen. Jablonski diagram. Online, 1995.

36. Cheng Cheng, Jiejie Li, and Xiaoyu Cheng. Photoluminescence lifetime and absorption spectrum of pbs nanocrystal quantum dots. *Journal of Luminescence*, 188:252–257, August 2017.

37. Sazzadur Chowdhury, M. Ahmadi, and Miller W. C. A comparison of pull-in voltage calculation methods for mems-based electrostatic actuator design. In *1st International Conference on Sensing Technology*, November 2005.

38. Jennifer Chu. Mit researchers 3-d print colloidal crystals. Online, August 2018.

39. Marcel S. Claro, Ido Levy, Abhinandan Gangopadhyay, David J. Smith, and Maria C. Tamargo. Self-assembled bismuth selenide (bi2se3) quantum dots grown by molecular beam epitaxy. *Scientific Reports*, 9(1), March 2019.

40. Robert M. Clegg. Chapter 1 förster resonance energy transfer—FRET what is it, why do it, and how it's done. In *Fret and Flim Techniques*, pages 1–57. Elsevier, 2009.

41. F. H. Combley and C. N. Booth. Nuclear physics phy303. Online, 1999.

42. CTS. Semiconductor and thin film etchants for microelectronic circuits. Online, 2015.

43. Alexander P Demchenko. Fluorescence detection techniques. In *Introduction to Fluorescence Sensing*, pages 65–118. Springer Netherlands, 2008.

44. Stephen Derenzo, Martin Boswell, Marvin Weber, and Kathleen Brennan. Scintillation properties. Online, February 2019.

45. Ali Eftekhari. Tungsten dichalcogenides (WS2, WSe2, and WTe2): materials chemistry and applications. *Journal of Materials Chemistry A*, 5(35):18299–18325, 2017.

46. D. Engelkemeir. Nonlinear response of NaI(tl) to photons. *Review of Scientific Instruments*, 27(8):589–591, August 1956.

47. Qianqian Fang and David A. Boas. Monte carlo simulation of photon migration in 3d turbid media accelerated by graphics processing units. *Optics Express*, 17(22):20178, oct 2009.

48. N. Fernández-Delgado, M. Herrera, A.H. Tavabi, M. Luysberg, R.E. Dunin-Borkowski, P.J. Rodriguez-Cantó, R. Abargues, J.P. Martínez-Pastor, and S.I. Molina. Structural and chemical characterization of CdSe-ZnS core-shell quantum dots. *Applied Surface Science*, 457:93–97, November 2018.

49. Mark Fox. *Optical Properties of Solids*. OXFORD UNIV PR, 2010.

50. J. Frenkel. On the transformation of light into heat in solids. i. *Physical Review*, 37(1):17–44, January 1931.

51. Girija Gaur, Dmitry S. Koktysh, Daniel M. Fleetwood, Robert A. Weller, Robert A. Reed, Bridget R. Rogers, and Sharon M. Weiss. Optical response of monolayer cdte/cds quantum dots to x-rays and gamma-rays. August 2015.

52. Gibin George, Shanell L. Jackson, Zariana R. Mobley, Bhoj R. Gautam, Dong Fang, Jinfang Peng, Duan Luo, Jianguo Wen, Jason E. Davis, Daryush Ila, and Zhiping Luo. Fast luminescence from rare-earth-codoped BaSiF6 nanowires with high aspect ratios. *Journal of Materials Chemistry C*, 6(27):7285–7294, 2018.

53. Joseph I. Goldstein, Dale E. Newbury, Joseph R. Michael, Nicholas W.M. Ritchie, John Henry J. Scott, and David C. Joy. *Scanning Electron Microscopy and X-Ray Microanalysis*, chapter 1, pages 2–4. Springer, 2018.

54. M.I. Golovei, M.Yu. Rigan, I.D. Olekseyuk, and Yu.V. Voroshilov. The system (cd3 as2)1-x (2cd se)x. *Inorganic Materials*, 9:1354–1356, 1973.

55. Nathan I. Hammer, Todd Emrick, and Michael D. Barnes. Quantum dots coordinated with conjugated organic ligands: new nanomaterials with novel photophysics. *Nanoscale Research Letters*, 2(6):282–290, June 2007.

56. Jordan Hanania, Kailyn Stenhouse, and Jason Donev. Band gap. Online, November 2015.

57. Lingze Duan Hemang Jani. Acid-free sol-gel fabrication of quantum-dot thin films for ultrafast nanophotonics research. In *2015 IEEE Photonics Conference (IPC)*, October 2015.

58. Robert Hofstadter. The detection of gamma-rays with thallium-activated sodium iodide crystals. *Physical Review*, 75(5):797–810, March 1949.

59. Jennifer Hollingsworth. Dr. jennifer hollingsworth interview. Interview, March 2019.

60. Syed Arshad Hussain. An introduction to fluorescence resonance energy transfer (fret). 2009.

61. S. Ithurria, M. D. Tessier, B. Mahler, R. P. S. M. Lobo, B. Dubertret, and Al. L. Efros. Colloidal nanoplatelets with two-dimensional electronic structure. *Nature Materials*, 10(12):936–941, October 2011.

62. John Jackson. *Classical Electrodynamics*, page 646–654. John Wiley & Sons, Inc., 1999.

63. Jian Tang Weihua Tang Jie Zhou, Yun Liu. Surface ligands engineering of semiconductor quantum dots for chemosensory and biological applications. *Materials Today*, 20(7), September 2017.

64. D. C. Joy and S. Luo. An empirical stopping power relationship for low-energy electrons. *Scanning*, 11(4):176–180, February 1989.

65. Hai-Ping Huang Fang-Feng Cheng Jun-Jie Zhu, Jing-Jing Li. Quantum dots for dna biosensing. *SpringerBriefs in Molecular Science*, 2013.

66. Poopathy Kathirgamanathan, Lisa M. Bushby, Muttulingam Kumaraverl, Seenivasagam Ravichandran, and Sivagnanasundram Surendrakumar. Electroluminescent organic and quantum dot LEDs: The state of the art. *Journal of Display Technology*, 11(5):480–493, May 2015.

67. Sunghwan Kim and Youl-Hun Seoung. Fabrication and characterization of 3d printed polyvinyl toluene based plastic scintillator. *Journal of the Korean Physical Society*, 75(12):953–956, December 2019.

68. E. H. Kisi and M. M. Elcombe. u parameters for the wurtzite structure of ZnS and ZnO using powder neutron diffraction. *Acta Crystallographica Section C Crystal Structure Communications*, 45(12):1867–1870, December 1989.

69. P. Kleimann, J. Linnros, C. Frojdh, and C.S. Petersson. An x-ray imaging pixel detector based on a scintillating guides screen. *IEEE Transactions on Nuclear Science*, 47(4):1483–1486, August 2000.

70. Glenn F. Knoll. Radiation measurement. Online, November 2017.

71. Miguel Lara-Castro, Adrian Herrera-Amaya, Marco Escarola-Rosas, Moisés Vázquez-Toledo, Francisco López-Huerta, Luz Aguilera-Cortés, and Agustín Herrera-May. Design and modeling of polysilicon electrothermal actuators for a MEMS mirror with low power consumption. *Micromachines*, 8(7):203, June 2017.

72. Chris Lee. Liquid shell gives inertial confinement fusion a smoother burn. Online, December 2016.

73. Jieun Lee. *Spatial and temporal control of quantum dots for on-chip integration.* phdthesis, University of Michigan, 2014.

74. Seungyong Lee. Synthesis of optimized inp/zns core/shell nanocrystals and tio2 nanotubes for quantum dot sensitized solar cells. Master's thesis, Sogang University, 2002.

75. Suhua Jiang Lei Du, Zhejun Liu. Inkjet-printed cdte quantum dots-polyurethane acrylate thin films. *Hindawi Journal of Nanomaterials*, July 2017.

76. E. Lifshitz, M. Brumer, A. Kigel, A. Sashchiuk, M. Bashouti, M. Sirota, E. Galun, Z. Burshtein, A. Q. Le Quang, I. Ledoux-Rak, and J. Zyss. Air-stable PbSe/PbS and PbSe/PbSexS1-xCore-shell nanocrystal quantum dots and their applications†. *The Journal of Physical Chemistry B*, 110(50):25356–25365, December 2006.

77. Jaehoon Lim, Wan Ki Bae, Donggu Lee, Min Ki Nam, Joohyun Jung, Changhee Lee, Kookheon Char, and Seonghoon Lee. InP@ZnSeS, core@composition gradient shell quantum dots with enhanced stability. *Chemistry of Materials*, 23(20):4459–4463, October 2011.

78. Heng Liu and Philippe Guyot-Sionnest. Photoluminescence lifetime of lead selenide colloidal quantum dots. *The Journal of Physical Chemistry C*, 114(35):14860–14863, August 2010.

79. William López-Pérez, Nicolás Simon-Olivera, Javier Molina-Coronell, Alvaro González-García, and Rafael González-Hernández. Structural parameters, band-gap bowings and phase diagrams of zinc-blende sc1-xInxP ternary alloys: A FP-LAPW study. *Journal of Alloys and Compounds*, 574:124–130, October 2013.

80. lumen. Huygens' principle. Online, 2018.

81. Zhiping Luo, John G Moch, Shardai S Johnson, and Chien Chon Chen. A review on x-ray detection using nanomaterials. *Current Nanoscience*, 13(4), July 2017.

82. S. Mahajan, Meenu Rani, R. B. Dubey, and Jagrati Mahajan. Synthesis of cdse crystal using hot injection method. *International Journal of Latest Research in Science and Technology*, 2(1):518–521, February 2013.

83. Petr Malinský, Petr Slepička, Vladimír Hnatowicz, and Václav Švorčík. Early stages of growth of gold layers sputter deposited on glass and silicon substrates. *Nanoscale Research Letters*, 7(1):241, 2012.

84. J. Casey Marnocha. Effect of wannier-mott exciton on semiconductor quantum dot photo-absorption spectra. Technical report, University of Wisconsin – Milwaukee, 2017.

85. Mathieu Massicotte, Fabien Vialla, Peter Schmidt, Mark B. Lundeberg, Simone Latini, Sten Haastrup, Mark Danovich, Diana Davydovskaya, Kenji Watanabe, Takashi Taniguchi, Vladimir I. Fal'ko, Kristian S. Thygesen, Thomas G. Pedersen, and Frank H. L. Koppens. Dissociation of two-dimensional excitons in monolayer WSe2. *Nature Communications*, 9(1), April 2018.

86. Daniel Craig Mayo. *Zinc Oxide Nanowire Gamma-Ray Detector with High Spatiotemporal Resolution*. PhD thesis, Vanderbilt University, May 2017.

87. Jordan McEwen. Jablonski diagram. Online, July 2016.

88. MEMSCAP. Polymumps. Online, 2012.

89. Matthew Millard. Fast fission neutron detection using the cherenkov effect. Master's thesis, Clemson University, December 2014.

90. Katharina Müller. Cherenkov radiation. Online, 2014.

91. Koichi Momma and Fujio Izumi. VESTA 3for three-dimensional visualization of crystal, volumetric and morphology data. *Journal of Applied Crystallography*, 44(6):1272–1276, oct 2011.

92. Douglas C. Montgomery. *Design and Analysis of Experiments*, chapter 6.3, pages 241–253. John Wiley & Sons, Inc., 8 edition, 2013.

93. Teja Muppirala. Creating a spherical matrix. Online, January 2013.

94. Ali Naeem, Francesco Masia, Sotirios Christodoulou, Iwan Moreels, Paola Borri, and Wolfgang Langbein. Evidence of giant oscillator strength in the exciton dephasing of cdse nanoplatelets measured by resonant four-wave mixing. April 2014.

95. Curtis Neveu. Concept of fret. Online, February 2016.

96. NIST. X-ray mass attenuation coefficients. Online, July 2004.

97. Y. Noda, S. Ohba, S. Sato, and Y. Saito. Charge distribution and atomic thermal vibration in lead chalcogenide crystals. *Acta Crystallographica Section B Structural Science*, 39(3):312–317, June 1983.

98. S. Normand, A. Iltis, F. Bernard, T. Domenech, and P. Delacour. Resistance to irradiation of LaBr3:ce and LaCl3:ce single crystals. *Nuclear Instruments and Methods in Physics Research Section A: Accelerators, Spectrometers, Detectors and Associated Equipment*, 572(2):754–759, March 2007.

99. K. Opachich, P. Ross, J. Koch, A. MacPhee, O. Landen, D. Bradley, P. Bell, S. Nagel, T. Hilsabeck, N. Chen, S. Udin, A. Gopal, and J. Feng. High yield structured x-ray photo-cathode development and fabrication. Technical report, National Security Technologies, LLC, October 2015.

100. Yekaterina Opachich, Andrew MacPhee, Otto Landen, Ning Chen, Ashwini Gopal, Salah Udin, Terry Hilsabeck, Eric Huffman, Jeffrey Koch, Jun Feng, Parick Ross, Dave Bradley, and Sabrina Nagel. High-yield x-ray photocathodes for next-generation imaging detectors. *Instruments, Detectors, and Sensors*, April 2017.

101. S. Ozturk and G. Unel. A simple cherenkov detector for educational purposes. August 2017.

102. Sayanu Pamidighantam, Robert Puers, Kris Baert, and Harrie A C Tilmans. Pull-in voltage analysis of electrostatically actuated beam structures with fixed–fixed and fixed–free end conditions. *Journal of Micromechanics and Microengineering*, 12(4):458–464, June 2002.

103. Jeong Min Park, Jae Hwan, JeonYoung Hee Lee, Dong Jin Lee, Hyun Park, Ho Hwan Chun, and Han Do Kim. Synthesis and properties of uv-curable polyurethane acrylates containing fluorinated acrylic monomer/vinyltrimethoxysilane. *Polymer Bulletin*, 72, April 2015.

104. Ammasi Periasamy and Richard Day. *Molecular Imaging: FRET Microscopy and Spectroscopy (Methods in Physiology Series)*, chapter 2, page 196. Academic Press, 2011.

105. Photek Limited, 26 Castleham Road, St Leonards on Sea, East Sussex, TN38 9NS, United Kingdom. *Photochron 5*, April 2017.

106. T. R. Pisanic II, Y. Zhang, and T. H. Wang. Quantum dots in diagnostics and detection: principles and paradigms. *The Analyst*, 139(12):2968–2981, June 2014.

107. Nuclear Power. Organic scintillators. Online, 2019.

108. Nuclear Power. Nai(tl) scintillation counter. Online, 2020.

109. PubChem. Octadecylamine. Online.

110. PubChem. Oleic acid. Online.

111. PubChem. Oleylamine. Online.

112. Devin Pugh-Thomas. *Luminescent Quantum Dots for High Temperature Sensing*. PhD thesis, University of Virginia, May 2012.

113. Riikka L. Puurunen, Jaakko Saarilahti, and Hannu Kattelus. Implementing ald layers in MEMS processing. In *ECS Transactions*. ECS, 2007.

114. Eric A. Quintero. The cosmic ray muon energy spectum via cerenkov radiation. Bachelors Thesis, Massachusetts Institute of Technology, June 2010.

115. Freddy T. Rabouw and Celso de Mello Donega. Excited-state dynamics in colloidal semiconductor nanocrystals. *Topics in Current Chemistry*, 374(5), August 2016.

116. Lewis S. Ramsdell. The crystal structure of some metallic sulfides*. *American Mineralogist*, 10(9):281–304, 09 1925.

117. T. S. Rao-Sahib and D. B. Wittry. X-ray continuum from thick elemental targets for 10–50-keV electrons. *Journal of Applied Physics*, 45(11):5060–5068, November 1974.

118. E. I. Rashba. Gigantic oscillator strengths inherent in exciton complexes. In *Springer Tracts in Modern Physics*, pages 150–170. Springer Berlin Heidelberg, 1975.

119. Soline Richard, Henri-Jean Drouhin, Nicolas Rougemaille, and Guy Fishman. Structure of spin-split evanescent states in the fundamental gap of zinc-blende-type semiconductors. *Journal of Applied Physics*, 97(8):083706, April 2005.

120. Michael Richmond. Counting gamma rays with a scintillation detector. Online.

121. Melissa A. Rivera. Metal to ligand and ligand to metal charge transfer bands. Online, September 2019.

122. Thiago Lopes Rocha, Nélia C. Mestre, Simone Maria Teixeira Sabóia-Morais, and Maria João Bebianno. Environmental behaviour and ecotoxicity of quantum dots at various trophic levels: A review. *Environment International*, 98:1–17, jan 2017.

123. Seth Rodriguez. Putting it all together - particle detectors. Online, 2015.

124. Nina Roelofs. Time of flight techniques. Online.

125. Nina Roelofs. Neutron time-of-flight. Online, 2019.

126. Saint-Gobain. Crystal scintillation materials. Online, 2018.

127. FRED SCHAUFELE, IGNACIO DEMARCO, and RICHARD N. DAY. FRET imaging in the wide-field microscope. In *Molecular Imaging*, pages 72–94. Elsevier, 2005.

128. E. Schrödinger. An undulatory theory of the mechanics of atoms and molecules. *Physical Review*, 28(6):1049–1070, December 1926.

129. Gurpreet S. Selopal, Haiguang Zhao, Guiju Liu, Hui Zhang, Xin Tong, Kanghong Wang, Jie Tang, Xuhui Sun, Shuhui Sun, François Vidal, Yiqian Wang, Zhiming M. Wang, and Federico Rosei. Interfacial engineering in colloidal "giant" quantum dots for high-performance photovoltaics. *Nano Energy*, 55:377–388, January 2019.

130. Michael Shattan. Linear and mass attenuation coefficients. Lecture, December 2018.

131. Nitzan Shauloff, Sagarika Bhattacharya, and Raz Jelinek. Elastic carbon dot/polymer films for fluorescent tensile sensing and mechano-optical tuning. *Carbon*, 152:363–371, November 2019.

132. Anastassios Siarkos. *Exciton Center-of-Mass Motion in Quantum Wells and Quantum Wires*. PhD thesis, Humboldt-Universitat zu Berlin, 2000.

133. Lutfan Sinatra, Jun Pan, and Osman M. Bakr. Methods of synthesizing monodisperse colloidal quantum dots. Online, 2017.

134. LaVern A. Starman. *CHARACTERIZATION OF RESIDUAL STRESS IN MICROELECTROMECHANICAL SYSTEMS (MEMS) DEVICES USING RAMAN SPECTROSCOPY*. PhD thesis, Air Force Institute of Technology, April 2002.

135. 3D Systems. Projet mjp 3600 series. Online, 2019.

136. PaR Systems. Radiographic non-destructive testing systems. Online, 2019.

137. Ali Taheri, Shahyar Saramad, Samira Ghalenoi, and Saeed Setayeshi. Fabrication, testing and simulation of a high spatial resolution alpha-particle imager based on ZnO nanowires in a polycarbonate nanoporous membrane. *The European Physical Journal C*, 73(12), November 2013.

138. Ali Taheri and Marzieh Sheidaiy. Scintillation and optical behavior of GaN nanowires in the presence of low-energy x-ray photons: A geant4 simulation. *Radiation Measurements*, 77:5–11, jun 2015.

139. Sydor Technologies. History. Online, 2020.

140. Ung Thi Dieu Thuy, Le Anh Tu, Nguyen Thu Loan, and Nguyen Quang Liem Tran Thi Kim Chi. Comparative photoluminescence properties of type-i and type-ii cdte/cds core/shell quantum dots. *Optical Materials*, 53:34–38, January 2016.

141. Kateřina Tomanová, Václav Čuba, Mikhail G. Brik, Eva Mihóková, Rosana Martinez Turtos, Paul Lecoq, Etiennette Auffray, and Martin Nikl. On the structure, synthesis, and characterization of ultrafast blue-emitting CsPbBr3 nanoplatelets. *APL Materials*, 7(1):011104, January 2019.

142. Philipp Tonndorf, Robert Schmidt, Philipp Böttger, Xiao Zhang, Janna Börner, Andreas Liebig, Manfred Albrecht, Christian Kloc, Ovidiu Gordan, Dietrich R. T. Zahn, Steffen Michaelis de Vasconcellos, and Rudolf Bratschitsch. Photoluminescence emission and raman response of monolayer MoS_2, MoSe_2, and WSe_2. *Optics Express*, 21(4):4908, February 2013.

143. Nicholas Tsoulfanidis and Sheldon Landsberger. *Measurement and Detection of Radiation*, chapter 8, page 247. Number 4. CRC Press, 2015.

144. Nicholas Tsoulfanidis and Sheldon Landsberger. *Measurement and Detection of Radiation*, chapter 4, pages 146–149. Apple Academic Press Inc., 2015.

145. Nicholas Tsoulfanidis and Sheldon Landsberger. *Measurement and Detection of Radiation*, chapter 8, page 249. Apple Academic Press Inc., 2015.

146. Mark E. Tuckerman. Fermi's golden rule. Online, April 2008.

147. R. M. Turtos, S. Gundacker, S. Omelkov, B. Mahler, A. H. Khan, J. Saaring, Z. Meng, A. Vasil'ev, C. Dujardin, M. Kirm, I. Moreels, E. Auffray, and P. Lecoq. On the use of CdSe scintillating nanoplatelets as time taggers for high-energy gamma detection. *npj 2D Materials and Applications*, 3(1), October 2019.

148. R.M. Turtos, S. Gundacker, A. A. Polovitsyn, S. Christodoulou, M. Salomoni, E. Auffray, I. Moreels, P. Lecoq, and J.Q Grim. Ultrafast emission from colloidal nanocrystals under pulsed x-ray excitation. *Journal of Instrumentation*, 2016.

149. Electronics Tutorial. Semiconductor basics. Online.

150. Ulrich, Zachariasen F., and W. Ueber die kristallstruktur des alpha-und beta-cd s, sowie des wurtzits. *Zeitschrift fuer Kristallographie*, 62:260–273, 1925.

151. Boston University. Electrons, photons, and the photo-electric effect. Online, August 1999.

152. C. Vatankhah and A. Ebadi. Quantum size effects on effective mass and band gap of semiconductor quantum dots. *Research Journal of Recent Sciences*, 2(1):21–24, January 2013.

153. Viribus. Led blacklight, gooseneck lamp with clamp, uv blacklight fixture for stain detection, black light lamp for blacklight posters, blacklight party, art – ultraviolet curing, great for fluorescent paint. Online, February 2017.

154. Gregory H. Wannier. The structure of electronic excitation levels in insulating crystals. *Physical Review*, 52(3):191–197, August 1937.

155. Nathan J. Withers, Krishnaprasad Sankar, Brian A. Akins, Tosifa A. Memon, Tingyi Gu, Jiangjiang Gu, Gennady A. Smolyakov, Melisa R. Greenberg, Timothy J. Boyle, and Marek Osiński. Rapid degradation of CdSeZnS colloidal quantum dots exposed to gamma irradiation. *Applied Physics Letters*, 93(17):173101, October 2008.

156. Long Xiao, Hui Tan, Li Tao, and Chun Wang. Break the electron speed limit to generate cherenkov radiation on a chip. In *2017 International Workshop on Antenna Technology: Small Antennas, Innovative Structures, and Applications (iWAT)*. IEEE, March 2017.

157. Hao Xu, Volodymyr Chmyrov, Jerker Widengren, Hjalmar Brismar, and Ying Fu. Mechanisms of fluorescence decays of colloidal CdSe–CdS/ZnS quantum dots unraveled by time-resolved fluorescence measurement. *Physical Chemistry Chemical Physics*, 17(41):27588–27595, 2015.

158. Weigao Xu, Weiwei Liu, Jan F. Schmidt, Weijie Zhao, Xin Lu, Timo Raab, Carole Diederichs, Weibo Gao, Denis V. Seletskiy, and Qihua Xiong. Correlated fluorescence blinking in two-dimensional semiconductor heterostructures. *Nature*, 541(7635):62–67, December 2016.

159. Jinlei Yao, Brent W. Rudyk, Carl D. Brunetta, Kathyrn B. Knorr, Heather A. Figore, Arthur Mar, and Jennifer A. Aitken. Mn incorporation in CuInS2 chalcopyrites: Structure, magnetism and optical properties. *Materials Chemistry and Physics*, 136(2-3):415–423, October 2012.

160. S.F. Yin, Z.M. Zhao, W.L. Luan, and S.-T. Tu. In-situ strain gauge: Based on photoluminescence of quantum dots. *Procedia Engineering*, 130:1788–1794, 2015.

161. Yumeng You, Xiao-Xiao Zhang, Timothy C. Berkelbach, Mark S. Hybertsen, David R. Reichman, and Tony F. Heinz. Observation of biexcitons in monolayer WSe 2. *Nature Physics*, 11(6):477–481, May 2015.

162. Peter Y. Yu and Manuel Cardona. *Fundamentals of Semiconductors*, chapter 3, pages 121–127. Springer Berlin Heidelberg, 2010.

163. Huai-Xin Wei Qing-Dong Ou Yan-Qing Li Jian-Xin Tang Yue-Qi Liu, Dan-Dan Zhang. Highly efficient quantum-dot light emitting diodes with sol-gel zno electron contact. *Optical Materials Express*, 2017.

164. B. Van Zeghbroeck. Chapter 2: Semiconductor fundamentals. Online, 2011.

165. Yang Zhang, Yan Chen, Michael Mietschke, Long Zhang, Feifei Yuan, Stefan Abel, Ruben Hühne, Kornelius Nielsch, Jean Fompeyrine, Fei Ding, and Oliver G. Schmidt. Monolithically integrated microelectromechanical systems for on-chip strain engineering of quantum dots. *Nano Letters*, 16(9):5785–5791, September 2016.

REPORT DOCUMENTATION PAGE

Form Approved
OMB No. 0704–0188

The public reporting burden for this collection of information is estimated to average 1 hour per response, including the time for reviewing instructions, searching existing data sources, gathering and maintaining the data needed, and completing and reviewing the collection of information. Send comments regarding this burden estimate or any other aspect of this collection of information, including suggestions for reducing this burden to Department of Defense, Washington Headquarters Services, Directorate for Information Operations and Reports (0704–0188), 1215 Jefferson Davis Highway, Suite 1204, Arlington, VA 22202–4302. Respondents should be aware that notwithstanding any other provision of law, no person shall be subject to any penalty for failing to comply with a collection of information if it does not display a currently valid OMB control number. **PLEASE DO NOT RETURN YOUR FORM TO THE ABOVE ADDRESS.**

1. REPORT DATE *(DD–MM–YYYY)*	2. REPORT TYPE	3. DATES COVERED *(From — To)*
03-26-2020	Master's Thesis	Jul 2018 - Mar 2020

4. TITLE AND SUBTITLE

X-Ray Detection and Strain Sensing Applications of Colloidal Quantum Dots

5a. CONTRACT NUMBER

5b. GRANT NUMBER

NA000103

5c. PROGRAM ELEMENT NUMBER

6. AUTHOR(S)

Sherburne, Michael D., 2d Lt

5d. PROJECT NUMBER

5e. TASK NUMBER

5f. WORK UNIT NUMBER

7. PERFORMING ORGANIZATION NAME(S) AND ADDRESS(ES)

Air Force Institute of Technology
Graduate School of Engineering and Management (AFIT/EN)
2950 Hobson Way
WPAFB OH 45433-7765

8. PERFORMING ORGANIZATION REPORT NUMBER

AFIT-ENG-M20-M-060

9. SPONSORING / MONITORING AGENCY NAME(S) AND ADDRESS(ES)

P-24 Plasma Physics Group, Physics Division Los Alamos National Laboratory
PO Box 1663, Mail Stop E526
Los Alamos, NM 87545
tweber@lanl.gov

10. SPONSOR/MONITOR'S ACRONYM(S)

LANL

11. SPONSOR/MONITOR'S REPORT NUMBER(S)

12. DISTRIBUTION / AVAILABILITY STATEMENT

Distribution Statement A. Approved for Public Release; Distribution Unlimited.

13. SUPPLEMENTARY NOTES

This work is declared a work of the U.S. Government and is not subject to copyright protection in the United States.

14. ABSTRACT

This thesis investigates CQDs as a fast 10 keV-100 keV x-ray scintillator by functionalizing and experimentally characterizing both the PL spectra and PL decay of eight varieties of CQDs. In addition, x-ray modeling was conducted to roughly compare scintillating capabilities between different CQDs. Ground work for future pulsed x-ray scintillator decay tests were discussed. All variants were evaluated for their stability and temporal decay characteristics. Functionalization used four fabrication methods: loading the nanomaterials into a polymer matrix, dispersion of CQDs as a thin-film on top of quartz, dispersion of CQDs within a 3D printed honeycomb matrix, and drawing them into a PCF. It was found that CQDs dispersed within a 3D printed honeycomb matrix showed CT properties which brought down their temporal PL decay time by at least half. In addition, the blue shifting of the emission wavelength in a CQD/SU-8-5 system due to CT could have useful implications in future photonic circuits. The fastest calculated biexponential model THA over the tested structures was seen in the CQD-loaded polymer matrix. Commercially available spherical CQDs showed a faster decay time than the experimentally commercially made NPLs. CdS showed to have the fastest decay time with a calculated biexponential model THA of 545 ps within a CQD-loaded polymer, but its QE was poor due to being a core-only material. InP/ZnS was the next fastest decaying material with a calculated biexponential model THA of 562 ps within a CQD-loaded polymer with a better QE due to being a core-shell which makes the most promising of the materials studied in this thesis for x-ray scintillating applications. Furthermore, x-ray modeling of alloyed CQD technology showed promise in higher QE for x-ray scintillation than conventional CQDs. In addition to the x-ray application oriented experiments, the stress-strain optical sensing properties of InP/ZnS were explored. Initial tests showed both useful and unique wavelength results of the CQD emission while undergoing strain when coated onto a pre-treated metallic surface. The optical spectra from the CQDs also showed the yield strength point of the material under strain. This could also have implications to quickly diagnose issues within 3D printed materials and later use on airframes.

15. SUBJECT TERMS

Fabrication, Non-Destructive Testing, quantum dots, temporal response, x-ray diagnostic.

16. SECURITY CLASSIFICATION OF:			17. LIMITATION OF ABSTRACT	18. NUMBER OF PAGES	19a. NAME OF RESPONSIBLE PERSON
a. REPORT	b. ABSTRACT	c. THIS PAGE			Major T. V. Laurvick, AFIT/ENG
U	U	U	UU	398	19b. TELEPHONE NUMBER *(include area code)* (937) 255-3636, x4382; tod.laurvick@afit.edu